UNIVERSITY OF SOUTHAMPTON

Faculty of Engineering and Physical Sciences
School of Electronics and Computer Science
Flexible Nanoelectronics

Polyoxometalate Nanoscale Electronic Devices

by

Emilie Gérouville

M.Sc.

ORCID iD: 0000-0003-2569-5198

A thesis for the degree of
Doctor of Philosophy

February 2025

University of Southampton

Abstract

Faculty of Engineering and Physical Sciences
School of Electronics and Computer Science

Doctor of Philosophy

Polyoxometalate Nanoscale Electronic Devices

by Emilie Gérouville

Electronic memories play a crucial role in our ever more digital world. Traditional technologies are reaching their limits as new computing paradigms continue to increase their demand for computing power, efficiency, and miniaturisation.[1] Resistive random access memories (RRAM) have emerged as promising candidates to solve these issues.[2] Specifically, polyoxometalate (POM) -based devices show particular potential due to their rich redox properties.[3]

This thesis explores the development of POM-based nanoscale electronic devices for next-generation memory applications and neuromorphic computing. Throughout this work, I show that the phosphomolybdate POM, $H_3PMo_{12}O_{40}$ is promising: it demonstrates rich redox activity especially when carefully deposited in nanogap separated Al/Au asymmetric coplanar electrodes.[4] By adding a thin poly(methyl methacrylate) (PMMA) layer between the metal electrodes and the POM film, device performance can be enhanced, while addressing challenges such as device-to-device and cycle-to-cycle variations. My analysis reveals that a complex combination of factors explains the switching mechanism of these devices including: the POM redox reactions, environmental factors such as moisture, and device structure-related effects.

I showcase the ability of these devices to mimic some operation of the biological brain and specific neural responses such as nociception, opening new possibilities for artificial neural network technologies.

This work advances the field of nanoelectronics by optimising both device architecture and material selection. My findings pave the way for the development of more efficient and tuneable bio-inspired computing systems. These POM-based devices offer solutions to overcome current technology limitations, potentially shaping future electronic systems.

Contents

List of Figures

List of Tables

Declaration of Authorship

I declare that this thesis and the work presented in it is my own and has been generated by me as the result of my own original research.

I confirm that:

1. This work was done wholly or mainly while in candidature for a research degree at this University;
2. Where any part of this thesis has previously been submitted for a degree or any other qualification at this University or any other institution, this has been clearly stated;
3. Where I have consulted the published work of others, this is always clearly attributed;
4. Where I have quoted from the work of others, the source is always given. With the exception of such quotations, this thesis is entirely my own work;
5. I have acknowledged all main sources of help;
6. Where the thesis is based on work done by myself jointly with others, I have made clear exactly what was done by others and what I have contributed myself;
7. None of this work has been published before submission

Signed:..... Date:.....

Acknowledgements

I would like to start by thanking my incredible supervisor: Dr. Dimitra Georgiadou. She has always been available to help me out regardless of time or topic. She was always active and involved in my work, pushing me to do my best. I would also like to thank Prof. Nick Harris who gave me some valuable advice on how to take a step back and see the project as a big picture.

I would like to also thank the technicians and lab managers without whom my work would have been literally impossible. Especially Gary Vaughan, Owain Clark, Neil Sessions, Andrew Gill, and Mike Perry. They are the ones getting things moving around the labs!

Thank you also to all of my colleagues for the fun times together: Chris Madden, Evangelia Founta, Evangelos Moutoulas, Yuxin Xia, Roshni Babu, Sujay Kumar Vishwanath, and Mohit Kumar Gautam.

Of course, I would not have been able to accomplish so much without the love and support of my family. I would like to thank Papy who was always happy to read over any of my works, and thank him for letting us stay at Casinha da Vinha to write this thesis! Many thanks also to my mom, dad and sister who were always there for me, even during the hard days. Thank you also to anyone who was just willing to hear me go on about my work!

And the most special and precious thanks for last: Tom. You are an amazing partner and carried me through everything! I could not have done it without you!

To Mamy

Chapter 1

Introduction

1.1 Electronic memories: challenges and opportunities

Electronic memories play a crucial role in our increasingly digital world. They store vast amounts of data which need to be rapidly accessible. As society continues to expand its demands on cutting-edge computing paradigms, these vital electronic components also need to push the limits of computing power, efficiency, and miniaturisation. Traditional memory technologies such as static random-access memory (SRAM), dynamic random-access memory (DRAM), and flash memory are struggling to keep up.[1] Their limitations are becoming more apparent as we move towards more complex and data-intensive applications such as artificial intelligence, and the Internet of Things (IoT).

Historically, there has always been a drive to develop faster computing technologies.[1] For example, the SRAM was physically moved for it to be closer to the central processing unit (CPU). The DRAM has its own high-speed bus to the CPU for it to load the operating system faster. In parallel, storage density was increasing at a staggering rate. Every two years, the number of transistors on a chip were doubling following Moore's law.[5] Currently, one remaining big challenge is the memory wall or Von Neumann bottleneck.[6] Transistor-based architectures (such as CPU and graphics processing unit, GPU) need to transport information between the memory and the processor, which requires lots of energy and time. To overcome this barrier, new solutions need to be developed. For example, more efficient electronic memory devices or improved computing techniques such as bio-inspired or in-memory computing.[7] Among the various novel memory technologies being researched, resistive random access memory (RRAM) has emerged as a promising candidate.[8,9]

RRAM devices offer several properties that could revolutionise electronic memories and help overcome the Von Neumann bottleneck.[10] They are two-terminal structures

sandwiching a carefully chosen switching material.[11–13] This active layer can switch between high resistance state (HRS) and low resistance state (LRS), representing binary data. This transition usually requires very little energy ($\approx 10^{-16}$ J/s).[14,15] They are faster (order of 100 ps) than the conventional hard disk drives (HDD) and flash memory.[16] Compared to the traditional SRAM and DRAM, it has higher density[17] as it can be extremely small (nanoscale)[18], even down to a single molecule[19–23] or monolayer[24]. These types of devices can also be integrated directly in the CPU or GPU, drastically reducing the energy and time needed to transport information.

RRAM devices also have the potential for multiple resistance states within a single cell, unlocking the door to multi-bit storage and expanding storage density. Redox-based RRAM (ReRAM), a subset of RRAM, are a good example.[25,26] ReRAM devices use ions generated by redox reactions to induce changes in resistance.[27] It is therefore possible to choose a material which can have multiple redox states and can therefore undergo a series of redox reactions, each corresponding to a unique resistance level. This interplay between chemistry and electronics creates a wide range of accessible states. This multi-state capability is especially promising for bio-inspired computing, where the aim is to mimic behaviour of biological neural networks. Other requirements for this are fast data access and efficient information processing. Overall, ReRAM multi-state possibilities align with these demands, and could bridge the world of electronics and biology.

However, ReRAMs also face challenges that need to be addressed before widespread adoption. A main concern is device variability: inconsistent performance between cells or even within a single cell.[28] It can present itself as fluctuations in switching voltages or resistance levels for example, making it difficult for reliable data storage and reading. Additionally, as mentioned above, there is a constant aim to lower the operating voltage and current to reduce power consumption.

In parallel, integration of ReRAMs into large-scale arrays adds new challenges. One issue is sneak paths, where unintended current flows through adjacent cells during read or write operations.[29] Another one is the ON/OFF ratio (the ratio between the HRS and LRS), which needs to be big enough to clearly distinguish the different states but can be challenging to maintain consistently across all devices and over time.[30] Cycling endurance and data retention time are other vital aspects.[31] ReRAM cells need to be reliably switched between states as many times as possible before degradation occurs (10^{10} cycles). It is important to ensure long-term data integrity under various environmental conditions. These issues highlight the need for new approaches in materials science and device architecture. New switching materials and electrode configurations need to be designed to mitigate these challenges and enhance the overall performance and reliability of ReRAM technology.

1.2 My approach

To address these challenges, I follow a two-part strategy: simultaneously optimising device architecture and material selection. I aim to develop ReRAM devices that overcome current limitations and pave the way for next-generation electronic memories.

The first part of my approach focuses on selecting a device architecture that can enhance the overall performance and reliability of ReRAM devices. I propose the implementation of asymmetric aluminium-gold coplanar nanogap separated electrodes, that offers some advantages over conventional vertical architectures. For instance, this design is better suited for hosting nanomaterials which typically do not form uniform films. In addition, the nanoscale of the gap ensures fast switching times, low power consumption, and high integration density.[32]

Traditionally, fabricating nanogap separated electrodes, especially with asymmetric metals, is costly and challenging (for example via electron-beam lithography). To overcome this, I will use the adhesion-lithography method.[33] This technique has several advantages. For example, it is capable of large-area patterning, is cost-effective, is compatible with flexible substrates, and provides high-throughput production. More details on this technique can be found in Chapter 4.

The second part is the selection of the active switching materials. As previously discussed, materials which can undergo multiple redox reactions are interesting for developing multi-bit storage devices. In this context, I have identified polyoxometalates (POMs) as promising candidates for ReRAM applications. POMs are a class of metal oxide clusters with many valuable properties.[34] Specifically, they have rich redox properties[35], they reversibly exchange multiple electrons with little structure change. Therefore, they can exist in multiple stable oxidation states, allowing for a wide range of discretely addressable resistance levels within a single memory cell as will be discussed in Chapter 3.[36–40]

The choice of POMs as the active material is further motivated by their unique physicochemical properties. They are easy to process as they are soluble in non-toxic water-based solvents[41]. They are also quite stable over a large range of temperatures (- 153 °C to 600 °C)[42,43], and it is possible to functionalise these molecules to tailor their properties to specific needs. For example, visible light functional groups can be added to make the POMs light-sensitive.[44,45] This could be used to control the memory state using light in addition to electricity.[46–52]

By combining these two approaches, I aim to create polyoxometalate-based nanoscale electronic devices with enhanced performance and functionality. This combination has the potential to create ReRAM devices that not only address current technological challenges but also open up new possibilities for neuromorphic computing. By

working on both architectural and material choices, I hope to contribute to the ongoing efforts to overcome the Von Neumann bottleneck and launch a new era of efficient, high-performance electronic memories.

1.3 Specific research objectives

Throughout this work on polyoxometalate-based nanoscale electronic devices, I will address a series of research questions.

The first objective of this project is to find the best methods to integrate POMs into the nanogap. More specifically, I will start by identifying the most suitable POM candidate and the optimal deposition technique. Then, I will try specific material combinations in order to enhance device performance.

The next goal is to disentangle the device operation mechanism. Therefore, I will begin by exploring how the POM rich redox properties affect device performance and if it is possible to control them to tune device operation. Next, other effects will be investigated such as environmental factors (moisture) and structural configurations.

The last aim is to use these POM-based devices in neuromorphic applications. I will investigate how they can be used to mimic complex behaviours of the biological brain and specific neurons.

By working through this plan, I aim to provide a better understanding of POM-based nanoscale electronic devices. This work seeks to connect material science and electronic device design to overcome current limitations and enable next-generation memory and computing technologies.

1.4 Summary and thesis outline

Overall, this work explores the use of polyoxometalate-based nanoscale electronic devices for neuromorphic computing. I will study material selection, switching mechanism and application in bio-inspired computing systems. The new knowledge generated throughout this project will help develop these memories to tackle the challenges conventional technologies face and open the door to new types of computing. The following chapters will cover the different aspects of this research.

First, a general overview of electronic memories is given in Chapter 2. It will present general concepts relevant to the field such as the fundamentals of ReRAM devices and in-memory computing techniques. Chapter 3 will narrow the scope to POM-based devices, explaining in greater detail the unique material properties that define the device performance.

Next, Chapter 4 describes the adhesion-lithography technique, used to fabricate the asymmetric aluminium-gold nanogap separated device electrodes. A selection of polyoxometalates are shown in Chapter 5, along with the optimising process of device fabrication to achieve optimal performance.

Chapter 6 delves into the different factors of the switching mechanism. More precisely, a combination of electrochemical studies, exploration of the effects of environmental factors and structural analysis are used to disentangle their different contributions. This understanding will help further optimise and control device performance and reliability.

Finally, Chapter 7 will showcase the use of these devices for neuromorphic applications. They will be used to mimic some learning processes that take place in the biological brain and the operation of some specific neurons (nociceptors).

The main findings and advancements made throughout this project are summarised in Chapter 8. I discuss the implications of this work for the fields of electronic memories and neuromorphic computing, and I suggest directions for future investigations.

This thesis aims to advance understanding of POM-based nanoscale electronic devices and how they might revolutionise memory technologies and computing architectures. By answering fundamental questions and exploring practical applications, this work seeks to contribute to the ongoing efforts to overcome current technological limitations and open the door to next-generation electronic systems.

Chapter 2

Electronic Memories

As mentioned in Chapter 1, as society becomes more digital, electronic memories serve as key components, holding information that drive analysis, creative solutions, and innovation. Currently, with the digitisation of nearly every aspect of our lives, the volume of data being produced is staggering. Therefore, traditional memory technologies such as static random-access memory (SRAM), dynamic random-access memory (DRAM), and flash memory are struggling to keep up.[1] New applications such as artificial intelligence and the Internet of Things require devices that are fast, energy-efficient, and dense. Resistive random access memories (RRAM) hold promise for low power consumption, fast switching times, and good scalability.[8,10] This chapter will discuss key concepts for these types of devices.

More precisely, resistive memories have some requirements.[26] Write pulses should have an amplitude of a few hundreds mV and duration shorter than 100 ns. The read voltage should be less than a tenth of the write voltage and the read pulse durations around the same time as the write pulse if not shorter. The read current should be minimum 1 μA and the ON/OFF ratio should be greater than 10. An ideal endurance ranges from 10^3 to 10^5 write/erase cycles. The data should be stored for at least 10 years under minimal stress (temperatures up to 85°C and constant read pulses) to be non-volatile. Of course, these values are guidelines: specific requirements vary depending on the target application.

A typical RRAM switching path is given in Figure 2.1. These devices operate based on a change in resistive state between two extreme states, high resistance state (HRS - n°1, 6) and low resistance state (LRS - n°3, 4) equivalent to the OFF and ON state or 0 and 1 in binary logic of a material (solid electrolyte[a], often a metal oxide) sandwiched between two electrodes. If the device switches from HRS to LRS, this process is called SET - n°2. The RESET process is when the device switches from LRS to HRS - n°5.

[a] A solid material that conducts ions but not electrons.

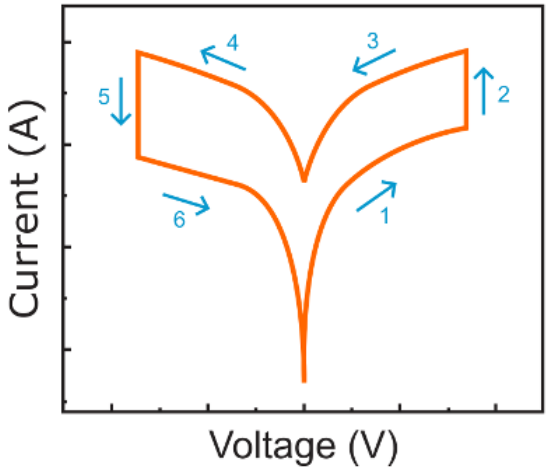

FIGURE 2.1: Typical I-V characteristic of a resistive memory device. Adapted with permission from[53]. Copyright 2019, Royal Society of Chemistry.

Resistive state switching can be induced by many ways[54] (see Figure 2.2), one of them being ion migration. If these ions were generated by an electrochemical process, the device is called redox random access memory (ReRAM).

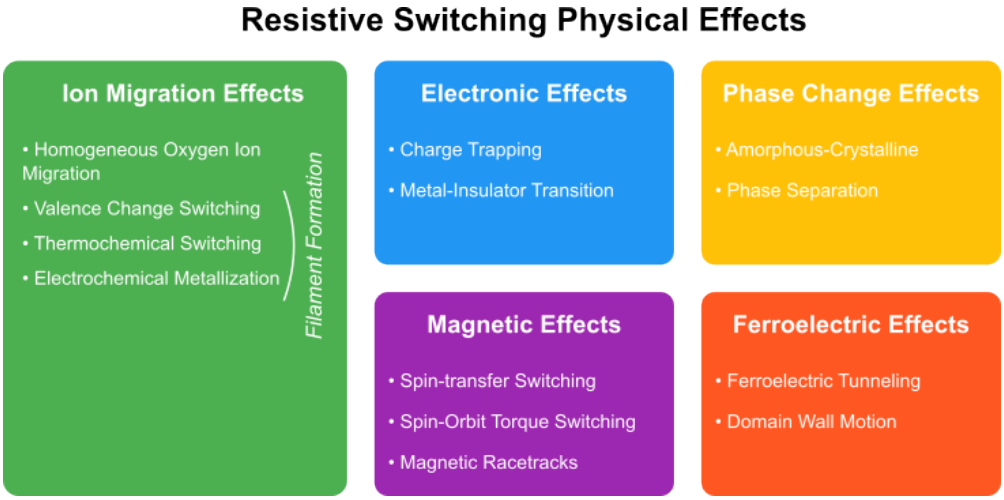

FIGURE 2.2: Possible physical effects in resistive switching memory devices. Adapted with permission from[54]. Copyright 2019, IOP Publishing.

2.1 Fundamentals of Redox-Based Resistive Switching Memories

This section will aim to explain the switching principles of redox-based resistive memories. As mentioned previously, these devices use migration of ions generated by a redox reaction in order to change the device resistance state, effectively switching it between two extreme resistance states. First, basic concepts of electrochemistry will be

introduced, followed by a more detailed insight into the possible resistive switching mechanisms.

2.1.1 Electrochemical reactions

Electrochemistry is the study of chemical processes that cause electrons to move, generating a current.[55] The electrons produced move from the oxidation to the reduction location. These reactions are called "*redox*" for short. Oxidation is the loss of electrons and reduction the gain of electrons:

$$\text{Reduction half reaction: } Ox_1 + n_1 e^- \rightleftharpoons Red_1$$

$$\text{Oxidation half reaction: } Red_2 \rightleftharpoons Ox_2 + n_2 e^-$$

$$\text{Total redox reaction: } n_2 Ox_1 + n_1 Red_2 \rightleftharpoons n_1 Ox_2 + n_2 Red_1$$

The current density produced by such reactions is given by the Nernst-Plank equation (see Equation 2.1). It takes into account the three mass transport mechanisms of ionic species mechanisms. Diffusion (first term) is the movement of molecules down a concentration gradient. Migration (second term) is the movement of ions under the influence of an electric field. Convection (third term) is due to the surrounding medium (often the liquid electrolyte) movement.

$$J = -D\nabla c - \frac{zF}{RT} Dc\nabla\phi + cu \tag{2.1}$$

With:
J: mass flux of an ionic species
D: diffusion constant
∇c: concentration gradient
z: ion charge number
F: Faraday constant
R: universal gas constant
T: temperature
$\nabla\phi$: electric field with ϕ the electrical potential
u: velocity of surrounding fluid

2.1.2 Principles of resistive switching

As mentioned above, many electronic and ionic effects come into play when switching RRAM devices between their two resistive states.[56] Here, I will detail further the very

common filament-based switching mechanisms.[57,58] More specifically, electrochemical metallisation switching memories (ECM)[59], valence change switching memories (VCM)[60], and thermochemical memories (TCM)[61]. ECM devices are based on the movement of metallic cations, while VCM devices use the movement of oxygen vacancy anions. Both of these types are bipolar (SET and RESET occur at opposite voltages), contrary to TCM type which is unipolar (SET and RESET occur at the same voltage polarity) and uses the movement of both cations and anions to operate. These mechanisms are called filamentary-based, as a conductive filament[b] is formed/ruptured to switch the device. The filament morphology is determined by many factors such as voltage, current, temperature, density and crystallinity of the solid electrolyte. The filament dynamics are mainly governed by the electrochemical reaction rate and ion mobility.[62]

ECM and VCM type devices often have an electroforming step. This step is done only once, the very first time the device switches from the HRS to the LRS. Often, a higher voltage than the subsequent cycles is needed. During this electroforming step, the main body of the conductive filament is built (= "*plug*" region), and will not dissolve entirely but rather only rupture when switching back to HRS as shown in Figure 2.3. Only the *disc* region will dissolve when the metal cations re-oxidise in the subsequent scans. In more detail, it is a thin region at the interface between the filament and one of the electrodes, typically the one with higher work function. This allows for a head start in the following cycles, explaining lower voltage requirements to switch. Therefore, even a relatively small change in the overall filament can lead to significant changes in the device resistance state.[60]

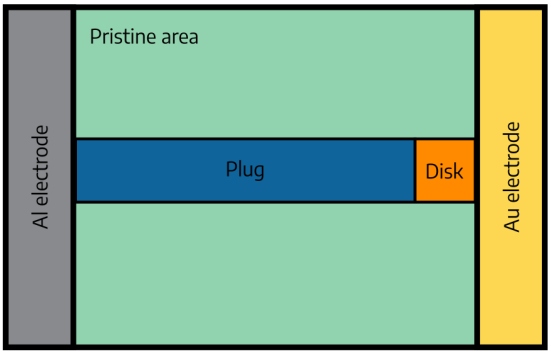

FIGURE 2.3: Sketch of conductive filament (CF) components: the plug is the main part of the CF and the disc simply connects the plug to the second electrode. Adapted with permission from[63]. Copyright 2012, John Wiley and Sons.

Finding and explaining the exact mechanism at the microscopic scale is a difficult task, but much progress has been done to characterise the switching process.[25,60] For example, by understanding the effect of moisture[64–66], material choice[57,67,68], or by trying to visualise the conductive filaments[67,69,70].

[b] A nanoscale conductive path formed in the insulating layer of a ReRAM device.

2.1.2.1 Electrochemical metallisation memory - ECM

ReRAM devices comprise a solid electrolyte between two electrodes. For ECM type devices, one of these electrodes must be "*active*", such as Ag or Cu. This means that it can electrochemically react to produce metal cations. The other electrode is called the counter electrode and must be "*inert*", for example Pt or Ir.[57] Therefore, a device stack could be Cu/HfO_2/Pt. To switch from the HRS to the LRS (SET process), the active electrode metal cations migrate to form a filament between the two electrodes. To switch from the LRS to the HRS (RESET process), this filament dissolves. There are many factors influencing this mechanism, which will be discussed in a following section. For instance, moisture, impurities, active and electrode[71] material choice.

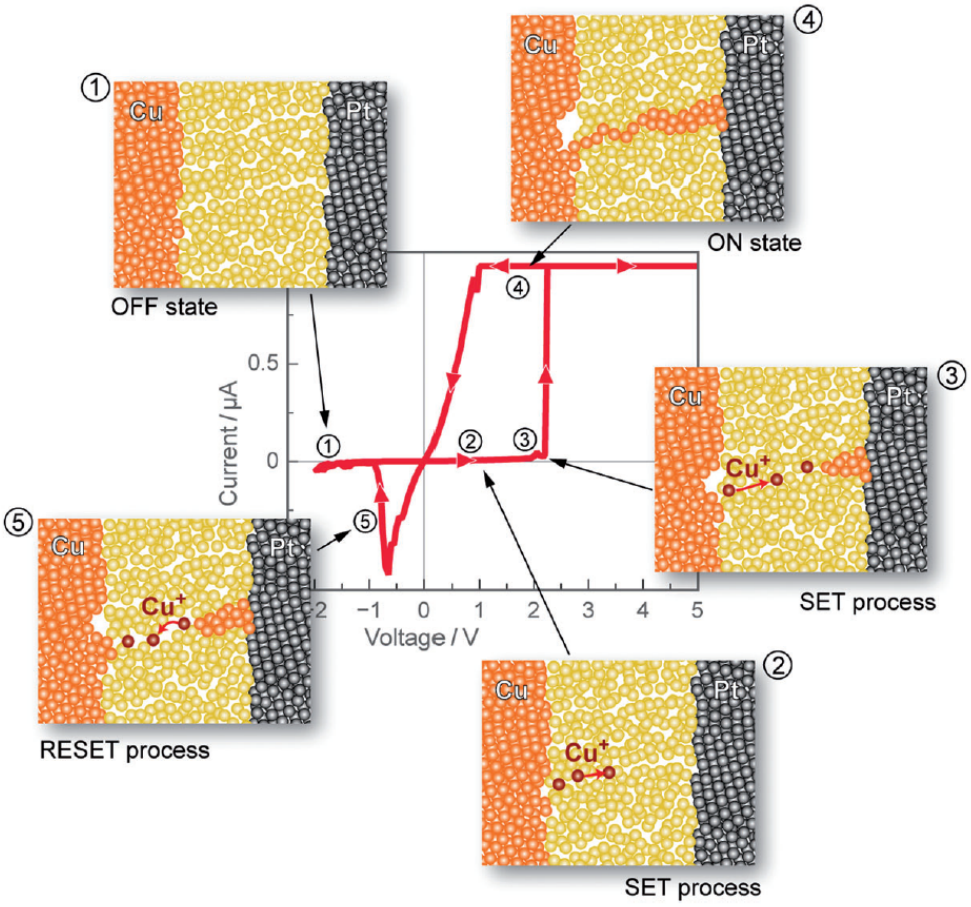

FIGURE 2.4: Schematic presentation of the processes during I-V sweep, including formation and dissolution of a metallic filament in electrochemical metallisation memories (ECM). The current saturation is due to the set current compliance (here 1 mA) used to prevent irreversible cell damage once the filament is formed. The value for the current compliance is chosen depending on the particular electrochemical system. It is also used to adjust the ON resistance (multi-level switching). The higher the current compliance is the lower is the ON resistance. Using different current compliances the ON resistance can be varied by orders of magnitude. Reproduced with permission from[25]. Copyright 2013, John Wiley and Sons.

The SET process is divided into three different steps (see Figure 2.4): 1. Oxidation of the active electrode to generate the metal cations by applying a potential, 2. Diffusion of these metal cations through the solid electrolyte, and 3. Nucleation and growth at the counter electrode. The RESET process is actually the oxidation of the filament, dissolving it by applying a reverse potential.[26]

2.1.2.2 Valence change memory - VCM

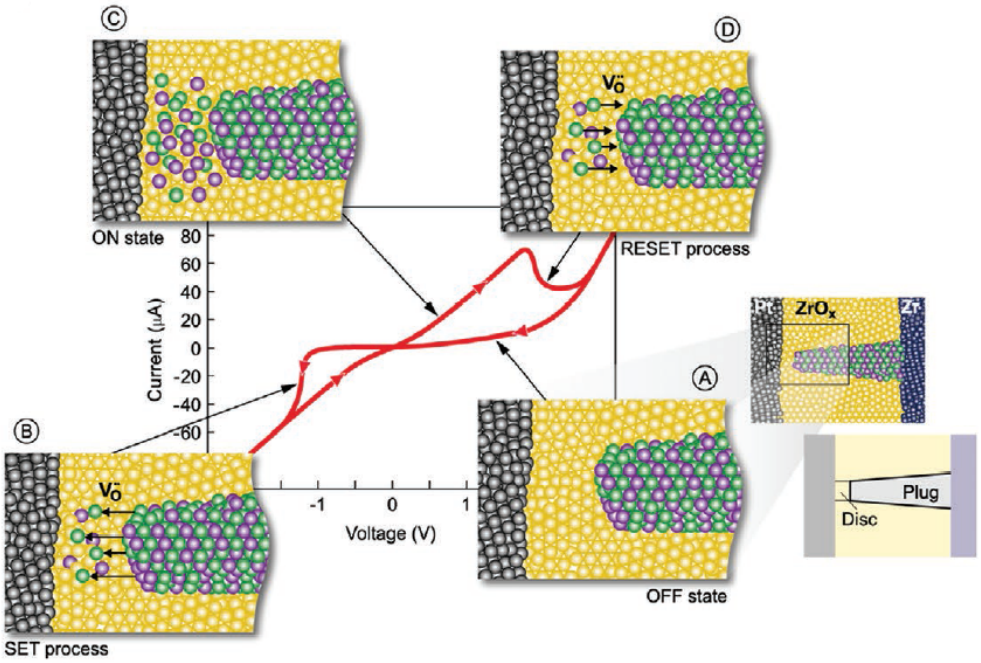

FIGURE 2.5: Schematic presentation of the operation principle and related I-V characteristic of a VCM cell. Pt-electrode is serving as a Schottky electrode with high work function; Zr is the ohmic electrode and ZrO_2 is the switching film. The device is SET to ON state within the disc. The undissolved filament behind is denoted as a plug. A is the OFF state, B represents the SET and C the ON state. The RESET process is given in D. Reproduced with permission from[63]. Copyright 2012, John Wiley and Sons.

For VCM type devices, the two electrodes also have some requirements to respect, but rather in terms of energy levels. One of the electrodes needs a high work function[c] in order to form a Schottky barrier[d] with the solid electrolyte, for example Pt or TiN. The other electrode needs to have a large oxygen affinity and form an Ohmic contact[e] with the solid electrolyte, such as Ta or Ti. This allows for redox reactions and/or ion exchange at the interface.[57] An example device stack is $Ti/HfO_2/Pt$. In this case, the switching is done by migration of oxygen vacancies (more mobile than metal cations)

[c]The minimum energy needed to remove an electron from a solid to a point immediately outside the solid surface.

[d]A potential energy barrier for electrons formed at a metal-semiconductor junction.

[e]Minimised energy barrier, allowing charge carriers to flow easily in both directions with minimal resistance.

which enriches or depletes an oxygen vacancy-based filament between the two electrodes, changing the valence state of the metal cations.

Switching occurs when a voltage is applied to the device (see Figure 2.5): this induces an increase in oxygen vacancy concentration near the cathode (n-conductivity), and therefore, an oxygen vacancy depletion in the larger cathode area (p-conductivity), this makes a p-n junction with diode like behaviour. The n-conductivity region propagates (called the virtual cathode) towards the anode. When the virtual cathode reaches or is near enough the cathode, the resistance drops and the device is switched to the LRS. If an opposite bias is applied, the oxygen vacancies are repelled from the anode and are pushed back towards the virtual cathode, breaking the filament and switching the device back to HRS.[26] Compared to ECM, the filament dissolves less during RESET: the "*plug*" is larger.

2.1.2.3 Thermochemical memories - TCM

These devices operate using thermal effects. A common example device would be Pt/NiO/Pt. As Joule heating (the process by which the passage of an electric current through a conductor produces heat) builds up in the device, redox reactions and ion migration can occur, building a conduction path through the solid electrolyte between two electrodes, switching the device to LRS. However, if the heating becomes too intense, the conduction path that is built can rupture, switching the device back to HRS. One way to control this is to set an adequate current compliance. If it is high, more current can flow which heats the device more.

The rupture mechanism shown in Figure 2.6 can be more detailed: as Joule heating increases, a high dissolution zone emerges leading to a hot spot. This increases the electric field and current density, and therefore the Joule heating. This creates a cycle as the dissolution also increases and so on, until rupture.

2.2 Effect of environmental moisture on ReRAM Performance

Now that some possible switching mechanisms for ReRAM devices have been detailed, it is important to understand the factors that can influence the device performance. For instance, material choice and device architecture can have a significant impact on the device switching characteristics, which will be discussed further in chapter Chapter 3. There are also environmental factors that can affect the device performance, such as moisture, which will be discussed in this section.

Moisture can play a vital role in the switching mechanisms presented above.[72] It is very hard to avoid moisture as it is in ambient air and can be absorbed through pores, grain

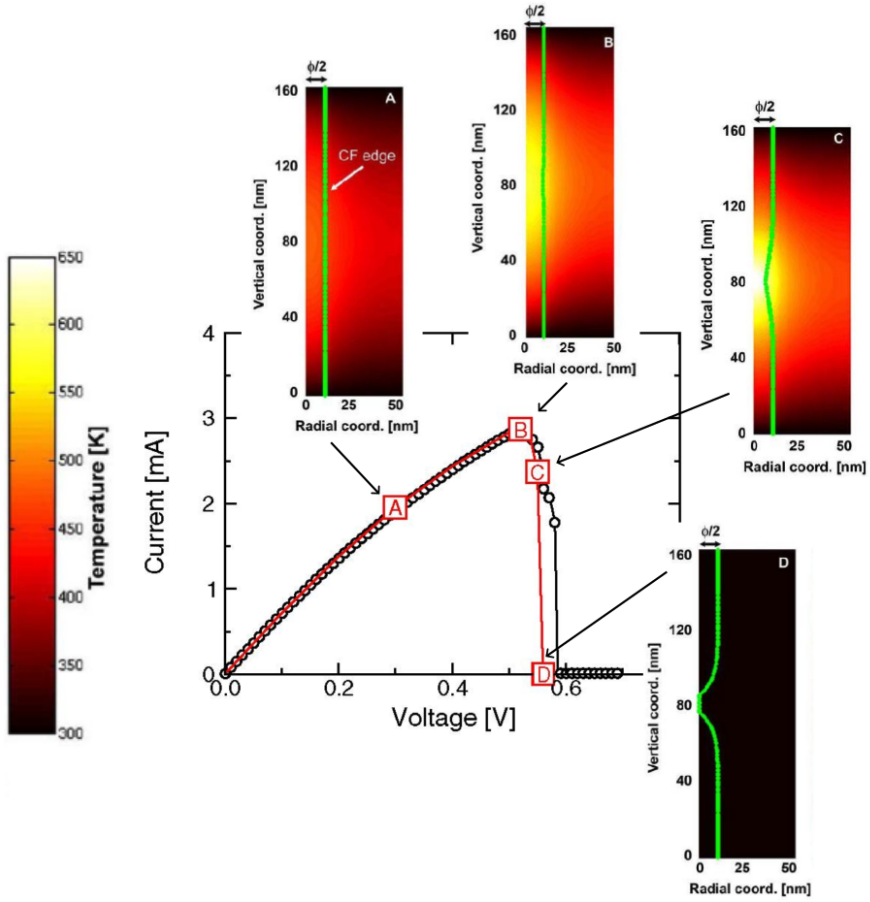

FIGURE 2.6: Simulation results for thermal dissolution of the conductive filament CF at different bias points. The dissolution is faster at the hot spot (the middle of the filament in the figure). The formation of a bottleneck further enhances Joule heating due to current crowding, resulting in a self-acceleration of RESET. Also shown (left) is the temperature profile along the cylindrical axis in the filament, for the four bias points. Adapted with permission from [61]. Copyright 2007, IEEE.

boundaries, and defects. The intake will also depend on the deposition parameters (technique, environment, ...). It is possible to remove moisture via annealing steps and/or placing the film in vacuum. Its three main impacts are:

1. to carry charges

Moisture can participate in increasing the conduction and hence reducing the resistance levels of the ON/OFF states of the device.[72–74] For instance by reducing the energy barrier for certain ions to migrate.[75,76] This is true up to a certain relative humidity (RH) percentage: where the maximum ion-ion interactions occur. If the RH is increased further, moisture may take over the reactions happening in the device.[65] Moisture can also be essential to the electroforming step, and therefore to the device switching.[27,64] For instance via helping the ions migrate through moisture H-bond matrix.[72] However, water can also increase resistance. It acts as a depletion region leading to upward band bending which decreases conductivity.[73,75,76]

2. to act as a candidate for counter reactions and/or produce counter ions

In ECM type devices, the active electrode reacts to produce metal cations which migrate to connect to the opposite electrode forming conductive filaments (CFs). Moisture can provide counter ions to these active metal ions. For example, OH^- ions (produced from water reduction) can counter-balance migrating Cu^{2+} ions (from copper oxidation reaction).[77] Note that the slowest reaction (water reduction or metal oxidation) is the one which will impact the device performance the most.[76]

Moisture can also react with the counter electrode even if it is made of noble metals (Pt, Pd). Therefore, even the "inert" electrode in ECM and VCM devices can participate in the formation of CFs, blurring the border between these two types of devices.[27]

3. to degrade materials via its corrosive properties

Moisture can undergo hydrolysis and decompose many materials. This can lead to unstable ON/OFF states. Usually this impact is bigger for high humidity conditions ($\geq$ 80 % relative humidity): bubbling can even occur at the electrodes due to O_2 and H_2 evolution. This can lead to formation of defects.[72]

2.3 In-memory computing with ReRAM devices

Once ReRAM devices have been optimised and understood in order to control their switching characteristics, they can be used to solve the memory wall mentioned in Chapter 1: moving data between the storage and processing units. For example, by performing computation tasks in memory.[78–81] These computing tasks can be digital or analogue, and are therefore performed differently and require different types of devices.[82]

2.3.1 Digital computing

Digital computing requires only two logic values: true or "1", and false or "0". In resistive memories, this can correspond to the LRS and HRS respectively. The idea is to input a voltage, and observe how this affects the device. Based on the result of the operation, a Boolean logic operator can be evaluated. Some examples of Boolean operators are "NOT", "AND", "OR", "XOR". There are different ways to exploit switching between these two resistance states to perform in memory computing. Figure 2.7 shows some examples which are detailed below.

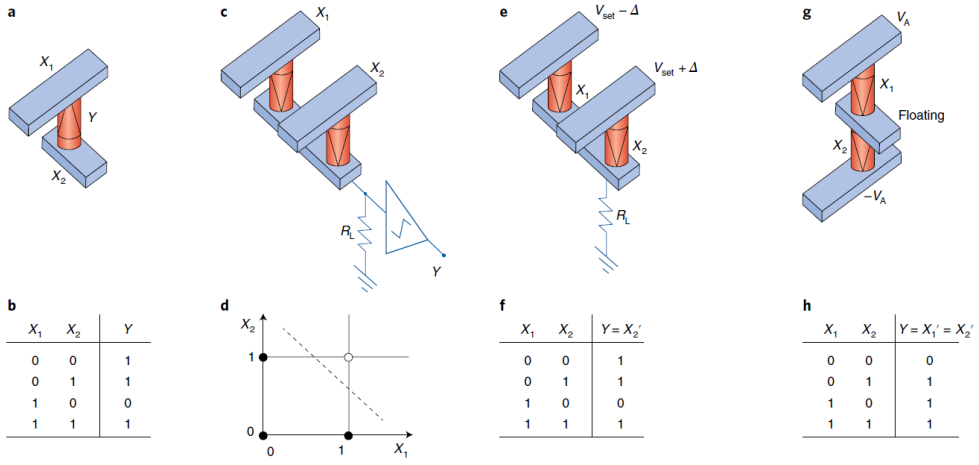

FIGURE 2.7: a, b, V-R logic gate (a) and corresponding truth table for material implication (IMP) operation (b). c, d, V-V logic, also known as the threshold logic gate (c), and the corresponding input/output characteristic for AND operation (d). e, f, Parallel R-R stateful logic gate for IMP operation (e) and corresponding truth table (f). g, h, Serial R-R stateful logic gate for OR operation (g) and corresponding truth table (h). Reproduced with permission from[83]. Copyright 2018, Springer Nature.

- V-R logic gate

Figure 2.7a shows an example of V-R logic gate, which requires only one device. The inputs are the voltages applied at the two electrodes (X_1, and X_2), and the output is the resulting resistance state of the device (Y). There are four input possibilities. If the voltages at the two electrodes are equal ($X_1 = X_2 = 0$ or $= 1$), the voltage across the device is cancelled (is zero), therefore, the device does not switch and remains in its initial state, for example "1" (LRS). Now, if the input voltages are different, switching only occurs for $X_1 = 1$ and $X_2 = 0$. If $X_1 = 0$ and $X_2 = 1$, the device will not switch as it is already in state "1". These four possibilities are summarised in Figure 2.7b. When looking closer at this logic table, the IMPLY Boolean logic operator appears.

- V-V logic gate or threshold logic

There are some limitations with the V-R logic gate. Cascade computing is the ability to chain multiple logic operations together, where the output of one operation directly serves as the input for the next. It is therefore not possible with V-R logic gates as the input and output are physically different (voltage and resistance state respectively). It is possible to translate the resistance state to a voltage, but this requires large circuits outside the memory. Another solution is to use a V-V gate, shown in Figure 2.7c. This setup is more complex as it requires 2 devices in parallel.

The inputs are the voltages applied to the individual devices, and the output is the resulting total voltage across both devices. This output voltage is compared to a threshold voltage and then characterised as "high" or "low", "1" or "0" respectively. For this

reason, this logic gate can also be named threshold logic gate. In Figure 2.7d, only the data point where both devices are in the "1" state is white.

V-V logic gates require a large external circuit to function properly as the output voltage needs to be compared to a threshold voltage. To remove this comparison step, and perform true in memory computing, or stateful logic, R-R logic gates can be used. These also require two devices in parallel.

- R-R logic gate or stateful logic

For R-R logic gates (shown in Figure 2.7e), the input is the resistance state of the first device, and the output is the resistance state of the second device. To operate this logic gate, voltages are applied to the two devices separately. The applied voltages are the set voltage +/- a small fraction of this set voltage (for example 10%): $V_{SET} \pm \Delta$. There are again four possibilities. If the first device is in the HRS, and the voltages applied to the first and second devices are $V_{SET} + \Delta$ and $V_{SET} - \Delta$, the voltage falls entirely onto the second device, therefore switching it to the LRS. However, if the first device is in the LRS, the first device will switch and only 2Δ voltage is applied to the second device, therefore not switching it. All the possibilities are summarised in the logic table Figure 2.7f. Looking closer at this table, the IMPLY Boolean operator can also be recognised.

In this configuration, it is possible to apply a second set of voltages to perform a second operation directly after the first, and so on sequentially. This means that this circuit can perform true computing in memory. To build different Boolean operators, it is possible to modify slightly the device arrangement. For example, in Figure 2.7g, an OR Boolean operator is shown by placing two memory devices in series. If the two devices are in the same state, the voltage divides equally between them and will be too low to switch them. However, if they are in different states, the device in HRS will receive enough voltage to SET, and therefore switch. The four possibilities are summarised in Figure 2.7h, and indeed show an OR logic table.

2.3.2 Analogue computing

Analogue computing can handle continuous data, and perform operations on them, for example addition, subtraction, multiplication, and division. Therefore, analogue computing requires a gradient between the two extreme states of digital computing. In resistive memories, this can be multilevel type devices. For example, sequential cycle modulation[84]: as more cycles are done on a single device, more redox reactions occur generating more ions. Therefore, when looking at a specific voltage, the current will linearly increase (or decrease depending on the voltage polarity) with the number of scans as shown in Figure 2.8a and Figure 2.8b.

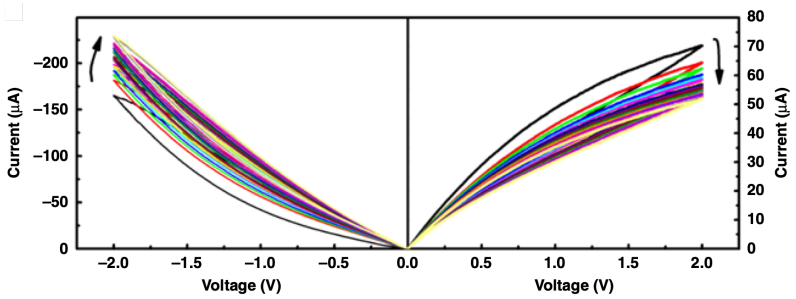

(A) Current-voltage curves of the ITO/PFTPA-Fc/Pt device.

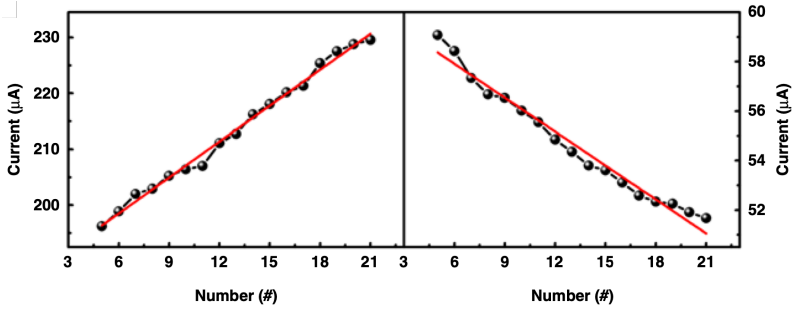

(B) Linear relationship between the device currents read at ± 2 V and voltage sweeping numbers.

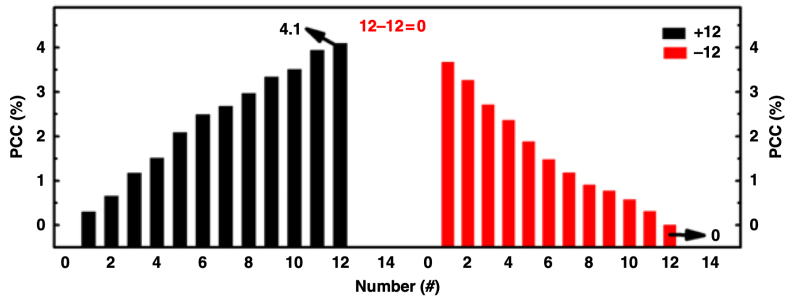

(C) Calibration of the PFTPA-Fc memristor with the operation of 12 - 12 =0 for decimal arithmetic calculations.

FIGURE 2.8: Consecutive memristive switching characteristics in low resistance state. Reproduced from[84]. Available under a CC-BY 4.0 licence.

With this sort of computing, the device must be calibrated: the percentage of current gained as cycles are performed must be determined. For this, an $X - X = 0$ operation is performed, i.e. X voltage pulses are applied to the device followed by X opposite polarity voltage pulses. After the first X pulses are applied, the current increase percentage is calculated and is associated to the number X. After the second batch of X pulses, this percentage should back to 0%.

In the example shown here, $X = 12$, and $12 = 4.1\%$ current increase (see Figure 2.8c). Knowing this, when they applied 5 pulses then 7 pulses, they observed a 4.1% current increase and indeed performed the "$5 + 7 = 12$" operation. To perform the other mathematical operations such as subtraction, opposite polarity voltage pulses can be applied, or multiplication, groups of pulse trains can be applied. Division $X \div Y$ is also possible, but requires a few steps as shown in Figure 2.9. First, load X then subtract Y

until the remainder (r) is smaller than Y: $X - Y - Y \ldots$. Second, change the remainder to $r \times 10$ or $r + r \times 9$. Finally, repeat these two steps until the remainder becomes zero: $r = 0$. In the same above example, $7 \div 5 = 1.4$ operation was performed. 7 was loaded, then 5 was subtracted once giving a quotient of 1 and a remainder of 2. The remainder was then changed to 20, and 5 was subtracted 4 times. Since only one remainder change was done, 4 is at the tenths position, and the quotient was 1. Therefore, the solution is indeed 1.4.

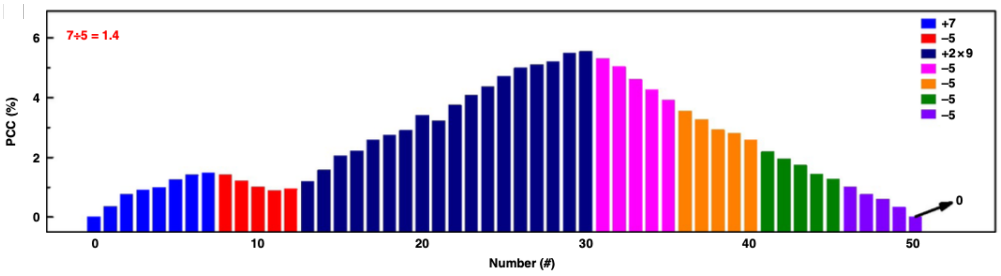

FIGURE 2.9: Fractional division conducted with a ReRAM device. Reproduced from [84]. Available under a CC-BY 4.0 licence.

2.3.3 Neuromorphic Computing with ReRAM

Neuromorphic computing aims to process information in a way similar to how biological neurons networks or the brain function.[85–87] ReRAM devices are good candidates for artificial neurons as they can present analogue behaviour, require low power, are non-volatile, and can be scaled down to the nanoscale.[54,88–91]

2.3.3.1 Biological systems

Figure 2.10a shows the structure of biological neurons. They are made of three main parts: cell body, dendrites, and axon. The cell body contains the nucleus and organelles. The dendrites are the receiving/input end of the neuron, and the axon conducts the nerve impulse to other neurons, muscle fibres, ... The axon terminates in axon terminals, which divide into synapses to connect two different neurons. There are two types of synapses (see Figure 2.10b): electrical and chemical. In electrical synapses, the two neurons are very close ($\approx$ 3 nm). In chemical synapses, the two neurons are slightly further apart ($\approx$ 20-25 nm), and require neurotransmitters to bridge the synaptic cleft.

In these neurons, information is carried as electrical signals. These electrical currents are ionic in nature, and are due to a change in polarisation of the cell membrane. If this change is above a certain threshold, an action potential or spike is generated. These action potentials can be carried along the neuron axon, and be transferred between two different neurons.

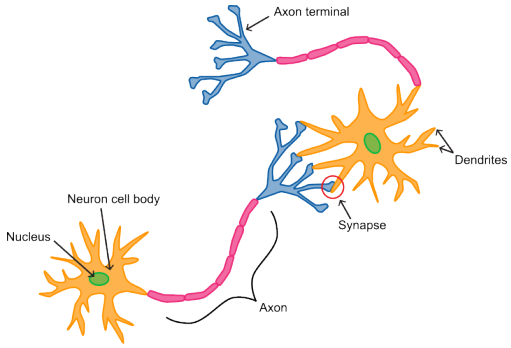

(A) Structure of multipolar neurons.

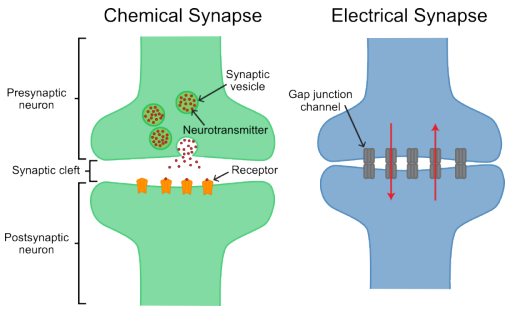

(B) Chemical and electrical synapses. Adapted with permission from [92]. Copyright 2014, Springer Nature.

FIGURE 2.10: Biological neurons and synapses structures.

Figure 2.11a shows the state of the membrane polarisation when resting. The inside of the membrane is negatively charged (majority of negatively charged proteins and phosphate ions), and the outside is positively charged (majority of Na^+ ions). These charges are separated which is a potentiation energy in volts, the resting potential. For most neurons, this value is ≈ -70 mV. The action potential is generated if the membrane is depolarised (i.e. its potential becomes less negative) to a certain threshold, usually ≈ -55 mV.

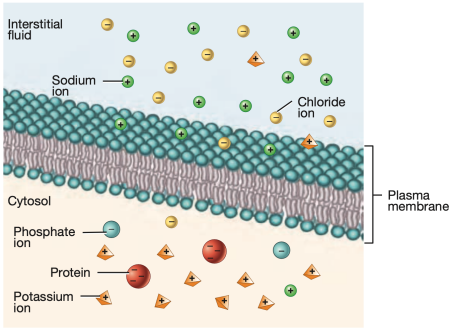

(A) The distribution of ions that produces the resting membrane potential.

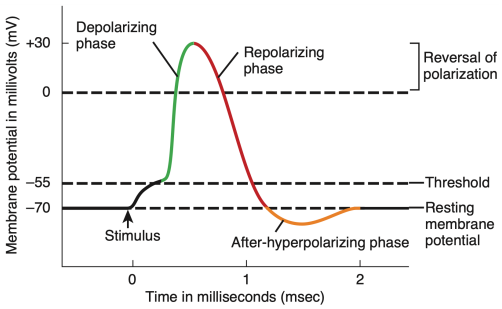

(B) When a stimulus depolarises the membrane to threshold, an action potential is generated.

FIGURE 2.11: Neuron plasma membrane and its polarisation over time. Reproduced with permission from [93]. Copyright 2017, John Wiley and Sons.

Figure 2.11b shows the action potential generation over time. At first, the membrane is slowly depolarised until the threshold. When this threshold is reached, voltage-gated ion channels open. The Na^+ channel opens quite fast, so Na^+ ions rush into the cell which quickly depolarises the membrane further. At some point, the K^+ ion channel also opens, so K^+ ions can flow out of the cell to compensate for the extra positive charges that entered the cell. This is called the repolarisation phase. Since K^+ channel is also slow to close, the membrane can get hyperpolarised for a short time (the membrane potential is more negative than its resting potential). Once the K^+ channel is fully closed, the membrane then returns to its resting potential. After generating this

action potential, there is a refractory period during which the neuron can not generate another action potential.

The action potential generation follows the all-or-nothing principle. This means that if the threshold is reached, the action potential is generated, its amplitude, and propagation speed is always the same. However, if the threshold is not reached, the action potential simply will not be generated.

Now that the action potential is generated, it can be carried along the cell axon. As the ion channels where the action potential was generated opened, this also caused the adjacent area to depolarise due to the Na^+ ions leaving the interstitial fluid. Therefore, adjacent areas also got depolarised to the threshold and open their ion channels and so on. This is called the positive feedback effect. The action potential self conducts along the axon membrane.

However, when the action potential reaches the end of the axon, it must communicate with a neighbouring neuron. This is called the synaptic transmission as these events occur at the synapse. In the chemical synapses, the action potential reaches the synaptic end bulbs of the pre-synaptic neuron which depolarises the membrane which in turn opens the Ca^{2+} ion channels. The Ca^{2+} ions rush into the synaptic bulb ends and causes the synaptic vesicles to release neurotransmitters into the synaptic cleft. These neurotransmitters diffuse to the neurotransmitter receptors on the post-synaptic neuron membrane. This opens ion channels which allow ions to flow changing the membrane potential. If the membrane potential reaches the threshold, a new action potential is generated and the process continues. The electrical synapses the action potential is directly transferred between them since they are physically close enough.

2.3.3.2 Modelling biological neurons

To link biology and electronic devices, there are many models which can be used (see Figure 2.12).[15,94]

When trying to mimic the synaptic transmission, the electrodes of a 2-terminal device can be seen as the pre-synaptic and post-synaptic neurons and the action potential is a voltage pulse. Typically, the objective is to replicate important behaviours from the brain such as plasticity or potentiation and depression, short and long term memory (STM, LTM), learning and forgetting.[89] These behaviours can be tuned depending on the pulse scheme applied (pulse duration, amplitude, frequency, ...). In Chapter 7, I will aim to mimic these behaviours with my own devices.

Plasticity means that the synaptic weight (the strength/amplitude of the connection between the two neurons) can be strengthened (potentiation) or weakened (depression). In a device sense, as voltage pulses are applied, the current level (or synaptic weight)

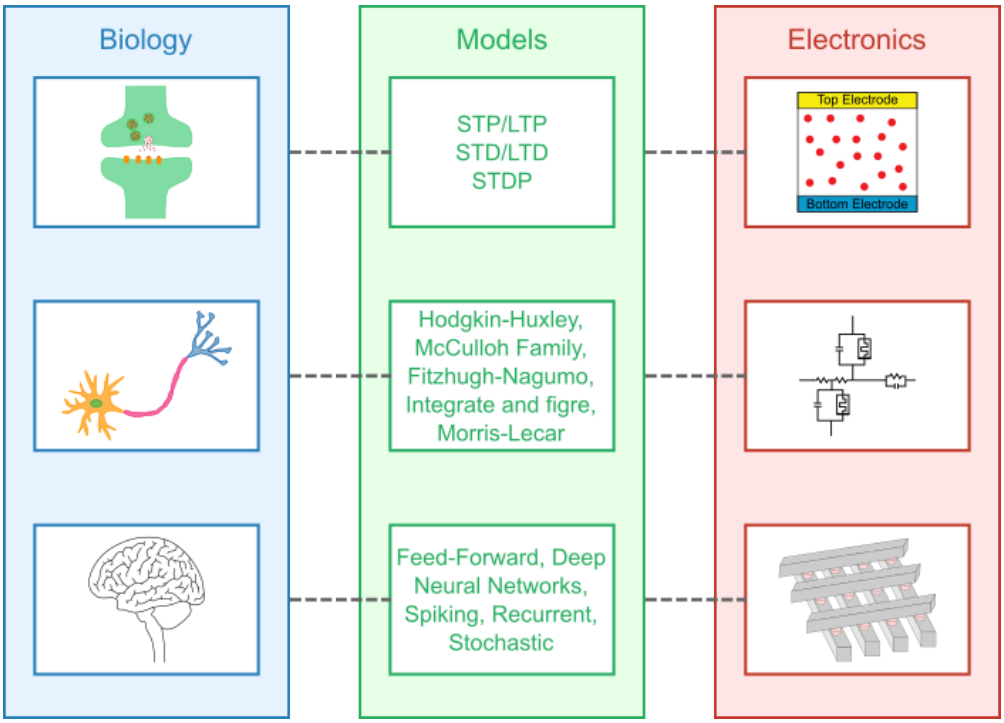

FIGURE 2.12: Various models used to link different levels of biology and electronic devices. Adapted with permission from [15]. Copyright 2019, John Wiley and Sons.

should increase or decrease respectively. Usually, this can be achieved by applying opposite polarity voltage pulses. However, Wang et al. have shown depression with consecutive pulses with the same polarity.[95] Their device design uses Ag nanoclusters embedded in dielectric film between inert Pt or Au electrodes. They mention that the Ag can gradually deplete at one electrode and accumulate at the other. By fine-tuning the pulse frequency, they can affect Ag accumulation/depletion speed and selectively induce potentiation or depression (see Figure 2.13).

As the name suggests, short (STM) and long (LTM) term memory imply the duration of the potentiation/depression effect. In biology, STM holds little information for immediate use while LTM stores more information and of prior events.[96] It is possible to change from STM to LTM by applying multiple pulses in a repeated manner: the more pulses are applied, the longer the memory.[97]

If no more voltage pulses are applied, the current will naturally decay back to its original state. This can be seen as forgetting. If re-learning is required, fewer pulses should be necessary to reach a similar current level compared to the initial learning step.

There are more models that aim to explain the action potential generation and conduction through a single neuron axon.[98] For example, the Hodgkin-Huxley model[99] is a series of differential equations which mathematically describe the flow of both Na^+ and K^+ ions during the action potential generation. The main equation describes the current I flowing through the membrane:

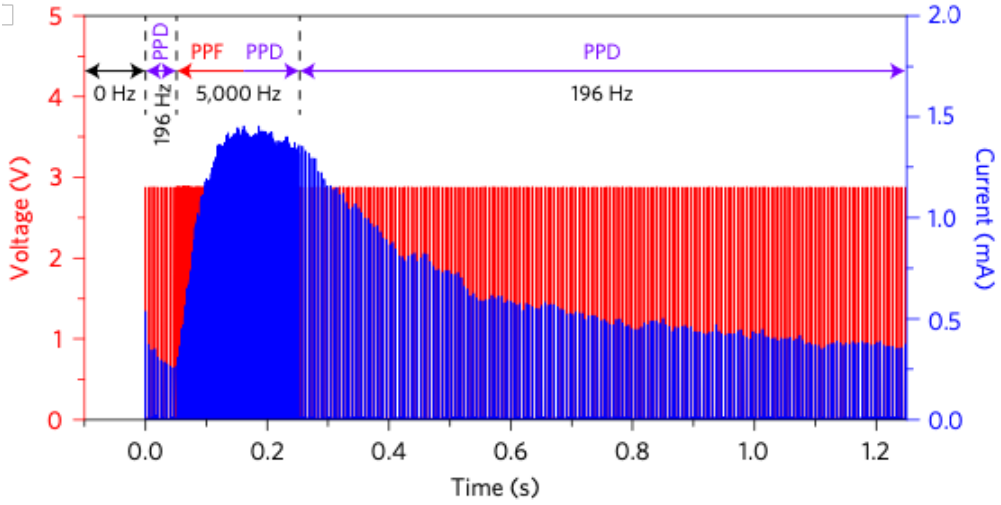

FIGURE 2.13: Experimental demonstration of paired pulse depression (PPD) following paired pulse facilitation (PPF) in the diffusive SiO_xN_y:Ag memristor by tuning the applied pulse frequency. PPD and PPF are observed for low-frequency (196 Hz) and high-frequency (5 000 Hz) respectively. Reproduced with permission from [95]. Copyright 2016, Springer Nature.

$$I = C_m \frac{dV_m}{dt} + g_{Na} m^3 h (V_m - V_{Na}) + g_K n^4 (V_m - V_K) + g_L (V_m - V_L) \tag{2.2}$$

With:
C_m: membrane capacity per unit area
V_m: membrane potential
g_{Na}: Na^+ conductance
m: Na^+ channel activation subunit
h: Na^+ channel inactivation subunit
V_{Na}: Na^+ displacement potential from the resting potential
g_K: K^+ conductance
n: K^+ channel activation subunit
V_K: K^+ displacement potential from the resting potential
g_L: leak conductance
V_L: leak displacement potential from the resting potential

Note: The subunits mentioned above are the proteins which change conformation to open/close the ion channels. Therefore, these values depend on time.

The first term is the capacitance term, the second term is the Na^+ current, the third term is the K^+ current, and the last term is the leak current. The following equations are used to determine the subunits m, h, and n:

$$\frac{dm}{dt} = \alpha_m(V_m)(1 - m) - \beta_m(V_m)m \tag{2.3}$$

$$\frac{dh}{dt} = \alpha_h(V_m)(1-h) - \beta_h(V_m)h \tag{2.4}$$

$$\frac{dn}{dt} = \alpha_n(V_m)(1-n) - \beta_n(V_m)n \tag{2.5}$$

Together, these 4 equations form the Hodgkin-Huxley ordinary differential equations (ODE). Their strength is the accuracy with which they describe the action potential generation and conduction in a neuron. However, they contain many parameters and many constants which need to be known to solve these equations. Pickett et al. have managed to use these equations to describe their neuristor made of two NbO_2-based nanoscale Mott memristors.[100]

As these devices aim to be as efficient as the brain (pJ per operation), there is much research in this area to expand it to new device architectures (for example to include light as stimulus[50,88,101]) and new materials (i.e. such as organics[102] and polyoxometalates[103]).

2.3.4 Case study: Nociceptor implementation with ReRAM

A specific example of neurons is the nociceptor. More precisely, it is a sensory neuron receptor that can sense noxious stimuli i.e. damage or potential damage to the body (mechanical stress, extreme heat, chemicals, ...).[93] Therefore, their main role is to transmit pain from the peripheral nervous system to the central nervous system. Again, there is a pre-set noxious threshold, which, when crossed, generates an action potential to generate a motor response.

The nociceptors operate in three modes: normal, relaxation, and sensitised. By default, when the nociceptor is in "normal" mode, no adaptation occurs. It enters the "relaxation" state when it detects a potential noxious stimulus. It gains an enhanced sensitivity and speed allowing it to respond as needed. If the stimulus is very intense, the nociceptor enters the "sensitised" mode, where it can either decrease the threshold (= allodynia) or increase the response (= hyperalgesia). These modes help the nociceptor to minimise response time in case of emergency.[104]

Drift and diffusive memristors are good candidates to mimic nociceptors.[105,106] Drift memristors can update weights for read-out layers, while diffusive memristors can be used as selectors, as they can filter out noxious signals, similarly to nociceptors. To realise these devices, ionotronic materials are ideal as they allow both ions and electrons to flow.

Rohit Abraham John et al.[105] opted for a halide perovskite, methylammonuim lead bromide ($CH_3NH_3PbBr_3$), as the active layer due to its rich ionic and electronic properties. On either side, they deposit a hole (HTL) and electron (ELT) transporting layers, PEDOT:PSS with an optional NiO_x layer and PO-T2T, respectively. These layers are themselves connected to ITO and Al electrodes, respectively (see Figure 2.14).

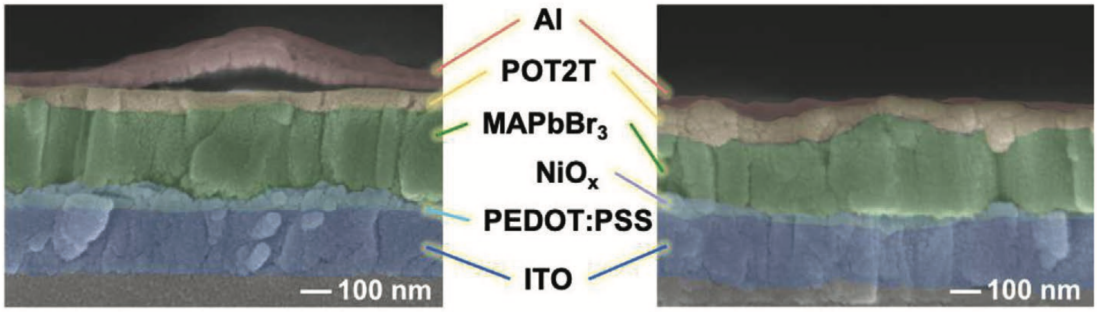

FIGURE 2.14: Cross-sectional SEM images of the diffusive and drift memristor structures with PEDOT:PSS and NiO_x hole transporting layers. Reproduced with permission from[105]. Copyright 2021, John Wiley and Sons.

They used the diffusive (no NiO_x layer) memristors as an artificial nociceptor, which they operated with voltage pulses (see Figure 2.15). The NiO_x layer acts as an ion source which supports the formation of conductive filaments. Therefore, this layer is added when making drift memristors which function as synapses, not nociceptors. The diffusive memristor operates by ion migration within the $MAPbBr_3$ layer. Under bias, negative ions and vacancies (Br^-, VMA^-) accumulate at the perovskite-HTL interface, while positive ions and vacancies (VBr^+, MA^+) accumulate at the perovskite-ETL interface. This accumulation of ions improves carrier injection and decreases the barrier. Overall, the behaviours presented here are due to the changes in the hole-injection barrier at the perovskite-PEDOT:PSS interface.

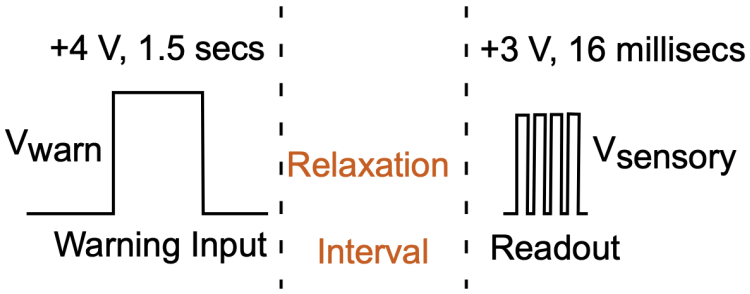

FIGURE 2.15: Nociceptive pulse schemes. Reproduced with permission from[105]. Copyright 2021, John Wiley and Sons.

Figure 2.16 shows the output for different tests they performed. First, in Figure 2.16a, they test different noxious pulse amplitudes while keeping the 3 s width constant. For increased noxious pulse voltage, the time at which the current noxious threshold (10 μA) is crossed decreases. This is the allodynia behaviour: the nociceptor reduces its

threshold. In addition, the output current increases, which is similar to hyperalgesia: the nociceptor increases its response. A similar behaviour is obtained when the pulse duration is increased while keeping the amplitude constant (Figure 2.16b).

As previously mentioned, the device needs to relax back to its initial state once no more pulses are applied: the nociceptor returns to its "normal" state. This is demonstrated in Figure 2.16c. The device is subjected to an initial noxious pulse, then the current is read at different times after that noxious pulse. If the relaxation interval is long enough, the current goes back to its initial level.

Figure 2.16d shows a different concept: self-healing. If a pulse of opposite polarity is applied for some time after a noxious pulse, the current levels can be lowered. This is akin to the active healing process in biology.

Jung Ho Yoon et al.[106] used a different vertical stack of Pt/SiO_x:Ag/Ag/Pt in a cross-bar array pattern. The mechanism at play here is the migration of Ag^+ ions which is why the additional layer of Ag is present: to avoid Ag depletion and therefore observe the "no adaptation" behaviour of nociceptors. The objective of this work was to demonstrate three key features: "threshold", "no adaptation", and "relaxation".

As the pulse width or amplitude is increased, the current threshold is crossed sooner (= allodynia), and the current level rises higher (= hyperalgesia) (Figure 2.17a and Figure 2.17b respectively).

A novelty here is the number of pulses in the pulse train also seems to have an effect (Figure 2.17c). Even if the pulse amplitude is lower, if more pulses are applied, the threshold can still eventually be crossed and generate a response. These three pulse schemes demonstrate the "threshold" behaviour of the device.

Figure 2.17d shows the "relaxation" behaviour. If a long enough time is left between the first noxious pulses and a second one, the current level can return to its initial state and not respond to the second pulse.

They also showed these behaviours for devices which were subjected to an initial highly noxious pulse. They found that those devices needed fewer pulses for the current to cross the threshold level. This is similar to the sensitised state of nociceptors: they want to protect the damaged area.

They also found a self-healing behaviour when pulses of opposite polarities were applied. However, this worked only for devices which were only slightly damaged (medium intensity noxious pulses were applied). This is similar to biology: if the noxious pulse is too intense, permanent damage can occur.

Finally, they discovered that their device could exhibit such behaviour when stimulated with temperature. As the temperature increased, the current level increased, and crossed the threshold earlier.

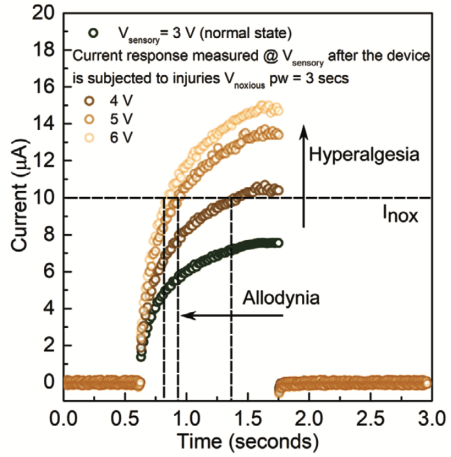

(A) Increasing amplitude (4 V, 5 V, and 6 V; pulse width = 3 s).

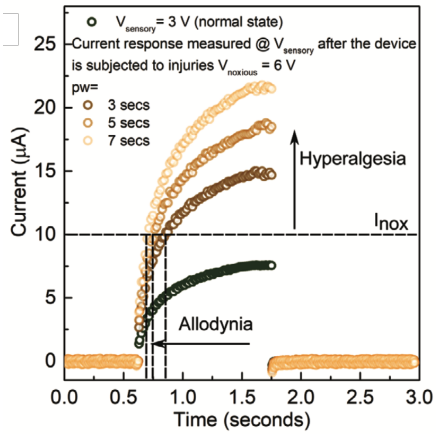

(B) Increasing pulse width (3, 5, and 7 s; amplitude = 6 V) of the noxious stimuli enhance the current response and reduce the incubation time/threshold, akin to hyperalgesia and allodynia in biology.

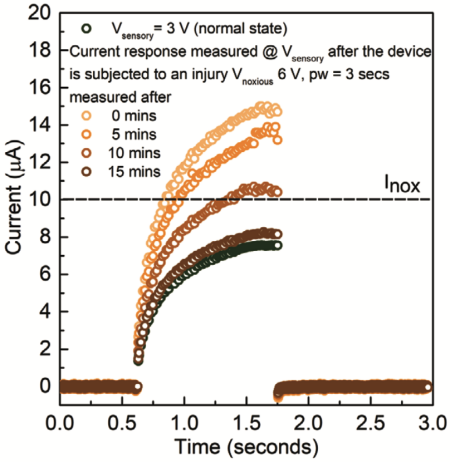

(C) The device is subjected to an injury of 6 V; pulse width = 3 s. The responses are measured post-injury at $V_{sensory}$ = 3 V after waiting for 5, 10, and 15 min respectively.

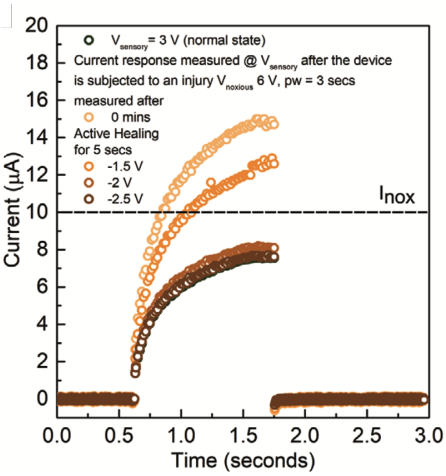

(D) The device is subjected to an injury of 6 V, pulse width = 3 s. Next, active healing pulses of -1.5 V, -2 V, and -2.5 V are applied for 5 s and the responses are measured post-healing at $V_{sensory}$ = 3 V.

FIGURE 2.16: Nociceptive signal processing in halide perovskite (HP) diffusive memristors. Sensory inputs of mild amplitude ($V_{sensory}$ = 3 V) generate normal-state responses, while intense voltage shocks of high amplitude ($V_{noxious}$ > 4 V) generate sensitised responses. Normal-state responses are initially read at $V_{sensory}$ = 3 V. The devices are next subjected to noxious stimuli, after which the sensitised responses are measured once again at $V_{sensory}$ = 3 V. The diffusive threshold switching behaviour enables passive healing with time (c) and active healing with curing pulses of opposite polarity (d). Reproduced with permission from [105]. Copyright 2021, John Wiley and Sons.

The presented behaviours can be seen as similar to device ageing, but they are quite specific to nociceptors. For example, typical devices will show decreased sensitivity over time due to repeated pulses, but nociceptor devices show no adaptation: their current levels are the same after many cycles. Another aspect is sensitisation after

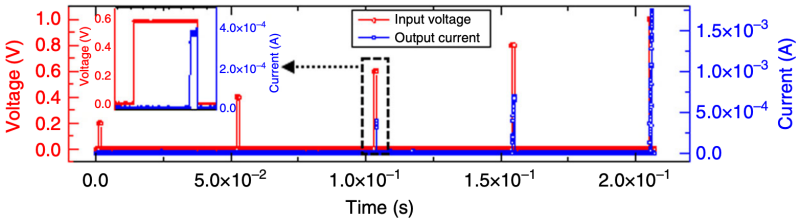

(A) A train of 1 ms wide input voltage pulses (red curve) of variable pulse amplitudes (0.2 to 1.0 V) and the corresponding output currents (blue curve). A higher input voltage leads to a larger output current.

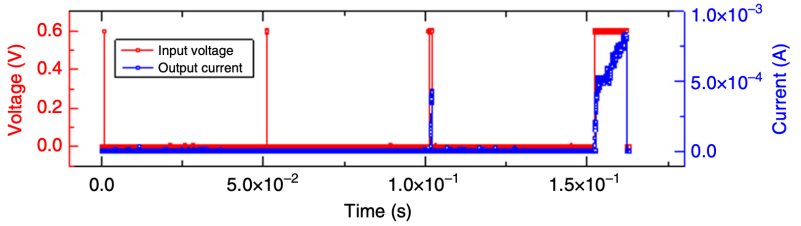

(B) A train of input voltage pulses (red curve) composed of a variable range of pulse widths from 10 μs to 10 ms, with a 0.6 V amplitude, and its output currents (blue curve).

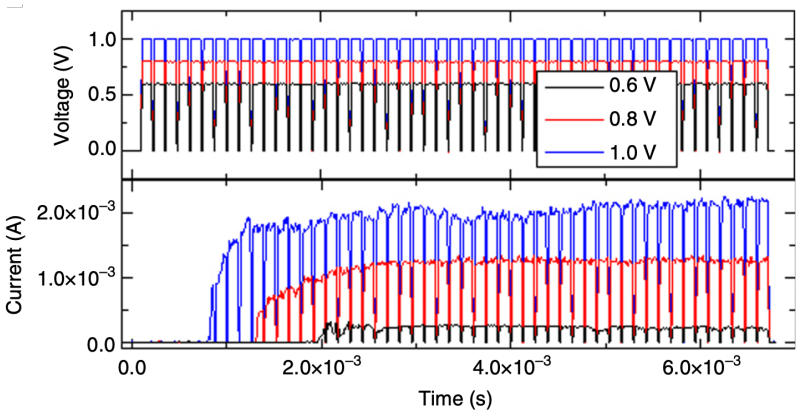

(C) Response of the device to multiple number of 100 μs pulses with different amplitudes (0.6, 0.8, and 1.0 V). A higher amplitude results in a shorter incubation time (1.9, 1.3, and 0.8 ms, respectively) in addition to a higher current. The TE was biased while the BE was grounded during all electrical measurements.

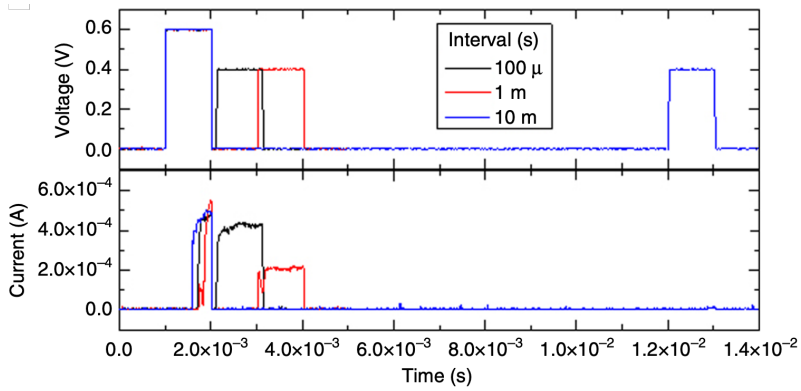

(D) (upper panel) Relaxation characterisation using a 0.6 V pulse followed by a 0.4 V pulse with different interval times between the two pulses ranging from 100 μs to 10 ms, and (lower panel) the corresponding output currents.

FIGURE 2.17: Pulse response of the memristive nociceptor. Reproduced from [106]. Available under a CC-BY 4.0 licence.

injury. Most devices show reduced performance after a harmful input, but nociceptor devices actually gain sensitivity after a noxious pulse (allodynia and hyperalgesia). These changes are reversible unlike permanent damage, for example by applying an opposite polarity pulse to induce active recovery or healing. Overall, these protective functions (threshold detection, maintained sensitivity, enhanced response after injury, and active recovery) make a true artificial nociceptor rather than showing degradation.

2.4 Benchmarking ReRAM performance

Benchmarking is an important part of device development.[107,108] For instance, in resistive memory devices, important factors include ON/OFF ratio, endurance[f], and retention[g]. This step is particularly important for ReRAM devices as many combinations of materials and architectures are being studied. Also, some areas for improvement are endurance and retention as there is still some device-to-device and cycle-to-cycle variability.[28] Being able to showcase consistent behaviour for many cycles will help adoption of this technology for the above-mentioned applications.

Endurance characterisation can be quite time-consuming and challenging as it is necessary to record HRS, and LRS in each cycle. Lanza et al.[31] share some recommendations to accurately record device endurance. First, carefully monitor the switching process during the first few ≈ 10 cycles. This means to monitor the current with high temporal resolution (≈ 100 measurements per pulse) when applying the read, write, read, and erase voltage pulses. As this is not sustainable when testing 10^5 cycles, it is possible to record only one current point per read voltage pulse. This will yield less information, but still enough to build a reliable endurance plot. This procedure can realistically be used for up to 10^6 or 10^7 cycles. To test device-to-device variability in parallel, the same procedure can be followed on multiple devices. The obtained data can be plotted on the same graph for added value for example colour coded. Finally, if testing more than 10^7 cycles, it is fine to test the current for only a few randomly selected read pulses per decade. In total, this will produce enough statistical data. Ideally, 10^{10} cycles should be tested.

Stathopoulos et al.[107] also share some recommendations, but also suggest a full device characterisation procedure. The first batch of characterisation tests are to study the functionality of devices in three steps. First, they evaluate the switching dynamics by applying alternating polarity voltage pulses. This allows to find the direction of resistance change. They continue by applying voltage ramps to quantify the change in resistance. This first step determines the device switching regime (bipolar, unipolar or hybrid), switching voltage, and scanning bias range. Next, they apply non-switching

[f] The number of write cycles a memory cell can tolerate before failing.
[g] The ability of a memory device to maintain stored information over time.

pulses to determine the volatility, metastability, and timescale of resistance changes. The third and last step is to record temperature-dependent I-V curves in order to identify the charge conduction mechanism and interface barrier height or defect activation energy parameters.

The next test module is to investigate the necessity of an electroforming step. They apply increasing voltage pulses until a change in resistance is observed. To avoid damaging the device, they suggest setting current compliances or applying short pulses. Once the device is formed, the functionality tests are repeated.

The third series of tests is to assess the device performance, i.e. its memory capacity, retention, and endurance. This section is less precise than what Lanza et al. shared, but the overall idea is the same. They aim to identify the number of available memory states by applying an increasing number of pulses and count how many distinguishable states are observed. For retention, they program the device to the previously found states and continuously read the device for as long as possible. Finally, endurance is tested by applying opposite polarity pulses to repeat switching cycles until degradation is observed.

The final device characterisation steps they suggest is to: first, identifying a suitable model for the tested device; second, recording experimental data to extract parameters required by the model; and finally, fitting the model with these parameters to enable device simulation.

2.5 Summary

Redox-based resistive memories (ReRAMs) offer many advantages such as low power consumption, fast switching, high density (3D stacking, small devices), offering it as a solution to many of the challenges that current memory systems face. Throughout this chapter, I discussed the fundamental principles, the factors affecting switching behaviour, the use of ReRAM for in-memory computing applications such as digital, analogue, and neuromorphic computing, and how to thoroughly test device performance.

ReRAMs operate on the principle of resistance switching: the device transitions between high and low resistance states. There are three main types of filamentary switching. First, electrochemical metallisation (ECM), which uses the active metal cations to form conductive filaments. Second, the valence change memory (VCM), which uses oxygen vacancy migration to form conductive filaments. Finally, the thermochemical memories (TCM), which form conductive filaments via heating the metal electrodes.

Environmental factors, particularly moisture, play a big role in ReRAM performance, affecting charge transport, counter reactions, and device longevity.

ReRAM devices show significant promise for in-memory computing applications in digital and analogue domains, as well as for neuromorphic computing, as these devices can mimic synaptic behaviour, which can be used for brain-inspired computing systems.

Thorough endurance and reliability testing and characterisation are important for the development and optimisation of ReRAM devices, as this is still one of the areas which can be improved. Thorough testing is important as reliable 10^{10} of cycles are necessary for applications which require precise control (like in-memory computing applications).

However, other challenges remain to be addressed. For example, smaller device geometries are harder to fabricate and maintain consistent performance due to increasing sneak currents. Additionally, device-to-device and cycle-to-cycle variability continues to be significant. Unfortunately, as the switching mechanisms are not yet fully understood, optimising devices can prove difficult. There is considerable room for research in geometry or material choice to improve device performance.

In summary, ReRAM devices are being developed for new types of in-memory computing such as neuromorphic computing due to their many advantages which could solve issues current memories are facing.

Chapter 3

Polyoxometalates in Memory Devices

Chapter 2 discussed an up and coming type of electronic memory: the redox-based resistive memory (ReRAM). It was mentioned that many factors can affect the performance of these devices, such as the material choice, device architecture, and environmental factors. This chapter will focus on the use of polyoxometalates (POMs) as the active switching layer.[3]

POMs are inorganic, usually anionic molecular metal oxide clusters with the general formula $[MO_x]_n$ with M = group 5 or 6 transition metals (V, Nb, Ta, Mo and W) in their highest oxidation state[109], x = 3-7, n = 6-368 and sizes ranging from 0.5 nm to the size of haemoglobin (diameter approximately 6 nm).[34,110,111] They are formed by self-assembling discrete components into larger, organised discrete (0D) anionic metal oxide structures.[112,113] A very common structure, called Keggin, is shown in Figure 3.1. It has a central XO_4 tetrahedral group, with X typically Si, P, B. This central group is surrounded by 12 MO_6 octahedral groups which are linked together by sharing neighbouring oxygen atoms.

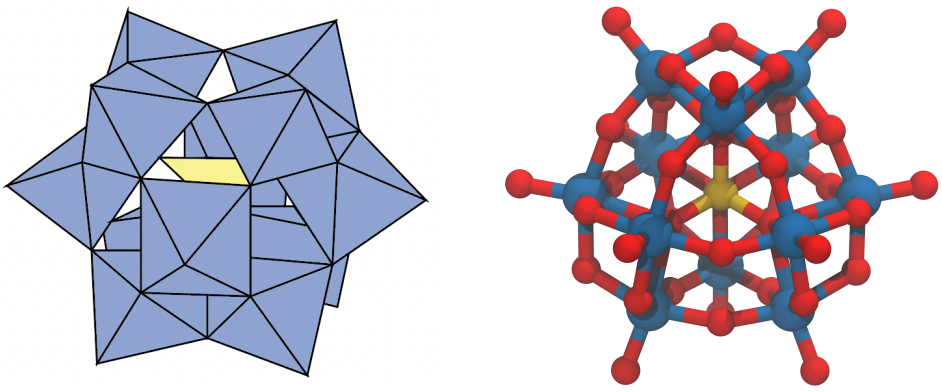

FIGURE 3.1: Keggin POM structure.

What sets POMs apart is their rich redox properties. They can undergo multiple, reversible oxidation and reduction processes with little structural deformation[114,115], leading them to be described as "electron reservoirs"[116] or "electron sponges"[117]. Besides electronics, their rich redox properties are interesting for other research areas such as: catalysis[118–122], buffer layers in solar cells[123–127], different battery components[128–132], supercapacitors[133–135], and fuel cells[136,137].

Polyoxometalates are very versatile by nature, in terms of size[138], structure[139–143], solubility[144], electronic properties[145–148], magnetism[149,150], thermal stability[151], and crystalline phases[152–155]. For example, POMs can be functionalised[156,157] for specific applications such as light detectors[158,159], encryption systems[160,161], spintronics[162], gas sensors[163,164]. Overall, POMs offer a level of control that is challenging to achieve with other materials.[165]

This chapter will discuss ways in which POMs can be implemented into redox-based resistive switching memories.[42] Different device architectures and active layer material combinations will be discussed along with device operating mechanisms. From POM only layers to more complex hybrid systems involving self-assembled monolayers (SAMs), polymer blends, and functionalised POMs, this chapter aims to present an overview of the current POM-based memory research scene.

3.1 Single POM layer devices

3.1.1 Charge conduction mechanism

As electronics continue to decrease in size, we are reaching the point where the studied systems are metal-molecule-metal configurations. Therefore, a key point to understand is how electrons flow at the single-molecule scale.[166] Conductance, current-voltage behaviour, and other switching properties are governed by these mechanisms. Therefore, knowing how the electrons flow can help optimise device performance, predict behaviour under various conditions, and design new structures and materials with enhanced properties. Additionally, it helps in determining the device operational limits, power consumption, and potential failure modes.

The charge conduction mechanisms are connected to the different device components energy levels, such as electrodes and switching layer materials.[167] The alignment of the metal electrodes Fermi levels with the highest occupied molecular orbital (HOMO) and lowest unoccupied molecular orbital (LUMO) energy levels of the switching material largely determines the nature of electron transport. Different transport mechanisms occur depending on how these energy levels align under applied bias. Other factors, such as the POM structure[168], applied voltage, charge transfer length, and trapped charges[169–172], also influence the mechanism.[173]

To determine the charge conduction mechanism, the relationship between the voltage and current needs to be determined.[174]

- $I \propto V$: Ohmic conduction (direct tunneling) or hopping conduction. Charge carriers move freely through the material or "hop" between localised states in the material.
- $\ln(I/V^2) \propto V^{-1}$: Fowler-Nordheim (FN) tunnelling. Quantum mechanical tunneling of electrons through a triangular potential barrier due to an applied bias.
- $\ln(I/V) \propto V^{1/2}$: Poole-Frenkel emission. Field-enhanced thermal excitation of trapped electrons into the conduction band.
- $I \propto V^2$: space charge limited conduction (SCLC) - Child's law. Current flow limited the build-up of injected charges in the material
- $\ln(I) \propto V^{1/2}$: thermionic emission. Thermal excitation of charge carriers over a potential barrier.

The link between the voltage and current can be found by plotting the necessary voltage and current functions similarly to what Glezos et al. did as shown in Figure 3.2.

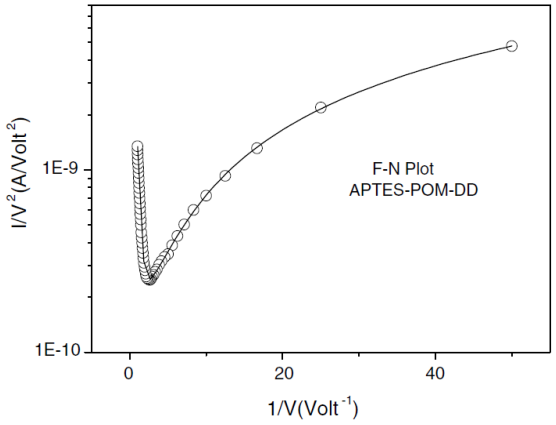

FIGURE 3.2: Determining the charge conduction mechanism by comparing experimental results (symbols) with tunneling theory (solid line). Reproduced with permission from[175]. Copyright 2006, Elsevier.

Now that the theoretical approach is better understood, I can look at examples in the literature. Ghosh et al. found that their vertical crossbar $Au/PMo_{12}O_{40}/Au$ device had a Schottky emission for the OFF or high resistance state (HRS), and for the ON or low resistance state (LRS) state a Poole-Frenkel emission.[176] Sterin et al. also studied a vertical device ($Glass/ITO/Na_6V_{10}O_{28}/Cr/Au$) and determined for HRS an ohmic conduction at low voltages (< 0.86 V) and then SCLC at higher voltages (0.86 V to 1.28 V), and for LRS an Ohmic conduction.[177] After identifying the charge conduction mechanism in their device, Sterin et al. were able to elucidate the switching mechanism. The observation of SCLC indicated a build-up of carriers at the electrode-oxide interface, with

some carriers being trapped, while others contributing to the overall device conductivity. Therefore, understanding charge conduction mechanisms can provide crucial insights into the physical processes of resistive switching.

Other authors compared different voltages ranges[175,178–182]. However, they used different POM-based material combinations in their active switching layers and will therefore be discussed later.

Alternatively, mathematical models can be fit to the data to predict the charge transport mechanism. For example, Amoroso et al.[183] used the Poisson equation to calculate the electric field in the device, so they could use a modified Fowler-Nordheim model (Equation 3.1) to fit the F-N tunneling behaviour they observe in a gate-all-around charge-trap (GAA-CT) memory.

$$J_n = AF_{eq}^2 exp(\frac{-B}{F_{eq}}) \tag{3.1}$$

with:
J_n: the tunneling current density (A/cm^2)
A: a constant related to the effective mass and barrier height (A/V^2)
F_{eq}: the effective electric field that accounts for the cylindrical geometry (V/cm)
B: a constant related to the effective mass and barrier height (V/cm)

3.1.2 Switching mechanism

Now that the different techniques to determine charge transport have been explained, it is possible to better understand the various mechanisms that are used to explain switching for single POM layer devices electronic memory devices.[184]

3.1.2.1 Oxygen vacancies

This is the mechanism described in Chapter 2 when detailing the valence change memories (VCM). Sterin et al.[177] used this mechanism to explain the switching in their $Na_6V_{10}O_{28}$ vertical device (Glass/ITO/POM/Cr/Au). From literature[185–187] and XPS, they claimed that oxygen vacancies pre-existed. More precisely, Figure 3.3 shows the mechanism they believe is causing the switching. At first, a positive bias is applied to the top electrode, which triggers the POM reduction reaction, which generates oxygen vacancies, then as the bias is further applied, the oxygen vacancies migrate via tunneling towards the bottom electrode where they accumulate. Conductive filaments (CFs) connecting both electrodes are formed, leading the device to switch to LRS: an Ohmic contact behaviour is observed. Finally, when applying an opposite bias, the oxygen

vacancies at the top electrode start to deplete, rupturing the CFs, switching the device back to HRS.

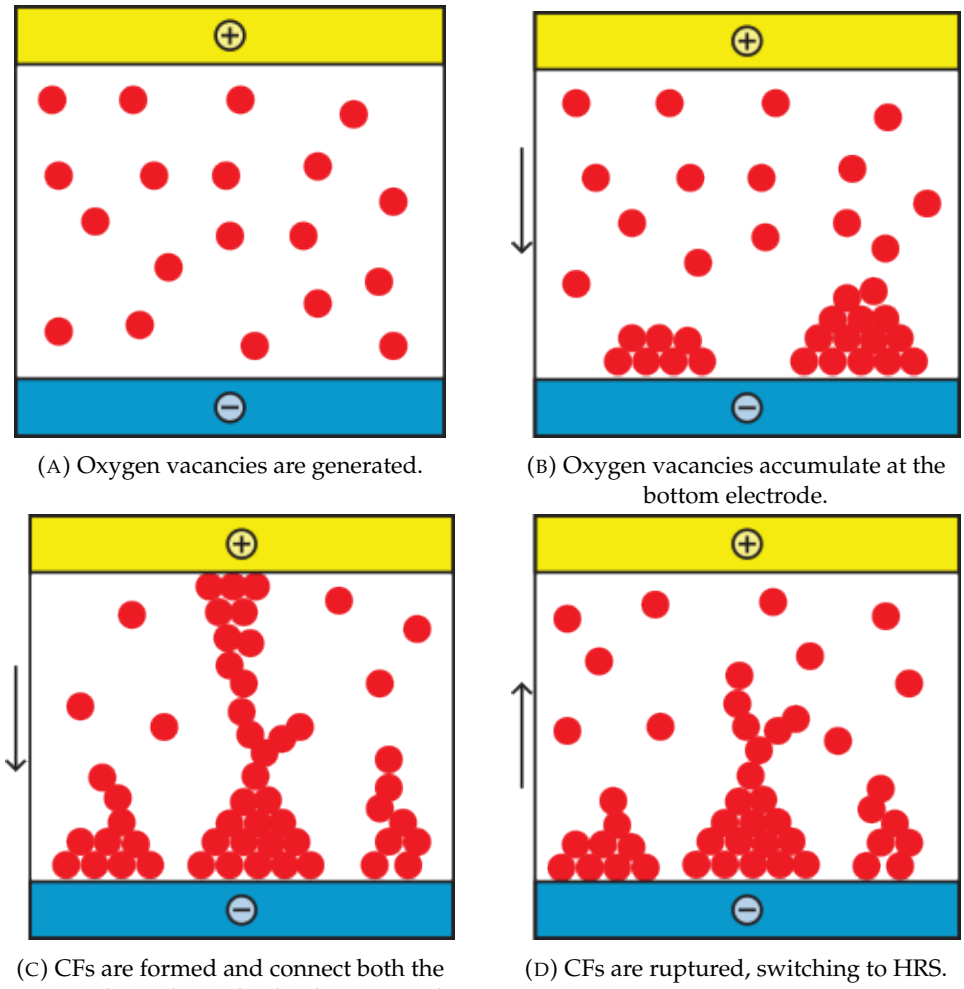

(A) Oxygen vacancies are generated.

(B) Oxygen vacancies accumulate at the bottom electrode.

(C) CFs are formed and connect both the bottom and top electrode, the device switches to LRS.

(D) CFs are ruptured, switching to HRS.

FIGURE 3.3: Oxygen vacancy-based switching mechanism. Adapted with permission from[53]. Copyright 2019, Royal Society of Chemistry.

Chen et al.[53] also claim an oxygen vacancy migration as their switching mechanism. However, as they use a combination of POM and PMMA (poly(methyl methacrylate)) in their active layer, a more thorough discussion will be held further in the chapter.

3.1.2.2 POM oxidation state

Ghosh et al.[176] studied $(NH_4)_3PMo_{12}O_{40}$ in a vertical device (glass - for support/paper/Au/POM/Au) and found that when the POM got reduced (by exposure to 365 nm UV light), its dielectric constant decreases due to the electron accumulation and charge transfer between Mo(VI) and Mo(V) states, as observed via electron paramagnetic resonance (EPR). Additionally, the POM conductivity changed: a combination of hopping and tunneling explain the charge transport mechanism in the reduced state,

while only tunneling was observed for the oxidised POM. They also observed changes in electronic structure: oxygen vacancies and defects were observed via Raman and X-ray diffraction (XRD) spectroscopy. Overall, all these changes in POM properties when reduced allow the device to switch between different resistance states.

Other groups[185,188] have reported spontaneous reduction of POM when in contact with Al and the resulting changes in energy level alignment. This allows for improved electron flow and mobility and therefore device performance. Douvas et al.[188] also specified that POMs get more reduced depending on their deposition method: spin-coat films are thinner and are therefore more reduced than drop-cast films. This is because the thinner films have a large proportion of POMs close to the Al interface which can therefore more easily get reduced. Both groups also discussed the effect of the POM structure. More precisely, the Wells-Dawson POMs can accommodate more electrons than the Keggin structure as it has more metal atoms and its LUMO is lower. Additionally, the POM counter-cations play a role. For instance, Douvas et al.[188] highlighted the oxidation of their ammonium counter-cations NH_4^+ into NH_3^+ in parallel to the reduction of the POM anion.

Linnenberg et al.[37] studied $[V_6O_{13}(OCH_2)_3CCHR'SR_2]^{2-}$ (with R = Me or Ph) as a single molecule deposited flat on a gold surface as the bottom electrode with a Pt STM tip as the top electrode. They found that when the POM accepts electrons (i.e. gets reduced), the energy level alignment changes which allows the materials to switch between HRS and LRS. They were able to use the different number of transferred electrons from the gold electrode to the POM to showcase different available resistance states, as shown in Figure 3.4.

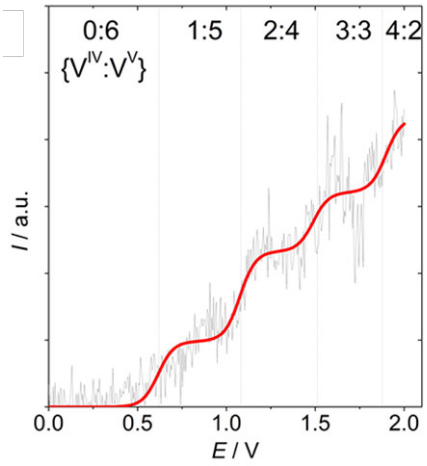

FIGURE 3.4: Experimental single-point STS data of single scans (grey) of R = Me at room temperature shown with the corresponding electron population for each transition; fitted data (dose-response function) are indicated in red. Reproduced with permission from[37]. Copyright 2018, American Chemical Society.

Many other groups[36,189–191] were also able to use the different POM oxidation states for different memory states. For example by modelling a $[W_{18}O_{54}(SO_3)_2]^{-4}$-based flash three terminal devices that used the POM in the channel as shown in Figure 3.5.

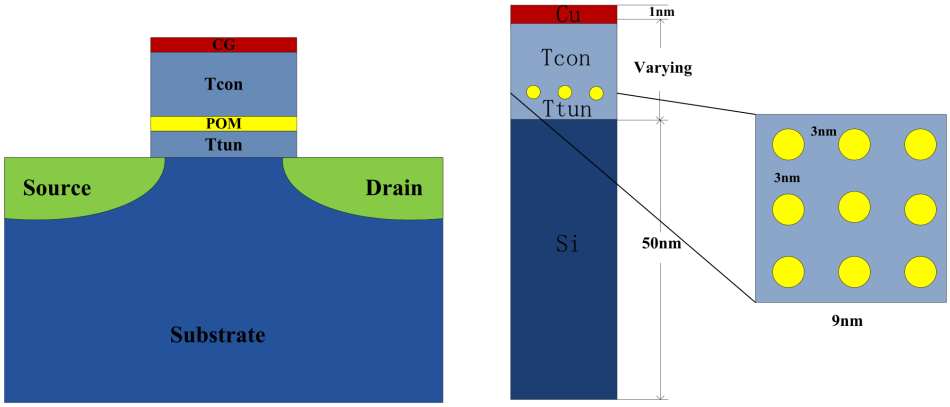

(A) Schematic of a POM flash memory with nine POM molecules.

(B) 3x3 arrangement of POM molecules in the floating gate.

FIGURE 3.5: 3-terminal POM-based device schematic. Reproduced with permission from[36]. Copyright 2021, IOP Publishing.

Georgiev et al.[189] compared two different device structures: fully depleted silicon-on-insulator (FDSOI) and bulk conventional transistor. FDSOI devices are semiconductor-based with an architecture in which the active layer of silicon (where the transistor channel is formed) is very thin and fully depleted of mobile charge carriers when the transistor is in its off state. They made three main observations. First, the short-channel effects[a] were less pronounced in the FDSOI device: it has lower leakage currents, higher drive currents, and a steeper subthreshold slope than the bulk device. Second, the FDSOI device presented a threshold voltage (gate voltage at which the drain current reaches 10^{-7} A) shift depending on all the redox states of the POM (both the 2x and 1x reduced states), while the bulk device was affected only when the POM was reduced once. Thirdly, the charges in the FDSOI device were further away from the Si/SiO_2 interface than in the bulk device. Therefore, the influence of the trapped charges in the floating gate on the threshold current is smaller in the FDSOI device. These three observations lead to say that the FDSOI device has better I-V characteristics, with a narrowing of the threshold voltage window in comparison with the bulk device. This suggests that they could offer more reliable, lower-power, and higher-performance flash memory cells compared to the bulk devices.

Ding et al.[36] used kinetic Monte-Carlo and Tsu-Esaki models to analyse their device. They started by optimising the device geometry, specifically the tunneling and control oxide layer thicknesses, as shown in Figure 3.5. They found that the 10 and 2 nm respectively gave the best compromise between retention and leakage currents. Then,

[a] Phenomena that occur in transistors as their channel lengths are reduced to very small dimensions (typically below 100 nm).

they optimised the device operating pulse durations in order to optimise the POM reduction and oxidation. They found that + 8 V writing pulses between 5.3 and 7.7 μs long would reduce once the POM. However, 29.6 μs long writing pulse could directly reduce the POMs twice. There is a compromise between storage density and power consumption: the 1x reduced POMs-based devices will need lower power (shorter pulses), but have lower storage density than the 2x reduced POMs. The switching threshold voltage increased with the number of electrons in the POM layer, allowing for multi-level devices. For the "erase pulses" (opposite polarity voltage compared to the "write pulses"), shorter times were necessary for the POM to oxidise: minimum 0.7 μs long pulses were necessary.

Nadal et al.[191] showed that reducing the POMs increased the negative charge density (due to more electrons being present), which repelled the electrons in the channel and therefore lowered the drain current. They also mentioned that the POM arrangement affected performance (see Figure 3.6), especially the distance between them and the substrate which can modify the switching threshold voltage. Specifically, POMs placed closer to the substrate (1.5 nm, filled circles) have a bigger impact on the threshold voltage shift compared to those placed farther away (3 nm, empty circles). Additionally, the distribution of POMs influenced performance: a regular 3x3 matrix arrangement showed behaviour closest to the ideal analytical model, while other configurations like the 5-POM cross formation deviate from this ideal, potentially affecting the consistency and predictability of the device electrical characteristics.

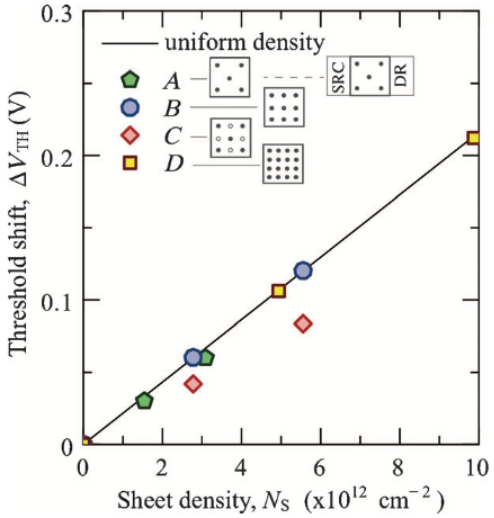

FIGURE 3.6: Comparison of the threshold voltage shift ΔV_{th} due to idealised sheet charge in the oxide (line), and due to a POM floating gate (symbols), versus sheet charge density (normalised by the electron charge). The different lateral configurations of the POMs are schematically illustrated. POMs represented by filled circles reside 1.5 nm above the Si- body; POMs represented by empty circles are 3 nm above the Si Body. Therefore, in configuration C four of the POMs have reduced impact on the potential and electron density in the channel of the transistor, hence on ΔV_{th}.
Reproduced with permission from[191]. Copyright 2013, John Wiley and Sons.

3.1.2.3 POM orientation

Lapham et al.[192] found that their device, symmetric Au coplanar electrodes hosting $[W_{18}O_{54}(SO_3)_2]^{-4}$, switching mechanism was affected by the POM orientation. More precisely, they modelled a single molecule between the two Au electrodes with different configurations (see Figure 3.7). They determined that the number of oxygen atoms in contact with the electrodes affected the electron transport properties and current flow through the molecule. More contact points lead to higher conductance and current flow, due to an increased number of conduction channels between the electrodes.

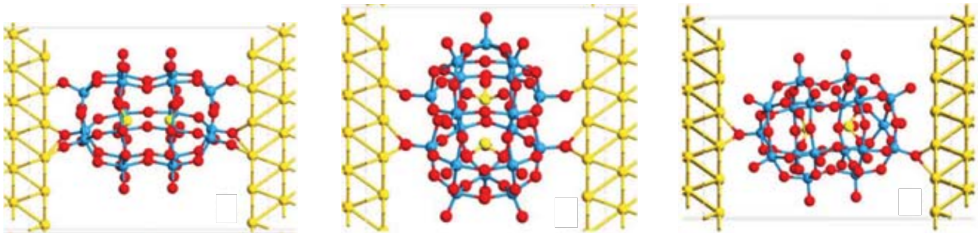

FIGURE 3.7: Au-POM-Au molecular junctions with different orientations and different number of contacts. The POM molecule is $[W_{18}O_{54}(SO_3)_2]^{-4}$ where S = Yellow, W = Blue and O = Red. Reproduced from[192].

3.1.2.4 POM type

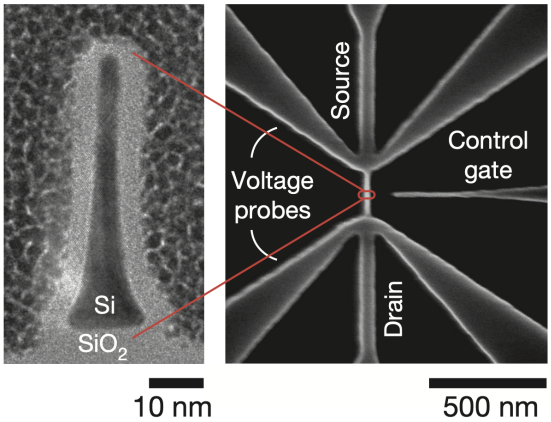

FIGURE 3.8: A cross-sectional transmission electron microscope (TEM) image (left) of the memory device with an SEM image (right) of the $\sim$ 5-nm Si nanowire channel with side control gate. Reproduced with permission from[43]. Copyright 2014, Springer Nature.

Busche et al.[43] investigated a nanowire flash three terminal memory device as shown in Figure 3.8. They used the Wells-Dawson POM but looked at the influence of different moieties: $[M_{18}O_{54}(XO_n)_2]^{-m}$ with M = W or Mo, X = P, S, or Se, n = 3 or 4, and m = 2 to 8. W was chosen as it can resist to higher temperatures. Se offers the best balance between stability and activity. Therefore, the best POM was $[W_{18}O_{54}(SO_3)_2]^{-4}$. They found that the SO_3 moieties also participated: Se could oxidise ($Se^{IV} \rightarrow Se^{V}$) after the

first pulse was applied and therefore helped create a new type of "write once/erase" memory.

3.1.2.5 Other effects

Several groups found different other conduction mechanisms in their devices.

Kan et al.[193] were studying the use of liquid state $H_3PMo_{12}O_{40}$ in a device developed for reservoir computing (RC). RC is a machine learning approach that utilises a fixed, randomly connected network (the "reservoir") to process input signals. The reservoir is very good at temporal data processing, making it particularly useful for time-series prediction and pattern recognition. The particularity of RC systems is that only the output layer requires training, simplifying the learning process. The POM solution is interesting for RC applications: the random distribution of POMs creates the necessary non-linear transformations[b]. In this situation, they found that the proton migration in the water solvent combined fast response, nonlinear dynamics, and memory capacity that made it surprisingly effective for certain types of RC tasks.

Gonzalez et al.[39] used $Na_9[Er(W_5O_{18})_2]$x35 H_2O as a single magnet device. They also found that the water in their system played a role, however slightly different from above. By heating the POM and therefore changing its hydration level, the POM structure changed slightly which modified the magnetism properties of the material. This can therefore be used to create different memory levels for different hydration levels.

Kato et al.[145] also found that heating the POM changed its ferroelectric properties. They studied a Preyssler-type POM ($K_{12}[Tb^{3+} \subset P_5W_{30}O_{110}]$). However, they attributed the change in properties to the migration of the central Tb^{3+} ion instead of changes in hydration level as mentioned above.

3.1.3 Conclusions

Throughout this section, I looked into devices using POM as the active switching layer. I showed the different charge conduction mechanisms can occur, such as Ohmic conduction, Fowler-Nordheim tunnelling, and space charge limited conduction (SCLC), which can be determined through current-voltage analysis. Then different switching mechanisms were discussed. For example, oxygen vacancy migration, which can form conductive filaments. Changes in POM oxidation state which can change energy level alignment and therefore conductivity. The POM orientation (number of contacts with the electrodes) and type (enabling different redox reactions) also affect the device performance. Additionally, device architecture (FDSOI vs. bulk devices), POM arrangement, and environmental conditions (hydration levels) were also found to affect device

[b]The output is not directly proportional to the input, and the principle of superposition does not hold.

behaviour. All these parameters can be tuned to optimise device metrics such as retention, endurance, and power consumption.

3.2 Alternating SAM-POM monolayers

This section will discuss alternating POM and self-assembled monolayers (SAMs). The aim is to develop molecular memories and other nanoscale electronic devices.[194] Various SAM materials, their interactions with POMs, and the resulting devices electrical characteristics will be explored.

3.2.1 Silane-based SAMs

The first SAM I will discuss is (3-Aminopropyl)triethoxysilane (APTES). It has a silane group, which can attach to silica substrates, and an amine group on the other end, which can be positively charged and interact with the anion of $H_3PW_{12}O_{40}$. An example device is shown in Figure 3.9.

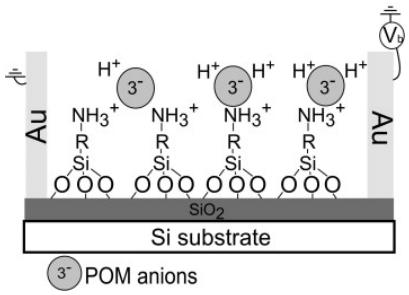

(A) Side view of a device showing monolayer structure. Reproduced with permission from[195]. Copyright 2012, Elsevier.

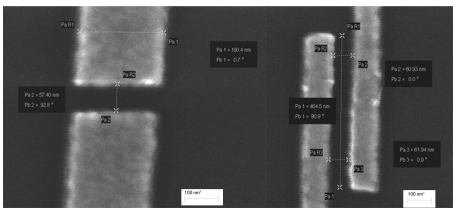

(B) Scanning Electron Micrographs of a junction area in the case of 50 nm-distant, 200-nm opposite fingers geometry electrodes (left) and of 50 nm-distant, with 500 nm overlap, parallel fingers geometry (right) electrodes, taken before application of the molecular layer. Reproduced with permission from[180]. Copyright 2011, Elsevier.

FIGURE 3.9: APTES/POM monolayers device architecture examples.

Now that the device structures are established, it is possible to understand how charges move through them, as this determines their electrical behaviour and potential applications (see Section 3.1.1). As described in the previous section, the charge conduction mechanism can be identified by the relationship between the voltage and current. Velessiotis et al.[180] and Makarona et al.[181] found that at low voltages, direct tunneling was at play, while they identified Fowler-Nordheim tunneling dominated at high voltages. They noted that the threshold voltage at which this transition occurs increases with the distance between the electrodes (for coplanar type device architectures). Overall, the POM ability to accept electrons is the source of the hysteresis they observe in their

devices. More precisely, they link the charge conduction mechanism and switching behaviour: the POM capturing then de-trapping electrons cause the hysteresis.

In a later work, Velessiotis et al.[195] also looked into the temperature dependence of the charge transfer mechanism. For temperatures above 200 K, a hopping mechanism was identified, while tunneling was found for temperatures lower than 150 K. Between 150 and 200 K, a combination of both mechanisms was determined. These findings may help guide future device development, as the temperature can be used to modulate the device performance.

It was also noted that POM number (linked to the POM concentration in solution prior to deposition) was more important than the POM position.[180] Balliou et al.[196] mention that POMs form nanoclusters and hyperstructures. The nanoclusters are already present in solution if the concentration is low ($< 10^{-5}$ M), and deposit as such in films. However, the hyperstructures are formed when the POMs are deposited to make films. Film coverage increases with solution concentration. They also connect this to the POM oxidation state: if the nanoclusters are present, the electron transfer is hindered, which prevents POM re-oxidation. Overall, film morphology, oxidation state, and device performance are influenced by the initial POM solution concentration. More precisely, lower concentrations lead to reduced POM species and localised electron states, suppressing conductivity, while higher concentrations produce larger structures with itinerant electron states, allowing for tunable HOMO-LUMO levels and improved contact formation in molecular electronic devices.

3.2.2 Amine-based SAMs

Diamine has two amine groups and can therefore interact between POM ($H_3PW_{12}O_{40}$) layers as shown in Figure 3.10. Glezos et al.[175] and Douvas et al.[179] still used an initial APTES layer to deposit the first POM layer on the substrate, as it helps form more reproducible films, but they then applied an alternating layer pattern between POM and DD.

Glezos et al.[175] started by describing the charge transport mechanism. They observed tunneling across their studied voltage range and noted that the POM ability to trap electrons allows for charge storage. If there were multiple POM layers, they observed charge hysteresis in the I-V curves. They also noted that the potential barrier lowers and stabilises. This hysteresis could be used for the creation of memory devices.

Douvas et al.[179] investigated the influence of the DD layers a bit more. For instance, they looked into the number of layers and found that the more layers, the more available pathways and therefore the more tunneling could occur (see Figure 3.11a). They also studied the influence of the ending layer. If POMs were the last layer, the electrode width also came into play (see Figure 3.11b). For a short gap between the electrodes

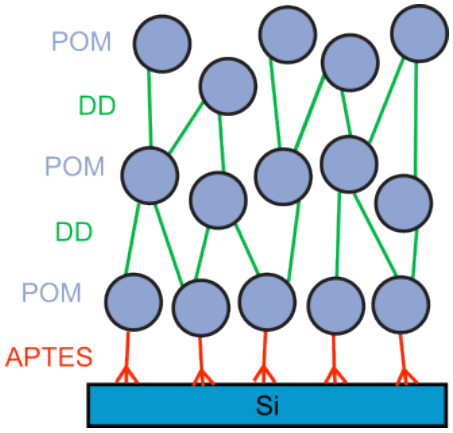

FIGURE 3.10: Schematic diagram of APTES-(POM-DD)$_2$POM multilayer film (3-POM layer film) prepared with the layer-by-layer (LBL) method on Si wafer. Adapted with permission from [175]. Copyright 2006, Elsevier.

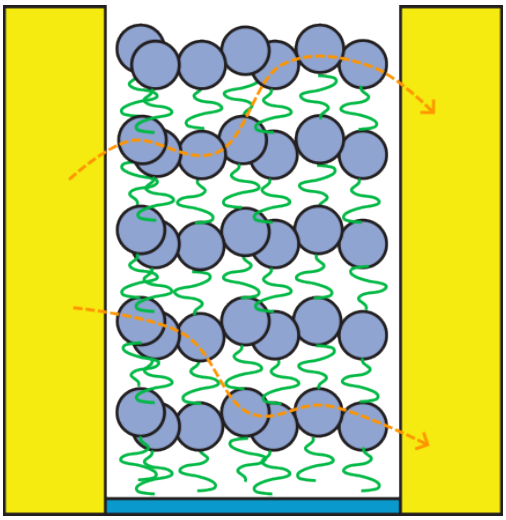

(A) When more layers are added to the structure, alternative paths are offered to the electrons and FN tunneling can be realised even at relatively wide gaps.

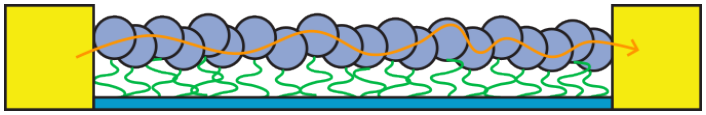

(B) When the gap becomes relatively wide (150 nm), the electrons can never acquire enough energy to tunnel through to the other electrode and percolation dominates.

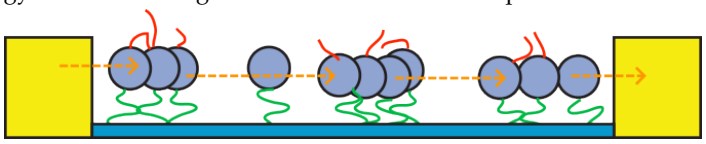

(C) In case of DD- ending films the electrons tunnel through the aggregates formed (due to the presence of the DD final layer) irrespective of gap width.

FIGURE 3.11: Schematic diagram of the transport mechanism model through the various film types at the high-voltage regime. For POM-ending films electron transport occurs through POM molecules. Adapted with permission from [179]. Copyright 2008, American Chemical Society.

(50 nm), there is tunneling. However, if there is a large gap between the electrodes (150 nm), the threshold voltage increases and percolation occurs. If DD was the last layer, the film morphology was patchy and electrons could tunnel through the POM patches regardless of the distance between the electrodes (see Figure 3.11c). Once again, film morphology influences device performance.

3.2.3 Thiol-based SAMs

While APTES and DD self-assembled monolayers work for silicon substrates, different SAMs are needed when working with other electrode materials, i.e. gold. Huez et al.[197,198] used 6-aminohexane-1-thiol hydrochloride (HS-$(CH_2)_6$-NH_3^+/Cl^-, called C6) to attach the POMs ($H_3PMo_{12}O_{40}$) to a gold electrode.

Similarly to other studies mentioned in this chapter, they show that the film morphology influences the conduction channels and that the POM oxidation state impacts the device performance. If the POM is reduced, the energy levels move and can increase up to 10x the conduction level. They also remind that the POMs can be re-oxidised in air by heating them. They also studied the effect of the counter-cations.[198] They found that changes in interface dipoles and hybridisation depend on the nature of the counter-cation. The changes affected both the energy alignment of the POM LUMO relative to the electrode Fermi level, and the strength of the electronic coupling between the POM and the electrodes. These effects influence electron transport within the POM molecule, which in turn can influence device performance. In this study, they suggested that larger, softer cations with lower charge density, such as TBA^+ may be more effective in tuning the POM electronic behaviour. However, the counter-cation choice is still specific to the application requirements.

3.2.4 Conclusions

In this section, I explored the use of alternating POM and SAM monolayers in electronic devices. I presented work using different SAM materials such as APTES, DD, and C6. Researchers found that the POM concentration, film morphology, and oxidation state influenced device performance. They showed that the charge conduction mechanisms depend on voltage, temperature. These parameters can be fine-tuned in order to create optimal electronic devices for specific applications.

3.3 POM blends

To harness POM capabilities and fine-tune their electronic properties for specific uses, it is possible to blend POMs with other materials. This allows for the customisation

of properties, such as charge conduction, stability, and fabrication. In this section, two significant POM blend systems are mainly discussed: POM:PMMA (poly(methyl methacrylate)) to use PMMA ion-conducting properties and POM:SWCNT (single-walled carbon nanotubes) to exploit SWCNTs electron-conducting properties, which can help with charge transfer from POM redox reactions.

3.3.1 POM:PMMA blends

First I will discuss POM and PMMA blends. PMMA is a synthetic polymer which can promote H^+ conduction.[53,199–201]

The charge conduction mechanism can be identified as explained in Section 3.1.1. For example, Glezos et al.[202] found that at low voltages Fowler-Nordheim tunneling dominates. Chaidogiannos et al.[182] and Velessiotis et al.[200] rather identified Simmons tunneling for low voltages and Fowler-Nordheim for high voltages. The next paragraphs link these mechanisms with device performance.

Glezos et al.[202] and Velessiotis et al.[200] looked into factors which can influence this charge transport mechanism: the POM intermolecular distance and the electrode distance respectively. The POM intermolecular distance can be correlated with the initial POM concentration. They found that if the distance between POMs is too large (1.5 - 3.6 nm), then tunneling occurs, while SCLC happens if the distance is small ($\approx$ 1.5 nm). In regard to the electrodes, as the distance increases ($>$ 50 nm), Ohmic hopping dominates due to hopping conductivity between POMs, but if the distance is small ($<$ 50 nm) tunneling is observed with negative resistance quantum effects observed in ultra-thin (10 nm) POM films. These findings allow for the optimisation of device structural parameters such as inter-electrode distances and POM distribution.

Both Chaidogiannos et al.[182] and Glezos et al.[202] noted that the electrode material also affects performance. They found that Au electrodes gave better performance than Al electrodes. They attributed this to the absence of an oxide layer on the Au electrodes and a better energy level alignment (the Au Fermi level with respect to the HOMO-LUMO gap of the POM:polymer composite).

Understanding the switching behaviour is also important to implementing these devices as electronic memories. As mentioned above, Chen et al.[53] claimed that oxygen vacancy migration is at play in their device. They used a $H_3PW_{12}O_{40}$:PMMA blend. They used the PMMA only as an inert matrix to encapsulate the POM. It doesn't participate in the switching, especially since it doesn't contain oxygen vacancies itself. Regardless, the PMMA still allows for the oxygen vacancies to migrate via tunneling. Hu et al.[199] rather suggested that the POM redox states are key: as the POM oxidises and reduces, the counter-cations migrates and change the effective barrier which changes the conductivity level, allowing for multilevel switching.

Chaidogiannos et al.[182] and Glezos et al.[202] created patterned structures of the polyoxometalate (POM) molecules embedded in polymer matrices at the nanoscale. This could potentially allow creation of molecular electronic devices or nanostructures with the POM molecules as active components. Therefore, they compared different polymers: PMMA, poly(vinyl alcohol) (PVA), and (meth)acrylate copolymer (PHECIMA) made of hydroxy ethyl methacrylate (40% w/w), cyclohexyl methacrylate (30% w/w), isobornyl methacrylate (23% w/w), and acrylic acid (7% w/w).

PVA showed good lithographic performance, but the POM concentration changed during processing due to the POM presence in the developer, making it unsuitable. The second polymer, PHECIMA demonstrated interesting electrical properties (conductivity peaks and photocurrent effects were observed) but poor lithographic results. Therefore, PMMA was selected as it provided both stable POM concentrations after processing and good lithographic performance in the nanometre range.

3.3.2 POM:SWCNT blends

Another material option that has been used in POM blends is single-walled carbon nanotubes (SWCNTs). They can be used to carry the electrons from the POM redox reactions. The target application of this material system is reservoir computing (RC). The random distribution of POMs within the blend generates the required non-linear transformations, as discussed earlier. Additionally, POM redox properties provide memory capacity. Finally, the tunability of POM concentration in the blends allows for tailoring of the reservoir properties for specific computational tasks, making them a versatile platform.

Azhari et al.[203] made 2D and 3D devices. The fabrication steps (see Figure 3.12) are quite different from what has been presented so far. For the 2D films, they deposit the SWCNTs and POMs on a cellulose filter paper substrate, then transfer it to the device by dissolving the cellulose filter paper with acetone vapour. The 3D device is fabricated by immersing a melamine sponge in the SWCNT:POM dispersion, then drying it in an oven. To operate this 3D device, the two probe tips are simply inserted into the sponge.

They found that the 2D device had a denser film, but the 3D network had more SWCNT junctions, which led to higher overall junction resistance and lower current flow. This increased resistance improved the nonlinear dynamics, which is beneficial for reservoir computing. They note that the tip penetration, sponge size and dimensions influence highly the device performance. Increasing the tip penetration depth led to stronger non-linearity due to higher resistance and increased interaction between the current and POM molecules. The memory capacity exponentially increased with the sponge size. Additionally, device dimensions affected the network density and connectivity, impacting the nonlinear dynamics and information processing capabilities. Overall,

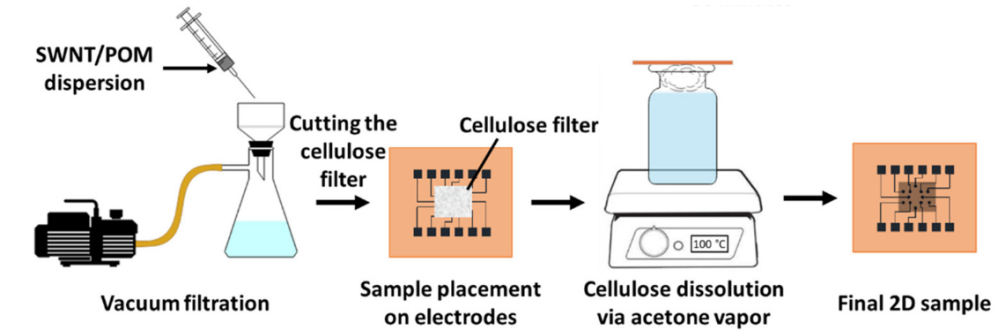

(A) 2D sample fabrication via the vacuum-assisted wet transfer process.

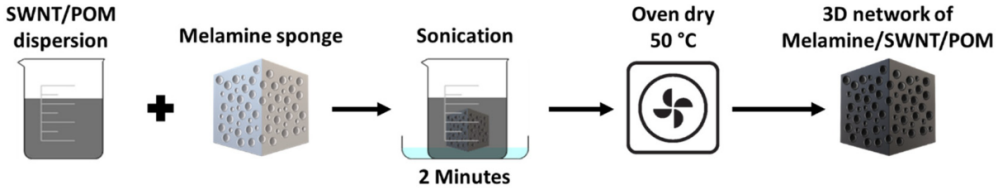

(B) 3D sample fabrication via the template method.

FIGURE 3.12: SWCNT:POM blend-based 2D and 3D device fabrication. Reproduced from[203]. Available under a CC BY-NC 3.0 licence.

the 3D SWCNT:POM blend has unique structural properties and tunable parameters, which enhance nonlinear dynamics, memory capacity, and performance in reservoir computing tasks compared to the 2D film.

Akai-Kasaya et al.[204] tested their device for the NARMA2 task. NARMA stands for Non-linear AutoRegressive Moving Average. The idea is to predict the next value of a sequence based on the previous 2. Unfortunately, their device did not perform as well as expected from their previous estimations[205]: they only observed short-term memory behaviour, the memory capacity and nonlinear processing ability was lower than predicted. To reach the predicted levels, work can be done on optimising the fabrication process to increase uniformity and consistency of the samples.

Wu et al.[206] also studied the use of SWCNT and POM blends for RC. However, they added a new component: poly(butyl methacrylate) (PBMA). As explained above, the stochastic and probabilistic electron transfers create some negative differential resistance (NDR) peaks in the device I-V curves. Added to the current noise and fluctuations, this makes for rich non-linear physical dynamics, which are good for this type of application. They manage to succeed the NARMA10 task where this time the next value of a sequence is found based on the previous 10. Compared to the pristine SWCNT:PBMA networks, the POM-based composite had improved performance and higher short-term memory capacity.

3.3.3 Other blends

Zhang et al.[207] were investigating reservoir computing with POMs, similarly to other groups described above. The main difference is that they used a $H_3PW_{12}O_{40}$ and P3HT blend: they used Ag/P3HT:POM blend/Ag device architecture. They found that the POM counter-cation played a key role in solubility. For example, using organic cations like tetrakis(decyl)ammonium (TDA), the solubility in organic solvents increased. They identified the switching mechanism to be due to Ag conductive filament formation and rupture as mentioned in Chapter 2. POMs can accelerate Ag ion migration by capturing them and facilitating their hopping through the polymer matrix, leading to a higher diffusion coefficient compared to pristine polymer. Their devices were able to reach over 90 % accuracy in emotion classification.

3.3.4 Conclusion

Throughout this section, I explored the use of polyoxometalate blends as active layers to enhance and optimise device performance. I mainly focused on two polymers blends: POM:PMMA, which uses PMMA ion-conducting ability and POM:SWCNT, which uses the electron transport properties of SWCNTs. The work presented here showed that POM intermolecular distance, electrode distance, and electrode material could influence the charge conduction mechanism and therefore device responses. Switching mechanisms were attributed to either oxygen vacancy migration or the multiple POM redox states. Additionally, a new type of application was introduced: reservoir computing (a form of neural network). Understanding these parameters can help develop and optimise new devices with tailored characteristics.

3.4 Functionalised POMs

POM functionalisation opens up new avenues for enhancing performance. It involves modifying POMs with specific ligands or groups, tailoring their properties for particular applications. This section explores two aspects of POM functionalisation. The first is enhancing deposition capabilities, which is important to create precise molecular memories with improved power efficiency and switching speeds. The second is to improve performance characteristics by fine-tuning the POM properties, such as ease of deposition, biocompatibility, withstanding harsh conditions.

3.4.1 For deposition

One of the main attractions of functionalising POMs is to be able to selectively deposit them where needed. This is helpful to create molecular memories which hold promise for ultra-low operating power and fast switching.[208] The choice of ligands[38,209,210] and deposition techniques[208] is very important as it will greatly impact device performance. Since these functionalised POMs will be confined on the surface, it is very common to use scanning tunnelling microscopy (STM) to test them, where the STM tip acts as a top electrode.

Petrovskii et al.[209] and Monakhov et al.[208] studied $[V_6^V O_{13}\ (OCH_2)_3CR_2]^{2-}$ (with R post-functionalised to any organic or inorganic group), a functionalised Lindqvist type POM. They attached this molecule to a gold substrate and used STM measurements to record I-V curves. They showed that the new groups can help stabilise and intake electrons. Additionally, they demonstrated that when a voltage is applied via the STM tip, the electrons re-organise (they can go into the ligands) and modify the structure. It is therefore possible to obtain multiple memory levels.

Yang et al.[211] functionalised $[V_6\text{-}(OH)_2]_2^-$ with cyclodextrine (CD) so they could attach it to a gold substrate, similarly to the work presented in the SAM/POM alternating monolayers section. However, their deposition technique was quite different: they used a mass spectrometer to mass-select the cation-free POM or CD molecules then soft-land them on the gold surface as intact supramolecular ions. This allowed for a fast deposition in ambient conditions. They explored the switching mechanism of their system and noted that once again, the POM redox states are at play. However, they noted that the missing counter-cations decreased the available number of states.

Laurans et al.[212] and Volatron et al.[213] functionalised $H_3PM_{12}O_{40}$ (M = W or Mo) with diazonium, so they could deposit the POM directly on a Si substrate. To get a uniform film, they simply needed to dip the substrate long enough (1 hour) in the functionalised POM solution. This timing is crucial because the more uniform monolayer conducts better than the less organised double layers.[213]

To explain the switching mechanism of their system, Laurans et al.[212] plotted an energy level diagram, shown in Figure 3.13 They showed that different POM metals have different energy level alignments and therefore interact differently with the applied voltage. More precisely, Mo can more easily be reduced due to its lower LUMO which opens more opportunities for fine-tuning and optimising device performance.

Glöß et al.[38] functionalised a Wells-Dawson POM: $(tBu_4N)_5[HP_2V_3W_{15}O_{59}((OCH_2)_3C\text{-}R)]$ with R = CH_2SMe or $NHCOC_6H_4SMe$. They found that the choice of R group modifies the self-assembly process of the POM on the gold surface and thus the energy level alignment of the materials with regard to gold Fermi level. When in direct contact with the gold surface, both POMs had their vanadium centres reduced from V^V to V^{IV}.

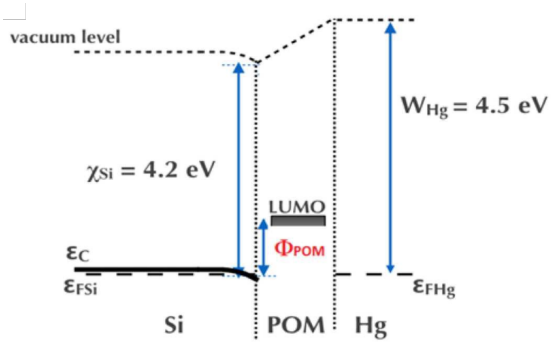

FIGURE 3.13: Schematic energy diagram of the Si/POM/Hg drop as deduce from the I-V measurements. Reproduced with permission from[212]. Copyright 2018, Royal Society of Chemistry.

This changes the band gap of the POMs compared to their isolated state. They were able to show multi-level switching by applying a voltage to the POMs and accessing the different vanadium oxidation states.

Gillet et al.[214] tested different thiol functionalised POMs to be attached to Pt nanoparticles. More precisely, they tested the influence of the POM charge by comparing three different POMs: first $(TBA)_3[PW_{11}O_{39}O(SiC_3H_6SH)_2]$ (POM-P) with a 3- charge, second $(TBA)_4[SiW_{11}O_{39}O(SiC_3H_6SH)_2]$ (POM-Si) which has a 4- charge and finally a 5- charge with $(TBA)_5[AlW_{11}O_{39}O(SiC_3H_6SH)_2]$ (POM-Al). They mainly used conductive atomic force microscopy (c-AFM) to analyse the charge transport properties. They noted that many factors besides the POM charge influenced performance such as the POM polarisability. Additionally, they found that as the POM charge increases, the polarisability decreases. Higher-charged or less polarisable POMs experience stronger Coulomb blockade (lower electron flow) therefore reducing charge transport. They mathematically link polarisability to the system dielectric constant using the Clausius-Mossotti model: when the polarisability increases, so does the dielectric constant. Therefore, a new factor to consider when investigating charge transport mechanisms is the POM polarisability.

3.4.2 For performance

While the ability to precisely deposit functionalised POMs is important for device fabrication, another strength of functionalisation lies in the possibility of enhancing POM performance aimed at different applications.

3.4.2.1 Biocompatibility

One particular example is the development of biocompatible POM-based systems. Vogelsberg et al.[215] functionalised a Lindqvist POM V_6O_{19} with a DNA origami. They

deposited this combination of a gold surface and use an STM tip as the top electrode as shown in Figure 3.14.

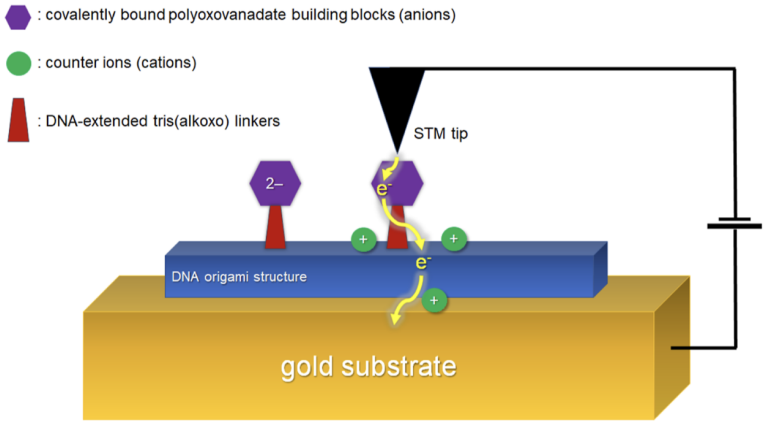

FIGURE 3.14: "Metal-DNA-origami-polyoxovanadate" heterostructure enabling the implementation of memristive functions via multi-logic functions as offered by POV6 (colour code: violet) and a synaptic dynamic as offered by the interplay between the gold surface (colour code: dark yellow), DNA-origami (colour code: blue), and counter ions (colour code: green). Reproduced with permission from[215]. Copyright 2023, American Chemical Society

Via scanning tunneling microscopy (STM) measurements and DFT calculations, they show that electrons re-organise when a voltage is applied, which modifies the molecular structure and therefore induces switching.

3.4.2.2 Harsh condition switching

Other functionalised POMs are designed to withstand extreme conditions, expanding their use to challenging environments, for example high temperatures. One approach is to combine the POM with a more high-temperature stable component: a metal-organic framework (MOF).[216] This is what Huang et al.[178] and Chen et al.[217] did: they synthesised $[Co_2(bpdo)_4(H_2O)_6](\alpha\text{-}GeW_{12}O_{40})x4H_2O$ (bpdo = 4,4'-bipyridine-N,N'-dioxide), shown in Figure 3.15a).

Both studied showed that the molecule can undergo reversible structural changes when heated due to water loss, similar to Gonzalez et al.[39]. During this process, the material exhibits thermochromism: it can change colour depending on the temperature as shown in Figure 3.15b.[218] They demonstrated multi-level switching: different colours or structures can be obtained for multiple temperatures. In terms of charge conduction mechanism (see Section 3.1.1), they identified Ohm's law for low voltages, and SCLC for high voltages. They used these mechanisms to explain the switching behaviour of their device. At first, thermally activated electrons are injected (Ohmic regime), then as the voltage increases, a space-charge field forms (SCLC regime) which slows down

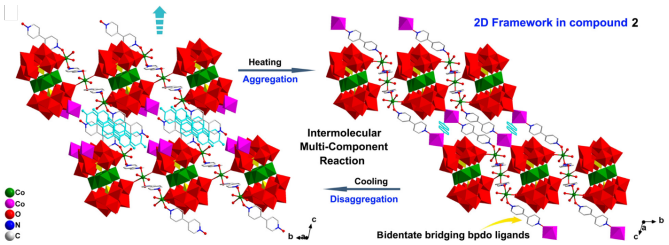

(A) Thermal-induced reversible structural and dimensional transformation between 1 and 2, accompanied by intermolecular three-component aggregation or disaggregation process. WO_6: red; PO_4: yellow; Co_4O_{16} core: green; $[Co(H_2O)_6]^{2+}$: purple; bpdo guest: turquoise.

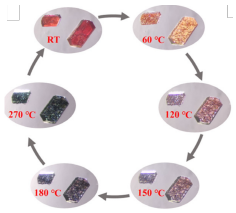

(B) Reversible multiple thermochromism of crystal 1.

FIGURE 3.15: Structure and thermochromism properties of $(Co_2\ (bpdo)_4(H_2O)_6)(\alpha\text{-}GeW_{12}O_{40}).4H_2O$. Reproduced with permission from [178]. Copyright 2021, John Wiley and Sons.

further carrier injection. Eventually, more carriers will be injected and overcome this barrier, switching the device between the high and low resistance states.

Other groups have also observed thermochromism for other POM structures. For example, Yu et al.[219] showed it for three different POM structures including both 2D layers: $Ni^{II}(1,4\text{-cby})_2[H_2(\gamma\text{-}Mo_8O_{26})]x4H_2O$, $Co^{II}(1,4\text{-cby})_2[H_2(\gamma\text{-}Mo_8O_{26})]x6H_2O$, and a 1D chain $Ni^{II}(1,3\text{-cby})(H_2O)(\beta\text{-}Mo_8O_{26})_{0.5}x2H_2O$.

3.4.3 Conclusion

In this section, I discussed how functionalising POMs can open new ways of enhancing their performance for specific applications. The work presented here focused on two approaches: fine-tune POM deposition capabilities and tailor POM properties for specific applications. Some approaches are to add organic ligands, combine POMs with different molecules such as DNA origami to enhance biocompatibility, or metal organic frameworks to improve high-temperature stability. These modifications affect electron re-organisation, energy level alignment and charge transport mechanisms which all in turn affect device performance. Overall, functionalising POMs offers a versatile approach to tailor their properties and enable new types of memory devices.

3.5 Encapsulating POMs

Building upon previous investigations[196] of POMs in molecular memory structures, Balliou et al.[220,221] explored the impact of encapsulating $H_3PW_{12}O_{40}$ layers to enhance device performance. By adding protective layers above and below the active POM components, they improved charge retention and were able to control carrier exchange dynamics. The first layer they tested was isopentylamine (IPA)[220] on top of the POM

layer, under the top aluminium electrode: $Si/SiO_2/APTES/POM/IPA/Al$. As described in a previous section, on top of the APTES layer, POMs form uniform nanoislands. They drew an energy level diagram shown in Figure 3.16a for all the involved layers. Similarly to other studies, it showed that Al Fermi level is slightly above the POM LUMO, facilitating electron transfer into the POM molecular orbitals. This alignment is once again key to the device operation: as a negative bias is applied to the gate, the Al Fermi level rises, allowing more POM energy levels to become accessible for charge storage. At the other interface, the SiO_2 layer serves as a tunneling barrier. Therefore, the switching effect is due to the charging and discharging of the POM layer.

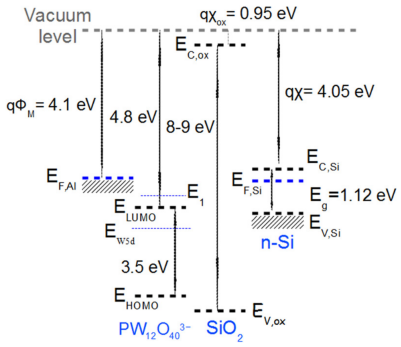

(A) Band diagram of the MIS structure layers before contact formation neglecting band bending, The estimated HOMO-LUMO gap of $PW_{12}O_{40}^{3-}$ is in accordance with Ref[222].

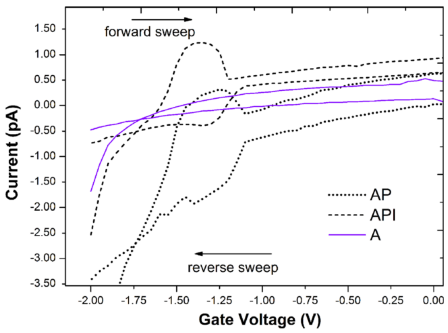

(B) Current-voltage characteristics monitored for [-2, 2] V voltage cycles and samples A (APTES only), AP (APTES+POM), and API (APTES+POM+IPA). The double staircase step was in all cases 50 mV, while the measurements were performed under RT conditions in dark electromagnetically shielded probe station.

FIGURE 3.16: $Si/SiO_2/APTES/POM/IPA/Al$ device energy level alignment and I-V curve. Reproduced with permission from[220]. Copyright 2014, AIP Publishing.

They then analysed the measured I-V curves (see Figure 3.16b) to identify the charge conduction mechanism for several voltages as discussed in Section 3.1.1.

1. - 2 V to 0 V: Electrons tunnel through the POM layer
2. At 0 V: Al Fermi level is higher than the POM LUMO, therefore some POM molecular levels are already full of electrons
3. 0 V to - 1.8 V: As Al Fermi level increases, more POM energy levels become available for electron occupation, increasing the current flow
4. - 1.7 V to -1.3 V: The Si becomes conductive, so electrons flow into the POM LUMO creating the maximum number of available conduction paths which translate in a conduction plateau
5. Beyond -1.3 V: Only a few electrons can tunnel resulting in a current decrease

As for the overall switching mechanism, they mention that POMs get reduced on the APTES which consumes the bridging oxygens creating oxygen vacancies, which can then be used to form conductive filaments as previously explained.

Then, they tested adding a Ta_2O_5 dielectric layer in order to further enhance device performance.[221] They investigated different configurations as shown in Figure 3.17. First, a device where the Ta_2O_5 dielectric layer is between the APTES layer and Si substrate is called P-Ox and shown in Figure 3.17a. Second, a device where the Ta_2O_5 dielectric layer is on top of the IPA layer, called Ox-P and shown in Figure 3.17b. Finally, a device where the active switching layers are sandwiched between two Ta_2O_5 dielectric layers, called Ox-P-Ox as shown in Figure 3.17c.

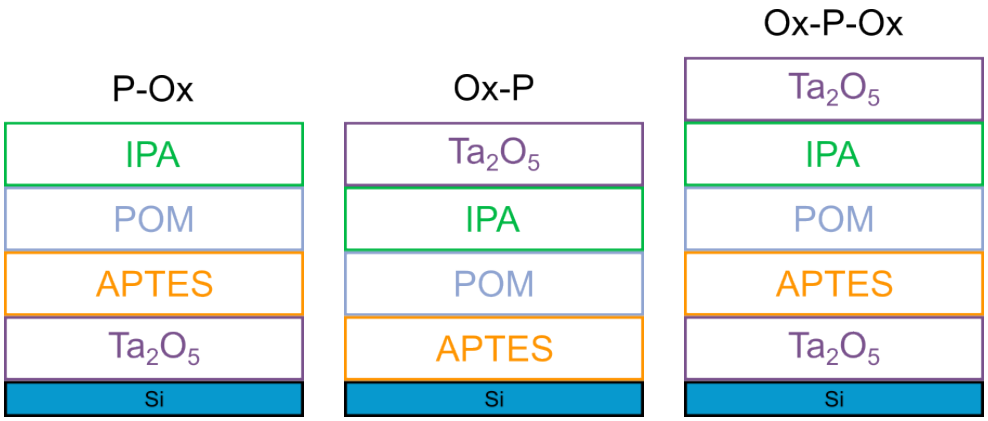

(A) P-Ox configuration (B) Ox-P configuration (C) Ox-P-Ox configuration

FIGURE 3.17: Tested arrangements of POM/Ta_2O_5 layers. Adapted with permission from[221]. Copyright 2016, American Chemical Society.

Before comparing the different configurations, they described the switching and charge transport mechanism. If the applied bias is negative, there is a Schottky barrier between the POM and the metal electrode. This hinders oxygen vacancies migration, which then get adsorbed at the POM/Ta_2O_5 interface, resulting in a large memory window. Therefore, they proved that by adding this dielectric layer, it can inject holes (generate oxygen vacancies) and trap charges, overall enhancing device performance.

Both P-Ox and Ox-P configuration have an enhanced programming speed compared to the Ox-P-Ox arrangement, as they respond to short pulses (100 μs instead of 100 ms). However, they exhibit limited charging ability due to pronounced back tunneling (the trapped carriers tunnel quickly back out of the material) when compared to the Ox-P-Ox structure. Between them, the Ox-P structure retains approximately half the charge of the P-Ox structure, showing the impact of layer arrangement on charge storage capacity. The Ox-P-Ox structure offers a larger memory window, as it can trap an increasing number of charges for programming voltages up to + 20 V, demonstrating superior charge storage capabilities. However, it operates at a lower programming

speed (100 ms) due to the presence of slow traps[c] within the Ta_2O_5 layers. All three device structures show comparable retention times, with no significant decay observed until after 10^4 seconds. There is a trade-off between charge storage capacity and programming speed for these devices.

In summary, this section looked at encapsulating POMs in memory devices to enhance performance. Different layers were tested including isopentylamine (IPA) and Ta_2O_5. These layers helped improve charge retention and control carrier exchange dynamics. Devices with the Ta_2O_5 layer demonstrated a trade-off between charge storage capacity and operation speed. Overall, the work presented here participates in the development of POM-based memory devices and suggested ways to enhance device behaviour.

3.6 Summary

Throughout this chapter, I have shown the potential of polyoxometalates in the field of redox-based resistive switching memories due to their rich redox properties and nanoscale dimensions. This chapter has explored different approaches for integrating POMs into memory devices, showing the versatility and tunability of these molecules.

The main switching mechanism in POM-based devices involves the redox reactions of the POMs themselves. However, other factors such as oxygen vacancy migration, POM orientation, and film morphology can also play a role in the device performance. The multiple redox states of POMs allow the creation of multi-level memory devices, potentially increasing data storage density for the same active area size.

Both two-terminal and three-terminal devices have been successfully fabricated. POMs were used in standalone layers, but also as alternating monolayers with SAMs, blends with polymers or carbon nanotubes, and as functionalised molecules, enabling a large variety of device applications and performance.

It is possible to further improve these designs. For instance, further reducing device size via new scalable fabrication techniques, would require less power to operate the devices and switching could be faster. One idea is to use nanogap-based devices as will be shown in Chapter 5. Another way would be to keep developing new hybrid materials containing POMs. This could create devices with enhanced performance and new functionalities.

The multi-level switching capability of POMs can be used for neuromorphic computing. [103,223] More work could be done on POM-based synaptic devices for brain-inspired computing architectures. Another application to target can be in-memory computing to create more efficient computing architectures.

[c]Slow traps are defects or impurities in a semiconductor material that capture and release charge carriers (electrons or holes) at a relatively slow rate compared to the device's operating speed.

In summary, POM-based memory devices show promise in nanoelectronics. While challenges remain, the rich and versatile properties of POMs offer many possibilities for next-generation technologies. Continued research in this area has the potential to advance data storage and processing.

Chapter 4

POM-Based Memory Devices Fabrication

As discussed in Chapter 2 and Chapter 3, many architectures and material choices are being studied for the two-terminal redox-based resistive switching memory (ReRAM) devices. To aim for faster switching and lower power consumption the two electrodes can be designed to be as close as possible without being shorted, i.e. have a nanogap between them. Another factor to consider is the arrangement of the electrodes. To host nanomaterials, coplanar geometries are better suited because in vertical or sandwich configurations, the electrodes could too easily be shorted: nanomaterials can form non-uniform films which often present pinholes. Therefore, coplanar nanogap separated electrodes are ideal for this work. A possible fabrication technique is e-beam lithography, but it is quite expensive and can difficulty fabricate asymmetric electrodes. Therefore, an alternative low-cost, high-throughput, large area fabrication technique is adhesion-lithography.[4]

In terms of material choice, polyoxometalates (POMs) are quite promising, as they have many available redox states, which can be used as various switching states, as was discussed in Chapter 3. Additionally, they are easy to process, as they are soluble in non-toxic water-based solvents, they have a large thermal stability range (- 195 to + 400 °C), and can be easily functionalised offering many chemical and structural possibilities.[34,110,111]

4.1 Electrode fabrication

The coplanar electrodes used to fabricate the devices studied throughout this project are made via adhesion lithography.[4] This procedure is depicted in Figure 4.1. First, a

uniform layer of aluminium is deposited by thermal evaporation on clean glass substrates. Then, the aluminium is patterned via standard photolithography (Figure 4.1a). The patterned substrates are then treated with a self-assembled monolayer (SAM) solution (Figure 4.1b). The chosen SAM is octadecylphosphonic acid (ODPA) because its head group (the phosphonic acid) chemisorbs to the native aluminium oxide layer (alumina), and its hydrophobic tail will ensure weak adhesion with gold (Figure 4.1c). Then, gold is deposited over the entire substrate (Figure 4.1d). However, because gold does not adhere very well to glass, a small (5 nm) seed layer of Al is deposited first. Finally, an adhesive polymer glue, is applied on the substrate (Figure 4.1e). After it has dried ($\pm$ 30 min), it is peeled off (Figure 4.1f). Because the adhesion forces between gold and the SAM are weak, the polymer removes the gold deposited on top of the aluminium as it is peeled off, while the gold deposited on top of the glass remains. The leftover SAM can be removed by UV-ozone ashing, leaving a nanogap between the aluminium and gold coplanar electrodes (Figure 4.1g). For a detailed protocol of the fabrication process, see Section A.1.

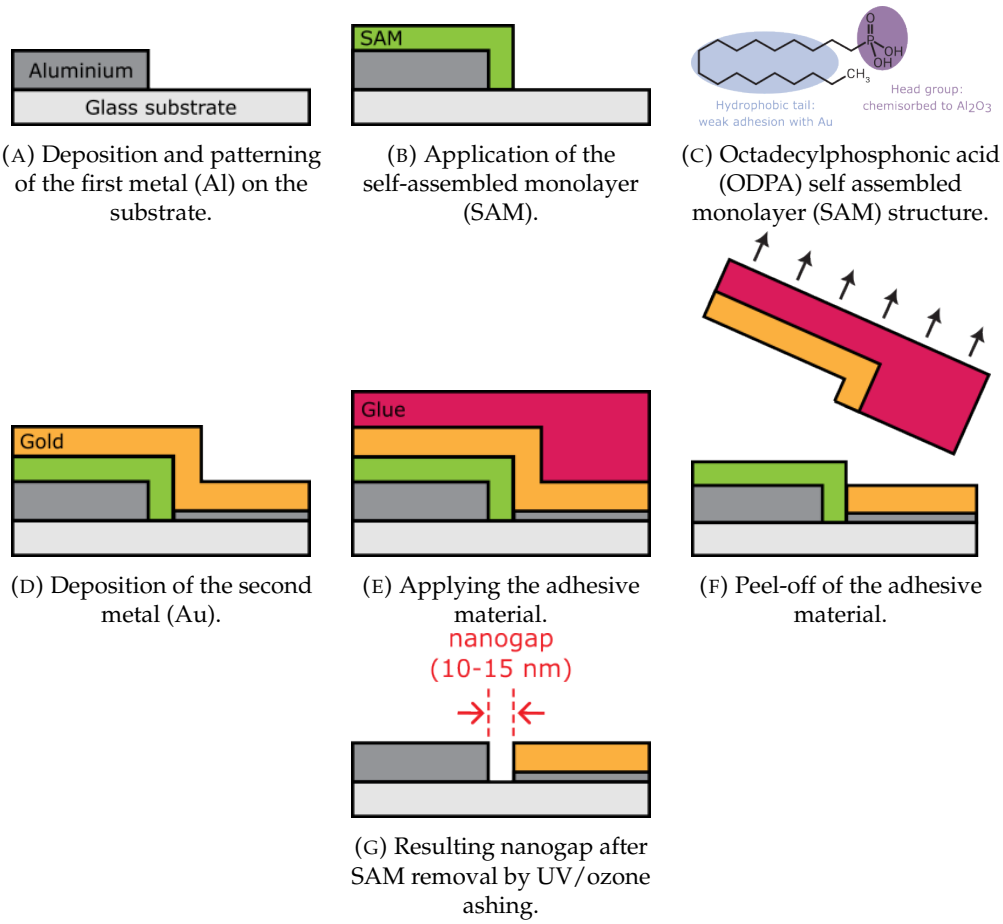

(A) Deposition and patterning of the first metal (Al) on the substrate.

(B) Application of the self-assembled monolayer (SAM).

(C) Octadecylphosphonic acid (ODPA) self assembled monolayer (SAM) structure.

(D) Deposition of the second metal (Au).

(E) Applying the adhesive material.

(F) Peel-off of the adhesive material.

(G) Resulting nanogap after SAM removal by UV/ozone ashing.

FIGURE 4.1: Adhesion lithography steps. Adapted from[4]. Available under a CC-BY 4.0 licence.

This fabrication technique was chosen as it presents many advantages. These coplanar electrodes can accommodate nanomaterials (such as POMs), it is compatible with

flexible substrates, and a variety of (opto)electronic devices designs are possible.[33,224]

4.2 Empty nanogap device characterisation

Before using these electrodes to make fully optimised and functioning devices with the active layer, I characterised a reference blank device[a]. This was done to ensure that the fabrication process is successful, namely the nanogap is of good quality and that the electrodes are not shorted. The characterisation was done using a combination of morphological studies and electrical measurements.

4.2.1 Nanogap morphology

The quality of the nanogap can be assessed via morphology studies. The nanogap should be smooth and consistent all around the perimeter of the interface of the two metals. Good techniques to observe this include atomic force microscopy (AFM) and scanning electron microscopy (SEM).

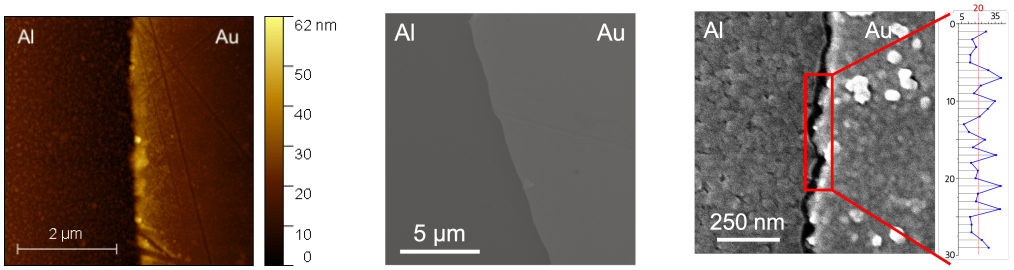

(A) AFM image (B) SEM image (C) High resolution SEM image

FIGURE 4.2: Micrographs of the as-fabricated nanogap separated coplanar electrodes.

Figure 4.2a depicts an AFM image of the interface between the two metals. It confirms that the two metals are indeed coplanar. I used the Gwyddion analysis software to extract surface roughness and grain size values from the AFM images. A value of RMS = 2.25 nm was obtained for aluminium, and RMS = 2.59 nm for gold. The surface roughness is the same order of magnitude for both metals, indicating that both metals have a similar smoothness. The grain size for aluminium is 43.01 nm and 44.61 nm for gold. These values are also of the same order of magnitude, meaning both metals have similar grain sizes. This is important for the peeling off step of the adhesion lithography process. The two metals must have similar grain sizes to avoid delamination.

SEM (Figure 4.2b) and high-resolution SEM (Figure 4.2c) images gathered by my colleague Dr. Evangelos Moutoulas, show that the nanogap is smooth and uniform all along the interface between both metals. This confirms that no delamination occurred

[a]No switching or active layer is deposited.

during the peeling process. Dr. Evangelos Moutoulas estimated the nanogap size to be around 20 nm from the high-resolution SEM images.

4.2.2 Nanogap reference device electrical characterisation

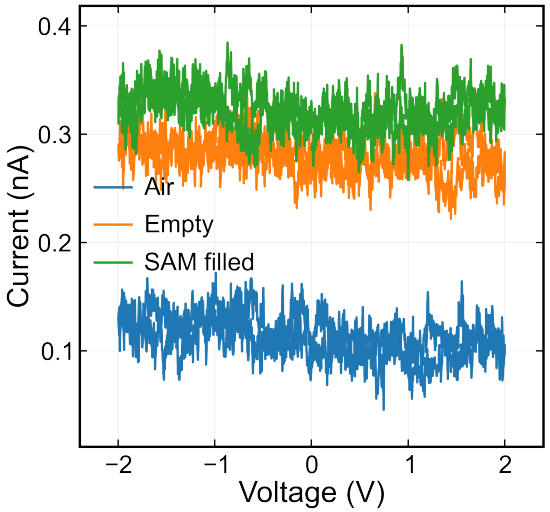

FIGURE 4.3: I-V curves of the open circuit (tips in air) empty SAM filled nanogap.

Next, I studied the electrical behaviour of the as-fabricated electrodes. A voltage was applied between the two metals via two micro-manipulators probe tips (one on each metal) and a Keysight B1500A source-measure unit (SMU). More details about this method can be found in Section A.2. More precisely, the voltage was swept from 0 V to + 2 V, then to - 2 V, and back to 0 V. This voltage range remains low enough that phenomena due to a large electric field being applied to the devices do not occur, such as the soft breakdown of the dielectric properties of the material.[225] The electric field is very high as the distance between the electrodes is short ($\approx$ 20 nm). As a reminder, $E = V/d$, where E is the electric field, V the applied voltage, and d, the distance between electrodes. Therefore, in this device, the electric field in the nanogap is around $20x10^9$ V/m or 20 GV/m. A comparison of the open circuit (the two tips are in air, not in contact with the electrodes), SAM filled nanogap, and the empty nanogap can be seen in Figure 4.3. For both the nanogap curves (empty and SAM filled), the current range is low (nA range) confirming the electrodes are not shorted. If the electrodes were shorted, the current would reach compliance - the maximum current value chosen to protect the devices from irreversible electrical breakdown. In addition, their current levels are still higher than the open-circuit indicating that indeed there has been a good contact between the electrodes and the probe station tips.

In summary, the adhesion lithography process and the SAM cleaning are successful: the nanogap is smooth and uniform and the electrodes are not shorted.

4.3 POM deposition techniques

The nanogap can then be filled by POMs via various deposition techniques. Since POMs have rich redox properties, it is possible to look into electro-deposition techniques.[226,227] However, solution processing is another popular choice for thin film deposition due to its low cost, good scalability, and versatility (with different solvents, materials, substrates, patterning techniques).[228,229] More specifically, throughout this work, I explored two different techniques: spin-coating and drop-casting. The general concept of these techniques will be described here, but more details (solution specifications, spin speeds, ...) will be given when comparing them throughout the rest of the manuscript.

When spin-coating, a solution of the material to deposit is made, then dropped onto the middle of a substrate, which is then spun, as shown in Figure 4.4. Finally, the solvent is removed, leaving only the material, by annealing the substrate for 5 minutes at the solvent boiling point temperature. The spin speed will influence the final film thickness. Again, more details will be given when appropriate.

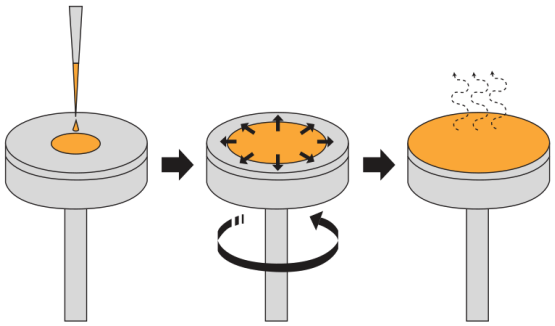

FIGURE 4.4: Spin-coating deposition technique schematic.

To drop-cast, a solution of the material to deposit is made. Then is dropped onto the middle of the substrate, but no spinning is done. The substrate is left to dry in air until all the solvent has evaporated ($\pm$ 20 minutes) as shown in Figure 4.5.

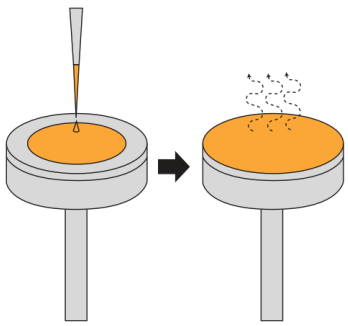

FIGURE 4.5: Drop-casting deposition technique schematic.

4.4 Summary

This chapter focused on explaining the experimental fabrication techniques used for this work. More specifically, a detailed procedure of the adhesion-lithography and polyoxometalate deposition techniques was given.

A-lith is a low-cost, high-throughput, large area fabrication technique that allows for the fabrication of coplanar nanogap separated electrodes. This platform is ideal for hosting nanoparticles such as POMs. The pristine electrodes were characterised to ensure the quality of the nanogap. AFM, SEM, and high-resolution images showed their successful fabrication. No delamination was observed, and the nanogap was estimated to be around 20 nm. Additionally, electrical characterisation confirmed that the electrodes were not shorted.

The two POM deposition techniques chosen for this work are spin-coating and drop-casting. They are both solution processing techniques which make them low cost, scalable, and versatile.

Together, the combination of the polyoxometalates and the asymmetric nanogap separated coplanar electrodes are ideal candidates for the design of redox-based resistive switching memory devices.

Chapter 5

POM-Based Memory Devices

As mentioned in Chapter 3, polyoxometalates (POMs) are excellent candidates for use as active/switching layers in electronic memories. Their rich redox properties hold promise for multilevel devices[36–39], which can be used to advance current memory technologies to the next level. In parallel to working on the material choice, the device architecture can also be optimised. For instance, as discussed in Chapter 4, nanogap separated coplanar electrodes are good platforms to host nanomaterials such as polyoxometalates. The more traditional vertical/sandwich structure would too easily be shorted as POMs do not form perfectly homogeneous films and could be penetrated by the top electrode. In particular, electrodes made via adhesion lithography[4] are quite interesting as this technique is compatible with flexible substrates, large areas, and cost-efficient. Additionally, different electrode patterns can be made enabling many applications such as diodes[230], photodetectors[224], and electronic memories[225].

In this chapter, I explore the combination of these asymmetric coplanar nanogap separated electrodes with POMs to form redox-based resistive memory (ReRAM) devices. At first, the material choice will be discussed: various POMs will be compared. Then the deposition technique will be optimised in order to form the best performing devices possible. Finally, I show further device performance optimisation by adding a poly(methyl methacrylate) (PMMA) layer in the switching material.

5.1 Preliminary results

In this section, I present some preliminary results that helped me familiarise with the studied system. To better understand POM materials, I chose to compare 4 different commercially available and structurally simple POMs (Keggin structure as shown in

Figure 5.1): $H_3PW_{12}O_{40}$, $H_3PMo_{12}O_{40}$, $Na_3PMo_{12}O_{40}$, and $(NH_4)_3PMo_{12}O_{40}$. They allow a comparison of the transition metal and the counter-cation. The POMs were deposited via spin-coating (at 2000 rpm for 30 s with a 10 s ramp) from a 10 mg/mL solution in nitromethane on empty asymmetric nanogap separated coplanar electrodes fabricated via adhesion lithography (a-lith), see Section 4.1. I investigated both the film morphologies and electrical characteristics of these preliminary devices.

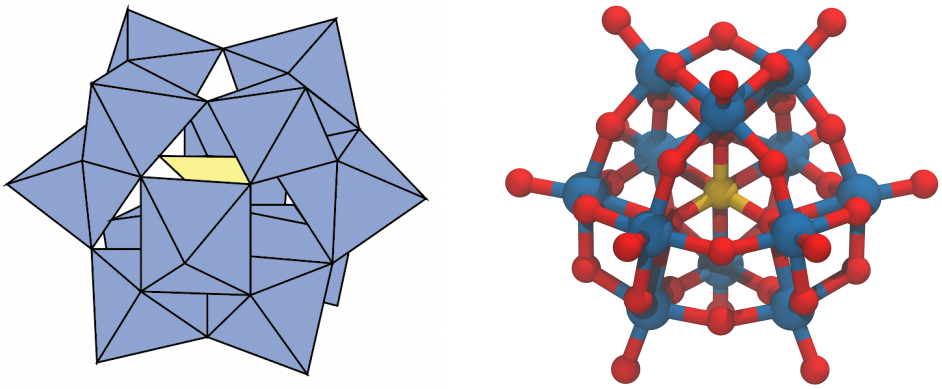

FIGURE 5.1: Keggin POM structure.

5.1.1 Film morphology

I first characterised film morphologies using atomic force microscopy (AFM), as shown in Figure 5.2. The roughness and grain size values extracted from the AFM images using the Gwyddion analysis software can be found in Table 5.1.

TABLE 5.1: Roughness and grain size values for various POM films ($H_3PW_{12}O_{40}$, $H_3PMo_{12}O_{40}$, $Na_3PMo_{12}O_{40}$, and $(NH_4)_3PMo_{12}O_{40}$) spin-coated onto ODPA-free electrodes.

	RMS Al (nm)	**RMS Au (nm)**	**Grain size Al (nm)**	**Grain size Au (nm)**
$H_3PW_{12}O_{40}$	3.62	3.19	58.03	47.14
$H_3PMo_{12}O_{40}$	5.88	7.69	53.56	69.56
$Na_3PMo_{12}O_{40}$	4.57	4.45	61.55	57.70
$(NH_4)_3PMo_{12}O_{40}$	25.72	22.25	52.84	77.45

$H_3PW_{12}O_{40}$ (Figure 5.2a) forms a very similar film on gold and aluminium: the RMS roughness value of the film deposited on gold (RMS = 3.19 nm) is of the same order of magnitude than the film deposited on aluminium (RMS = 3.62 nm). This is also seen in the image: the dispersion of the aggregates is quite similar even if the number and size of aggregates (58.03 nm on aluminium vs 47.14 nm on gold) is slightly different for both metals. $H_3PMo_{12}O_{40}$ (Figure 5.2b) forms a smoother film on aluminium (RMS = 5.88 nm) than on gold (RMS = 7.69 nm). As observed in the image, fewer and larger aggregates are formed on gold (69.56 nm) compared to more and smaller on aluminium

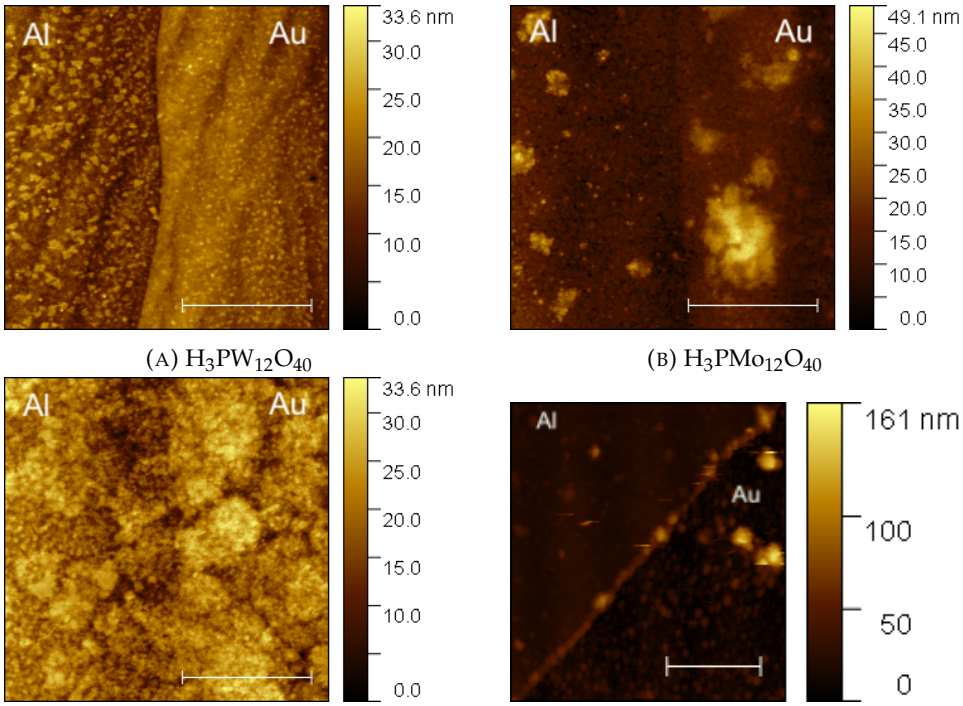

(A) $H_3PW_{12}O_{40}$ (B) $H_3PMo_{12}O_{40}$

(C) $Na_3PMo_{12}O_{40}$ (D) $(NH_4)_3PMo_{12}O_{40}$

FIGURE 5.2: Comparing the various POM films morphologies via AFM, the scale bar is 2 μm.

(53.56 nm). $Na_3PMo_{12}O_{40}$ (Figure 5.2c) forms a uniform film over both metals: the roughness values are of the same order of magnitude for both metals (RMS = 4.57 nm on aluminium, and RMS = 4.45 nm on gold). However, aggregates are slightly larger on aluminium (61.55 nm on aluminium and 57.70 nm on gold). $(NH_4)_3PMo_{12}O_{40}$ (Figure 5.2d) forms a smoother film on gold (RMS = 22.25, and RMS = 25.72 on aluminium). Larger aggregates are formed on gold (77.45 nm, and 52.94 nm on aluminium). Overall, the AFM images show that each POM forms films differently: there are different aggregate sizes and patterns visible for each POM.

I also recorded scanning electron microscopy (SEM) images as presented in Figure 5.3. They allow for a more zoomed out view of the films and get a broader picture of the morphology.

Both $H_3PW_{12}O_{40}$ (Figure 5.3a) and $H_3PMo_{12}O_{40}$ (Figure 5.3b) films are hard to notice on the SEM images: very few bright spots are visible. A possible explanation is that they form quite thin, smooth, and uniform films. $Na_3PMo_{12}O_{40}$ (Figure 5.3c) and especially $(NH_4)_3PMo_{12}O_{40}$ (Figure 5.3d) show more aggregates (bright spots on the image). This observation is also corroborated by the film roughness values presented in Table 5.1: the RMS values for $(NH_4)_3PMo_{12}O_{40}$ are much higher than the other POMs. This can be explained by the fact that $(NH_4)_3PMo_{12}O_{40}$ did not dissolve as well as the other POMs in solution: a more milky solution can be seen in Figure 5.4.

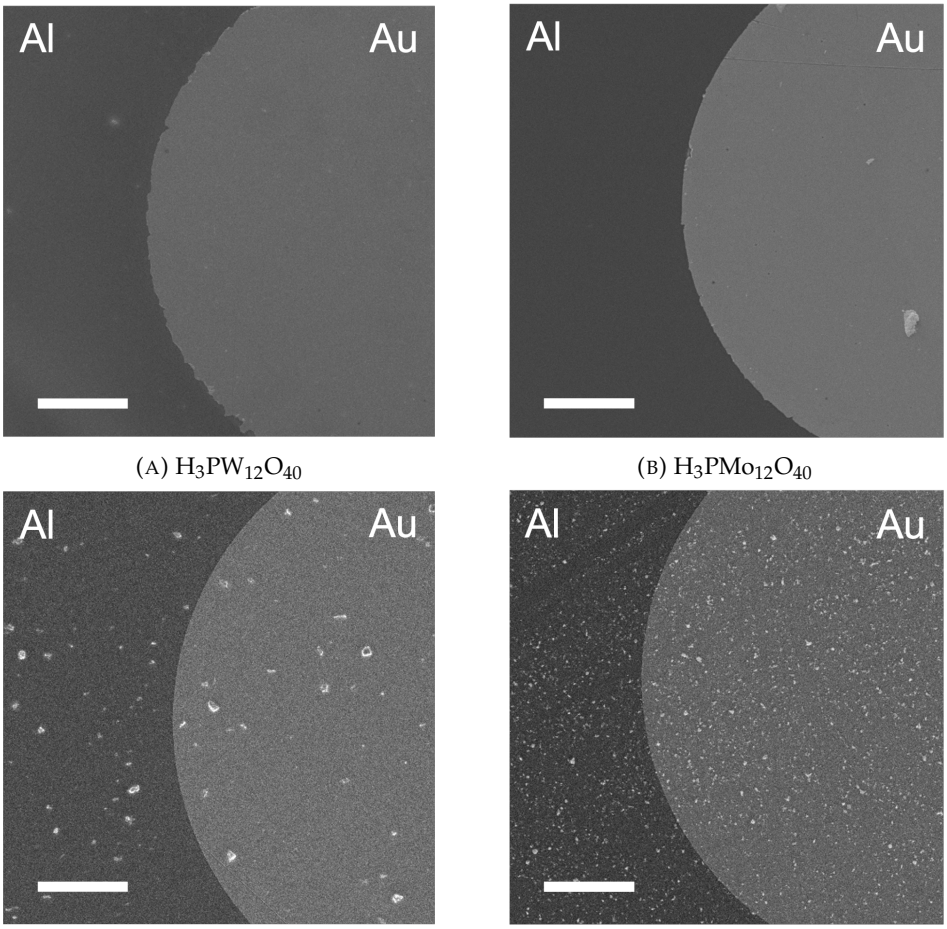

(A) $H_3PW_{12}O_{40}$ (B) $H_3PMo_{12}O_{40}$

(C) $Na_3PMo_{12}O_{40}$ (D) $(NH_4)_3PMo_{12}O_{40}$

FIGURE 5.3: Comparing SEM images of various POM film morphologies spin-coat onto ODPA-free electrodes.

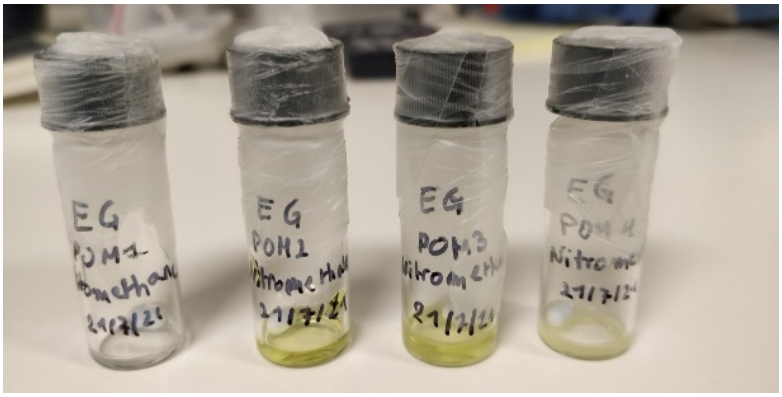

FIGURE 5.4: Pictures of $H_3PW_{12}O_{40}$, $H_3PMo_{12}O_{40}$, $Na_3PMo_{12}O_{40}$, $(NH_4)_3PMo_{12}O_{40}$ 10 mg/mL solutions in nitromethane.

In summary, each POM has different film forming properties. The results seem to indicate that film forming properties not only depend on the transition metal and the counter-cation of the POM, but also the metal on which the POM is deposited.

5.1.2 Electrical performance

The same films were then electrically characterised by using a probe station to apply a voltage with a Keysight B1500A SMU via probe tips on each metal (Al and Au) and recording the current. From the gathered data, I plot I-V curves. I define a good device as one that has a large hysteresis, i.e. different current levels for the same voltage during the forward and reverse scans, that switches at low voltages for low power consumption, and is consistent for many cycles, ideally 10^{10}.[31,107] Throughout this work, I will use the POM redox peak positions and amplitude in the I-V curves to compare the tested devices. These peaks need to be discernable i.e. have a high ON/OFF ratio (ideally, at least 1) and at low voltage for low power consumption (ideally, lower than +/- 1 V).

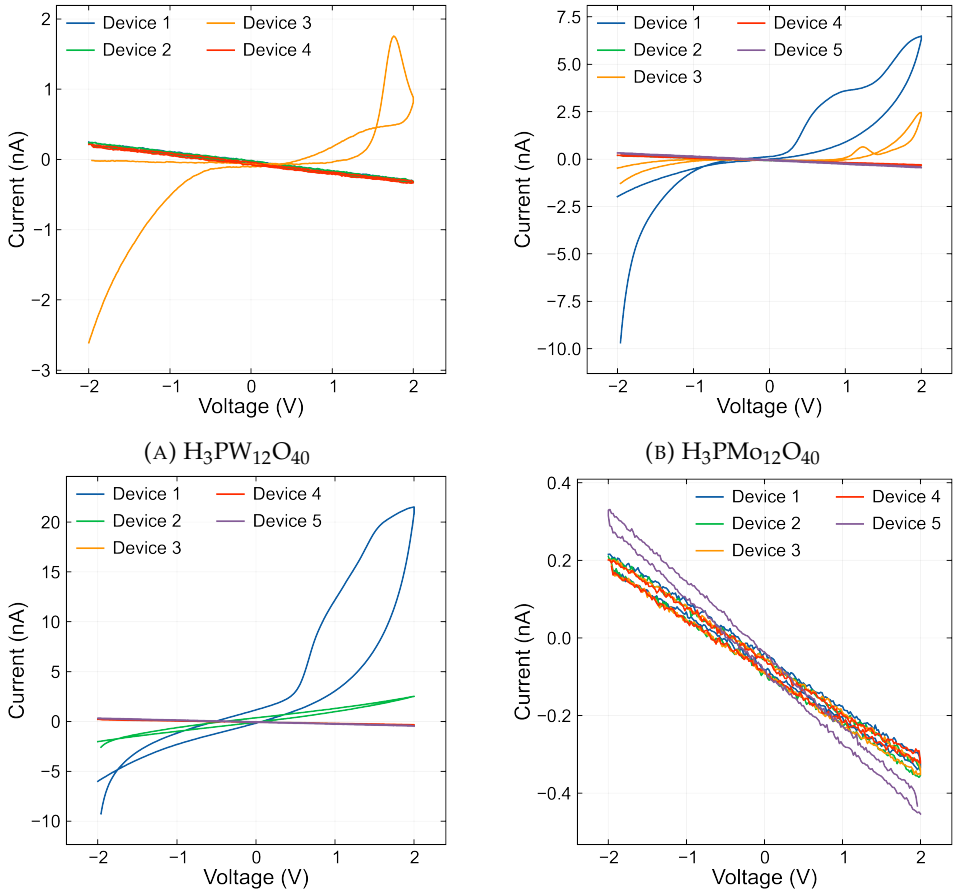

(A) $H_3PW_{12}O_{40}$ (B) $H_3PMo_{12}O_{40}$

(C) $Na_3PMo_{12}O_{40}$ (D) $(NH_4)_3PMo_{12}O_{40}$

FIGURE 5.5: I-V characteristics of multiple devices based on different POMs deposited via spin-coating (2000 rpm, 30 s) from nitromethane solution (10 mg/mL) onto ODPA-free electrodes.

For the first electrical measurements, the voltage was swept from - 2 V to 2 V (forward sweep), back to -2 V (reverse sweep). Figure 5.5 shows the obtained I-V curves for a number of measured devices for the different tested POMs. A first observation to make is that the currents obtained for these devices is higher than the reference empty

and open circuit I-V curves (see Figure 4.3), except for $(NH_4)_3PMo_{12}O_{40}$ which has similar current levels and shows no redox peaks; it behaves like the reference empty nanogap. This can be linked to the film morphology discussion: $(NH_4)_3PMo_{12}O_{40}$ did not penetrate the nanogap and rather formed many aggregates at the surface due to its poor solubility. For the other POMs, there is some device-to-device variability, but for each POM, at least one device exhibits a large peak in the positive voltage region.

The devices exhibiting higher currents and distinct peaks were scanned multiple times to investigate their endurance characteristics, as shown in Figure 5.6. The peaks remain visible for all POMs apart from $(NH_4)_3PMo_{12}O_{40}$, but seem to decay after only a few scans, decreasing the ON/OFF ratio. This can be improved by optimising the film deposition procedure, as will be discussed in the next sections.

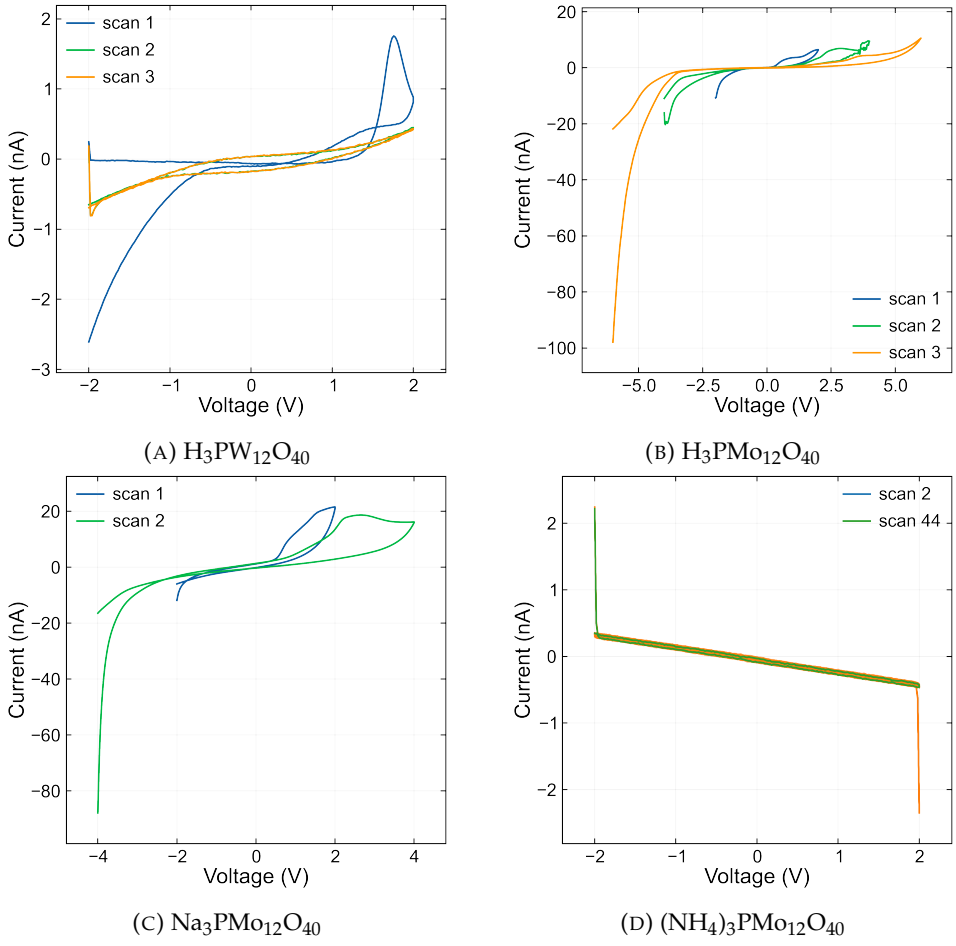

(A) $H_3PW_{12}O_{40}$ (B) $H_3PMo_{12}O_{40}$

(C) $Na_3PMo_{12}O_{40}$ (D) $(NH_4)_3PMo_{12}O_{40}$

FIGURE 5.6: I-V characteristics of multiple scans of a single device based on different POMs deposited via spin-coating (2000 rpm, 30 s) from nitromethane solution (10 mg/mL) onto ODPA-free electrodes.

Finally, I plot together the different POMs for an easier comparison (Figure 5.7). It seems that the Mo-based POMs give higher currents compared to the W-based POM, with the Na^+ counter-cation giving the highest current compared to the H^+ counter-cation in the Mo-POMs. A possible explanation is the alignment of the energy levels.

Figure 5.8 shows that $H_3PMo_{12}O_{40}$ LUMO (- 5.1 eV) lies bellow $H_3PW_{12}O_{40}$ LUMO (- 4.6 eV). This means that $H_3PMo_{12}O_{40}$ is more easily reduced: electrons can more easily flow into its LUMO level from either the Al or Au electrode.[231] Therefore, higher currents are more easily reached. This will be further discussed in Section 6.1.4.

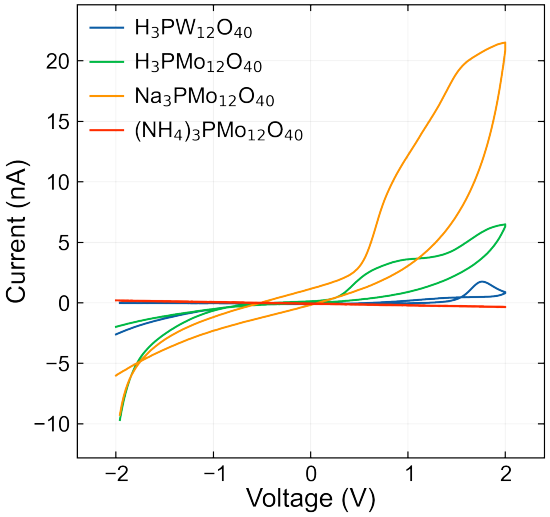

FIGURE 5.7: I-V characteristics of devices based on various POMs deposited via spin-coating (2000 rpm) from nitromethane solution (10 mg/mL) onto ODPA-free electrodes.

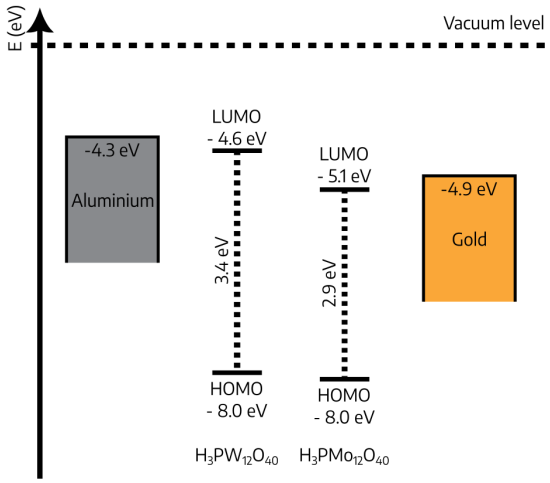

FIGURE 5.8: HOMO/LUMO energy level alignment of $H_3PW_{12}O_{40}$ and $H_3PMo_{12}O_{40}$ with Al and Au Fermi energy level, values taken from[185].

In summary, $(NH_4)_3PMo_{12}O_{40}$-based devices do not show any redox activity. They seem to show a similar response to the bare, ODPA-free, nanogap electrodes. The second POM $Na_3PMo_{12}O_{40}$ has the highest currents and broader peak, closely followed by $H_3PMo_{12}O_{40}$. Finally, $H_3PW_{12}O_{40}$ showed higher device-to-device variability. Therefore, Mo-based POMs with smaller counter-cation seem to be the most promising.

5.1.3 Conclusions

From this preliminary study on the different POMs, it seems that Mo-based POMs with small counter-cations hold promise for designing redox-based resistive memory devices. To continue this work, $H_3PMo_{12}O_{40}$ was selected as it showed pronounced redox peaks for multiple devices, which were stable for a few scans (2 or 3).

In the next part of this study, I will optimise $H_3PMo_{12}O_{40}$ deposition in the nanogap in order to increase the scan-to-scan stability (endurance) and decrease the device-to-device variability of these POM-based devices.

5.2 Deposition technique comparison

Now that I established $H_3PMo_{12}O_{40}$ as the most promising POM for this work, the deposition process will be optimised. As mentioned in the previous section, the endurance of the devices still has room for improvement. In this section, spin-coating at different speeds and drop-casting will be compared. The initial POM solution specifications are 10 mg/mL in methanol as it is less hazardous than nitromethane due to environmental considerations, safety handling, and waste management. For the spin-coated films, three speeds were tested: 1000 rpm, 2000 rpm, and 3000 rpm. Their thickness was measured using a stylus profilometer (see Section A.4) and the obtained values are 150, 80, 20 nm respectively. They will therefore be named SC 150 nm, SC 80 nm, and SC 20 nm, respectively. The drop-cast film was too rough to get an accurate thickness measurement. However, it is estimated to be 300-400 nm thick. It will be labelled as DC for the rest of this work.

5.2.1 POM film characterisation

Figure 5.9 shows optical microscopy images of the different tested deposition techniques, i.e. spin-coated and drop-cast films. Regardless of spin speed, the spin-coated films all show long lamella-type domains uniformly over both aluminium and gold metals. The drop-cast film is visually much rougher, non-uniform and exhibits some pinholes[a]. Also because of these pinholes, the underlying electrode metals (aluminium and gold) are visible, which may slightly tint the colour of the film. However, as more clearly seen in Figure 5.9b, the film colour itself is the same on both metals.

UV/Vis spectroscopy is another technique used to characterise these films, allowing insight into the POM oxidation state. The POM UV/Vis spectra can be split into two main regions[232]: the POM signature region where two ligand-to-metal (O $\rightarrow$ Mo) charge

[a] Corroborating the idea that sandwich architectures are not ideal for POM-based devices.

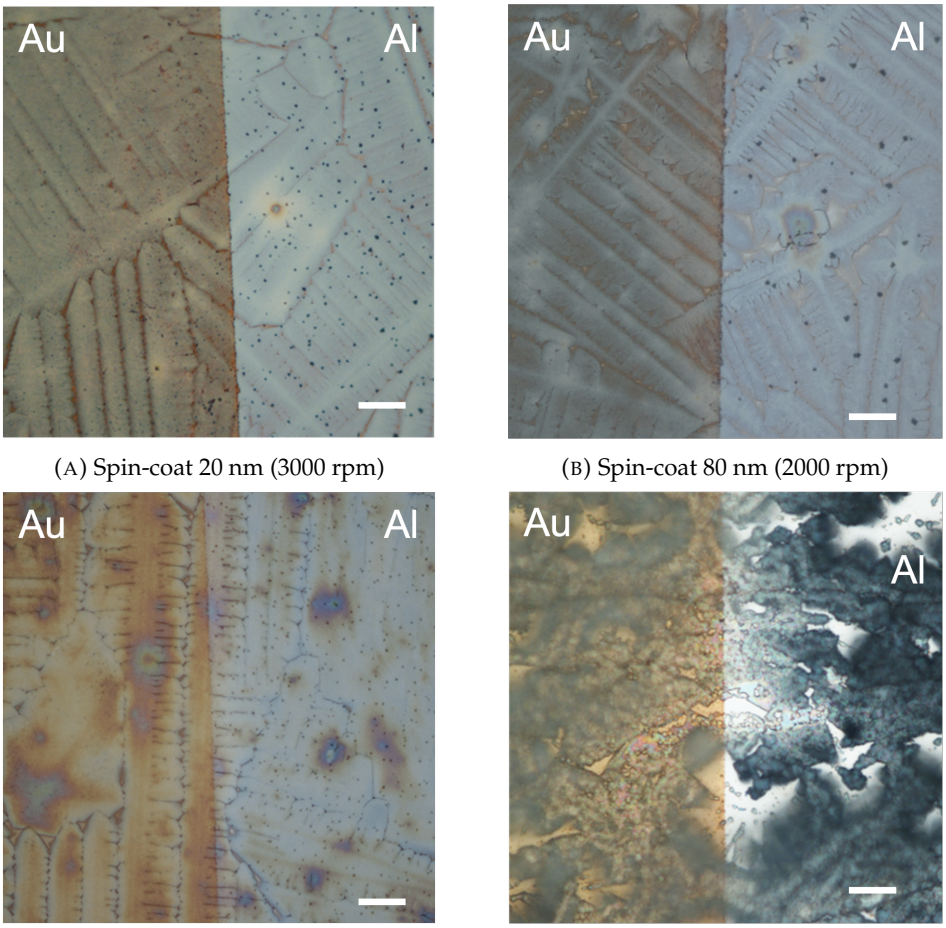

(A) Spin-coat 20 nm (3000 rpm)

(B) Spin-coat 80 nm (2000 rpm)

(C) Spin-coat 150 nm (1000 rpm)

(D) Drop-cast

FIGURE 5.9: Optical microscopy images, comparing the film morphologies of $H_3PMo_{12}O_{40}$ films deposited via different techniques, the scale bar is 10 μm.

transfer peaks appear (200-750 nm) and the POM reduced region (750-1400 nm) where the intervalence charge transfer broad peak becomes apparent if the POM is reduced.

The spectra recorded for $H_3PMo_{12}O_{40}$ deposited via different techniques on a quartz substrate are shown in Figure 5.10. In the POM signature region, the two peaks appear at 222 and 316 nm, highlighted by grey dashed lines. Their intensity increases with film thickness. In the POM reduced region, the thicker drop-cast film, appears to be more reduced as the intervalence charge transfer broad peak is more pronounced. A possible reason could be the increased moisture content due to the fact that the drop-cast film does not get annealed. Moisture can enable POM reduction by participating in a counter reaction. This will be discussed further in Section 6.2.

5.2.2 Electrical performance

I tested the electrical performance of devices made from different deposition techniques. The voltage was scanned from 0 V to + 2 V (forward sweep), to -2 V (reverse

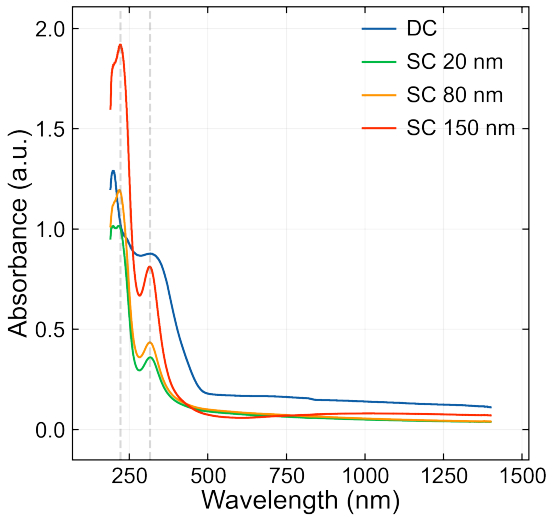

FIGURE 5.10: Raw Absorbance UV/Vis spectra of $H_3PMo_{12}O_{40}$ films spin-coat and drop-cast on quartz substrates.

sweep), back to 0 V. Figure 5.11 shows the obtained I-V curves for different devices for the different spin-coating speeds, hence film thicknesses.

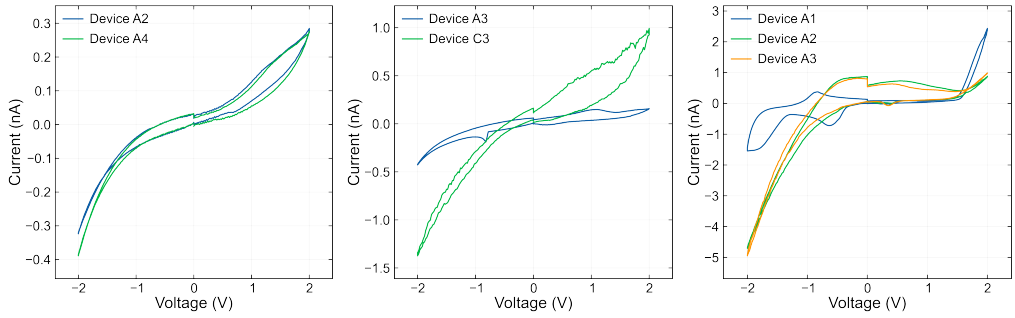

(A) Spin-coat 20 nm (3000 rpm) (B) Spin-coat 80 nm (2000 rpm) (C) Spin-coat 150 nm (1000 rpm)

FIGURE 5.11: Device-to-device variability of the spin-coated films.

As the film thickness increases, some devices exhibit some redox peaks. The thickest film (SC 150 nm) has the most pronounced peak. As mentioned in Chapter 2 and observed in the previous section, device-to-device variability is still a challenge for redox-based resistive memories. A possible solution to this will be discussed in the next section. As discussed above, the redox peak intensity (the biggest possible) and voltage position (the lowest possible) will be my benchmark to compare devices. Therefore, device A1 for the SC 150 nm film is the best of all the presented devices as it clearly exhibits redox activity. Devices A4 and A3 were chosen for the SC 20 and 80 nm, respectively, due to their higher current levels. Another aspect to consider is the memory window. For the SC 20 and 80 nm devices, it is around 0.2 nA, while it is around 1 nA for the SC 150 nm device. These are quite small values compared to the requirements detailed in the introduction of Chapter 2. Therefore, applications which don't require

such large memory windows are better options, such as neuromorphic computing. Figure 5.12 shows the scan-to-scan variability for the selected devices.

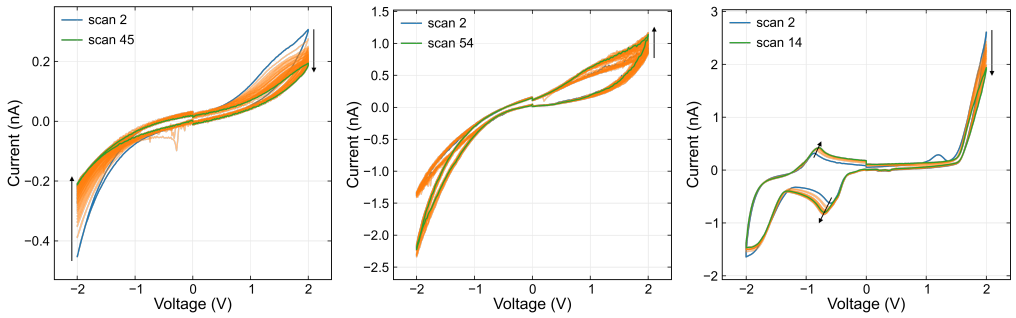

(A) Spin-coat 20 nm (3000 rpm) (B) Spin-coat 80 nm (2000 rpm) (C) Spin-coat 150 nm (1000 rpm)

FIGURE 5.12: Scan-to-scan variability of the spin-coated films.

For the SC 20 nm film, no redox peaks are visible, but the overall shape of the I-V curve remains similar as scans are recorded. It can be observed that the overall current is decreasing upon consecutive scans. This indicates that some degradation (of the POMs and/or of the electrodes) is occurring, which decreases the conductivity.[25,72]

The SC 80 nm film is more consistent: the current levels change less than the SC 20 nm film as scans are measured. There are a few middle scans where the current at - 2 V changed. This can be due to a contact issue between the tips and the device electrodes. The current at + 2 V, increases slightly with the scan number. This could be due to charge accumulation as scans are performed.[95]

The SC 150 nm film shows quite a different response: redox peaks become apparent at around - 0.8 V. This can be explained by the fact that more material is present (the film is thicker). Since it is thicker, there is likely more moisture trapped in the film, which can help enable the POM redox reaction by offering a counter-balance reaction (as will be further discussed in Chapter 6).[27,76,77] These redox peaks were visible for only 14 scans. As discussed in Chapter 2, scan-to-scan variability is another challenge of redox-based resistive switching devices. Again, this will be discussed further in the next section. The current at the redox peak maximum (at around - 0.8 V) increases as scans are done, while the current at + 2 V decreases with the scans. Similarly to the SC 20 nm films, this can be associated with the electrode metals or POM degradation. Another indication is the large tail which appears starting at + 1.5 V. A solution to this will be suggested when discussing the DC films.

Another observation to make is comparing the current levels with regard to the film thickness. As seen throughout Figure 5.12, as the film thickness increases, the current levels also increase. An explanation can be that more POMs are present, which can enable more redox reactions to occur. This will be further discussed in Section 6.4.

The other deposition technique which I compared is drop-casting. From the film morphology study, they appear to be much thicker than the spin-coated films. Figure 5.13 shows the obtained I-V curves for different devices for the drop-cast deposition technique.

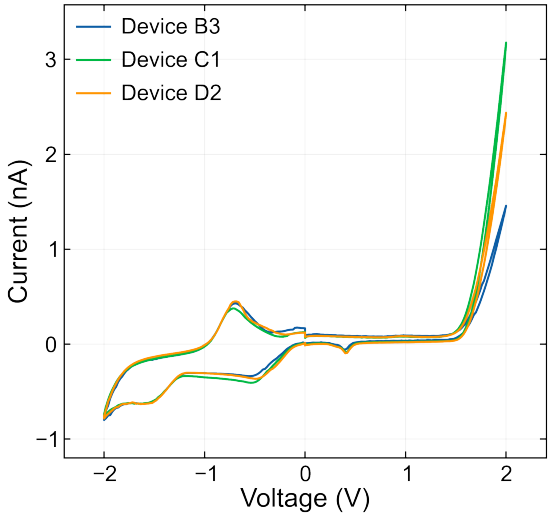

FIGURE 5.13: Device-to-device variability of the drop-cast $H_3PMo_{12}O_{40}$ film.

Similarly to the thickest spin-coated film (SC 150 nm), redox peaks are quite prominent at around - 0.8 V. There is little device-to-device variability: only the current level at + 2 V is different. Figure 5.14a shows the scan-to-scan variability of device D2. The overall shape of the I-V curve changes little as scans are recorded. The current at + 2 V decreases, similar to the SC 20 and 150 nm films, while at the redox peak maximum (around - 0.8 V) increases with the scan number. The "tail" observed between + 1.5 and + 2 V can be due to electrode metal or POM degradation. The DC films may have even more moisture trapped compared to the SC 150 nm films, as they were not annealed to evaporate the solvent, but left to dry in air. To help prevent electrochemical side reactions to occur, the same device was scanned from 0 V to + 1.5 V only (forward sweep), to -2 V (reverse sweep), and back to 0 V as shown in Figure 5.14b. This indeed helped to mitigate the material degradation and enhanced the redox peaks, which are now better defined. The current levels at the redox peak maxima increase with sequential scans. This can be explained by ion migration. There are more reactants available for the redox reaction at that peak as scans are done increasing the conductivity level.[233,234] This will be discussed further in Section 6.1.

5.2.3 Conclusions

$H_3PMo_{12}O_{40}$ films are formed uniformly over both the aluminium and gold electrodes. The spin-coated films all show some long lamella type domain, while the drop-cast film is visibly much thicker and shows some pinholes. The thicker films (SC 150 nm and

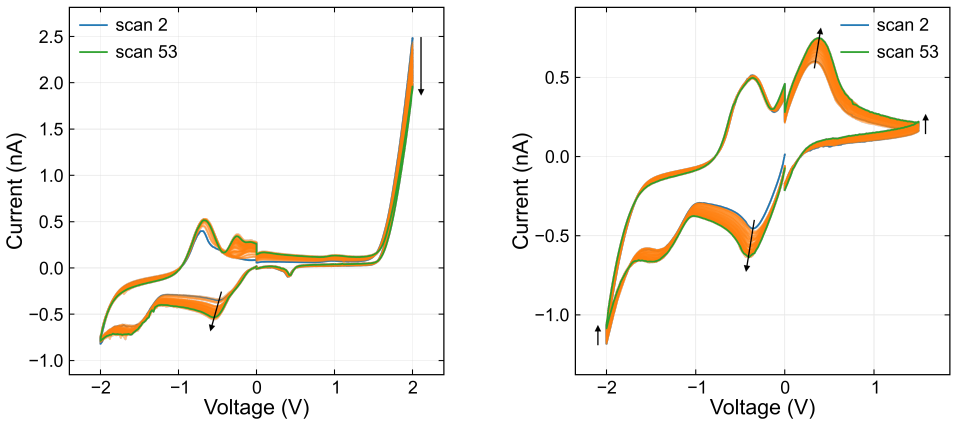

(A) Full - 2 to + 2 V scan range

(B) Short - 2 to + 1.5 V scan range

FIGURE 5.14: Scan-to-scan variability of the drop-cast $H_3PMo_{12}O_{40}$ film for different scan ranges. Changing the scan range can help prevent material degradation.

drop-cast) exhibit redox peaks in their I-V curves, due to the more material and moisture present (which can enable POM redox reaction by acting as the counter-balance reaction). The current level at the top of these redox peaks increases as scans are performed, while the current at the maximum positive voltage range decreases with the scan number. This can be explained by migration of the reactants which accumulate as scans are recorded[235] (see Section 6.1), and electrode metal and/or POM degradation respectively. Unfortunately, there is still some device-to-device and scan-to-scan variability. This is a known challenge of the redox-based resistive switching devices and will be addressed in the next section.

The spin-coating deposition method is more reliable than the drop-casting technique: it allows for a more consistent film deposition throughout different fabrication batches. It also allows for a more controllable thickness. Therefore, I retain the spin-coat 150 nm film (1000 rpm) as best candidate for the rest of this work.

5.3 Device optimisation

As discussed in the previous sections, there is still some device-to-device and scan-to-scan variability. It can be caused by reactions between the POM and the Al electrode, such as spontaneous reduction. In this section, I discuss a possible solution: adding a poly(methyl methacrylate) (PMMA) layer between the electrodes and the POM. PMMA is a synthetic polymer which can help with proton conduction.[53,199,200]

5.3.1 Film morphology

I start by discussing the PMMA film morphology. Figure 5.15 shows optical microscopy images of different thicknesses of spin-coated PMMA films. All films are very smooth and uniform, it is quite hard to even confirm with the naked eye that the film is there. Electrical characterisation or film thickness measurements can help to confirm it.

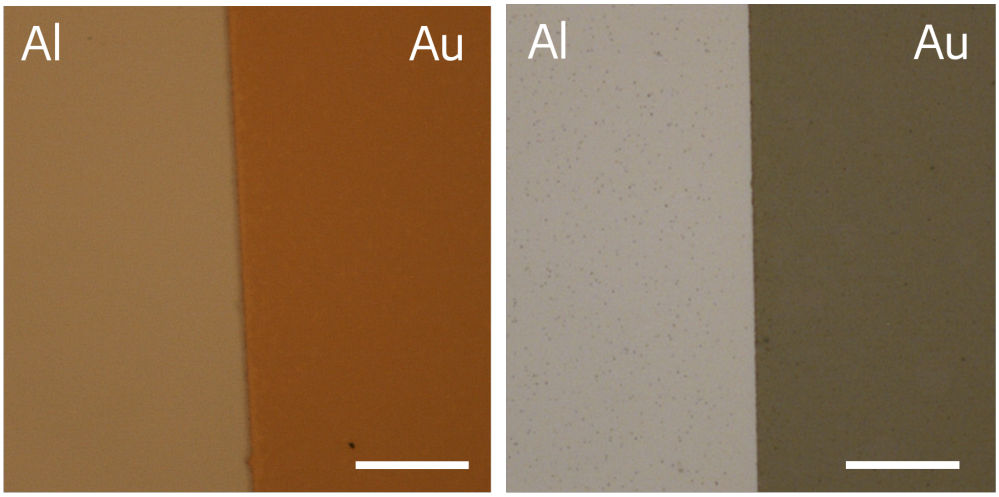

(A) PMMA 28 nm (B) PMMA 32 nm

FIGURE 5.15: Optical microscopy images of different PMMA thickness films. The scale bar is 25 μm.

I tested three different PMMA and SC 150 nm POM layer configurations as shown in Figure 5.16. First the PMMA layer on top of the POM layer (Figure 5.16a), then the PMMA layer under the POM layer (Figure 5.16b), and finally, a PMMA layer under and on top of the POM layer (Figure **??**). Compared to the PMMA alone films, there are more visible particles which are due to the addition of the POM layer. However, the only configuration where the POM film is clearly distinguishable is the PMMA/POM one (Figure 5.16b). This might be due to the fact that adding the PMMA layer above the POM layer could wash it away. The PMMA solution specifications are 15 mg/mL in propylene glycol methyl ether acetate (PGMEA), which could dissolve the POM. Note that the POM film deposited via spin-coating on top the PMMA layer has a very different morphology compared to when it is deposited on the ODPA-free nanogap electrodes. Hexagonal shape domains are obtained instead of the long lamella domains seen on the bare electrodes. Other groups[53,182,199,200,202] have looked at combining PMMA and POMs, but as blends, not as independent layers. My approach aims to further optimise a deposition technique which I have already shown works quite well.

Electrical characterisation can help determine if the underlying POM layer is washed away or not by the PMMA layer.

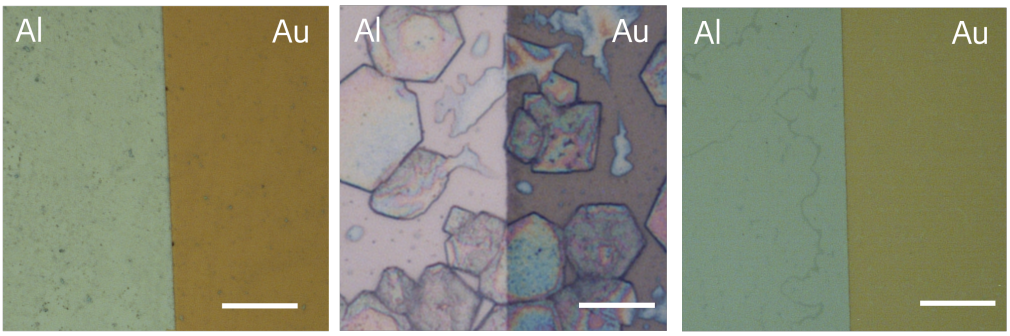

(A) POM/PMMA (B) PMMA/POM (C) PMMA/POM/PMMA

FIGURE 5.16: Optical microscopy images of various POM 150 nm and PMMA 32 nm layer configurations, the scale bar is 25 μm.

5.3.2 Electrical performance

Figure 5.17a shows the recorded I-V curves for different thicknesses of PMMA films deposited on Al/Au nanogap electrodes. These curves are quite noisy and have low currents (pA), similarly to the empty nanogap (shown in Chapter 4). Additionally, they do not exhibit any redox peaks.

However, when adding the POM layer on top, a more interesting I-V curve shape is observed (Figure 5.17b). This figure shows only the PMMA/POM layer configuration with different underlying PMMA film thicknesses. From this plot, the PMMA 34 nm film seems to perform best: the current levels are the highest and the redox peaks are the most pronounced. Therefore, this 34 nm film thickness was kept for the next steps of this study.

Next, I compared the different PMMA and POM layer configurations. Figure 5.17c shows all the tested configurations (PMMA/POM, POM/PMMA, PMMA/POM/PMMA), and Figure 5.17d shows only the two configurations where the PMMA layer is deposited on top of the POM layer (POM/PMMA, PMMA/POM/PMMA). As suggested in the film morphology discussion, depositing the PMMA layer on top of the POM layer probably washes it away. Indeed, no redox peaks and very low current levels are seen for these two configurations. Therefore, the optimal configuration is PMMA/POM.

The aim of adding the PMMA layer was to improve the device-to-device and scan-to-scan variability by preventing side reactions at the POM/Al electrode interface. Figure 5.18 shows these two graphs. From Figure 5.18a, all tested devices (only 13 different devices shown here) exhibit redox peaks and similar overall shapes and current levels. There is definitely less device-to-device variability when compared to the POM films. Figure 5.18b shows that the redox peaks were visible for at least 178 scans. This is also much better than the POM films, which were discussed in previous sections. The SC 150 nm was stable for 14 scans (Figure 5.12c), and the DC for 50 scans (Figure 5.14b).

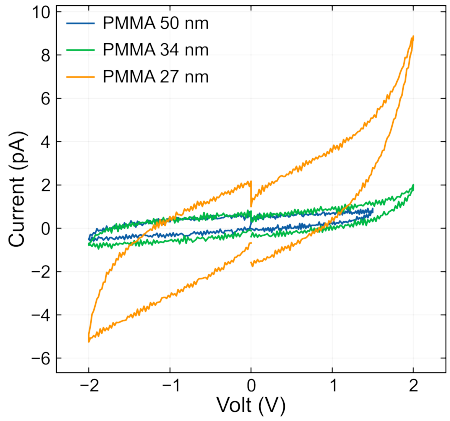

(A) Different thicknesses of PMMA alone films.

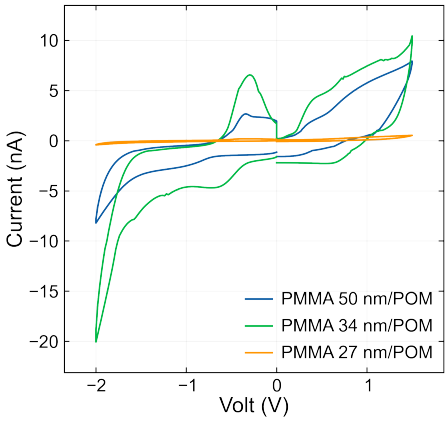

(B) PMMA/POM films with varying PMMA thicknesses and the same 150 nm spin-coat POM film on top.

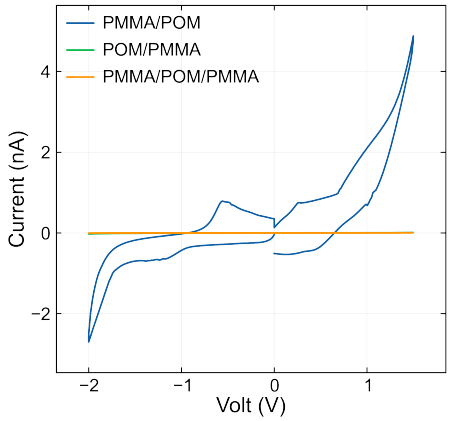

(C) Different layer stacking arrangements with the same 34 nm PMMA and 150 nm POM spin-coat films.

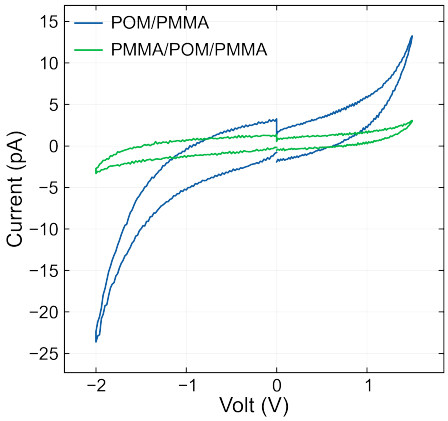

(D) Only the layer arrangements where the PMMA layer is on top of the POM layer.

FIGURE 5.17: I-V curves for different PMMA thicknesses and different PMMA-POM layers configurations.

Similarly to the POM films, the current levels at the maximum of the redox peaks increase as scans are recorded. Again, the redox reaction reactants ($H_3PMo_{12}O_{40}^{3-}$) are in higher concentration as scans are done, as will be discussed in Section 6.1.

5.3.3 Conclusions

In this section, I discussed adding a PMMA layer to improve device-to-device and scan-to-scan variability, which was a success. The idea was to add it as a layer to prevent reactions between the POM and the Al electrode. All devices show redox peaks, which were stable for at least 178 scans. However, to obtain this result, some optimisation was required. First, the PMMA layer thickness then the PMMA and POM layer configuration. It was found that the optimal thickness was 34 nm for the PMMA layer. For the configuration, the POM layer had to be deposited on top of the PMMA layer to avoid

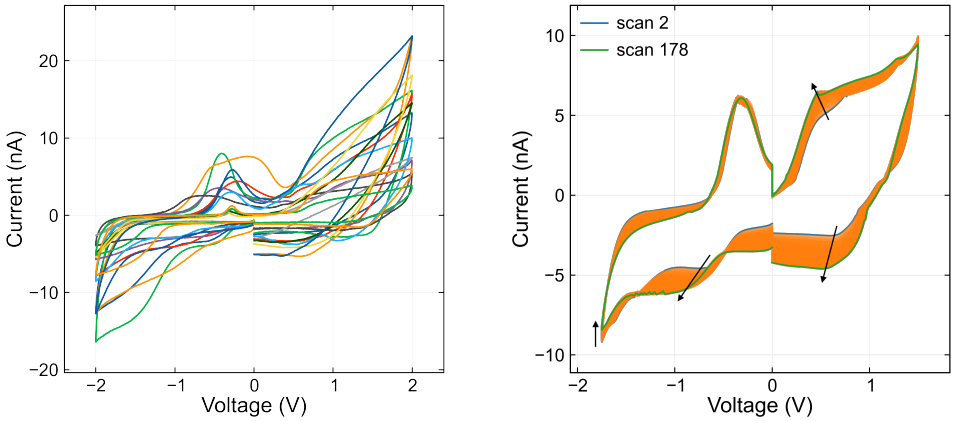

(A) Device-to-device variability (B) Scan-to-scan variability

FIGURE 5.18: Variability of the I-V curves for the PMMA 32 nm + POM 150 nm configuration.

it being washed away. Therefore, the optimal device is the PMMA SC 34 nm/POM SC 150 nm.

5.4 Summary

This chapter discussed the optimisation of polyoxometalate (POM) -based memory devices using the asymmetric coplanar nanogap separated electrodes fabricated via adhesion lithography. First, I compared commercially available simple Keggin POMs: $H_3PW_{12}O_{40}$, $H_3PMo_{12}O_{40}$, $Na_3PMo_{12}O_{40}$, and $(NH_4)_3PMo_{12}O_{40}$. Among these options, $H_3PMo_{12}O_{40}$ emerged as the most promising candidate due to its pronounced redox peaks over multiple devices and scans.

I investigated the influence of the ODPA SAM layer on device performance. ODPA-free nanogap electrodes showed better performance: the POMs were able to penetrate the nanogap.

I then compared various deposition methods: spin-coating at different speeds and drop-casting. The thicker films, spin-coating 150 nm and drop-cast films, were optimal. They showed the most pronounced and stable redox peaks. However, to aim for reproducible fabrication, the spin-coated film was selected.

A poly(methyl methacrylate) (PMMA) layer was added to address device-to-device and scan-to-scan variability, common challenges in redox-based resistive switching devices. The thickness of this PMMA layer and its configuration with the POM layer were optimised. The 34 nm spin-coated PMMA layer followed by the 150 nm spin-coated POM layer improved device and scan consistency.

Overall, the optimised device structure is a 34 nm spin-coated PMMA layer followed by a 150 nm spin-coated $H_3PMo_{12}O_{40}$ layer on ODPA-free nanogap electrodes. This configuration resulted in devices that consistently exhibited redox peaks and for at least 178 scans, a clear improvement compared to the initial designs.

This showcases the potential of POM-based memory devices and provides a good initial device ready for further development. The next chapters will discuss the switching mechanisms of these devices and explore their application for neuromorphic computing. This will involve studying how these POM-based devices can emulate brain functions and neurons.

Chapter 6

POM-Based Redox Memory Devices Mechanism Investigation

In the previous chapter, I discussed the process of optimising $H_3PMo_{12}O_{40}$ Keggin polyoxometalate (POM) -based redox resistive memory devices (ReRAM) using the asymmetric nanogap separated coplanar electrodes fabricated via adhesion lithography. The optimised device design is a 34 nm spin-coated PMMA layer followed by a 150 nm spin-coated $H_3PMo_{12}O_{40}$ layer on ODPA-free nanogap electrodes. This configuration produced devices that consistently exhibited redox peaks and for at least 178 scans, a clear improvement compared to the initial designs.

Accurately determining the switching mechanism for such ReRAM devices is challenging. There are many electrochemical and physical processes at the nanoscale that compete between each other to take into account. For example the POM film quality itself depending on the deposition technique, concentration, solvent, the POM redox reactions, the ambient moisture and temperature, the ionic species present, the quality of the electrode fabrication. Given the complexity of these interacting factors and the challenge in understanding the switching mechanism, a systematic approach is necessary to unravel this intricate process.

I will start by combining electrical characterisation, spectroscopic analysis, and controlled environmental studies, to build different hypotheses which could explain the switching mechanisms of suboptimal POM-based devices without the PMMA layer. This initial investigation will highlight the critical role of POMs in the switching process, given their fundamental redox properties. In the final section, I will explore the role of PMMA by investigating how the POMs distribute throughout the PMMA layer and its potential to enable vertical device architectures via more uniform film formation compared to direct POM deposition.

6.1 Electrochemical study

I found in Chapter 5 that the redox properties of the POM play an important role in my device behaviour: redox peaks are visible in the recorded I-V curves. This section will dive deeper into the electrochemical approach to the analysis of these redox curves and explore how the oxidation state of $H_3PMo_{12}O_{40}$ influences device performance. Only the suboptimal devices without the PMMA layer will be discussed throughout this section to better focus on the impact of the POM in the device response.

Here, I will study specific redox reactions, concentration profiles, formation and role of conductive filaments (CFs), oxidation state of $H_3PMo_{12}O_{40}$ and its control. I will use many complementary techniques including electrical characterisation, X-ray photoelectron spectroscopy (XPS), and UV/Vis spectroscopy to gain a better understanding of the electrochemical processes at play. By integrating these various aspects of electrochemical behaviour, I aim to elucidate the underlying mechanisms governing my $H_3PMo_{12}O_{40}$-based devices and how they relate to device performance.

To illustrate the electrochemical nature of these solid-state devices operation, Figure 6.1 presents side by side the drop-cast POM device I-V response and $H_3PMo_{12}O_{40}$ liquid state cyclic voltammogram. The expected "duck shape"[233] for current-voltage plots is present in both plots. This highlights the electrochemical nature of my solid-state device operation. The difference is the number and position of peaks showing the unique reaction environment within my device compared to a liquid electrolyte system.

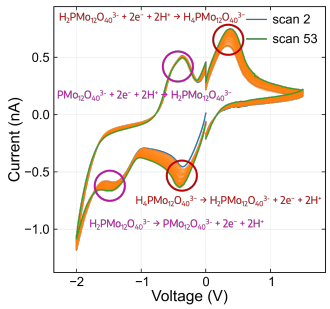

(A) Stabilisation of the drop-cast $H_3PMo_{12}O_{40}$ film by scanning until only + 1.5 V.

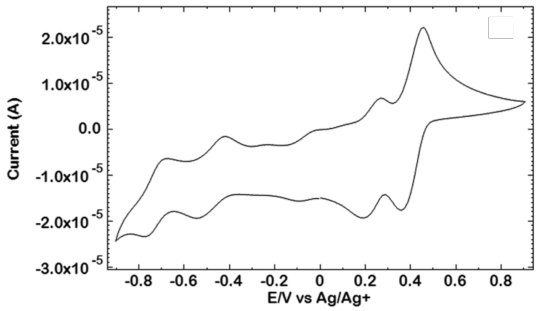

(B) Cyclic voltammograms in acetonitrile for $H_3PMo_{12}O_{40}$ at 0.5 mM with 100 mM LiTf, 100 mV/s. Reproduced with permission from[236]. Copyright 2016, American Chemical Society.

FIGURE 6.1: Comparing solid-state $H_3PMo_{12}O_{40}$ I-V curve and liquid-state cyclic voltammetry.

6.1.1 Identifying redox reactions

$H_3PMo_{12}O_{40}$ typically undergoes two electron transfer reactions[237–243]. They can be written in different ways: by changing the number of protons[244] (Equation 6.1), or changing the oxidation state of some POM metals[245] (Equation 6.2):

$$PMo_{12}O_{40}^{3-} + 2e^- + 2H^+ \rightleftharpoons H_2PMo_{12}O_{40}^{3-} \tag{6.1}$$

$$PMo_{12}^{VI}O_{40}^{3-} + 2e^- \rightleftharpoons PMo_{10}^{VI}Mo_2^{V}O_{40}^{5-} \tag{6.2}$$

I will use Equation 6.1 half reaction notation for the rest of this chapter. Therefore, the two pairs of redox peaks in Figure 6.1a can be seen in Equation 6.3 (circled in purple) and Equation 6.4 (circles in red). The POM undergoes two sequential two-electron transfer reactions. As a reminder, the two peaks with the positive currents are the oxidations (release of electrons), and the two peaks with the negative currents are the reductions (gain of electrons). For more details, see Section 2.1.1. The ability of the POM to undergo these reversible redox reactions is crucial for the switching behaviour of these ReRAM device, as it allows for controllable changes in the device conductivity.

$$PMo_{12}O_{40}^{3-} + 2e^- + 2H^+ \rightleftharpoons H_2PMo_{12}O_{40}^{3-} \tag{6.3}$$

$$H_2PMo_{12}O_{40}^{3-} + 2e^- + 2H^+ \rightleftharpoons H_4PMo_{12}O_{40}^{3-} \tag{6.4}$$

6.1.2 Concentration profile study

To explain the increasing redox peak current levels as scans were performed, I suggested in Chapter 5 (Section 5.2.2 and Section 5.3.2) and in Section 2.3.2 that the reactants for the redox reactions were migrating and accumulating, becoming more available.[235] Elgrishi et al. explain this phenomenon through concentration profiles.[233] Figure 6.2 shows a typical "duck shape" cyclic voltammogram and the concentration profile of the different redox reactions participants all along the cyclic voltammogram curve. The blue line shows the oxidised species ($PMo_{12}O_{40}{}^{3-}$) and the orange line the reduced species ($PMo_{12}O_{40}{}^{5-}$). These profiles show the concentration vs the distance to the aluminium electrode. This is because Al is the active electrode as it can so easily react with the POM (again, due to their energy level alignment).

At point n°1, there is only the oxidised $PMo_{12}O_{40}{}^{3-}$. It migrates towards the active Al electrode as a negative bias is applied until it reaches it and starts being reduced into $PMo_{12}O_{40}{}^{5-}$ (point n°2). Therefore, $PMo_{12}O_{40}{}^{3-}$ concentration decreases while $PMo_{12}O_{40}{}^{5-}$ concentration increases near the Al electrode. At point n°3, the current is dictated by the arrival of new $PMo_{12}O_{40}{}^{3-}$ to the electrode via diffusion from the bulk. As $PMo_{12}O_{40}{}^{5-}$ is generated, it will decrease $PMo_{12}O_{40}{}^{3-}$ mass transport slowing down the reaction, which is why the current decreases as further negative bias is scanned. Point n°4 is the switching potential where the bias is now swept positively. Therefore, $PMo_{12}O_{40}{}^{5-}$ starts to re-oxidise into $PMo_{12}O_{40}{}^{3-}$ and therefore decreasing $PMo_{12}O_{40}{}^{5-}$ concentration (point n°5). Similarly to the opposite scanning direction, at point n°6, the current is limited by the delivery of new $PMo_{12}O_{40}{}^{5-}$ to the aluminium

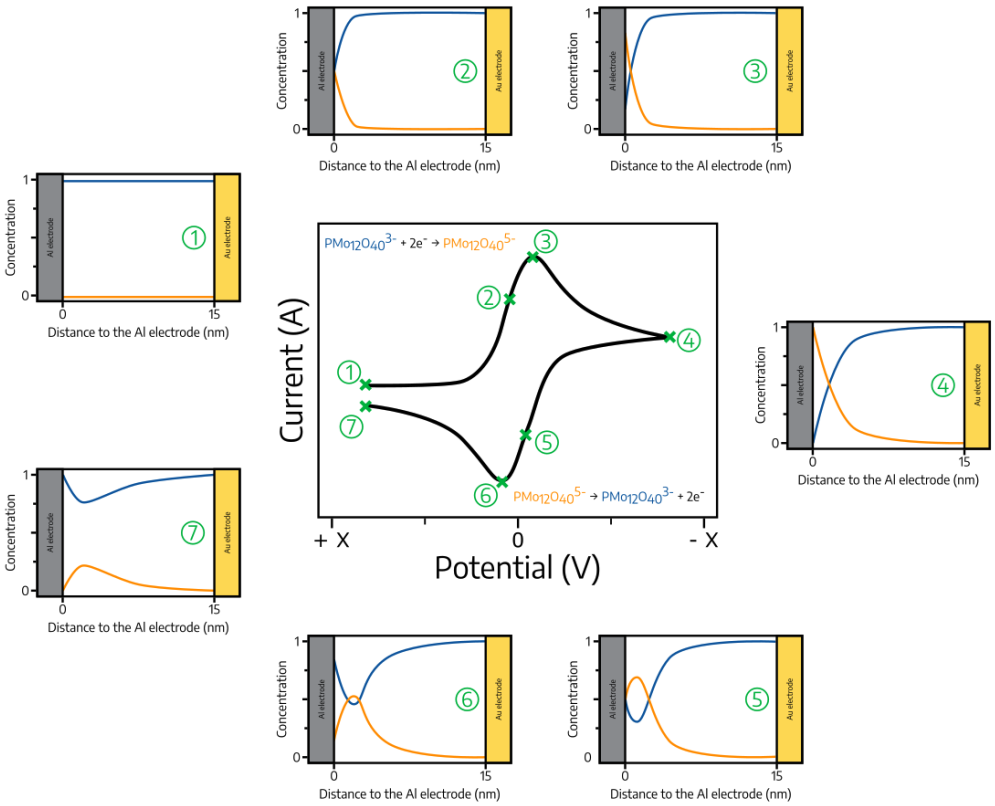

FIGURE 6.2: In the middle, a typical "duck shape" cyclic voltammagram. Around it are concentration profiles for $PMo_{12}O_{40}{}^{3-}$ (blue) and $PMo_{12}O_{40}{}^{5-}$ (orange) as a function of the distance from the aluminium electrode at various points along the voltammogram curve. Adapted from[233]. Available under a CC-BY licence.

electrode. At point n°7, the current decreases as $PMo_{12}O_{40}{}^{5-}$ has reduced mass transport. In summary, at points n°3 and 6, the current level is determined by the arrival of new reactants. As mentioned in Chapter 5 and will be discussed in the next section, reactants do not migrate all the way back to their initial position. Therefore, when the next voltage scan is done, there already are some reactants available which means that higher currents can be reached at points n°3 and 6.

Besides diffusion of redox reactants, another factor that can influence the redox peak current levels is the formation of conductive filaments (CFs) as I will discuss in the next section.

6.1.3 Conductive filaments

As mentioned in Chapter 2.1.2, Figure 2.3 showed a conductive filament (CF), which is used to explain the switching mechanism for ReRAMs. These CFs can be formed by redox reactions of an active electrode metal. As a reminder, the formation of the CFs is when the active electrode (Ag, Cu) is reduced to form metal cations which migrate as the potential is applied and accumulate to form the filaments. When the CF bridges

the two electrodes, the devices switches to its low resistance state (LRS). When an opposite bias is applied, the metal cations re-oxidise and rupture the conductive filament, switching the device back to high resistance state (HRS).[26]

In my device architecture, there is an aluminium electrode which has been reported to also participate in the switching. For instance, Semple et al.[225], studying the same coplanar nanogap electrodes as the ones in this work, suggested that Al could form bridges via Al migration into the nanogap where it is slightly shorter. Karthäuser et al.[246] find that simply depositing Al on and ITO and ZnO substrates is enough to support device switching. They mention that the Al layer oxidises into Al_2O_3 at the interface, and that this oxide layer is responsible for device switching. In addition to the conductive bridging, they also suggest that charges can be transported through defects or changes in tunneling barriers can also modify conductivity in the material. Additionally, it has been shown that the surface oxide layer of metals can form exudates during solidification.[247] These are new particles which can influence the surface behaviour. Adding the energy level alignment with the POM, the Al electrode is likely the active electrode in my system.

While conductive filaments offer insights into the switching mechanism, the oxidation state of the POM itself can affect its electronic, optical, and chemical properties and therefore device performance as mentioned in Chapter 3.[36,37,176,185,188–191] To gain a deeper understanding of this aspect, I turn my attention to assessing and controlling the POM oxidation state.

6.1.4 Assessing POM oxidation state in pristine films

As already mentioned in Chapter 5 (see Figure 5.8), $H_3PMo_{12}O_{40}$ can spontaneously be reduced when in contact with an Al electrode due to their Fermi and lowest unoccupied molecular orbital (LUMO) energy level alignments. To investigate this in my devices, X-ray Photoelectron Spectroscopy (XPS) measurements were done and analysed by collaborators at University College London: Aysha Riaz, Dr. Curran Kalha, and Dr. Anna Regoutz. XPS makes it possible to determine the elemental composition and chemical states of the POM films. This will provide an insight into how the POM oxidation state can influence switching mechanism and device performance, which can help design and optimise devices.

The same films as in Section 5.2 were tested: $H_3PMo_{12}O_{40}$ films deposited on a-lith Al/Au substrates via spin-coating at different speeds (SC 20 nm, SC 80 nm, SC 150 nm) and drop-casting (DC) without the PMMA layer. To compare the metal electrode substrate influence, the data was collected on two points: on the aluminium electrode and on the gold electrode.

Figure 6.3 shows the core electronic levels of carbon (C), phosphorus (P), and oxygen (O) atoms in all the different deposited $H_3PMo_{12}O_{40}$ films on both electrodes. The C1s core level spectrum (Figure 6.3a) was recorded as it is used as a reference in XPS measurements. It shows a main peak around 285 eV which is associated with C-C/C-H and/or adventitious carbon (C^0). The DC sample, both on Al and Au electrodes shows some slightly higher binding energy (BE) environments which could be due to C-O or C=O bonds. The P2p core level spectra (Figure 6.3b) show little variation between the different samples. The main peak is found around 134.1 eV, which indicates a metal phosphate environment: H_3PO_4 and H_3PO_3 are expected around 135 eV and 134 eV, respectively.[248] The O1s core level spectra (Figure 6.3c) have a main peak around 531 eV which is compatible with a P-O environment. There is likely also a contribution from the Mo-O environment, which is around 530.5 eV. The peaks towards higher BE can be attributed to organic carbon-oxygen environments. As observed in the C1s spectra, the DC sample on the Al electrode has increased shoulders in the higher BE region.

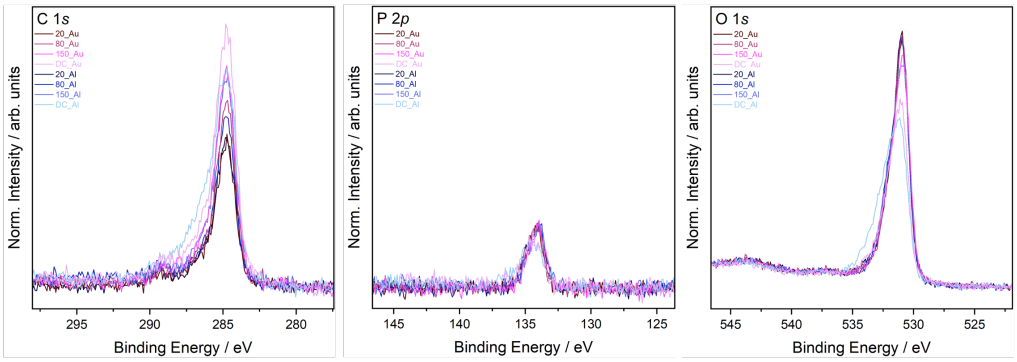

(A) Carbon (C) (B) Phosphorus (P) (C) Oxygen (O)

FIGURE 6.3: Core electronic levels of different atoms in $H_3PMo_{12}O_{40}$ film on an a-lith substrate.

The molybdenum (Mo) core electronic level for all the tested $H_3PMo_{12}O_{40}$ films, for both electrodes is shown in Figure 6.4. Here, the data collected on the aluminium (Figure 6.4a) and gold (Figure 6.4b) electrodes are plotted separately to better show the difference in the spectra. Both spectra depict the main Mo3d5 peak at 233.2 eV which is consistent with Mo^{+6} oxidation state. The shoulder at lower BE, observed more prominently in the Al samples, could be due to a different oxidation or chemical state (Mo^{+5} at 232 eV and Mo^{+6} at 233 eV). The SC 150 nm samples on both Au and Al electrodes show the most prominent shoulder. The DC sample seems to have a shift to higher BEs, which could be due to charging as will be discussed below.

The underlying aluminium and gold substrates were also analysed by recording the Al2p (Figure 6.5a) and Au4f (Figure 6.5b) core level spectra. First, the peaks are visible which indicates that the POM films are not homogenous, as XPS is a very surface sensitive technique. The main peak in the Al2p spectra is at 75 eV, which is expected

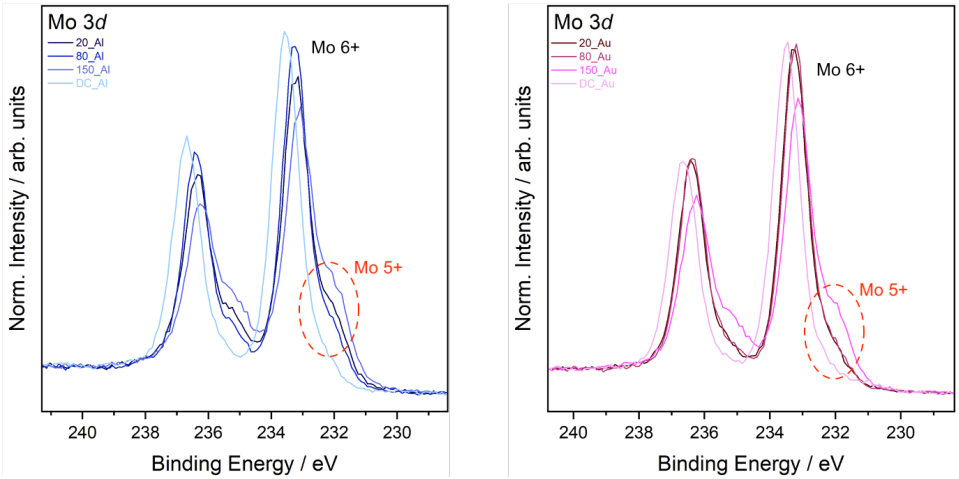

(A) On the aluminium electrode. (B) On the gold electrode.

FIGURE 6.4: Molybdenum (Mo) core levels of a $H_3PMo_{12}O_{40}$ film on the different electrodes of the a-lith substrate.

for an Al-O chemical state; Al metal would appear at around 72.7 eV. A typical BE for metallic Au is 84 eV, but a wide range of values are observed here.

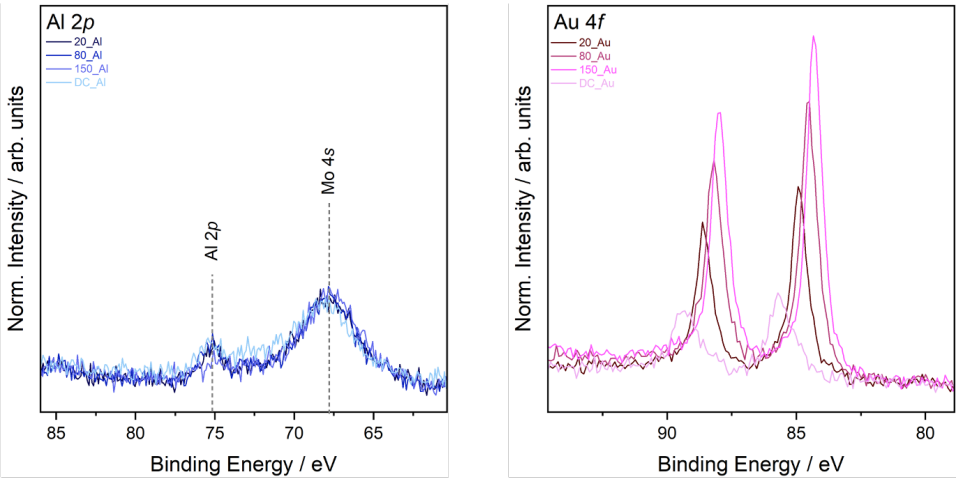

(A) Aluminium electrode. (B) Gold electrode.

FIGURE 6.5: Core Al and Au XPS spectra of the underlying electrodes.

To further study the reason why the Au peak position was so spread out, all the tested element peaks were normalised with regard to the expected 84 eV Au peak as shown in Figure 6.6. All spin-coated samples show a consistent shift relative to Au. However, the drop-cast sample exhibits some charging effect. This means the observed shift to higher binding energies is not because of chemical state changes. Instead, an explanation could be that e^- are accumulating during the measurement as the gold electrodes are electrically isolated from the rest of the a-lith substrate.

Overall, between the Al and Au measurement spots, there is little difference in chemical states for P and O. However, for Mo3d there are shoulders observed on the Al electrode

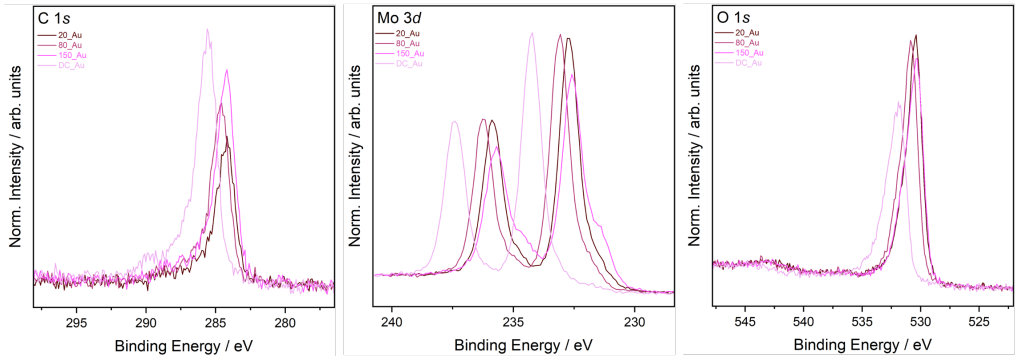

(A) Carbon (C) (B) Molybdenum (Mo) (C) Oxygen (O)

FIGURE 6.6: Charging effect with regard to the Au electrode substrate core electronic level of the different atoms in $H_3PMo_{12}O_{40}$ films on an a-lith substrate.

suggesting that, as expected, spontaneous reduction occurs. The DC samples always shift to higher BEs and have more C/O environments. The SC 150 nm sample had the most prominent shoulder Mo3d indicating more reduction. The metal electrode substrate responses were visible meaning the films are not homogenous.

6.1.5 Controlling and monitoring POM oxidation state

The XPS study provided some insights into the oxidation state of $H_3PMo_{12}O_{40}$ in pristine films: it can be influenced by the deposition technique and substrate electrode. However, to fully understand the impact of oxidation state on device performance, it is important to have more precise control over the POM redox states.

UV-Vis spectroscopy is another useful technique to monitor the broad intervalence charge transfer peak around 900 nm, which is indicative of reduced Mo species. Here, I compare two methods to purposefully reduce $H_3PMo_{12}O_{40}$ and monitor the oxidation state changes using UV-Vis spectroscopy. The idea is to more fully understand the influence of ambient or process parameters on the POM oxidation state of my films.

First, two techniques to reduce $H_3PMo_{12}O_{40}$ were compared: thermal treatment and UV light exposure. Figure 6.7 shows the obtained results. The two tested samples are the drop-cast $H_3PMo_{12}O_{40}$ films on quartz substrates without an underlying PMMA layer. The spin-coated 150 nm films were also tested, but their results are presented in Section C.1 of Appendix C. The drop-cast samples were illuminated at 254 nm or annealed at 60 °C[a] for an increasing amount of time. Figure 6.7a and Figure 6.7c show the recorded UV/Vis absorption spectra for different treatment durations. The plots are normalised with regard to the Mo-O_b peak (316 nm). Figure 6.7b and Figure 6.7d show the absorbance at 900 nm (the broad intervalence charge transfer peak) of the normalised absorption plots vs treatment time.

[a]MeOH boiling point.

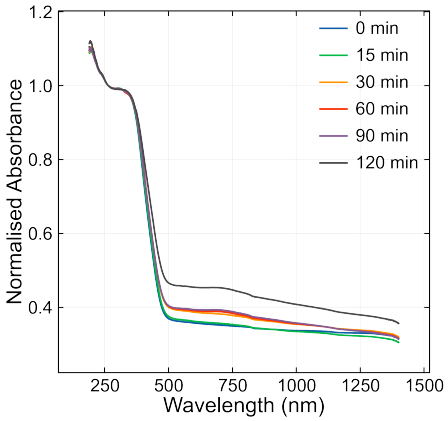

(A) UV/Vis spectra when illuminated at 254 nm.

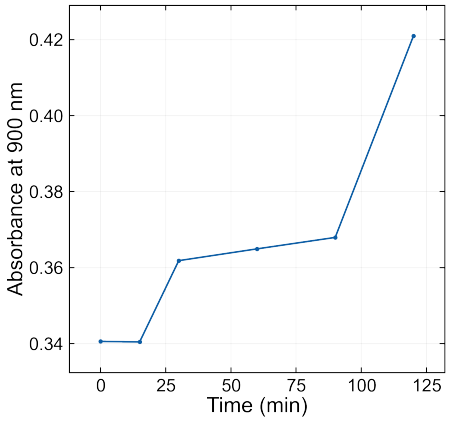

(B) Absorbance at 900 nm when illuminated at 254 nm.

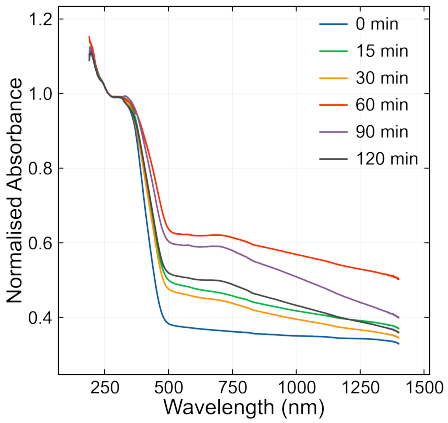

(C) UV/Vis spectra when heated at 60 °C.

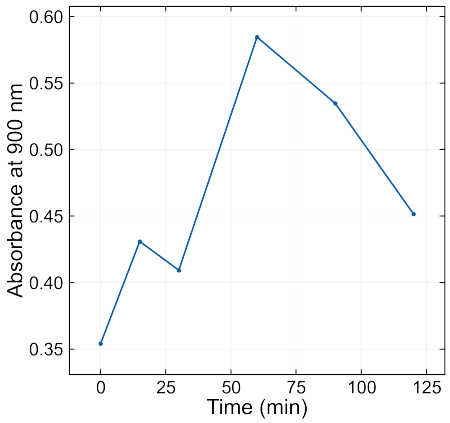

(D) Absorbance at 900 nm when heated at 60 °C.

FIGURE 6.7: Comparing illumination (254 nm) and annealing (60 °C) techniques to control the reduction of a drop-cast $H_3PMo_{12}O_{40}$ film. The UV/Vis spectra are normalised at the Mo-O_b peak (316 nm).

It can be observed that for the illuminated sample, the absorbance at 900 nm increases as the exposure time increases. This suggests that $H_3PMo_{12}O_{40}$ is continuously being reduced. For the annealed sample, the absorbance at 900 nm first increases then decreases as the annealing time increases. This means the POMs first reduce then re-oxidise. Since the illuminated film does not re-oxidise, it suggests that heating the film is necessary for re-oxidisation as Huez et al. mentioned.[197,198]

The next factor that I investigated is the annealing temperature. 5 min annealing steps were done at 60, 100, and 150 °C after measuring the reference room temperature spectrum. Figure 6.8a shows the obtained UV/Vis spectra normalised with regard to the Mo-O_b peak (316 nm). Figure 6.8b shows the absorbance at 900 nm vs annealing temperature. A similar response to the increasing annealing time is obtained: at first the POM gets reduced, but then re-oxidises. However, the re-oxidation occurs much sooner if the annealing time is to be considered: after a total of 15 minutes at temperatures up to 150 °C vs 60 minutes at 60 °C. As mentioned in Chapter 3, heating POMs

can help re-organise their electrons and therefore promote re-oxidation.[39,145,197]

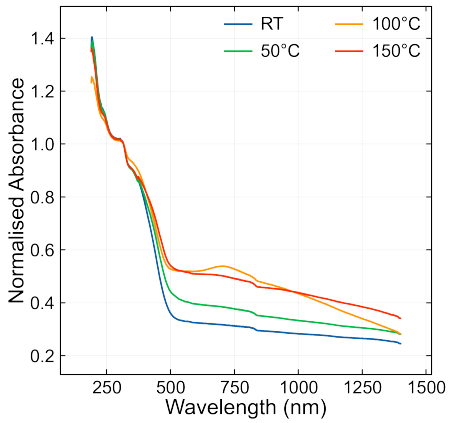

(A) UV/Vis spectra normalised at the Mo-O_t peak (196 nm).

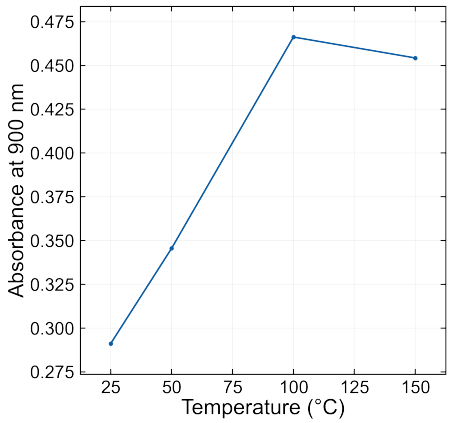

(B) Absorbance at 900 nm.

FIGURE 6.8: Controling the reduction of a drop-cast $H_3PMo_{12}O_{40}$ film by 5 min annealing steps at increasing temperatures. The UV/Vis spectra are normalised at the Mo-O_b peak (316 nm).

I deposited similar drop-cast films on a-lith substrates in order to test their electrical performance. Figure 6.9 shows the obtained I-V curves for the different annealing temperatures. It shows that overall, the current levels decrease and redox peaks disappear as the annealing temperature increases. A possible explanation could be the loss of water as the film gets annealed. Moisture plays an important role as will be discussed in the next section.

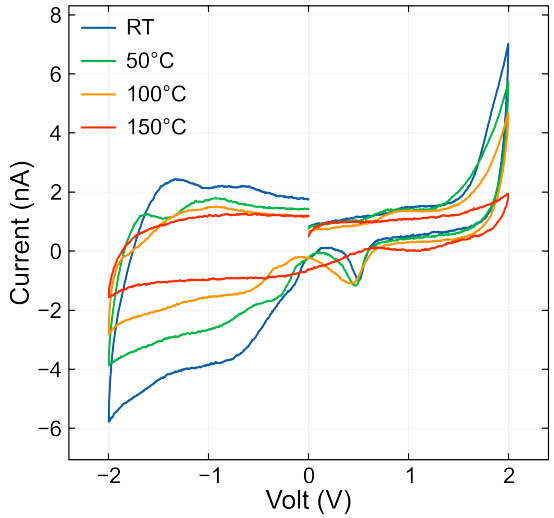

FIGURE 6.9: I-V curves of a drop-cast film annealed for 5 minutes at different temperatures.

Another observation that can be made from this figure is the fact that the I-V curves don't match up at the end of the scan. The last data point does not overlap with the first

data point at 0 V: there is a gap of about 1-2 nA. A possible explanation is charge built-up during the measurement. This will further be explored when discussing pulses in Section 7.1 of Chapter 7.

Overall, it seems that $H_3PMo_{12}O_{40}$ oxidation state does influence the device performance. It appears that both UV exposure and thermal treatment can reduce POMs, with thermal treatment also enabling re-oxidation. I observed that when the POM gets reduced, lower currents are recorded. This is in contrast to another group[197] who observed an increase in conductivity with reduced POMs. This highlights the complexity of POM behaviour and how device architecture and POM functionalisation can affect performance, as they studied functionalised POMs with a different device design.

6.1.6 Conclusions

In this section, I examined the electrochemical behaviour of my $H_3PMo_{12}O_{40}$-based ReRAM devices without the PMMA layer. The device I-V response exhibits a characteristic "duck shape" appearance, similar to liquid-state electrochemistry.[233,236] The POM undergoes two sequential two-electron transfer reactions[34], which form the basis of the device switching mechanism. The increasing current levels observed at the redox peaks during successive scans are explained by ion migration[233] and the growth of conductive filaments as scans are performed[60].

XPS analysis of $H_3PMo_{12}O_{40}$ films demonstrated some spontaneous reduction of POMs on aluminium electrodes, evidenced by shoulders appearing at higher/lower binding energies. Additionally, inhomogeneous film formation was observed as the underlying electrode metals were visible. UV/Vis spectroscopy showed that both UV exposure and thermal treatment can reduce POMs. Moreover, thermal treatment was found to enable the re-oxidation process.

Devices thermally annealed at temperatures up to 150 °C performed less well, highlighting the importance of carefully fine-tuning the process parameters during film forming. The Al electrode and its thin Al_2O_3 oxide layer may also contribute to the switching events[225,246], further complicating the possible mechanisms at play in the device operation.

Further studies are needed to fully understand the impact of all the electrochemical processes governing these ReRAM devices performance. For instance, by testing more temperatures and longer annealing times when purposefully reducing the POM, and comparing device performance for POMs reduced via UV illumination. Additionally, the effect of the added PMMA layer on the control of the POM oxidation state could be investigated.

Overall, this electrochemical perspective provided valuable insights into the fundamental processes governing my ReRAM device operation, paving the way for future optimisations and applications. Environmental factors can affect these processes: in the next section, I will examine how ambient moisture influences these devices.

6.2 Effect of Ambient Moisture

It was mentioned in Chapter 2 that moisture could affect ReRAM devices in different ways. For instance, by carrying charges[27,64,72,73,75,76], degrading materials[72], and participating in counter-reactions[27,76,77]. This highlights the need for a delicate balance when dealing with moisture content. A controlled amount of moisture can facilitate consistent ionic transport and improve reproducibility, but excessive moisture can lead to material degradation, unwanted side reactions, and increased variability in device performance.

This duality was also demonstrated in Chapter 5. Some I-V curves (see Figure 5.12c and Figure 5.14a) showed large tails in the positive bias regions (+ 1.5 to 2 V), which I attributed to material degradation due to moisture content. In parallel, the redox peaks, which were visible only for the thicker films (SC 150 nm and DC), were also attributed to moisture as its presence was necessary for it to act as a counter-reaction.

This section will dive into studying the effect of moisture on $H_3PMo_{12}O_{40}$ film fabrication and device performance, then on $H_3PMo_{12}O_{40}$ oxidation state. The following analysis centres on the POM-only devices, deliberately excluding the PMMA layer to highlight the base material's characteristics.

6.2.1 On film fabrication and device performance

To delve deeper into the effects of water on the drop-cast $H_3PMo_{12}O_{40}$ film morphology and electrical performance, I tested three samples with different moisture content: (i) a reference pristine sample made in a fumehood (46% humidity), (ii) a "water sprayed" sample made in a fumehood then sprayed with distilled water once the film had dried, and (iii) a sample made in a nitrogen environment glovebox with little moisture (< 0.1 ppm) all of them without the PMMA layer.

First, the film morphology was studied: Figure 6.10 shows images of the three samples. The reference fumehood sample (Figure 6.10a) shows a darker area in the bottom half of the film due to overnight reduction. $H_3PMo_{12}O_{40}$ LUMO is lower than Al Fermi level, so spontaneous reduction can occur[185,188], as detailed in Figure 5.8 and was explored in Section 6.1.4. The "water sprayed" sample (Figure 6.10b), also has a darker spot in the top half of the film, but it occurred as the film dried after being sprayed with the

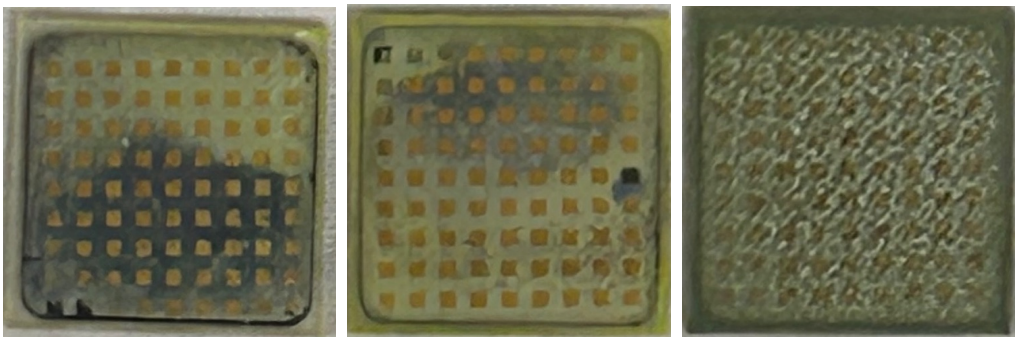

(A) Pristine fumehood film (B) Sprayed fumehood film (C) Glovebox film

FIGURE 6.10: Images of drop-cast $H_3PMo_{12}O_{40}$ films deposited on 2x2 cm a-lith electrodes with different moisture contents.

water. This is a first indication that moisture can enhance POM reduction. The glovebox sample (Figure 6.10c) does not exhibit any darker areas, suggesting $H_3PMo_{12}O_{40}$ did not get reduced.

Figure 6.11 shows the I-V curves of different tested devices for all three samples. These measurements were taken in ambient air. Both fumehood samples (Figure 6.11a and Figure 6.11b) have only one device which shows higher current levels. The other tested devices have very low current levels. In contrast, the glovebox sample (Figure 6.11c) has much more consistent devices, all with higher current levels and visible redox peaks. This also suggests that moisture is detrimental to the device performance.

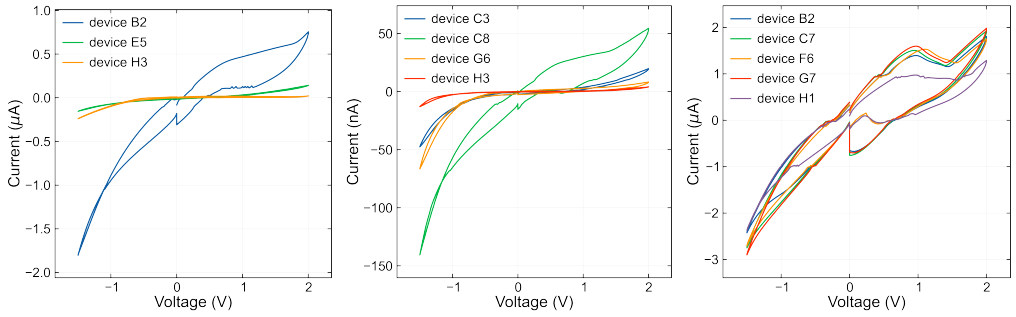

(A) Pristine fumehood film (B) Sprayed fumehood film (C) Glovebox film

FIGURE 6.11: Device-to-device variability of drop-cast $H_3PMo_{12}O_{40}$ films deposited on 2x2 cm a-lith electrodes with different moisture contents.

When looking at cycle-to-cycle variability, a similar conclusion is drawn: both the pristine (Figure 6.12a) and sprayed (Figure 6.12b) fumehood samples show large variation while the glovebox (Figure 6.12c) sample is more stable.

Overall, these film images and I-V curves suggest that increased moisture content can degrade the materials at play and decrease device performance. For instance, the lower current levels could be due to $H_3PMo_{12}O_{40}$ reduction (as seen in the film morphology) or hydrolysis[249]. Another possible source of material degradation could be that of the electrodes. Valov et al.[72] mention that water can be a strong corrosive agent. My device

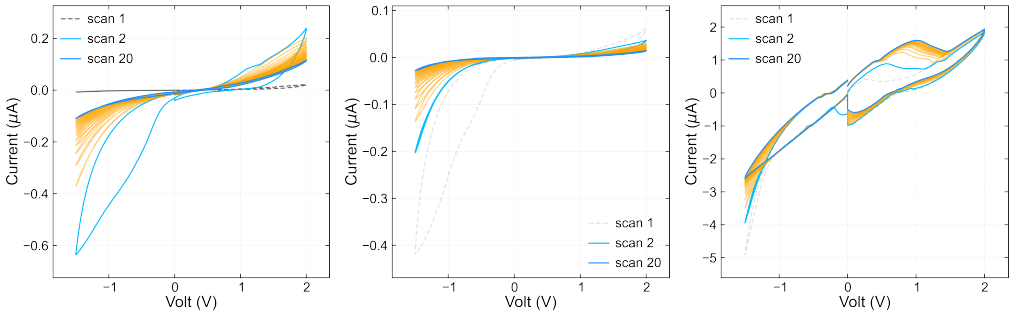

(A) Pristine fumehood film (B) Sprayed fumehood film (C) Glovebox film

FIGURE 6.12: Scan-to-scan variability of drop-cast $H_3PMo_{12}O_{40}$ films deposited on 2x2 cm a-lith electrodes with different moisture contents.

architecture has an aluminium electrode. This means that moisture could remove the passive oxidation layer and therefore corrode the exposed aluminium, degrading the electrode surface and therefore device performance.[250]

6.2.2 On POM oxidation state

Another experiment was done where I tested the effect of evaporating the film moisture. This time only two samples were tested: the pristine fumehood and glovebox $H_3PMo_{12}O_{40}$ samples without the PMMA layer. They were both annealed at 110 °C in the fumehood or glovebox, respectively, for an increasing amount of time to evaporate their water content, and I monitored their oxidation state via UV/Vis. The fumehood samples (Figure 6.13a and Figure 6.13b) were normalised to the Mo-O_b peak (316 nm) to account for changes in overall absorbance intensity during annealing in the ambient environment, whereas the glovebox samples were not normalised as the inert conditions minimized external factors affecting the absorbance. Regardless of normalisation, the overall trend is the same for each deposition environment.

As expected, both samples show the two peaks in the POM signature region (see Figure 6.13a and Figure 6.13c). However, the intervalence charge transfer broad peak varies from sample to sample as the annealing time increases, as expected from the previous section. To help observe the oxidation state change, I plot the absorbance at 900 nm (Figure 6.13b and Figure 6.13d) vs time. The fumehood sample first shows an increase followed by a decrease in absorbance as the annealing time increases. The glovebox sample shows an increase then a stabilisation of its absorbance at 900 nm. This behaviour was also visually observed in the film colour (see Figure 6.14): the fumehood sample first turns dark blue, then lightens back to yellow, while the glovebox sample stays dark blue as annealing time increases. The oxidised POMs are yellow, but turn blue when they are reduced.[34]

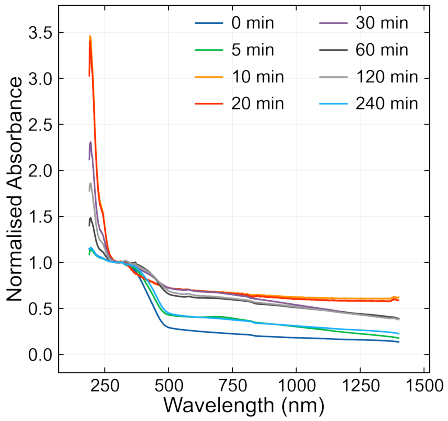

(A) UV/Vis spectra when annealed in the fumehood.

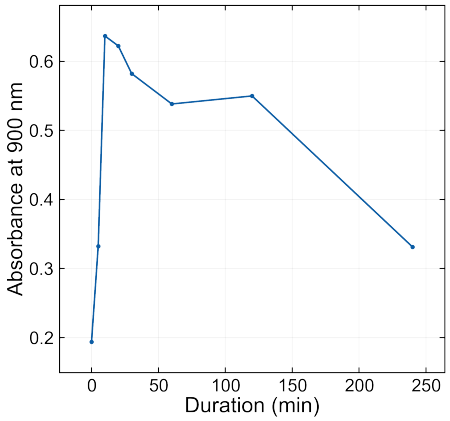

(B) Absorbance at 700 nm when annealed in the fumehood.

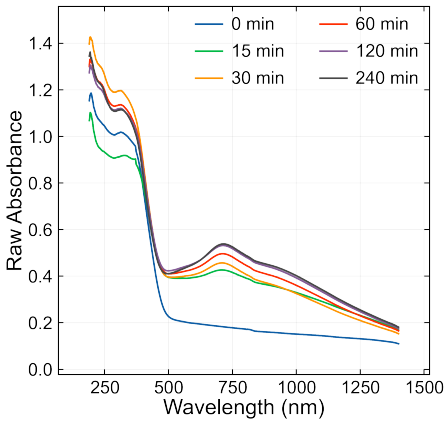

(C) UV/Vis spectra when annealed in the glovebox.

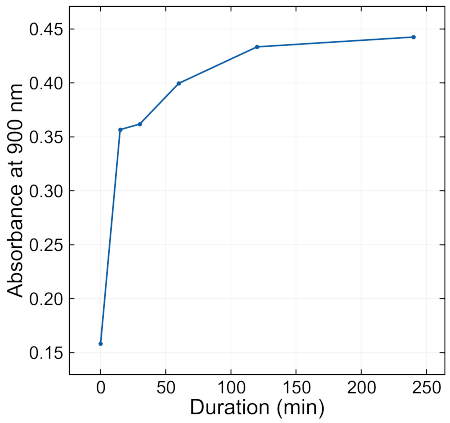

(D) Absorbance at 700 nm when annealed in the glovebox.

FIGURE 6.13: UV/Vis absorption spectra of $H_3PMo_{12}O_{40}$ drop-cast films annealed at 110 °C over time. The UV/Vis spectra are normalised at the Mo-O_b peak (316 nm).

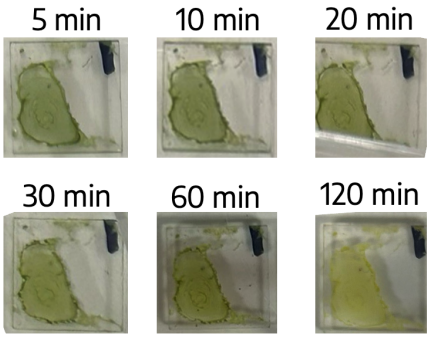

(A) Annealed in the fumehood.

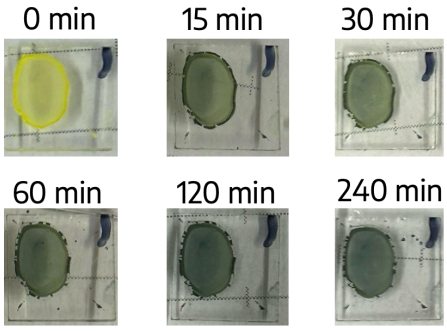

(B) Annealed in the glovebox.

FIGURE 6.14: Images of drop-cast $H_3PMo_{12}O_{40}$ films deposited on 1x1 cm quartz substrates annealed for increasing time at 110 °C in different environments.

Overall, it appears that the fumehood sample is first being reduced then can re-oxidise while the glovebox sample is only reduced and can not re-oxidise. Besides the difference in moisture content, oxygen could also play a role in the re-oxidation process. The glovebox is an inert N_2 environment and has < 0.1 ppm of oxygen compared to the $\approx$

209,500 ppm in ambient air. However, Lubben et al. studied both the influence of oxygen and moisture on ReRAM devices and found that oxygen had little effect, especially when compared to moisture.[66] They mention that moisture plays a more crucial role as it can offer additional charged species, similarly to the discussion in Section 2.2. In my case, when remembering the redox reactions the POM undergoes, there is indeed the need for a proton (Equation 6.5). Therefore, it is possible that moisture is needed for the POM to re-oxidise. This can also help explain why the thicker films (spin-coat 150 nm and drop-cast) described in Chapter 5 showed redox peaks, while the thinner films (spin-coated 50 nm) did not: the trapped moisture was able to act as a counter-balance reaction.

$$PMo_{12}O_{40}^{3-} + 2e^- + 2H^+ \rightleftharpoons H_2PMo_{12}O_{40}^{3-} \tag{6.5}$$

6.2.3 Conclusions

Throughout this study, I demonstrate two main contrasting effects of moisture on my $H_3PMo_{12}O_{40}$-based memristive devices without the underlying PMMA layer. On one hand, ambient moisture can act as a corrosive agent degrading device materials and performance.[72] Film morphology changes (black areas appear), decreased current levels, and fewer redox peaks were observed in devices exposed to higher humidity. Possible causes are the reduction of $H_3PMo_{12}O_{40}$ and/or corrosion of the aluminium electrode.[250]

On the other hand, moisture can play an important role in enabling the full redox potential of these devices. Samples fabricated and tested in a low-moisture glovebox environment showed only reduction of the POM, while those exposed to ambient humidity were able to undergo reversible redox cycling. This suggests that moisture can provide counter-reactions enabling $H_3PMo_{12}O_{40}$ to re-oxidise.[27,66,76,77]

Careful control and optimisation of ambient moisture levels may therefore be critical in developing stable and functional POM-based memristive devices.

While this study provided some insight into the effects of moisture on $H_3PMo_{12}O_{40}$-based memristive devices, further research is needed. For instance, more precise control and measure of moisture content in the films would allow establishing quantitative relationships between moisture levels and device performance. Additionally, the effect of the added poly(methyl methacrylate) (PMMA) layer on trapping moisture could be investigated.

Now that the impact of environmental factors on these devices is better understood, I can study the physical configuration of these POM-based systems. The structural

aspects of these devices, including POM distribution and device architecture, play an important role in device performance.

6.3 Structural analysis of PMMA/POM -based devices

The physical configuration of these POM-based devices plays an important role in their performance. In this section, I shift focus to the optimal device configuration: the 34 nm spin-coated PMMA layer followed by a 150 nm spin-coated $H_3PMo_{12}O_{40}$ layer on ODPA-free nanogap electrodes. I examined two structural aspects: the distribution of POMs within the PMMA layer and how PMMA could benefit vertical or sandwich device architectures. These studies can help gain valuable insights into optimising device design and performance.

6.3.1 POM distribution in PMMA matrix

Chapter 3 mentioned that POM orientation and distribution could influence device performance.[53,220] To investigate this influence for my devices, depth profile XPS measurements were performed by my collaborators at University College London: Aysha Riaz, Dr. Curran Kalha, and Dr. Anna Regoutz. The tested samples consist of three layers: a 40 nm thick Au electrode, followed by a spin-coated PMMA layer, topped by a spin-coated $H_3PMo_{12}O_{40}$ 150 nm layer. The substrate here is only a 40 nm thick gold electrode, instead of an a-lith substrate, to avoid the spontaneous reactions with aluminium. The three PMMA thicknesses were tested: 28, 34, and 48 nm, but only the PMMA 34 nm will be presented here, the other two can be found in Appendix C.

Figure 6.15 shows the obtained relative atomic percentages of C, Mo, and Au throughout the film. The etching time can be connected to the thickness etched through the film. These elements were chosen for comparison as they represent the different layers: C is found only in the PMMA layer, Mo is part of the POM ($H_3PMo_{12}O_{40}$) and Au is the substrate. At the film surface (etch time = 0 s), there is more Mo content showing that indeed the POM film is the top layer. As the etching time increases, or as the film thickness is decreased, the Mo content decreases, while the C content increases. There is a cross-over point where there is more C than Mo, suggesting that the PMMA layer has been reached. However, the Mo from the POM is still observed throughout the entire film (although decreasing) suggesting its presence all the way to the Au layer. At 450 s of etching, the Au content crosses both C and Mo suggesting that the Au substrate has been reached. Overall, this suggested that the POM film penetrates the PMMA layer when it is spin-coated on top.

To double-check that the POM indeed penetrates the PMMA layer during deposition, the relative atomic percentage of P can also be monitored, as it is also only present in the

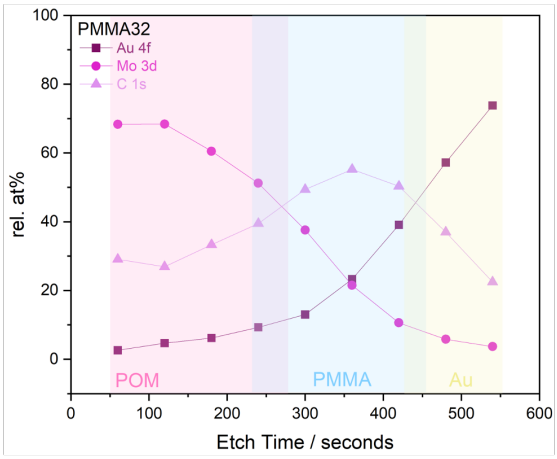

FIGURE 6.15: XPS depth profile of spin-coat PMMA 34 nm + $H_3PMo_{12}O_{40}$ 150 nm film on 40 nm gold layer.

$H_3PMo_{12}O_{40}$ layer. Table 6.1 shows the calculated relative atomic percentage of Mo, P, and Au throughout the film. As expected, the P content is quite low: its stoichiometric percentage is only 1/56 atoms. It does not exactly follow the changes in Mo: is no longer detected after 360 s of etching. A possible explanation is the difficulty to detect it, as it is in very low concentration in the film.

TABLE 6.1: Relative atomic percentage of molybdenum (Mo), phosphorus (P), gold (Au) throughout a spin-coat PMMA 34 nm + $H_3PMo_{12}O_{40}$ 150 nm film on 40 nm gold layer.

Etch time (s)	**Mo**	**P**	**Au**
60	91.0	5.5	3.5
120	85.9	8.2	5.9
180	85.1	6.2	8.7
240	79.0	6.6	14.4
300	69.6	6.4	24.0
360	45.2	5.7	49.1
420	21.3	n.d.	78.7
480	9.14	n.d.	90.9
540	4.8	n.d.	95.2

In summary, this study allowed to confirm that the POM layer, spin-coated on top of the PMMA layer penetrates it: Mo was detectable throughout the entire film thickness. This is important as it confirms that $H_3PMo_{12}O_{40}$ can still come into contact with the device electrodes, explaining the electrical device performance showed in Chapter 5: the POM redox reactions come into play even when deposited on-top of a PMMA layer.

6.3.2 PMMA mediated vertical/sandwich device architecture

It has been mentioned a couple of times throughout Chapter 5 and this chapter that POMs form non-uniform films which would make their integration into sandwich or vertical devices difficult. Since the top electrode is directly deposited on top the active layer, it could easily penetrate it and come into contact with the bottom electrode, shorting the device. Since PMMA forms very uniform films, it could help create vertical devices as the top electrodes would have a harder time penetrating the film to short the bottom electrode. I made some sandwich devices to confirm this hypothesis. I compared these structures:

1. the two combinations of different top electrode (TE) and bottom electrode (BE) Al/switching layer/Au or Au/switching layer/Al
2. the active switching layer was either PMMA alone or PMMA + POM or POM alone. The POM layer was always the SC 150 nm film, but different PMMA thicknesses were tested (28, 34, and 48 nm).

All the devices tested for all of these configurations can be found in Table C.2. Here, only the optimised switching layer will be discussed, i.e. PMMA 34 nm + POM 150 nm, shown in Figure 6.16. As suspected most devices are shorted: out of the 10 (Al/PMMA 34 nm + POM 150 nm/Au) + 20 (Au/PMMA 34 nm + POM 150 nm/Al) devices tested here, only 2 are not shorted.

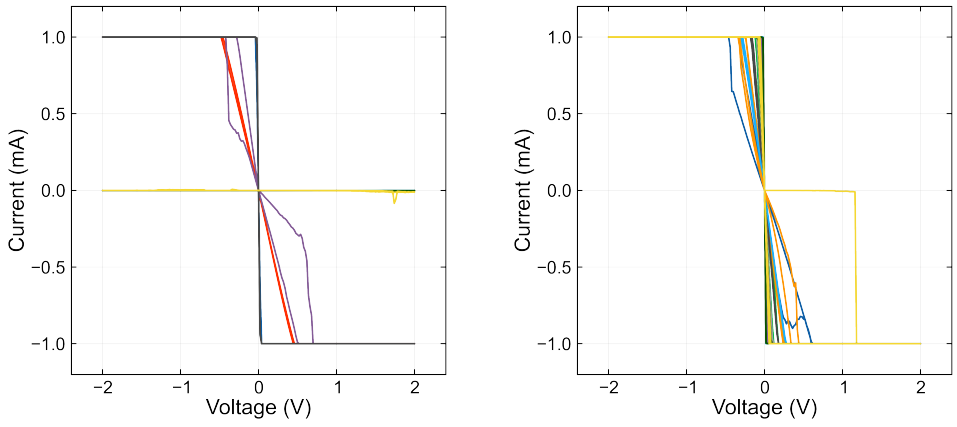

(A) Al/PMMA/POM/Au (B) Au/PMMA/POM/Al

FIGURE 6.16: I-V curves for all different Bottom Electrode (BE)and Top Electrode (TE) sandwich devices.

Figure 6.17a shows all the tested devices, regardless of their configuration. Out of the 154 devices, only 21 gave a response, an example of which is shown in Figure 6.17b. The redox peaks are not very pronounced and quickly disappear as scans are performed. The nanogap devices perform much better (Figure 6.17c): their I-V curves show more pronounced redox peaks and are more stable from scan-to-scan.

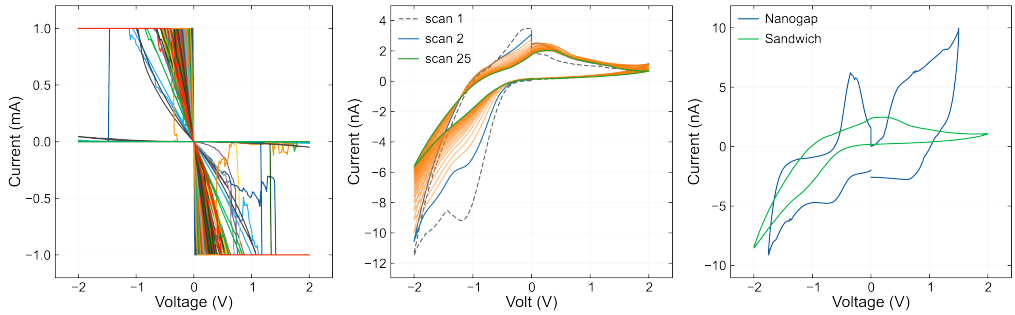

(A) I-V curves for all 154 tested sandwich devices (only 21 devices were not shorted).

(B) Example of a non-shorted sandwich device response: Al 40 nm/PMMA 34 nm/POM 150 nm/Au 40 nm.

(C) Comparison of the previous device response with the nanogap device architecture.

FIGURE 6.17: Device-to-device and scan-to-scan variability of tested sandwich devices and comparison with the nanogap.

As expected, sandwich architecture devices are not optimal for POM-based devices. The top electrode can easily penetrate the POM film and short the bottom electrode, even with the more uniform PMMA layer. In addition, the nanogap devices gave better responses when compared to non-shorted sandwich devices. The nanogap redox peaks were more pronounced and stable from scan-to-scan. This confirms that the nanogap architecture is more suitable for POM-based devices.

6.3.3 Conclusions

This structural analysis of the POM-based devices has shown two valuable insights. First, the depth profile XPS measurements demonstrated that the POM layer penetrates the underlying PMMA layer when spin-coated on top. The contact between the POM and the device electrodes remains intact explaining the observed redox behaviour even with the PMMA layer. Second, the comparison of vertical/sandwich and nanogap architectures confirmed that the sandwich configurations are poorly suited to host the non-uniform POM films they make. Many devices shorted due to top electrode penetrating through the film all the way to the bottom electrode. The nanogap architecture is a much better platform: it exhibits more pronounced and stable redox peaks. These findings showcase the vital role of device structure in POM-based memristive devices.

With an overall understanding of the electrochemical behaviour, environmental factors, and structural characteristics of these $H_3PMo_{12}O_{40}$-based devices, I can propose a mechanism that takes into account all these aspects to explain the observed switching behaviour.

6.4 Suggested mechanism

Throughout this chapter, I have explored different factors influencing device performance: electrochemical behaviour, effects of ambient moisture, POM distribution, and device architecture. Each study provided valuable insights into the interplay of these different factors. By synthesizing the gathered information, I can propose a comprehensive switching mechanism that accounts for the observed behaviours. This mechanism aims to explain how the redox reactions, ion movements, and environmental factors combine to produce the electrical characteristics that were observed. Figure 6.18 illustrates this proposed mechanism via energy level diagrams (left) and molecular schematics (right) of the device under different biasing conditions.

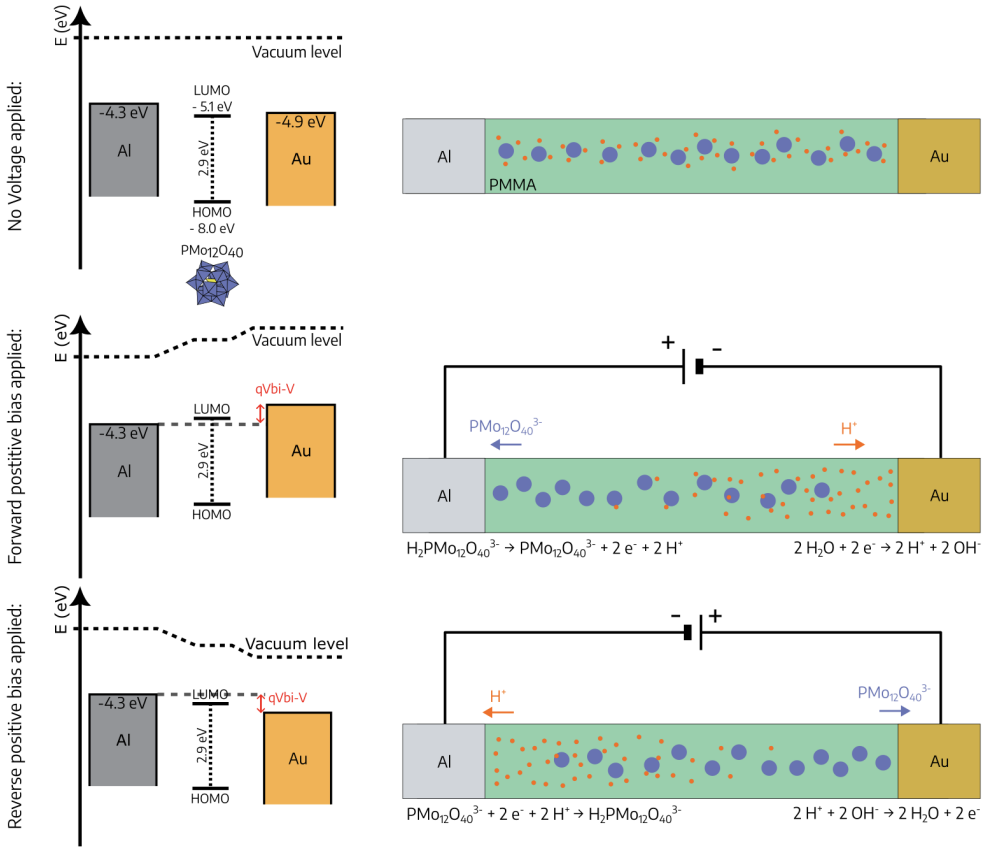

FIGURE 6.18: LEFT: Energy level diagrams (energy levels taken from [185]), and RIGHT: Molecular schematics when TOP no bias is applied, MIDDLE a positive forward bias is applied, BOTTOM when a positive reverse bias is applied.

Initially, no voltage is applied. The POM molecules penetrate the PMMA layer as was found in Section 6.3.1, and each POM anion has three surrounding protons to counterbalance its negative charge. The energy levels of the electrodes and POM are aligned with regard to the vacuum level. This equilibrium state changes when an external voltage is applied to the device.

When a forward positive bias (from 0 to + 2 V) is applied to the aluminium electrode, gold Fermi energy level shifts relative to the aluminium causing electrons to flow from the Au electrode to the Al electrode. This initiates a series of redox reactions and ionic movements within the device. As discussed in Section 6.1.3, the active electrode is probably Al due to its possible active participation in the switching process, and its close energy levels with $H_3PMo_{12}O_{40}$ and their spontaneous reaction as demonstrated in Section 6.1.4. Therefore, the POM molecules are oxidised at the Al electrode according to Equation 6.6 as determined in Section 6.1. To reinforce the idea that the POM's redox reactions are indeed at play, the device current levels can be linked to the number of POMs. Indeed, as shown in Section 5.2.2, as the film thickness increased, the number of POMs increased, and so did the current level. Of course, a more detailed study would be needed for a more thorough proof as this observation also takes into account the material above the nanogap covering both electrodes. The negatively charged POM species migrate towards the Al electrode due to the applied electric field. Concurrently, at the Au electrode, water undergoes a counter-balance reduction following Equation 6.7 as suggested in Section 6.2. The produced H^+ ions subsequently move towards the Au electrode also due to the applied electric field. While this forward bias drives the oxidation of POM molecules, the reverse reaction, reduction, occurs when the bias is reversed.

$$H_2PMo_{12}O_{40}^{3-} \rightarrow PMo_{12}O_{40}^{3-} + 2e^- + 2H^+ \tag{6.6}$$

$$2H_2O + 2e^- \rightarrow 2H^+ + 2OH^- \tag{6.7}$$

Upon application of a reverse positive bias (from + 2 to 0 V) to the Al electrode, the direction of electron flow is reversed, moving from the Al electrode to the Au electrode due to the shift in the relative positions of the Fermi levels of gold and aluminium. POM molecules get reduced, still at the active Al electrode, following Equation 6.8 as mentioned in Section 6.1. The electric field push the POM species towards the Au electrode this time. At the Au electrode, the water counter oxidation takes place (Equation 6.9) as supposed in Section 6.2, and H^+ ions move towards the Al electrode. This cyclic process of oxidation and reduction, coupled with ion movement, forms the basis of the device switching behaviour.

$$PMo_{12}O_{40}^{3-} + 2e^- + 2H^+ \rightarrow H_2PMo_{12}O_{40}^{3-} \tag{6.8}$$

$$2H^+ + 2OH^- \rightarrow 2H_2O + 2e^- \tag{6.9}$$

This proposed mechanism takes into account the electrochemical behaviour, the effects of ambient moisture, POM distribution, and the device architecture. It provides a starting point for understanding the complex interplay of factors governing device

performance. However, other mechanisms could also be suggested. A first alternative would be to have simultaneous POM oxidation and reduction at the aluminium and gold electrodes (depending on which way the voltage is applied) with water undergoing oxidation and reduction as a side reaction. A second option would be to only observe water splitting caused by the high electric field in the nanogap.[251]

As mentioned in Section 6.2, moisture is needed to observe the redox peaks in the I-V curves. However, it is very likely that the POMs play the main redox contribution role as the I-V curves of blank devices (Figure 4.3) show no redox peaks at all: moisture itself is not enough to explain the mechanism. Another factor to consider is that the oxidation and reduction peaks in the I-V curves are not exactly at the same voltage as would be expected for fully reversible solid-state redox reactions. This can be explained by a suboptimal scan speed, or the fact the moisture interferes with the POM redox reactions causing them to be less reversible.

Therefore, more work is needed to clarify the role of moisture in these devices. For example, confirm the root of the redox peaks in the I-V curves: are they due to water splitting or POMs. Investigations at the nanogap level with transmission electron microscopy (TEM) might also help observe traces of water splitting for example (via nanogap degradation). And finally, most of the work presented throughout this chapter was using suboptimal POM films without the PMMA layer. More work also needs to be done to further study the impact of the PMMA layer and its interactions with moisture.

6.5 Summary

This chapter discussed different factors which can influence $H_3PMo_{12}O_{40}$-based redox memory devices performance, providing some insight into their switching mechanism.

The electrochemical behaviour of the studied devices shows that their I-V curves are similar to the POM liquid-state cyclic voltammogram with $H_3PMo_{12}O_{40}$ undergoing sequential two-electron transfer reactions. The increase in current levels at redox peaks in the I-V curves for successive scans can be attributed to ion migration and the decrease in size of the conductive filament disc as scans are recorded.

I also investigated the influence of $H_3PMo_{12}O_{40}$ oxidation state on device performance. Both UV exposure and thermal treatment can reduce $H_3PMo_{12}O_{40}$, with thermal treatment in ambient air also enabling re-oxidation. Reduced POMs were associated with decreased device performance, contrasting with some previous studies that observed increased conductivity in reduced POMs. This suggests that many other factors, such as device architecture and POM functionalisation, can affect performance.

The effect of moisture in device performance showed a dual role: ambient moisture can degrade device materials and performance through corrosion of the electrodes, but it also enables reversible redox reactions. Samples fabricated and tested in low-moisture environments showed only reduction of the POM, while those exposed to ambient humidity underwent reversible re-oxidation. This suggests that moisture provides a valuable counter-reaction.

Depth profile XPS measurements showed that the POM layer penetrates the PMMA layer and still comes into contact with the device electrodes. Comparing different device architectures confirmed that vertical/sandwich devices are not ideal to use with the non-uniform POM films: the top electrode can penetrate the POM film and short the device. Therefore, my asymmetric coplanar nanogap electrodes are better suited.

By synthesizing these findings, I proposed a switching mechanism involving POM redox reactions, water-mediated counter-reactions, and ion migration. This model provides a foundation for understanding device behaviour. Future work could focus on clarify moisture's role in these devices, particularly in determining whether the redox peaks originate from water splitting or POM activity and the effect of the additional PMMA layer.

The insights gained from these studies can help with design and optimisation of POM-based memory devices. By carefully controlling moisture levels and POM oxidation state, it may be possible to tune device characteristics for specific applications, such as neuromorphic computing.

Chapter 7

Neuromorphic computing with POM-Based Redox Memory Devices

Now that the switching mechanism suggested in Chapter 6 is better understood, it is possible to control the devices and use them to target specific applications, for example neuromorphic computing. The idea is to mimic the function of biological neural networks to develop more efficient and powerful computing systems. The reason for this biological inspiration is that the human brain is extremely efficient. It has 10^{12} neurons, and requires only 10 fJ/event.[252] For comparison, a recent neuromorphic system developed by Intel has 10^9 neurons and consumes a maximum of 2 600 W to function.[253] This highlights the need for more power efficient devices.

Throughout this chapter, I will explore the potential of my optimised PMMA SC 34 nm + $H_3PMo_{12}O_{40}$ SC 150 nm memory devices for such applications, more precisely, by using their rich redox properties to create artificial neurons which can process information similarly to biological neurons. To do this, I applied pulsed electrical stimuli to the devices.

First, I investigate the devices responses to single pulses. This will allow for optimising input parameters in order to enhance device performance. Next, I explore the capabilities of these devices to mimic key brain functions. Finally, I study the ability of these devices to function as artificial nociceptors (the pain sensing neurons).

7.1 Single pulses

In this section, I explore the application of single pulses to the $H_3PMo_{12}O_{40}$-based devices as an important first step in optimising input settings. This helps to gain deeper insights into how these devices respond to various electrical stimuli, which can help

determine the most effective parameters for specific applications. Pulse duration, amplitude, and read voltage can be fine-tuned to enhance the devices performance and boost their potential for neuromorphic computing.

7.1.1 Pulse duration

First, I tested different pulse durations: 100 ns, 500 ns, 1 μs, 5 μs, 10 μs, 1 ms, 10 ms, 30 ms long + 0.3 V pulses, applied to the optimised PMMA SC 34 nm + $H_3PMo_{12}O_{40}$ SC 150 nm devices. This range of pulse durations (from ns to ms) helps to explore the device response to different timescales of electrical stimuli. The + 0.3 V pulse amplitude was chosen to match the redox peaks found in the I-V curves presented in Chapter 5.

All the responses can be seen in Figure 7.1. The "short pulses" (100 ns, 500 ns, and 1 μs) exhibit a sharp current increase followed by a slower decrease. This suggests a rapid initial response of the device, followed by a slower gradual relaxation. The quick rise in current could be attributed to the "*drift current*" due to the applied electric field or voltage pulse. The slower relaxation can be due to the "*diffusion current*" caused by the change in H^+ and $PMo_{12}O_{40}^{3-}$ ion concentration, identified in Chapter 6. The change in polarity at the end of the voltage pulse can be attributed to the slow diffusion of ions back to their initial position once the pulse is over. This response is very similar to that of the biological neurons, which was explained in Chapter 2, Figure 2.11.

The "medium pulses" (5, 10 μs) also have a sharp current increase (drift current), but the current level during the voltage pulse starts to decrease. This current decaying during the pulse can be due to an interplay between both the drift and diffusion currents. The sharp change of polarity at the end of the pulse can be seen as the sudden stop of the drift current, leaving only the contribution of the diffusion current. Finally, the ions slowly return to their equilibrium position bringing the current back to its initial level.

The "long pulses" (1, 10, 30 ms) also have their current level during the pulse decay, but all the way back to the initial level. The change in polarity is also extremely pronounced: spikes appear at the start and end of the pulse. The complete decay of current back to the initial level might indicate a full redistribution of ions: the H^+ and $PMo_{12}O_{40}^{3-}$ ions were able to fully diffuse back to their equilibrium position, while the spikes at the pulse boundaries could be due to charge accumulation and sudden discharge events due to the change in applied voltage. When the voltage is applied, charges accumulate at the Al/POM interface which causes the first current spike. When the voltage is removed, the accumulated charges suddenly discharge leading to the second spike. This is similar to capacitive effects in such devices.[254,255]

To gain a deeper insight of the different time scales at play, I calculate the rise and the fall times (see Table 7.1). The rise time, t_r, and fall time, t_f, are defined as the time it takes the signal to rise or fall from 10% to 90% of its final value.[30] The plots showing

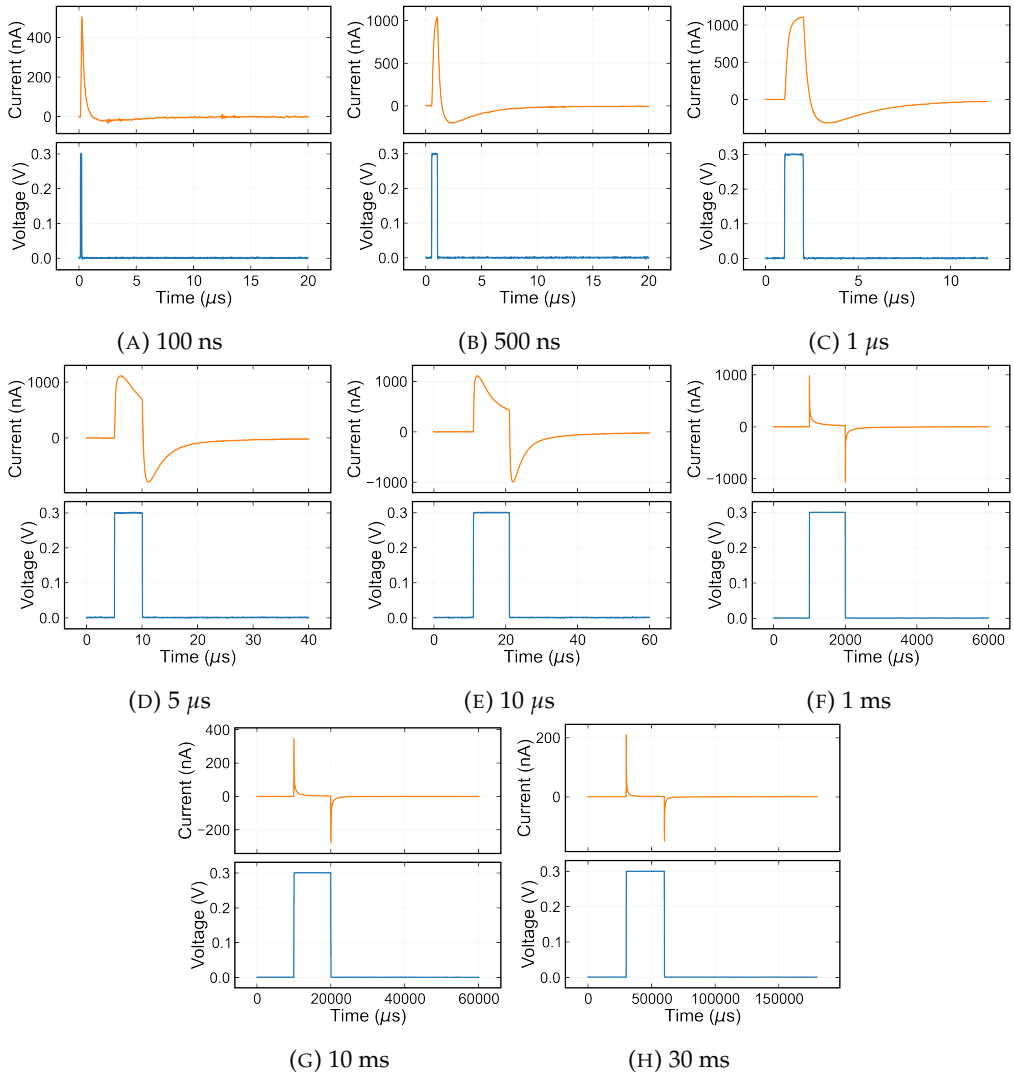

FIGURE 7.1: Single Pulse I-t (current vs time) and V-t (voltage vs time) curves for various pulse durations with a constant amplitude of + 0.3 V.

the calculations can be found in Section D.1. The rise time was calculated between the initial stable current and the top of the spike or the current maximum. The fall time was taken between that same current maximum and the stabilised current while the voltage is still applied for the longer pulse durations.

TABLE 7.1: Rise and fall times for different pulse lengths, with a read voltage of 0 V.

Pulse duration	Rise	Fall
100 ns	84 ns	553 ns
500 ns	281 ns	460 ns
1 μs	366 ns	484 ns
5 μs	374 ns	3 μs
10 μs	370 ns	6 μs
1 ms	4 μs	78 μs
10 ms	22 μs	52 μs
30 ms	68 μs	99 μs

In theory, since the input probe station is the same for all the measurements, the rise time should be constant. However, the number of data points collected was the same regardless of total measurement time. Therefore, for longer pulses, the data points are more spread out. This causes the calculated rise time to increase for longer pulses. A more accurate estimation of the rise time would be the one for the shortest pulse duration as the data points would be the closest together, i.e. the highest resolution. In addition, the rise time is also dictated by the speed of the input SMU. The faster the tool can increase the voltage, the shorter and more accurate the rise time.

The fall times appear to divide into the same groups as defined above. The short pulse (100 ns, 500 ns, 1 μs) fall times are in the order of hundreds of nanoseconds, the medium pulses (5, 10 μs) are in the order of microseconds, and the long pulses (1, 10, 30 ms) in the order of tens of microseconds. This strengthens the grouping categories and the influence of slower ion diffusion which, as the pulse duration increases, have more time to rearrange.

Overall, the behaviours observed for these single pulses can be attributed to the complex interplay between drift and diffusion currents caused by the applied voltage pulse and ion diffusion, respectively. In Chapter 6, I identified two ions: H^+ and $PMo_{12}O_{40}^{3-}$. The larger, less mobile $PMo_{12}O_{40}^{3-}$ ions move more slowly, affecting the longer-term device response. Since they move slower than the H^+ ions, the influence of their movement becomes more apparent for the longer pulse durations (ms range). At the end of the voltage pulse, the ions start to diffuse back to their original positions which can create a temporary current in the opposite direction which can explain the change in current polarity when the pulse is stopped. This effect is particularly evident in the current spikes observed at the beginning and end of longer pulses, where the sudden application or removal of voltage causes a rapid redistribution of these ions.[256]

The optimal pulse length for these devices appears to be 1, 5, or 10 μs. At these durations, the current inside the pulse does not decay. It allows for a balance between the drift and diffusion currents.

7.1.2 Pulse amplitude

Next, I investigated the effect of pulse amplitude on current response. Pulses of varying voltages (from + 0.05 V to + 0.3 V) were applied for a duration of 1 μs and a 1 μs gap between them, which was previously determined to be the optimal pulse length. Figure 7.2 presents the results of this experiment in two panels: the upper panel shows the current-time (I-t) curve, while the lower panel displays the corresponding voltage-time (V-t) curve.

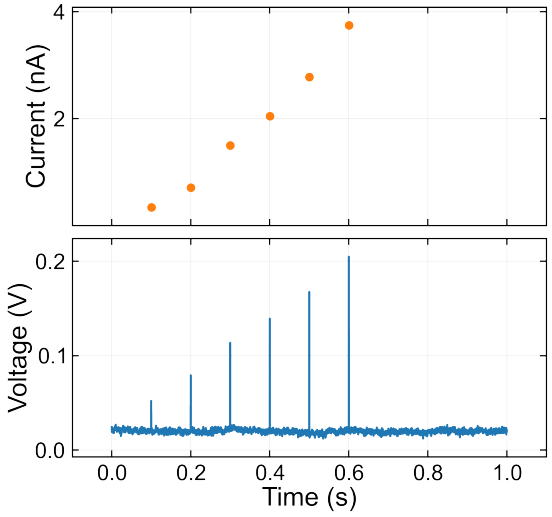

FIGURE 7.2: Testing increasing pulse amplitudes with a constant 1 μs long pulse and gap.

The lower panel (V-t) illustrates the series of voltage pulses applied over time. The spikes of increasing amplitude (the blue vertical lines) correspond to the applied voltage pulses, with each subsequent pulse having a higher amplitude than the previous one. The upper panel (I-t) shows the current response to these voltage pulses. The orange dots represent the peak current measured for each corresponding voltage pulse. From left to right on the graph, both the voltage pulses and the resulting current peaks show a clear increasing trend. As the voltage amplitude of each pulse increases, the peak current level proportionally increases. This behaviour is consistent with Ohm's Law, which states that current is directly proportional to voltage.

7.1.3 Read voltage

Next, I investigated the effect of the read voltage: 1 μs long pulses at + 0.3 V were applied. The read voltage is the voltage continuously applied: 0 V, 0.01 V, 0.05 V, and 0.1 V were tested. Figure 7.3 shows the obtained I-t and V-t curves.

As the read voltage increases, a shoulder in the I-t curve can be observed right before the + 0.3 V pulse response. It starts to be more visible for the 0.05 V read voltage and is directly due to the applied read voltage, similar to the case where two pulses would be applied. The current levels of the + 0.3 V pulse is much higher and therefore overshadows the device response to the + 0.05 V pulse. This makes it challenging to distinguish the individual effects of the two voltage levels. Regardless, the fact that a response can be obtained for 0.05 V means that these devices are very sensitive. This is very interesting because low voltages could be used to operate these devices helping design low-power consumption systems.

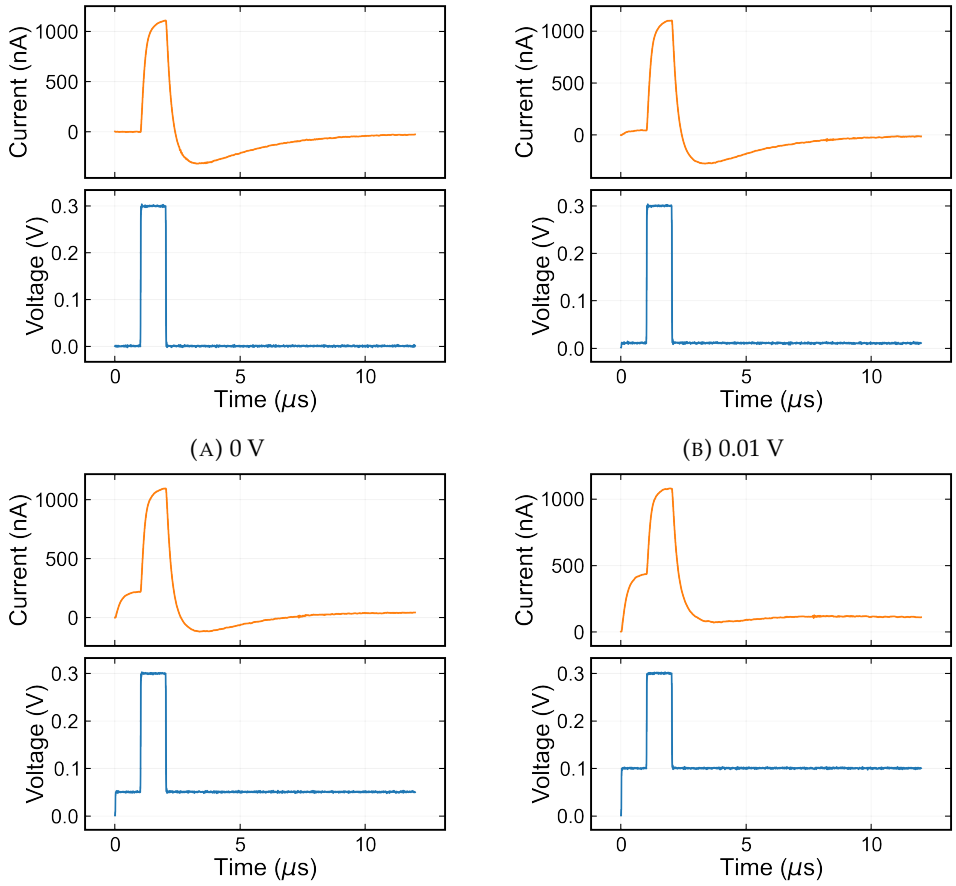

(A) 0 V (B) 0.01 V

(C) 0.05 V (D) 0.1 V

FIGURE 7.3: Single Pulse I-t and V-t curves for various read voltages.

Another observation to make is that current is also measured even without a bias being applied (0 V read voltage), this confirms that there are trapped charges which also participate in the current response as detailed in the previous section.

Overall, the read voltage does impact these devices even when it is very small (0.05 V). This is important to keep in mind when designing more advanced measurements as the read voltage could perturb the device response.

7.1.4 Conclusions

This section looked at the behaviour of PMMA and $H_3PMo_{12}O_{40}$ devices when single pulses were applied. I tested three key parameters: pulse duration, pulse amplitude, and read voltage. When testing different pulse durations, three distinct response types were observed: short (ns range), medium (μs range), and long pulses (ms range). The optimal pulse length of 1 μs was identified, as it balances the drift and diffusion currents. The response for this pulse duration closely mimics biological neuron signals, showcasing these devices potential for neuromorphic computing applications.

Then, I studied the influence of the pulse amplitude by applying 1 μs pulses at various voltages. As expected, the current level increases with the voltage amplitude. The final tested parameter was read voltage which was varied from 0 V to + 0.1 V. This showed the high sensitivity of these devices: responses were detectable at voltages as low as + 0.05 V. Furthermore, the trapped charges were identified as a contributing factor to the response, even in the absence of applied bias, current was measured.

Overall, the complex interplay between ion migration and diffusion within the devices was observed. I found that the pulse duration highly influences the devices response and that the devices are very sensitive, even to small voltages. This will help design more complex pulse schemes, aiming to mimic the brain, as will be shown in the next section.

7.2 Mimicking the brain

Now that single pulses are better understood, I can develop more complex input pulse schemes that aim to replicate some brain functionalities. In this section, three specific behaviours will be discussed.[257–259]

Short and long term memories indicate how long information is stored for. Short-term memory holds small amounts of information, not always consciously, for immediate use, while long-term memory has a much larger capacity and stores information of prior events.[96]

Plasticity is the brain ability to change the strength of the connections between neurons.[260] For example, when forming new memories or acquiring new skills this is very important. The connections formed between neurons can strengthen or weaken over time, depending on how frequently they are used.

Re-learning is the ability to more easily re-learn some information if I studied it once already. This is because part of the neural pathways that were established during the first learning are partially preserved or more easily reactivated.[261]

7.2.1 Short- vs Long- term memory

To mimic the different memory types, I applied an increasing number of pulses, and recorded the current. The pulse parameters are + 0.3 V amplitude and different lengths (100 ns, 1 μs, or 30 ms) to study the three main types of responses found when applying single pulses in Section 7.1. The + 0.3 V pulse amplitude was chosen as it is the voltage at which the POM redox peaks become apparent in the I-V curves (see Chapter 5). The results are shown in Figure 7.4. The desired behaviour is to observe a variable current

level when few pulses are applied, and a more stable current when many pulses are applied. This is equivalent to the short amount of time information is stored in the short-term memory when few pulses are applied, and the more stable stored information in the long-term memory when many pulses are applied. Overall, the three tested pulse durations do exhibit this response: the current level stabilises as more pulses are applied regardless of pulse duration. However, the behaviours are different depending on pulse duration.

The 100 ns long "short pulses" (Figure 7.4a) start by an increase in current level followed by a slow decrease which eventually stabilises as more pulses are applied. This overall trend is similar to the 10 μs long single pulse shown in Figure 7.1e. The current increased when the voltage pulse was applied, then the current level decreased even if the voltage was still applied. This response was attributed to the different migration speeds of the different ions at play (H^+ and $PMo_{12}O_{40}^{3-}$). This makes sense as 100 pulses each 100 ns long total to 10 000 ns or 10 μs. Therefore, the behaviour presented here can be seen as the single 10 μs long pulse, but cut up into 100 100 ns long pulses.

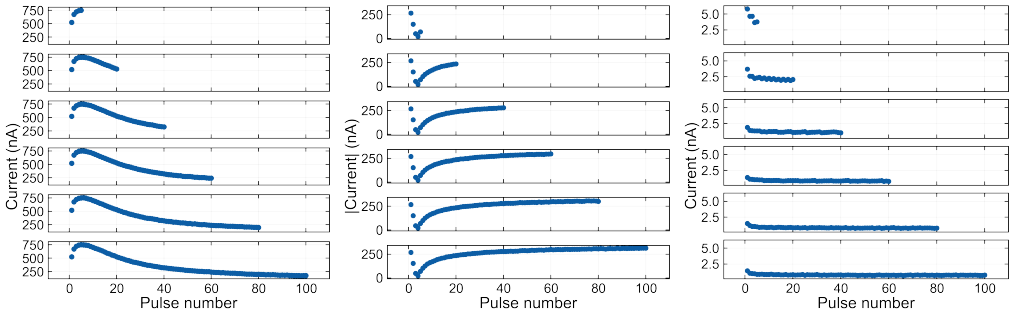

(A) 100 ns (B) 1 μs (C) 30 ms

FIGURE 7.4: Mimicking short vs long term memory with different pulse lengths at + 0.3 V.

The 1 μs "medium pulses" (Figure 7.4b) show a change in current polarity after the first 4 pulses: the 5^{th} pulse has a higher current level than the 4^{th} as the absolute current is plot here. This means that for the first 4 pulses, the current decreases, then increases for the following pulses. Eventually, the current stabilises when many (60 or more) pulses are applied. A possible explanation is that the device first needed to be "reset" back to its "0" state before it could start storing information. To help "initialise" the device, it is possible to apply longer or more intense voltage pulses. This is why this "resetting" step is not always clearly visible. For instance, there is no change in polarity in the 30 ms long pulses case (Figure 7.4c): already within the first pulse the device was ready to store information. This is an interesting parameter to consider when optimising power consumption. Shorter pulses mean less power is needed when compared to longer pulses, but maybe more of them will be needed which could in total amount to more power consumption.

Finally, the "long pulses", 30 ms (Figure 7.4c) exhibit a continuous decrease in current level which eventually stabilises as pulses are applied. In this particular case, each pulse train was applied to a different device. For the previous two cases, all pulse trains were applied to the same device. This explains why the first pulse of each train is at a different current level. Once I realised that waiting long enough (1-2 minutes) between each pulse train was enough to fully reset the device, I applied all pulse trains to the same device. This is why the current level is the same for the first pulse of each train for the "short" and "medium" pulse cases. The time needed to fully reset a device can already be seen in the single pulse plots: after a certain amount of time, the current level reached the same value as the initial one. Regardless of the device-to-device variability seen in Figure 7.4c, the stabilised current level is roughly the same for all devices (around 0.1 nA) which shows the consistency of this response.

I also tested the effect of the pulse voltage as shown in Figure 7.5 to further understand how input parameters influence the device's response. In this study, each pulse train was applied to a different device. Explaining the different current levels observed for each pulse train and each pulse voltage. As expected, the current level increases with the pulse voltage. However, the difference is more distinguishable between + 0.3 V (Figure 7.5a) and + 0.7 V (Figure 7.5b) compared to the difference between + 0.7 V and + 1.3 V (Figure 7.5c). For the + 0.3 V pulses, the current eventually stabilises around 2 nA in average, and around 25 nA in average for both the + 0.7 V and + 1.3 V pulses.

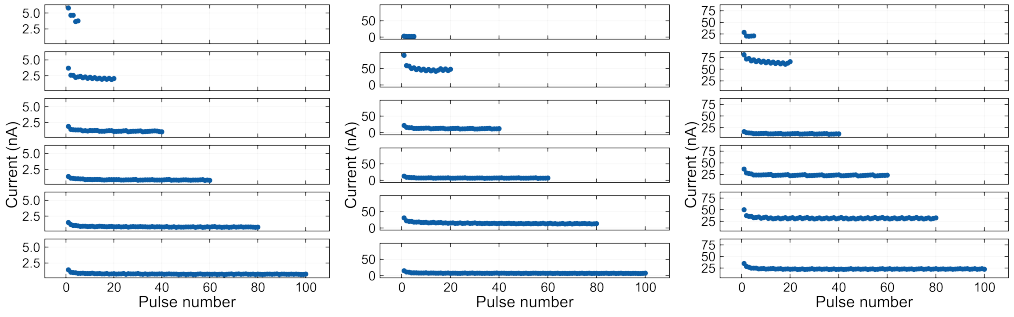

(A) + 0.3 V (B) + 0.7 V (C) + 1.3 V

FIGURE 7.5: Mimicking short vs long term memory with different pulse voltages with the same 30 ms width.

In summary, pulse duration affects the observed response when multiple pulses are applied. When many short pulses are applied, the overall behaviour is similar to a single longer pulse. Medium pulses show a decrease in current level until 0 A, where the current changes polarity and then increases. This can be explained by the need for multiple pulses to "reset" the device before it can store information. The longer pulses only show a decrease in current and don't need multiple pulses to be "reset" as it could have been done in a single longer pulse. The pulse voltage also affects the current level: higher amplitudes lead to higher current levels. Overall, these devices can exhibit both short- and long-term memory responses. When many pulses are applied, the

current level stabilises, which is equivalent to information being safely stored for longer periods of time, mimicking the behaviour of long-term memory in biological systems. This showcases the potential of my POM-based devices for neuromorphic computing applications.

7.2.2 Plasticity

Next, I mimicked plasticity by applying a first pulse train with an amplitude of + 0.3 V followed by a pulse train with an amplitude of - 0.3 V with different pulse durations. The current outputs can be found in Figure 7.6. The first tested pulse amplitude, +/- 0.3 V, was chosen as this is where POM redox peaks are seen in the I-V curves (Chapter 5). The pulse durations were chosen to allow comparison between the three main types of behaviours found when studying single pulses (Section 7.1).The idea is to showcase the strengthening and weakening of connections between neurons. When the current decreases, the connection between neurons weakens called "*depression*". When the current levels increase, the connection between neurons strengthens this time, called "*potentiation*". The responses observed here can be related to the comments made in the previous section.

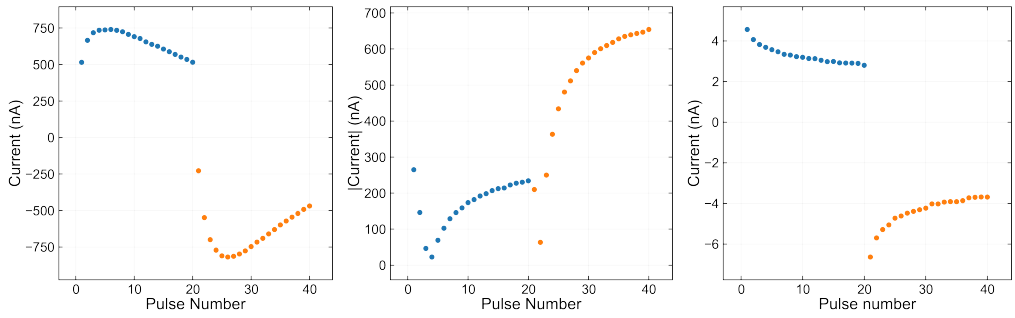

(A) 100 ns (B) 1 μs (C) 30 ms

FIGURE 7.6: Mimicking plasticity with different pulse lengths at +/- 0.3 V.

The short 100 ns long pulses (Figure 7.6a) start with a decrease in current level followed by an increase, regardless of voltage pulse polarity. The difference between the + 0.3 V pulses (blue) and the - 0.3 V pulses (orange) is the current polarity. As explained in the previous section (Section 7.1), this behaviour is similar to the single 10 μs long pulse: it can be seen as cut up into multiple shorter pulses. Therefore, these devices exhibit both an increase and decrease in current level, or both potentiation and depression. This is similar to Wang et al.[95]'s data presented in Figure 2.13 in Section 2.3.3.2. In my case, this could be explained by accumulation of $PMo_{12}O_{40}^{3-}$ - ions at the Al electrode (instead of Ag nanoparticles in Wang et al.'s devices) as discussed throughout Chapter 6. Therefore, to control the potentiation or depression in these devices, the number of applied pulses is more important than the pulse voltage polarity. However, to have a reliable and repeatable control, further optimisation work still needs to be done. For example,

testing the number of pulses on multiple devices, studying other factors such as pulse amplitude and duration.

The "medium pulses", 1 μs long show the same forming step as mentioned in the previous section. The first 4 pulses decrease the current, then the current rises after it changed polarity. Note that absolute current is plot here to better highlight this change in polarity. Again, both potentiation and depression responses are observed in my devices depending on pulse number rather than pulse amplitude.

The 30 ms long pulses exhibit a similar response to the one described in the previous section: the current level decreases as pulses are applied. The only difference between the + 0.3 V and - 0.3 V pulses is the current polarity (similarly to the 100 ns long pulses), but the overall behaviour is the same.

I also investigated the effect of the pulse voltage as shown in Figure 7.7. As expected, as the pulse voltage increases, so does the current level.

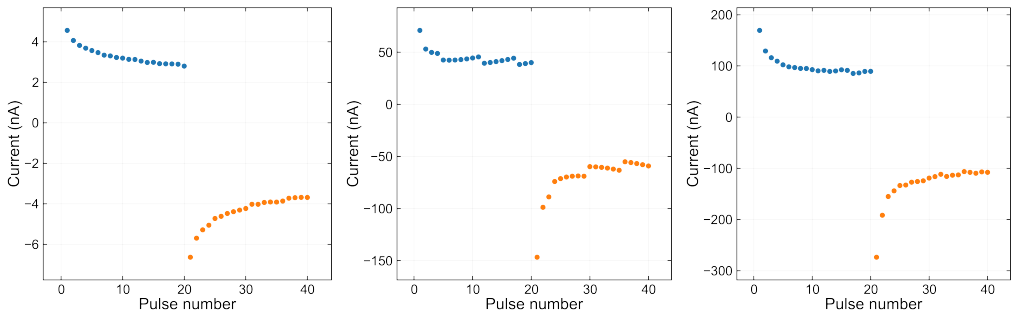

(A) +/- 0.3 V (B) +/- 0.7 V (C) +/- 1.3 V

FIGURE 7.7: Mimicking plasticity with different pulse amplitudes with the same 30 ms width.

Overall, similar responses as the short- and long- term memory study were observed. Regardless of pulse voltage polarity, amplitude and pulse duration, both potentiation and depression are observed in these devices. However, either potentiation or depression is observed depending on the number of pulses rather than pulse voltage polarity as other groups showcase[91,258,259] and particularly Wang et.al.[95] where their potentiation/depression results (Figure 2.13 in Section 2.3.3.2) are quite similar to the ones presented here. This offers an alternative way to mimic plasticity offering a promising path towards designing new neuromorphic systems. More work is still required to fully be able to control the potentiation and depression behaviour of these devices. For instance, confirming the number of pulses needed to induce potentiation or depression on multiple devices, and studying the influence of other factors (pulse amplitude and duration) on this number.

7.2.3 Re-learning

Finally, I investigated re-learning capabilities. The input pulse scheme is an initial (learning) 20 pulse train (+ 0.3 V), followed by a 10 μs long gap in order to let the current decay during which no pulses are applied, then a second (re-learning) 5 pulse train (also + 0.3 V), all pulses with different widths. + 0.3 V pulse amplitude was chosen as it is the voltage where POM redox peaks are found in the I-V curves (Chapter 5). In this section, all plots show the absolute current to better showcase the current levels during the different steps of the pulse scheme.

Different pulse durations were tested to compare the three main types of responses identified in the single pulse section (Section 7.1). It is expected for the current level after the second pulse train to be similar to the current level after the first pulse train. Indeed, fewer pulses (only 5) are needed in the second pulse train to reach the same current level than the initial pulse train (20 pulses). The neural pathway was not completely lost, therefore the information was easier to re-learn. This response can be seen for all three tested pulse durations in Figure 7.8.

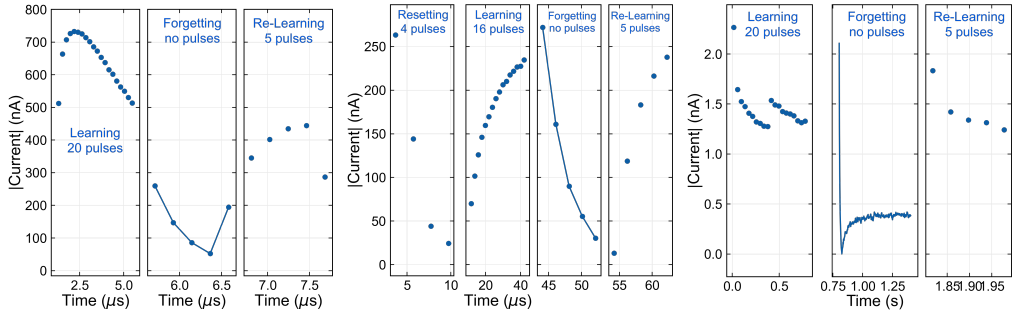

(A) 100 ns (B) 1 μs (C) 30 ms

FIGURE 7.8: Mimicking re-learning with different pulse lengths at + 0.3 V.

The behaviour observed in the first pulse train is the same as has been previously described for each pulse duration. The current level increases, then decreases for short pulses. For medium pulses, the current changes polarity as the device needs to be "reset" with the first 4 pulses. And for long pulses, only current decrease is observed. Regardless, in each case, the second pulse train ends with similar current levels as the first pulse train. Therefore, re-learning is observed in these devices.

I also studied the pulse voltage effect as shown in Figure 7.9. Therefore, different pulse amplitudes are tested with the same 30 ms pulse width. As expected, the current level increases with voltage amplitude. Regardless, the re-learning is still observed: the current level after the second pulse train is close to that of the first pulse train.

Finally, I explored different number of pulses in the initial pulse train as shown in Figure 7.10. The second pulse train always has 5 pulses in it. All pulses have a + 0.3 V amplitude and 1 μs width. For each case, it can be seen that a lower number of pulses

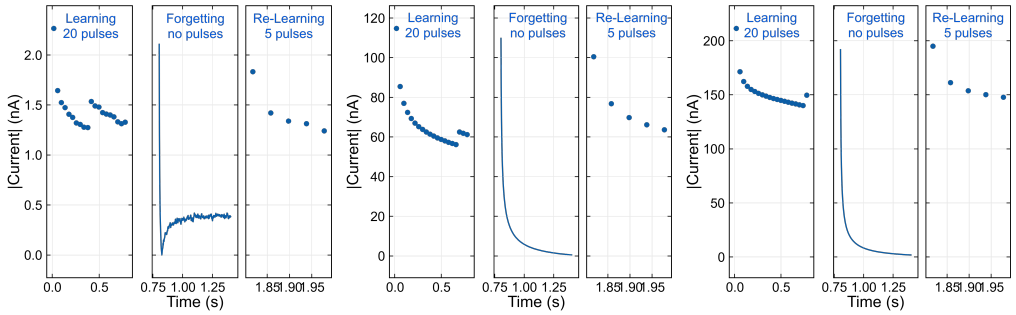

(A) + 0.3 V (B) + 0.7 V (C) + 1.3 V

FIGURE 7.9: Mimicking re-learning with different pulse voltages with the same 30 ms width.

as compared to the first pulse train is needed in the second pulse train. For instance, if 5 pulses are in the first pulse train, a similar current level is reached after only 2 pulses in the second pulse train (Figure 7.10a). If 10 pulses are in the first train, only 3 pulses are needed in the second train (Figure 7.10b). The case where 20 pulses are in the first train is the same as has been described above (Figure 7.10c). Since these pulses are 1 μs long, the first 4 pulses needed to "reset" the device are clearly visible. Similar to the previous sections using 1 μs long pulses, the current level decreases during the first 4 pulses then increases for the rest of the pulse train.

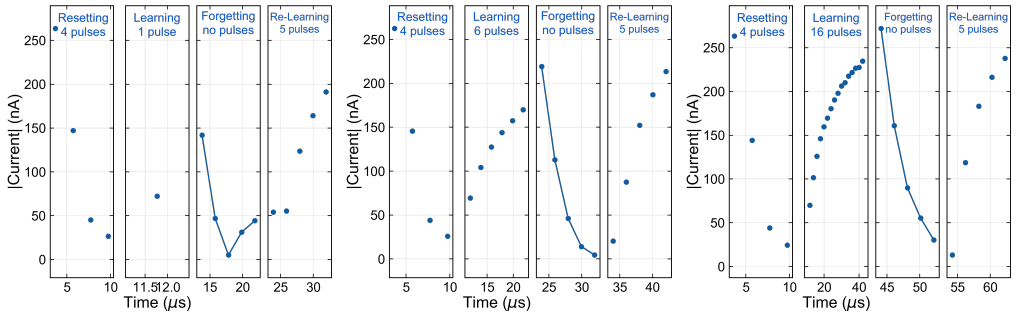

(A) 5 pulse initial train (B) 10 pulse initial train (C) 20 pulse initial train

FIGURE 7.10: Mimicking re-learning with different pulse number in the first pulse train with the same + 0.3 V amplitude and 1 μs width.

Overall, these devices exhibit re-learning capabilities regardless of the pulse parameters. Different pulse widths, amplitude and numbers all showed the re-learning behaviour. This highlights the possibility of using these devices to create more efficient neuromorphic computing systems.

7.2.4 Conclusions

Altogether, these devices are able to reproduce key behaviours of the brain, showing their promise for developing brain-inspired computing architectures.

These devices showed they can store information for different lengths of time (short and long term memory). Short 100 ns pulses showed an initial increase in current level followed by a decrease. Medium 1 μs pulses changed their current polarity after a few pulses, possibly due to the need to ”reset” the devices to the ”0” state before current levels could stabilise. Finally, long 30 ms pulses only showed current level decrease. Even if the response varied with pulse length, all showed a stabilised current level after enough pulses were applied, analogous to the long-term memory in biological systems.

Additionally, these devices could mimic changes in the strength of connections between neurons (plasticity). Both potentiation and depression were observed. However, this depended on the number of pulses rather the pulse voltage polarity. This offers new strategies for designing bio-inspired artificial neural networks. More work still needs to be done on this aspect to fully be able to control the potentiation and depression behaviour of these devices.

Finally, re-learning was also observed with these devices. Fewer pulses in a second train were needed to reach similar current levels to an initial pulse train. This behaviour was observed regardless of pulse duration, amplitude, and number, showing a consist response.

This is very promising for the development of neuromorphic computing platforms. The next steps would be to integrate these devices in circuits to develop large-scale arrays for artificial intelligence applications.

7.3 Mimicking nociceptors

To showcase the versatility of these devices, I also show that these devices can behave as specific neurons: nociceptors. As a reminder from Section 2.3.4, nociceptors are neurons which serve as pain sensors.[93] They operate in three distinct modes: normal, relaxation, and sensitised. As with any neuron, they use action potentials (APs) to communicate with adjacent neurons. For nociceptors, the AP generation threshold is given by the intensity of the pain stimuli, called ”noxious” stimuli. In electronics, the pain input can be represented by an input voltage pulse. If the current response is high enough, the artificial nociceptor will communicate it to the adjacent devices in order to trigger a response (generally a motor response).

In this work, I applied a noxious pulse followed by a sensory pulse train after a certain gap (see Figure 7.11). Different parameters of this input will be tested throughout this section.

The periodic shape of the current responses in the following discussion is due to the way the data is collected. As explained previously, the data collection resolution is

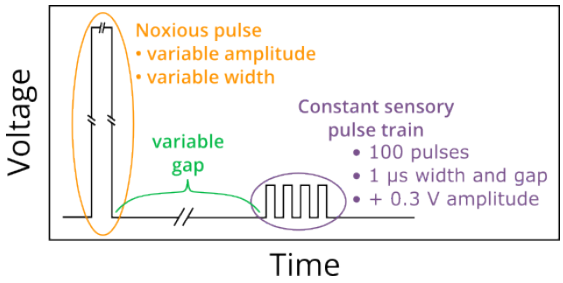

FIGURE 7.11: Nociceptive input pulse scheme: a variable noxious pulse (orange) followed by a 100 pulse (+ 0.3 V, 1 μs long) long sensory train (purple) after a variable gap (green).

limited: maximum 4000 data points can be collected by the software. Therefore, they were spread out across the entire duration of the input. This means that the current is not always measured at the same point along the sensory pulse train: some points are periodically at the top or at the bottom of the pulse, giving this sinusoidal pattern to the current response. Figure 7.12 shows a zoomed in view of the sensory pulse train recorded when testing the + 1.3 V noxious pulse amplitude. The red crosses represent an example of where the data points were collected. This is also why the period changes when the total input time changes: the points are differently spread out along the sensory pulse train.

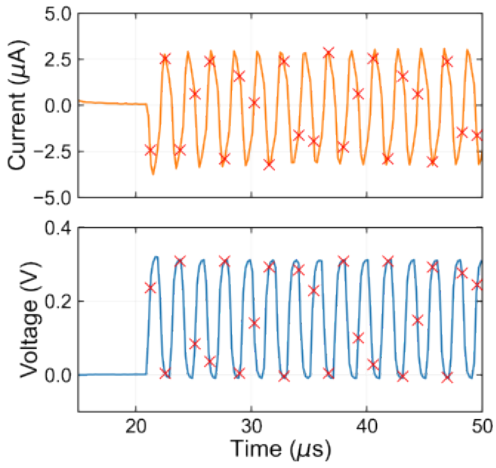

FIGURE 7.12: The red crosses represent an example of data collection points along the zoomed view of the sensory pulse train recorded when testing the + 1.3 V noxious pulse amplitude.

To start, I varied the noxious pulse amplitude. The noxious pulse width and gap between it and the sensory pulse train were kept constant at 1 μs and 10 μs, respectively. The noxious pulse amplitude ranged from 0.5 V to 2 V and the sensory pulse train amplitude was kept constant at + 0.3 V. The results are shown in Figure 7.13a. As expected, the output current increases with the noxious pulse amplitude: the more intense the pain (= noxious amplitude), the more intense the response.

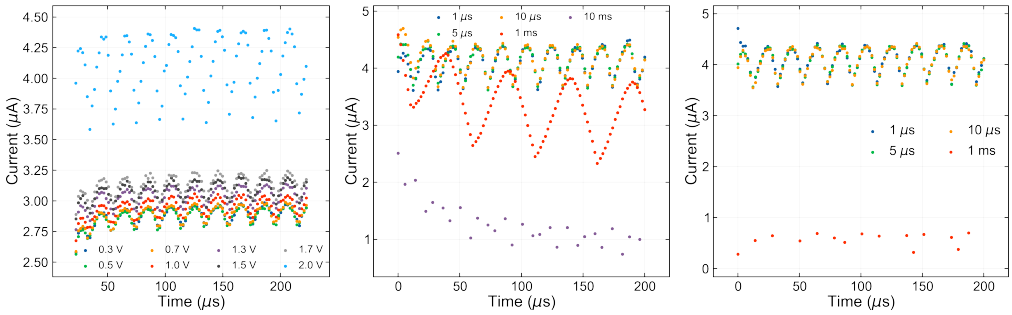

(A) Varying the noxious pulse amplitude with a constant 1 μs long pulse.

(B) Varying the noxious pulse width with a constant + 2 V amplitude.

(C) Varying the gap between the noxious pulse and the sensory pulse train.

FIGURE 7.13: Mimicking key nociceptor functions.

Figure 7.13b shows the results when the noxious pulse width is varied, while its amplitude was kept constant at + 2 V. The current level decreases when the noxious pulse width increases. The μs long pulses (1, 5, and 10 μs) are all close together. The 1 ms long pulses output current starts to decrease compared to the μs pulses, and the 10 ms pulses output even lower currents. Normally, the longer the pain (= noxious width), the higher the response. This is because nociceptors do not usually adapt or else our bodies could get used to the pain and get hurt. If they adapt, it usually requires much longer time frames than other neurons.[262] It appears that the ms pulses are long enough for these artificial nociceptor to enter a state where they can adapt. A real life example of this is adaptation to chronic pain.[263]

Finally, I investigated the gap between the noxious pulse and sensory train as shown in Figure 7.13c. It appears that a much longer gap is needed for an observable current output difference. All gaps in the μs range (1, 5, and 10 μs) have a similar response, while the 10 ms gap has a much lower output current. This is explained by the fact that the body had more time to recover from the initial pain and therefore the response is lower.

Overall, these devices can accurately reproduce expected behaviours of nociceptors. Their responses increase when the pain is more intense, they show adaptation if the noxious pulse is too long, and the gap between the noxious pulse and sensory train affects the device response. Therefore, from this preliminary study, it appears the device behaviours are better matched with nociceptors when the noxious pulse is in the μs range as it avoids the adaptation behaviour which isn't usually observed for nociceptors. Regardless, this is very promising for the development of artificial nociceptors for example in artificial skin.

7.4 Summary

This chapter explored the potential of $H_3PMo_{12}O_{40}$-based redox memory devices for neuromorphic computing. These devices can mimic several key functions of biological neural systems, offering new possibilities for developing new neuromorphic systems.

First, I studied the device behaviour when subjected to single pulses. Three distinct response types were observed: short (ns range), medium (μs range), and long (ms range) pulses. 1 μs long pulses are optimal as they balance the rapid response of H^+ ions with the slower $PMo_{12}O_{40}^{3-}$ ions. It was also seen that these devices can detect voltages as low as 0.05 V.

Next, I investigated the devices ability to mimic key brain functions. They exhibited short-term and long-term memory behaviours, synaptic plasticity and re-learning capabilities. These findings suggest that these devices can replicate biological neural processes.

Finally, I showed that the devices can operate as nociceptors. They can accurately replicate the intensity-dependent nature of pain signals by increasing their responses with noxious pulse amplitude. They displayed adaptation behaviour when longer noxious pulses were applied (ms range). This is similar to the longer timescale biological nociceptors need to adapt. Finally, they responded to different recovery times: longer gaps between noxious and sensory pulses resulted in lower output currents. This highlights the potential applications in advanced tactile sensing systems or artificial skin technologies.

Overall, the versatility of these POM-based redox memory devices highlights their potential for neuromorphic computing applications. These devices can participate in the development of more efficient and adaptable artificial intelligence systems.

Future work can explore the integration into larger-scale arrays and explore their collective behaviour.[264,265] Further research is needed to investigate their use in practical neuromorphic computing applications, such as pattern recognition and decision-making systems. As the gap between biological and artificial neural systems is closing, POM-based devices may play a role in advancing computing paradigms.

Chapter 8

Conclusions and Future Work

This thesis investigated the development of polyoxometalate (POM) -based nanoscale electronic devices for next-generation memory applications and neuromorphic computing. The aim is to address the challenges in electronic memories, such as the need for faster, more efficient devices capable of meeting the demands of more complex and data-intensive applications like artificial intelligence and the Internet of Things (IoT). More specifically, my approach to overcome these challenges is to optimise both the active material and the device architecture. Polyoxometalates are an excellent candidate due to their rich redox properties, they can reversibly exchange multiple electrons with little structural change. To host nanomaterials such as POMs, the chosen electrode design is asymmetric aluminium-gold coplanar nanogap separated electrodes, fabricated using adhesion-lithography.

First, I determined that $H_3PMo_{12}O_{40}$ is the most promising POM candidate among those tested, as it showed rich redox activity, especially when deposited as a thick film (drop-cast or spin-coated 150 nm). It was possible to further enhance device performance by adding a 32 nm spin-coated poly(methyl methacrylate) (PMMA) layer under the already optimised 150 nm spin-coated $H_3PMo_{12}O_{40}$ layer. This extra PMMA layer helped prevent spontaneous reduction of the POM on the Al electrode. This configuration demonstrated repeatable redox peaks over numerous scans (at least 178) and devices (hundreds) addressing the challenge of device-to-device and cycle-to-cycle variability common in redox-based resistive switching devices.

Next, I delved into the switching mechanisms of these POM-based devices, revealing a complex combination of factors. The electrochemical behaviour of the solid-state POM film resembles its liquid-state cyclic voltammogram, $H_3PMo_{12}O_{40}$ undergoes two sequential two-electron transfer reactions. The migration of the reactive POM species and the smaller "disc" region of conductive filaments as scans are performed explain the increasing current level with scan number. I looked into the role of environmental factors, moisture, and its effect on device performance. While ambient moisture can

degrade the electrodes through corrosion, it can also enable reversible redox reactions. This highlights the balance needed in controlling environmental conditions for optimal performance. Via depth profile XPS measurements, I showed that the POMs can penetrate the PMMA layer allowing them to still undergo redox reactions and operate the device. It was also confirmed that the coplanar device architecture is ideal for hosting POM films, as vertical or sandwich architectures are too easily shorted. Overall, the switching mechanism in these devices was attributed to the redox reactions of the POM and the counter-balance reactions of moisture, but more work is still needed to fully confirm the origin of the observed redox peaks.

Finally, I showcased the potential of these POM-based devices for neuromorphic computing. First, the devices response to different types of electrical pulses were studied in order to identify optimal input settings. These were then used to develop more advanced pulse schemes to assess device performance in neuromorphic applications. The devices successfully mimicked several key functions of biological neural systems, including short- and long-term memory, synaptic plasticity, and re-learning capabilities. Additionally, these devices can operate as nociceptors, accurately replicating the intensity-dependent nature of pain signals and displaying adaptation behaviour and recovery after a longer gap between the pain input and the sensory read-out. These findings open up possibilities for artificial neural networks and skin technologies.

In conclusion, this work examined POM-based nanoscale electronic devices for memory and neuromorphic computing applications. It successfully answered the initial research questions. The device architecture and material selection were optimised, the complex switching mechanisms were untangled, and practical applications in bio-inspired computing were demonstrated. This paves the way for further development of these devices, allowing them to become more efficient artificial intelligence systems.

However, some challenges remain, such as integration into larger-scale arrays and further distinguishing the different switching parameters. This will allow to confirm if these devices can help solve the Von Neumann bottleneck. Nevertheless, the versatility and potential of POM-based redox memory devices shown throughout this thesis highlight their promise in transforming nanoelectronics. As the gap between biological and artificial neural systems continues to narrow, these devices may play a role in overcoming current technological limitations in electronic memories and computing architectures.

Appendix A

Materials and Methods

A.1 Electrode fabrication

General information: this protocol aims to fabricate asymmetric coplanar nanogap separated electrodes.

Glassware:

- Beakers + substrate holders
- Crystallizing dish
- Clock glass (lid)
- Weighing boat (or clock glass)
- Vial

Equipment:

- Scale
- Magnetic stirrer
- Stir plate
- E-beam (metal deposition technique)
- Tweezers
- Oxygen plasma asher
- Oven

Materials:

- Substrates
- Solvents (DI Water, Acetone, IPA)
- DECON90
- Al, Au (electrode metals)
- ODPA (Octadecylphosphonic acid) - SAM
- Sticky polymers
- N_2 (to dry)

Protocol:

1. Clean substrates by sonicating them for 5 minutes in each cleaning solvent, rinsing them with the next solvent, and drying them with N_2 between each sonication process:
   (a) DECON90 solution according to package instructions
   (b) DI water
   (c) acetone
   (d) isopropanol (IPA)
2. Deposit 40 nm of Al on the clean substrates via thermal evaporation at 2 nm/s from Al wire
3. Perform standard photolithography to pattern the metal in the desired way
4. Make a 426 μmol/L solution of octadecylphosphonic acid (ODPA) in IPA ($\approx$ 28.6 mg for 200 mL)
5. Place substrates in a crystallising dish then pour enough ODPA solution to cover the substrates
6. Cover the crystallising dish and let sit overnight
7. Remove substrates from solution, rinse thoroughly with IPA to remove the excess ODPA, dry with N_2
8. Bake the substrates at 80 °C for 10 minutes to align ODPA hydrophobic tails
9. Check successful ODPA deposition by running some water on the substrate: if the water rolls off the Al onto the substrate in the photolithography patterns, the ODPA is successfully deposited only on the Al, making it hydrophobic

10. Deposit 5 nm Al + 30 nm Au (without breaking vacuum in between) via thermal evaporation, both at 2 nm/s from Al wire and Au pellets or wire
11. Apply the sticky polymer to the substrates, let it dry ($\approx$ 30 min), then peel off polymer using tweezers or tape
12. Remove the SAM in the nanogap by oxygen plasma asher to empty the nanogap
13. Check successful ODPA removal by running some water on the substrate: the water should now cover homogeneously the entire substrate as it should no longer be hydrophobic

A.2 Probe station

The probe station is composed of a mobile sample holder, two probe micropositioners, and a microscope, all of which are placed on a vibration isolation table (see Figure A.1).

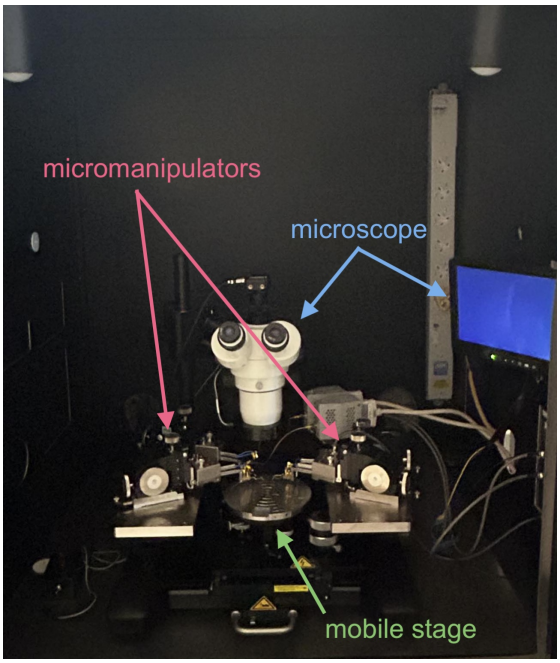

FIGURE A.1: Typical probe station setup.

The probes are two metal tips, both connected to a source measure unit (SMU), here a Keysight B1500A. Each tip is micropositioned on the tested device electrodes and is then connected via cable to the SMU anode and cathode, closing the electrical circuit.

Via software (EasyExpert), it is possible to modify parameters (voltage range, compliance, scan rate, ...), then run the experiment: a voltage range is swept, and the current is recorded.

A.3 AFM

Atomic Force Microscopy (AFM) traces the topography of samples with extremely high (up to atomic) resolution by recording the interaction forces between the sample surface and a sharp tip (the probe) mounted on a cantilever. As the probe approaches the surface, attractive forces between the surface and the probe cause the cantilever to deflect towards the surface. When the cantilever is brought closer to the surface, so that the probe makes contact with the surface, repulsive forces take over and cause the cantilever to deflect away from the surface. The cantilever deflections towards or away from the surface are detected by a laser beam, which reflects off the flat top of the cantilever. Therefore, any cantilever deflection will cause slight changes in the direction of the reflected beam. A position-sensitive detector (a photodiode) allows registering changes in the height (z-direction) due to the probe interactions with the surface. All these elements can be seen in Figure A.2.

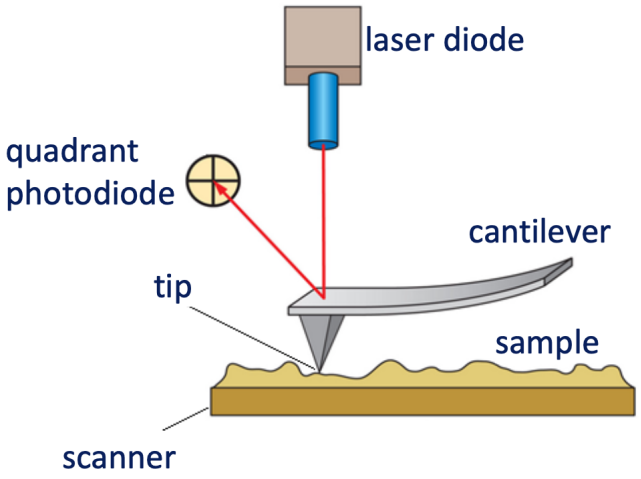

FIGURE A.2: Typical AFM setup.

The results obtained and presented in this thesis were obtained on Bruker Dimension Icon AFM, using their ScanAssist tapping mode. The images were processed and analysed with the open source Gwyddion software.

A.4 Stylus profilometer

The stylus consists of a probe (metal tip), which moves along a designated line (or area), recording the height profile (step size) of the sample. Similar to AFM, the height is recorded by detecting changes in a laser beam position, which reflects off a cantilever to which the probe is attached. The tool used throughout this work is the P16+ model from KLA Tencor.

Appendix B

Supporting Information for POM-Based Memory Devices

B.1 Additional film morphology characterisation

Throughout Chapter 5, I investigated different polyoxometalate (POM) candidates and deposition techniques in order to create my redox-based resistive memory devices (ReRAMs). In this supplementary section, I provide additional film morphology characterisation for the different POM candidates and deposition techniques.

Optical microscopy images were also taken for the POM films deposited on the ODPA-free, empty nanogap electrodes as shown in Figure B.1. The information they provide is quite similar to the SEM images which were presented in Section 5.1.1.

Finally, when comparing the different deposition techniques for $H_3PMo_{12}O_{40}$, optical microscopy images were presented (Section 5.2.1). SEM images, shown in Figure B.2, were also recorded, but did not provide much more additional information.

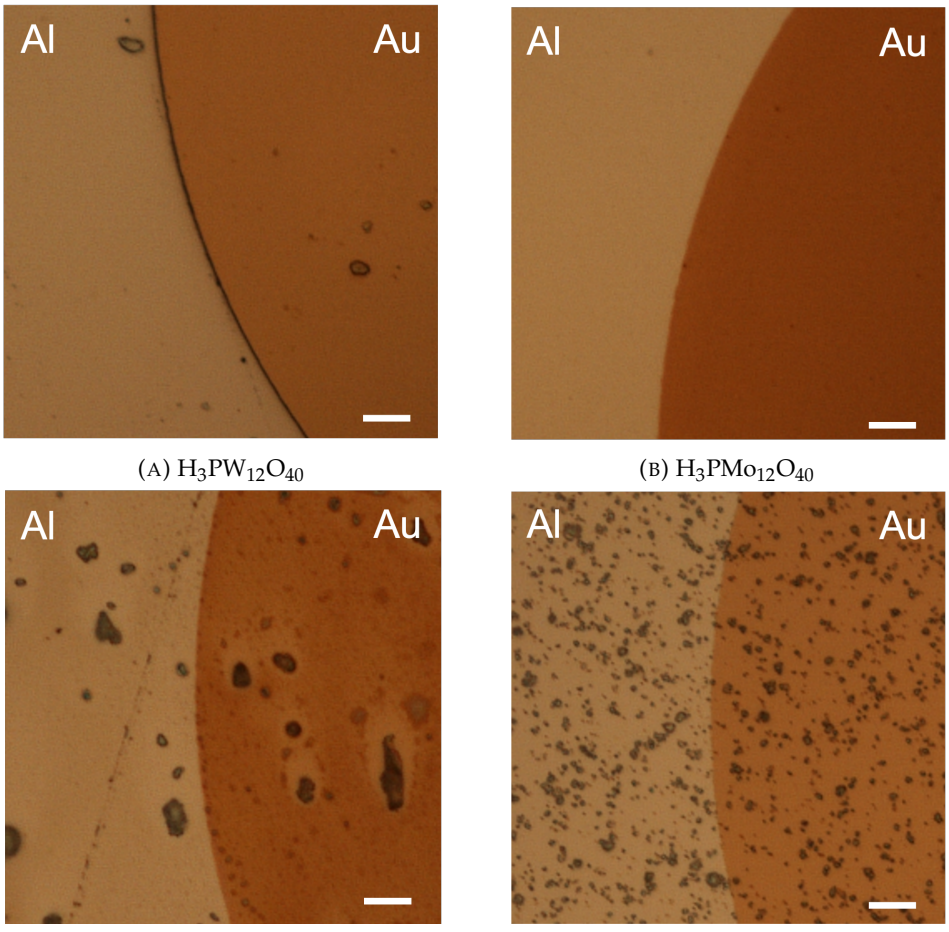

(A) $H_3PW_{12}O_{40}$ (B) $H_3PMo_{12}O_{40}$

(C) $Na_3PMo_{12}O_{40}$ (D) $(NH_4)_3PMo_{12}O_{40}$

FIGURE B.1: Comparing optical microscopy images of various POM film morphologies spin-coated onto ODPA-free nanogap electrodes.

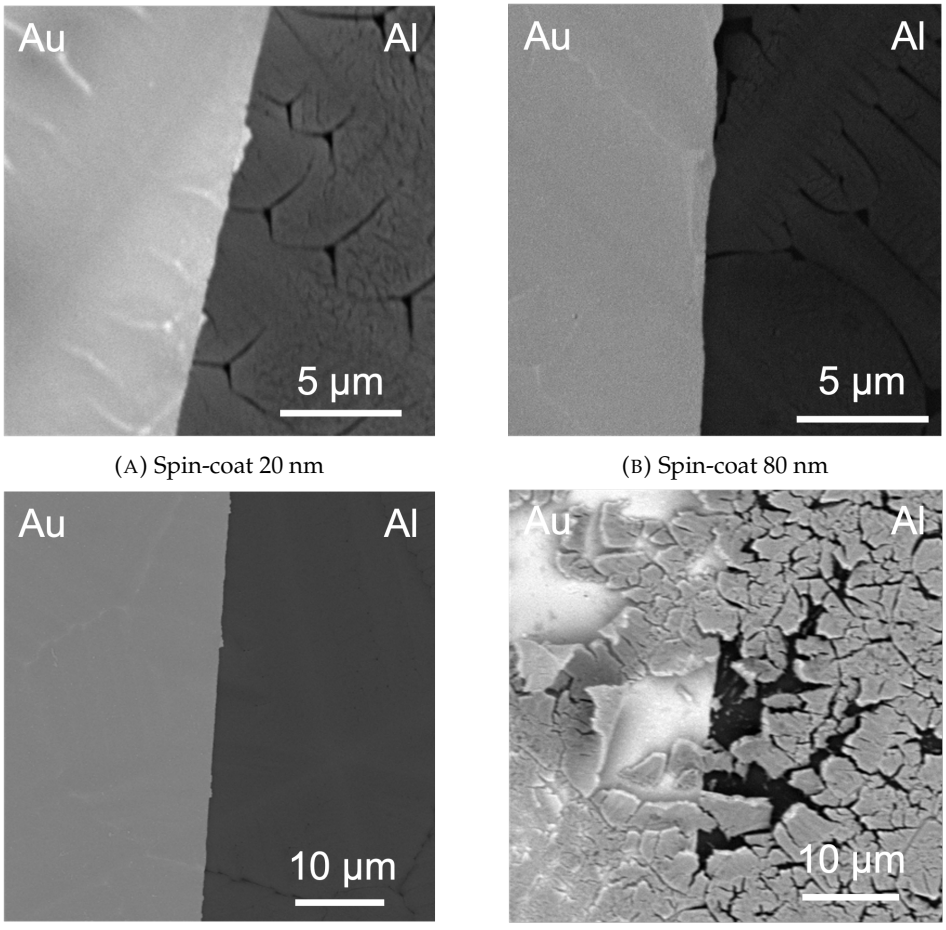

(A) Spin-coat 20 nm

(B) Spin-coat 80 nm

(C) Spin-coat 150 nm

(D) Drop-cast

FIGURE B.2: SEM images comparing the film morphologies of $H_3PMo_{12}O_{40}$ films deposited via different deposition techniques.

Appendix C

Supporting Information for Mechanism Investigation

C.1 Oxidation state of the SC 150 nm film

The same oxidation state study was done for the $H_3PMo_{12}O_{40}$ SC 150 nm films as with the DC films. First, I tested two different techniques to reduce the POM. The obtained results are shown in Figure C.1. Similarly to the DC samples, the absorbance at 900 nm for the illuminated sample always increases with exposure time. Additionally, the absorbance at 900 nm first increases then decreases for the annealed sample in the same manner as the DC sample. This indicates a reduction followed by re-oxidation that seems only possible with thermal treatment.

The second factor studied is the annealing temperature. The same process as with the DC films was done: 5 min annealing at 60, 100, and 150 °C and a reference measurement at room temperature. Figure C.2 shows the obtained results.

This time, a different response to that of the drop-cast sample is observed. For the spin-coat sample, the absorbance at 900 nm always increases with annealing temperature, the re-oxidation phase is not observed. Maybe less moisture is trapped, and therefore the counter-balance reactions can not occur.

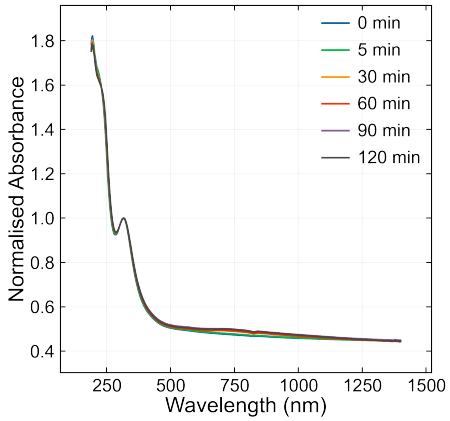

(A) UV/Vis spectra when illuminated at 254 nm.

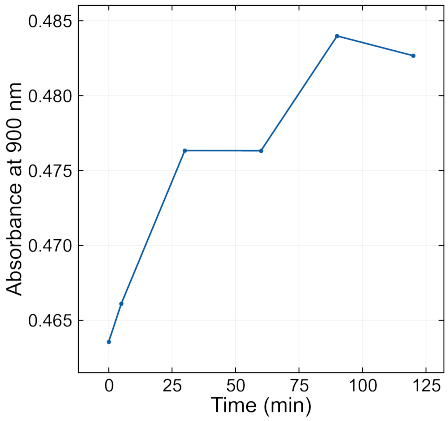

(B) Absorbance at 900 nm when illuminated at 254 nm.

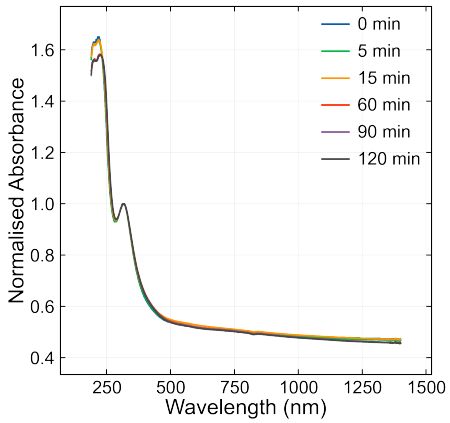

(C) UV/Vis spectra when heated at 60 °C.

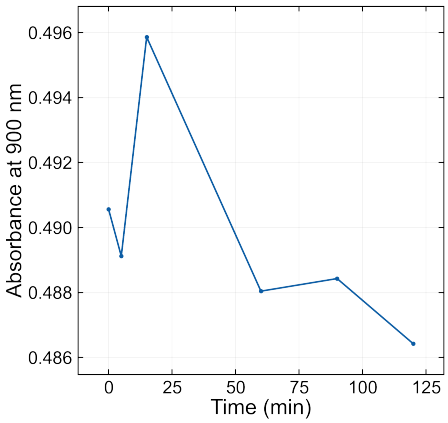

(D) Absorbance at 900 nm when heated at 60 °C.

FIGURE C.1: Comparing illumination (254 nm) and annealing (60 °C) techniques to control the reduction of a spin-coat $H_3PMo_{12}O_{40}$ film. The UV/Vis spectra are normalised at the Mo-O_b peak (316 nm).

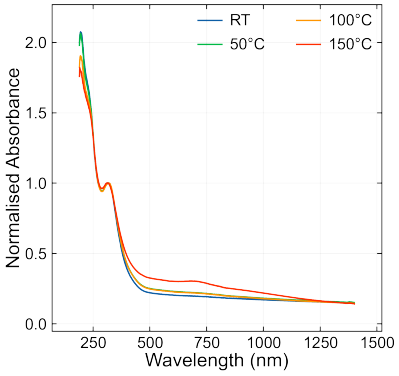

(A) UV/Vis spectra normalised at the Mo-O_t peak (196 nm).

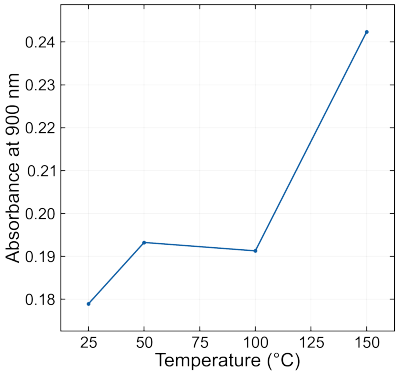

(B) Absorbance at 900 nm.

FIGURE C.2: Controling the reduction of a spin-coat $H_3PMo_{12}O_{40}$ film by 5 min annealing steps at increasing temperatures. The UV/Vis spectra are normalised at the Mo-O_b peak (316 nm).

C.2 Additional XPS depth profiles

Here I will present the results obtained for the other tested PMMA film thicknesses (28 and 48 nm). Figure C.3 shows the obtained relative atomic percentages of C, Mo, and Au throughout the films. Their response is quite similar to the 34 nm film: C crosses over Mo, but Mo never entirely disappears indicating the POM film penetrates the PMMA layer. The main difference comes with the etch time at which the Au atomic percentages cross over C. As expected, the Au is detected later when the PMMA film thickness increases.

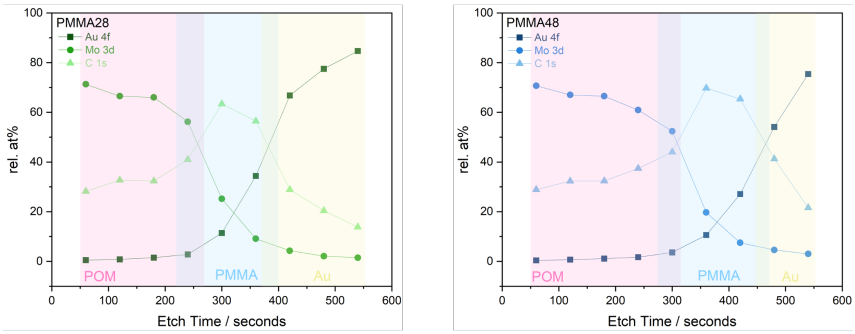

(A) 28 nm thick PMMA. (B) 48 nm thick PMMA.

FIGURE C.3: XPS depth profile of different thicknesses of spin-coat PMMA layers with the same spin-coat $H_3PMo_{12}O_{40}$ 150 nm film on 40 nm gold layer.

Phosphorus (P) relative atomic percentage was also measured for the 28 and 48 nm PMMA films as presented in Table C.1. The P content behaviour is similar to that of the 34 nm PMMA film: it does not perfectly match the Mo content. P is detected longer as the PMMA film thickness increases, suggesting that the POM distributes itself throughout the available PMMA volume.

TABLE C.1: Relative atomic percentage of molybdenum (Mo), phosphorus (P), gold (Au) throughout a spin-coat PMMA 28 and 48 nm + $H_3PMo_{12}O_{40}$ 150 nm film on 40 nm gold layer.

	PMMA 28 nm			**PMMA 48 nm**		
Etch time (s)	**Mo**	**P**	**Au**	**Mo**	**P**	**Au**
60	93.9	5.4	0.7	93.0	6.5	0.5
120	92.6	6.3	1.1	93.6	5.5	0.9
180	91.7	6.3	2.0	92.2	6.3	1.5
240	88.2	7.4	4.4	91.3	6.2	2.5
300	65.0	5.7	29.3	85.9	7.1	7.0
360	20.9	n.d.	79.1	60.8	6.7	32.5
420	6.0	n.d.	94.0	21.7	n.d.	78.3
480	2.6	n.d.	97.4	7.9	n.d.	92.1
540	1.7	n.d.	98.3	3.8	n.d.	96.2

C.3 Specific sandwich device configurations

Here, I show the I-V curves obtained for all the tested devices regardless of configuration. Indeed, most of the tested devices are shorted. Out of the total 154 tested devices, only 21 devices were not shorted.

TABLE C.2: All tested devices for each active layer configuration in sandwich devices.

Active layer	Al/...../Au	Au/...../Al
PMMA 28 nm	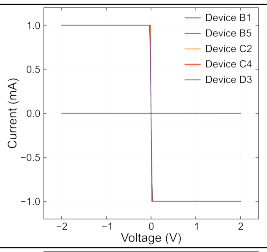	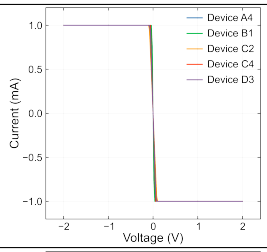
PMMA 28 nm + POM 150 nm	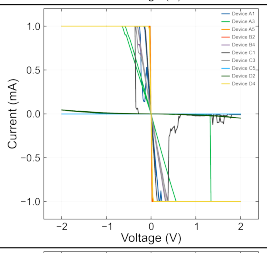	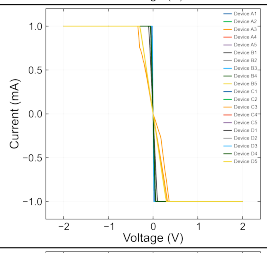
PMMA 34 nm	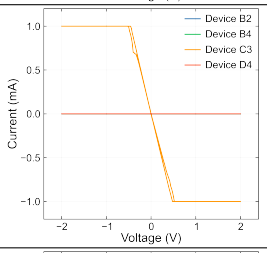	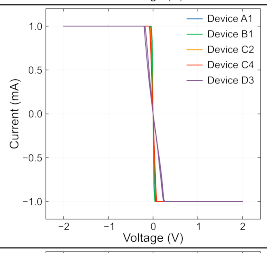
PMMA 34 nm + POM 150 nm	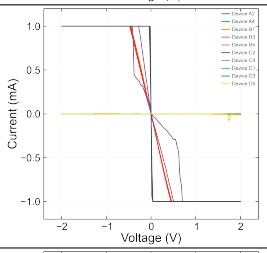	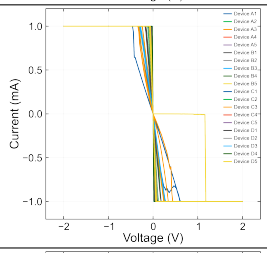
PMMA 48 nm	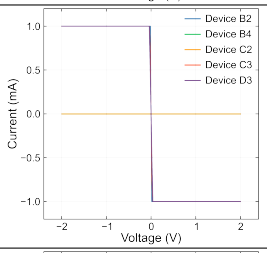	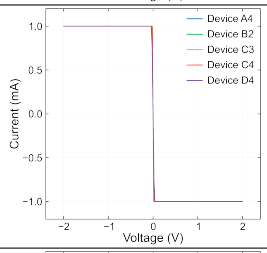
PMMA 48 nm + POM 150 nm	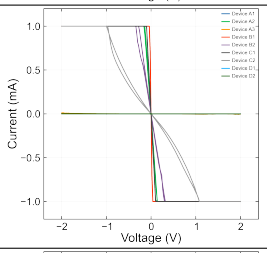	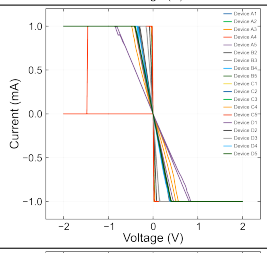
POM 150 nm	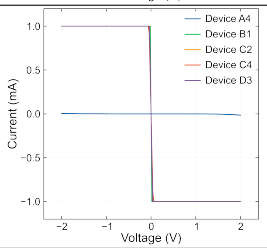	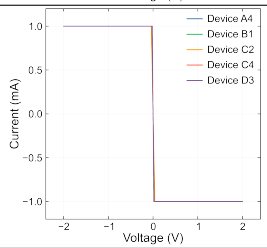

Appendix D

Supporting Information for Neuromorphic computing

D.1 Calculating rise and fall times

As a reminder, the rise and fall times are the total duration it takes for the signal to go from 10 % to 90 % of its final value. In Figure D.1, the blue curve is the raw data, the orange curve is the interpolation used to increase the data resolution. Again, only a maximum of 4000 data points could be collected regardless of the total input time. Therefore, the resolution for the longer pulses is less good. The green lines are the reference lines to show the initial and maximum current values, i.e. 0 and 100 %. The red lines represent the 10 and 90 % marker. The grey dashed lines show the intersection of data at 10 and 90 %, therefore the time between them is the rise or fall time.

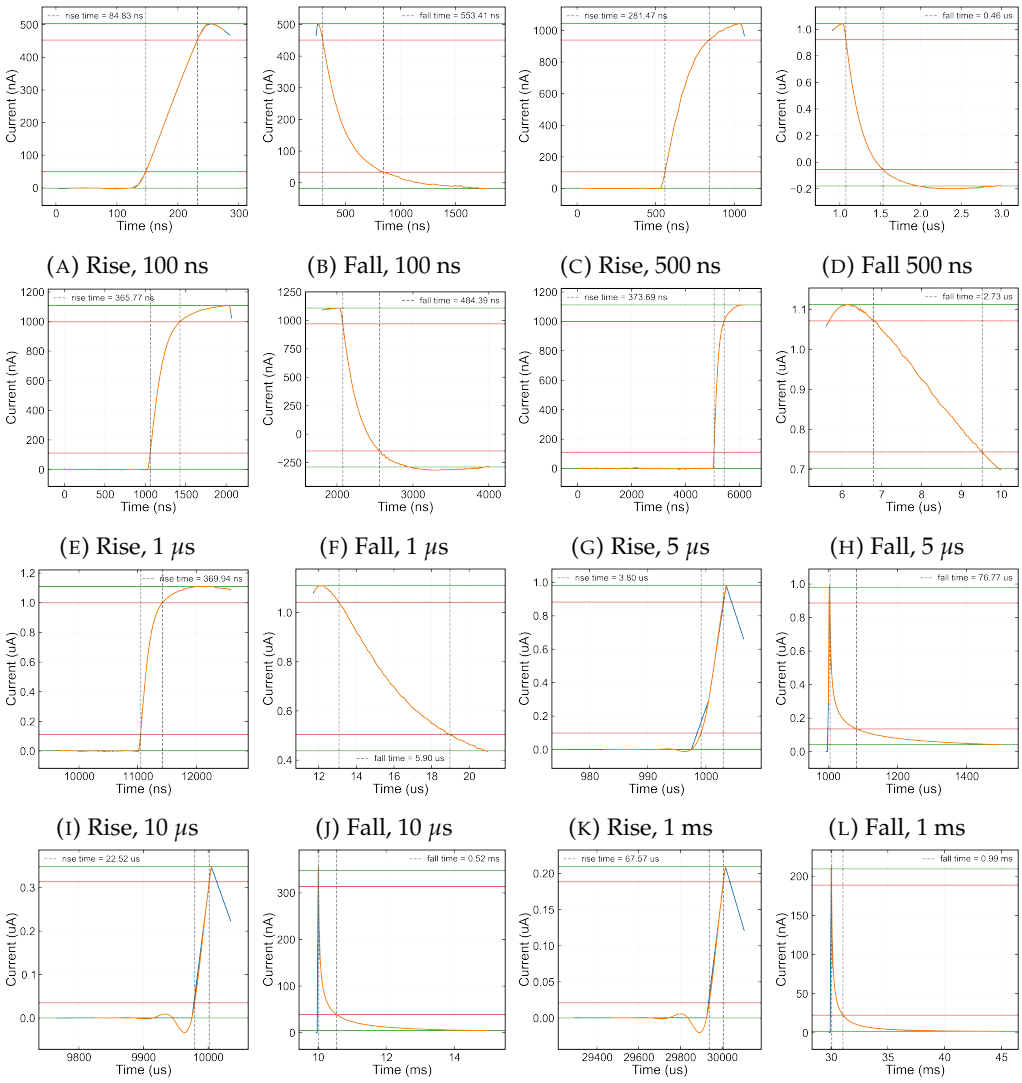

(A) Rise, 100 ns (B) Fall, 100 ns (C) Rise, 500 ns (D) Fall 500 ns

(E) Rise, 1 μs (F) Fall, 1 μs (G) Rise, 5 μs (H) Fall, 5 μs

(I) Rise, 10 μs (J) Fall, 10 μs (K) Rise, 1 ms (L) Fall, 1 ms

(M) Rise, 10 ms (N) Fall, 10 ms (O) Rise, 30 ms (P) Fall, 30 ms

FIGURE D.1: Rise and fall time calculations on + 0.3 V amplitude, various durations, 0 V read voltage single pulses.

References

[1] A. Redaelli and F. Pellizzer, Eds., *Semiconductor Memories and Systems*, ser. Woodhead Publishing Series In Electronic and Optical Materials. Cambridge, MA: Woodhead Publishing, 2022.

[2] IEEE International Roadmap for Devices and Systems, "Beyond CMOS and Emerging Materials Integration," 2023.

[3] H. Yang, G. Yue, T. Li, L. Du, H. Li, Z. Chen, and S. Zheng, "The Old Polyoxometalates in New Application as Molecular Resistive Switching Memristors," *European Journal of Inorganic Chemistry*, p. e202300264, Aug. 2023.

[4] J. Semple, D. G. Georgiadou, G. Wyatt-Moon, M. Yoon, A. Seitkhan, E. Yengel, S. Rossbauer, F. Bottacchi, M. A. McLachlan, D. D. C. Bradley, and T. D. Anthopoulos, "Large-area plastic nanogap electronics enabled by adhesion lithography," *npj Flexible Electronics*, vol. 2, no. 1, p. 18, Jun. 2018.

[5] G. E. Moore, "Cramming more components onto integrated circuits, reprinted from electronics, volume 38, number 8, april 19, 1965, pp.114 ff." *IEEE Solid-State Circuits Society Newsletter*, vol. 11, no. 3, pp. 33–35, 2006.

[6] M. A. Zidan, J. P. Strachan, and W. D. Lu, "The future of electronics based on memristive systems," *Nature Electronics*, vol. 1, no. 1, pp. 22–29, Jan. 2018.

[7] X. Zou, S. Xu, X. Chen, L. Yan, and Y. Han, "Breaking the von Neumann bottleneck: Architecture-level processing-in-memory technology," *Science China Information Sciences*, vol. 64, no. 6, p. 160404, Jun. 2021.

[8] P. Dimitrakis, I. Valov, and S. Tappertzhofen, Eds., *Metal Oxides for Non-Volatile Memory: Materials, Technology and Applications*, ser. Metal Oxides. Amsterdam: Elsevier, 2022.

[9] J. J. Yang, D. B. Strukov, and D. R. Stewart, "Memristive devices for computing," *Nature Nanotechnology*, vol. 8, no. 1, pp. 13–24, Jan. 2013.

[10] M. Lanza, A. Sebastian, W. D. Lu, M. Le Gallo, M.-F. Chang, D. Akinwande, F. M. Puglisi, H. N. Alshareef, M. Liu, and J. B. Roldan, "Memristive technologies for data storage, computation, encryption, and radio-frequency communication," *Science*, vol. 376, no. 6597, Jun. 2022.

[11] D. B. Strukov, G. S. Snider, D. R. Stewart, and R. S. Williams, "The missing memristor found," *Nature*, vol. 453, no. 7191, pp. 80–83, May 2008.

[12] L. Chua, "Everything You Wish to Know About Memristors But Are Afraid to Ask," *Radioengineering*, vol. 24, no. 2, pp. 319–368, Jun. 2015.

[13] B. Tellini, M. Bologna, K. J. Chandia, and M. Macucci, "Revisiting the Memristor Concept within Basic Circuit Theory," Feb. 2021.

[14] C. Baeumer, C. Schmitz, A. Marchewka, D. N. Mueller, R. Valenta, J. Hackl, N. Raab, S. P. Rogers, M. I. Khan, S. Nemsak, M. Shim, S. Menzel, C. M. Schneider, R. Waser, and R. Dittmann, "Quantifying redox-induced Schottky barrier variations in memristive devices via in operando spectromicroscopy with graphene electrodes," *Nature Communications*, vol. 7, no. 1, p. 12398, Aug. 2016.

[15] A. Pérez-Tomás, "Functional Oxides for Photoneuromorphic Engineering: Toward a Solar Brain," *Advanced Materials Interfaces*, vol. 6, no. 15, p. 1900471, Aug. 2019.

[16] A. C. Torrezan, J. P. Strachan, G. Medeiros-Ribeiro, and R. S. Williams, "Sub-nanosecond switching of a tantalum oxide memristor," *Nanotechnology*, vol. 22, no. 48, p. 485203, Nov. 2011.

[17] Y. Li, Z. Wang, C. Zhang, P. Gu, W. Chen, H. Li, J. Lu, and Q. Zhang, "Thiadizoloquinoxaline-Based N-Heteroacenes as Active Elements for High-Density Data-Storage Device," *ACS Applied Materials & Interfaces*, vol. 10, no. 18, pp. 15 971–15 979, May 2018.

[18] K. Terabe, T. Hasegawa, T. Nakayama, and M. Aono, "Quantized conductance atomic switch," *Nature*, vol. 433, no. 7021, pp. 47–50, Jan. 2005.

[19] A. Aviram and M. A. Ratner, "Molecular rectifiers," *Chemical Physics Letters*, vol. 29, no. 2, pp. 277–283, Nov. 1974.

[20] D. Bray, "Protein molecules as computational elements in living cells," *Nature*, vol. 376, no. 6538, pp. 307–312, Jul. 1995.

[21] C. Li, W. Fan, B. Lei, D. Zhang, S. Han, T. Tang, X. Liu, Z. Liu, S. Asano, M. Meyyappan, J. Han, and C. Zhou, "Multilevel memory based on molecular devices," *Applied Physics Letters*, vol. 84, no. 11, pp. 1949–1951, Mar. 2004.

[22] T. He, J. He, M. Lu, B. Chen, H. Pang, W. F. Reus, W. M. Nolte, D. P. Nackashi, P. D. Franzon, and J. M. Tour, "Controlled Modulation of Conductance in Silicon Devices by Molecular Monolayers," *Journal of the American Chemical Society*, vol. 128, no. 45, pp. 14 537–14 541, Nov. 2006.

[23] T. He, H. Ding, N. Peor, M. Lu, D. A. Corley, B. Chen, Y. Ofir, Y. Gao, S. Yitzchaik, and J. M. Tour, "Silicon/Molecule Interfacial Electronic Modifications," *Journal of the American Chemical Society*, vol. 130, no. 5, pp. 1699–1710, Feb. 2008.

[24] J. Chen, J. Su, W. Wang, and M. Reed, "Electronic memory effects in self-assembled monolayer systems," *Physica E: Low-dimensional Systems and Nanostructures*, vol. 16, no. 1, pp. 17–23, Jan. 2003.

[25] I. Valov, "Redox-Based Resistive Switching Memories (ReRAMs): Electrochemical Systems at the Atomic Scale," *ChemElectroChem*, vol. 1, no. 1, pp. 26–36, Jan. 2014.

[26] R. Waser, R. Dittmann, G. Staikov, and K. Szot, "Redox-Based Resistive Switching Memories – Nanoionic Mechanisms, Prospects, and Challenges," *Advanced Materials*, vol. 21, no. 25-26, pp. 2632–2663, Jul. 2009.

[27] I. Valov, M. Luebben, A. Wedig, and R. Waser, "(Invited) Mobile Ions, Transport and Redox Processes in Memristive Devices," *ECS Transactions*, vol. 75, no. 5, pp. 27–39, Aug. 2016.

[28] C. Bengel, S. Wiefels, V. Rana, H.-Y. Chen, Q.-T. Zhao, R. Waser, H. Padberg, F. Xi, and S. Menzel, "Experimental and Theoretical Analysis of Stateful Logic in Passive and Active Crossbar Arrays for Computation-in-Memory," in *2022 IEEE International Symposium on Circuits and Systems (ISCAS)*. Austin, TX, USA: IEEE, May 2022, pp. 2792–2796.

[29] M. A. Zidan, H. A. H. Fahmy, M. M. Hussain, and K. N. Salama, "Memristor-based memory: The sneak paths problem and solutions," *Microelectronics Journal*, vol. 44, no. 2, pp. 176–183, Feb. 2013.

[30] J. Millman and H. Taub, *Pulse, Digital, And Switching Waveforms Devices and Circuits for Their Generation and Processing*. McGraw-Hill International Book Company, 1965.

[31] M. Lanza, R. Waser, D. Ielmini, J. J. Yang, L. Goux, J. Suñe, A. J. Kenyon, A. Mehonic, S. Spiga, V. Rana, S. Wiefels, S. Menzel, I. Valov, M. A. Villena, E. Miranda, X. Jing, F. Campabadal, M. B. Gonzalez, F. Aguirre, F. Palumbo, K. Zhu, J. B. Roldan, F. M. Puglisi, L. Larcher, T.-H. Hou, T. Prodromakis, Y. Yang, P. Huang, T. Wan, Y. Chai, K. L. Pey, N. Raghavan, S. Dueñas, T. Wang, Q. Xia, and S. Pazos, "Standards for the Characterization of Endurance in Resistive Switching Devices," *ACS Nano*, vol. 15, no. 11, pp. 17 214–17 231, Nov. 2021.

[32] T. Li, V. K. Bandari, and O. G. Schmidt, "Molecular Electronics: Creating and Bridging Molecular Junctions and Promoting Its Commercialization," *Advanced Materials*, p. 2209088, Apr. 2023.

[33] D. J. Beesley, J. Semple, L. Krishnan Jagadamma, A. Amassian, M. A. McLachlan, T. D. Anthopoulos, and J. C. deMello, "Sub-15-nm patterning of asymmetric metal electrodes and devices by adhesion lithography," *Nature Communications*, vol. 5, no. 1, p. 3933, Sep. 2014.

[34] M. T. Pope, *Heteropoly and Isopoly Oxometalates*, ser. Inorganic Chemistry Concepts, C. K. Jørgensen, M. F. Lappert, S. J. Lippard, J. L. Margrave, K. Niedenzu, H. Nöth, R. W. Parry, and H. Yamatera, Eds. Berlin, Heidelberg: Springer Berlin Heidelberg, 1983, vol. 8.

[35] T. Ueda, "Electrochemistry of Polyoxometalates: From Fundamental Aspects to Applications," *ChemElectroChem*, vol. 5, no. 6, pp. 823–838, Mar. 2018.

[36] J. Ding, D. Mu, O. Badami, C. Medina-Bailon, X. Chang, D. Nagy, P. Lapham, V. Georgiev, and A. Asenov, "KMC-based POM flash cell optimization and time-dependent performance investigation," *Semiconductor Science and Technology*, vol. 36, no. 7, p. 075021, Jul. 2021.

[37] O. Linnenberg, M. Moors, A. Notario-Estévez, X. López, C. de Graaf, S. Peter, C. Baeumer, R. Waser, and K. Y. Monakhov, "Addressing Multiple Resistive States of Polyoxovanadates: Conductivity as a Function of Individual Molecular Redox States," *Journal of the American Chemical Society*, vol. 140, no. 48, pp. 16 635–16 640, Dec. 2018.

[38] M. Glöß, R. Pütt, M. Moors, E. Kentzinger, S. Karthäuser, and K. Y. Monakhov, "Exploring the Ligand Functionality, Electronic Band Gaps, and Switching Characteristics of Single Wells–Dawson-Type Polyoxometalates on Gold," *Advanced Materials Interfaces*, vol. 9, no. 21, p. 2200461, Jul. 2022.

[39] J. F. Gonzalez, V. Montigaud, V. Dorcet, K. Bernot, B. L. Guennic, F. Pointillart, and O. Cador, "Solvato Modulation of the Magnetic Memory in Isotopically Enriched Erbium Polyoxometalate," *Chemistry - A European Journal*, p. 10, 2021.

[40] P. Stoliar, P. Levy, M. J. Sanchez, A. G. Leyva, C. A. Albornoz, F. Gomez-Marlasca, A. Zanini, C. Toro Salazar, N. Ghenzi, and M. J. Rozenberg, "Nonvolatile Multilevel Resistive Switching Memory Cell: A Transition Metal Oxide-Based Circuit," *IEEE Transactions on Circuits and Systems II: Express Briefs*, vol. 61, no. 1, pp. 21–25, Jan. 2014.

[41] P. Cannon, "The solubility of molybdenum trioxide in various mineral acids," *Journal of Inorganic and Nuclear Chemistry*, vol. 11, no. 2, pp. 124–127, Sep. 1959.

[42] X. Chen, Y. Zhou, V. A. L. Roy, and S.-T. Han, "Evolutionary Metal Oxide Clusters for Novel Applications: Toward High-Density Data Storage in Nonvolatile Memories," *Advanced Materials*, vol. 30, no. 3, p. 1703950, Jan. 2018.

[43] C. Busche, L. Vilà-Nadal, J. Yan, H. N. Miras, D.-L. Long, V. P. Georgiev, A. Asenov, R. H. Pedersen, N. Gadegaard, M. M. Mirza, D. J. Paul, J. M. Poblet, and L. Cronin, "Design and fabrication of memory devices based on nanoscale polyoxometalate clusters," *Nature*, vol. 515, no. 7528, pp. 545–549, Nov. 2014.

[44] S. Fujimoto, J. M. Cameron, R.-J. Wei, K. Kastner, D. Robinson, V. Sans, G. N. Newton, and H. Oshio, "A Simple Approach to the Visible-Light Photoactivation of Molecular Metal Oxides," *Inorganic Chemistry*, vol. 56, no. 20, pp. 12 169–12 177, Oct. 2017.

[45] J. M. Cameron, D. J. Wales, and G. N. Newton, "Shining a light on the photosensitisation of organic–inorganic hybrid polyoxometalates," *Dalton Transactions*, vol. 47, no. 15, pp. 5120–5136, 2018.

[46] S. Song, J. Kim, S. M. Kwon, J.-W. Jo, S. K. Park, and Y.-H. Kim, "Recent Progress of Optoelectronic and All-Optical Neuromorphic Devices: A Comprehensive Review of Device Structures, Materials, and Applications," *Advanced Intelligent Systems*, vol. 3, no. 4, p. 2000119, Apr. 2021.

[47] J. Yang, T. Wang, Y. Wang, and H. Li, "Reversible photoluminescence switching in supramolecular ultrathin films architecture," *Dyes and Pigments*, vol. 149, pp. 902–907, Feb. 2018.

[48] D. Chong, X. Wan, and J. Zhang, "Charge-transfer complexes of dinuclear ruthenium compounds/polyoxometalates for multistate electrochromism covering ultraviolet, visible, and near-infrared region," *Journal of Materials Chemistry C*, vol. 5, no. 26, pp. 6442–6449, 2017.

[49] B. Bao, J. Fan, W. Wang, and D. Yu, "Novel linen/polyethyleneimine/sodium decadecanate photochromic fabric prepared by layer-by-layer self-assembly method," *Cellulose*, vol. 27, no. 11, pp. 6591–6602, Jul. 2020.

[50] J. Zhang, S. Dai, Y. Zhao, J. Zhang, and J. Huang, "Recent Progress in Photonic Synapses for Neuromorphic Systems," *Advanced Intelligent Systems*, vol. 2, no. 3, p. 1900136, Mar. 2020.

[51] D. Liu, L. Yuan, Y. Jin, H. Wu, Y. Lv, G. Xiong, G. Ju, L. Chen, S. Yang, and Y. Hu, "Tailoring Multidimensional Traps for Rewritable Multilevel Optical Data Storage," *ACS Applied Materials & Interfaces*, vol. 11, no. 38, pp. 35 023–35 029, Sep. 2019.

[52] K. Chen, H. Hu, I. Song, H. B. Gobeze, W.-J. Lee, A. Abtahi, K. S. Schanze, and J. Mei, "Organic optoelectronic synapse based on photon-modulated electrochemical doping," *Nature Photonics*, vol. 17, no. 7, pp. 629–637, Jul. 2023.

[53] X. Chen, P. Huang, X. Zhu, S. Zhuang, H. Zhu, J. Fu, A. S. Nissimagoudar, W. Li, X. Zhang, L. Zhou, Y. Wang, Z. Lv, Y. Zhou, and S.-T. Han, "Keggin-type polyoxometalate cluster as an active component for redox-based nonvolatile memory," *Nanoscale Horizons*, vol. 4, no. 3, pp. 697–704, 2019.

[54] S. Slesazeck and T. Mikolajick, "Nanoscale resistive switching memory devices: A review," *Nanotechnology*, vol. 30, no. 35, p. 352003, Aug. 2019.

[55] P. W. Atkins, L. Jones, and L. E. Laverman, *Chemical Principles: The Quest for Insight*, 6th ed. New York, NY: Freeman, 2013.

[56] F. Miao, J. Joshua Yang, J. Borghetti, G. Medeiros-Ribeiro, and R. Stanley Williams, "Observation of two resistance switching modes in TiO_2 memristive devices electroformed at low current," *Nanotechnology*, vol. 22, no. 25, p. 254007, Jun. 2011.

[57] S. Chen and I. Valov, "Design of Materials Configuration for Optimizing Redox-Based Resistive Switching Memories," *Advanced Materials*, vol. 34, no. 3, p. 2105022, Jan. 2022.

[58] R. Waser and M. Aono, "Nanoionics-based resistive switching memories," *Nature Materials*, vol. 6, no. 11, pp. 833–840, Nov. 2007.

[59] S. Tappertzhofen, H. Mündelein, I. Valov, and R. Waser, "Nanoionic transport and electrochemical reactions in resistively switching silicon dioxide," *Nanoscale*, vol. 4, no. 10, p. 3040, 2012.

[60] R. Waser, "Redox-Based Resistive Switching Memories," *Journal of Nanoscience and Nanotechnology*, vol. 12, no. 10, pp. 7628–7640, Oct. 2012.

[61] U. Russo, D. Ielmini, C. Cagli, A. L. Lacaita, S. Spiga, C. Wiemer, M. Perego, and M. Fanciulli, "Conductive-filament switching analysis and self-accelerated thermal dissolution model for reset in NiO-based RRAM," in *2007 IEEE International Electron Devices Meeting*. Washington, DC, USA: IEEE, 2007, pp. 775–778.

[62] G. Milano, M. Aono, L. Boarino, U. Celano, T. Hasegawa, M. Kozicki, S. Majumdar, M. Menghini, E. Miranda, C. Ricciardi, S. Tappertzhofen, K. Terabe, and I. Valov, "Quantum Conductance in Memristive Devices: Fundamentals, Developments, and Applications," *Advanced Materials*, vol. 34, no. 32, p. 2201248, Aug. 2022.

[63] R. Waser, Ed., *Nanoelectronics and Information Technology: Advanced Electronic Materials and Novel Devices*, 3rd ed. Weinheim: Wiley-VCH, 2012.

[64] T. Tsuruoka, K. Terabe, T. Hasegawa, I. Valov, R. Waser, and M. Aono, "Effects of Moisture on the Switching Characteristics of Oxide-Based, Gapless-Type Atomic Switches," *Advanced Functional Materials*, vol. 22, no. 1, pp. 70–77, Jan. 2012.

[65] T. Tsuruoka, I. Valov, C. Mannequin, T. Hasegawa, R. Waser, and M. Aono, "Humidity effects on the redox reactions and ionic transport in a $Cu/Ta_2O_5/Pt$ atomic switch structure," *Japanese Journal of Applied Physics*, vol. 55, no. 6S1, Jun. 2016.

[66] M. Lübben, S. Wiefels, R. Waser, and I. Valov, "Processes and Effects of Oxygen and Moisture in Resistively Switching TaO_x and HfO_x," *Advanced Electronic Materials*, vol. 4, no. 1, p. 1700458, Jan. 2018.

[67] A. Herpers, C. Lenser, C. Park, F. Offi, F. Borgatti, G. Panaccione, S. Menzel, R. Waser, and R. Dittmann, "Spectroscopic Proof of the Correlation between Redox-State and Charge-Carrier Transport at the Interface of Resistively Switching Ti/PCMO Devices," *Advanced Materials*, vol. 26, no. 17, pp. 2730–2735, May 2014.

[68] F. Mei, H. Shen, Y. Li, L. Li, G. Zang, M. Zhou, R. Ti, D. Yang, F. Huang, X. Lu, and J. Zhu, "Combination of conductive filaments and Schottky behavior in multifunctional $Sn_{1-x}Cu_xO_{2-\delta}$ memristor," *Applied Physics Letters*, vol. 111, no. 14, p. 143503, Oct. 2017.

[69] F. Borgatti, C. Park, A. Herpers, F. Offi, R. Egoavil, Y. Yamashita, A. Yang, M. Kobata, K. Kobayashi, J. Verbeeck, G. Panaccione, and R. Dittmann, "Chemical insight into electroforming of resistive switching manganite heterostructures," *Nanoscale*, vol. 5, no. 9, p. 3954, 2013.

[70] W. Sun, B. Gao, M. Chi, Q. Xia, J. J. Yang, H. Qian, and H. Wu, "Understanding memristive switching via in situ characterization and device modeling," *Nature Communications*, vol. 10, no. 1, p. 3453, Aug. 2019.

[71] L. Zheng, B. Sun, Y. Chen, T. Li, S. Mao, S. Zhu, H. Wang, Y. Zhang, M. Lei, and Y. Zhao, "The redox of hydroxyl-assisted metallic filament induced resistive switching memory based on a biomaterial-constructed sustainable and environment-friendly device," *Materials Today Chemistry*, vol. 10, pp. 167–174, Dec. 2018.

[72] I. Valov and T. Tsuruoka, "Effects of moisture and redox reactions in VCM and ECM resistive switching memories," *Journal of Physics D: Applied Physics*, vol. 51, no. 41, p. 413001, Oct. 2018.

[73] G. Milano, M. Luebben, M. Laurenti, S. Porro, K. Bejtka, S. Bianco, U. Breuer, L. Boarino, I. Valov, and C. Ricciardi, "Ionic Modulation of Electrical Conductivity of ZnO Due to Ambient Moisture," *Advanced Materials Interfaces*, vol. 6, no. 17, p. 1900803, Sep. 2019.

[74] K. Krishnan, A. Gubicza, M. Aono, K. Terabe, I. Valov, and T. Tsuruoka, "Impact of moisture absorption on the resistive switching characteristics of a polyethylene oxide-based atomic switch," *Journal of Materials Chemistry C*, vol. 9, no. 34, pp. 11 198–11 206, 2021.

[75] G. Milano, F. Raffone, M. Luebben, L. Boarino, G. Cicero, I. Valov, and C. Ricciardi, "Water-Mediated Ionic Migration in Memristive Nanowires with a Tunable Resistive Switching Mechanism," *ACS Applied Materials & Interfaces*, vol. 12, no. 43, pp. 48 773–48 780, Oct. 2020.

[76] G. Milano, M. Luebben, M. Laurenti, L. Boarino, C. Ricciardi, and I. Valov, "Structure-Dependent Influence of Moisture on Resistive Switching Behavior of ZnO Thin Films," *Advanced Materials Interfaces*, vol. 8, no. 16, p. 2100915, Aug. 2021.

[77] S. Tappertzhofen, I. Valov, T. Tsuruoka, T. Hasegawa, R. Waser, and M. Aono, "Generic Relevance of Counter Charges for Cation-Based Nanoscale Resistive Switching Memories," *ACS Nano*, vol. 7, no. 7, pp. 6396–6402, Jul. 2013.

[78] R. Dittmann and J. P. Strachan, "Redox-based memristive devices for new computing paradigm," *APL Materials*, vol. 7, no. 11, p. 110903, Nov. 2019.

[79] B. Zhang, W. Chen, J. Zeng, F. Fan, J. Gu, X. Chen, L. Yan, G. Xie, S. Liu, Q. Yan, S. J. Baik, Z.-G. Zhang, W. Chen, J. Hou, M. E. El-Khouly, Z. Zhang, G. Liu, and Y. Chen, "90% yield production of polymer nano-memristor for in-memory computing," *Nature Communications*, vol. 12, no. 1, p. 1984, Mar. 2021.

[80] A. Aviram, "Molecules for memory, logic, and amplification," *Journal of the American Chemical Society*, vol. 110, no. 17, pp. 5687–5692, Aug. 1988.

[81] B. Daly, T. S. Moody, A. J. M. Huxley, C. Yao, B. Schazmann, A. Alves-Areias, J. F. Malone, H. Q. N. Gunaratne, P. Nockemann, and A. P. De Silva, "Molecular memory with downstream logic processing exemplified by switchable and self-indicating guest capture and release," *Nature Communications*, vol. 10, no. 1, p. 49, Jan. 2019.

[82] A. Siemon, T. Breuer, N. Aslam, S. Ferch, W. Kim, J. Van Den Hurk, V. Rana, S. Hoffmann-Eifert, R. Waser, S. Menzel, and E. Linn, "Realization of Boolean Logic Functionality Using Redox-Based Memristive Devices," *Advanced Functional Materials*, vol. 25, no. 40, pp. 6414–6423, Oct. 2015.

[83] D. Ielmini and H.-S. P. Wong, "In-memory computing with resistive switching devices," *Nature Electronics*, vol. 1, no. 6, pp. 333–343, Jun. 2018.

[84] B. Zhang, F. Fan, W. Xue, G. Liu, Y. Fu, X. Zhuang, X.-H. Xu, J. Gu, R.-W. Li, and Y. Chen, "Redox gated polymer memristive processing memory unit," *Nature Communications*, vol. 10, no. 1, p. 736, Feb. 2019.

[85] G. Cauwenberghs, "Reverse engineering the cognitive brain," *Proceedings of the National Academy of Sciences*, vol. 110, no. 39, pp. 15 512–15 513, Sep. 2013.

[86] Y. Lee and T.-W. Lee, "Organic Synapses for Neuromorphic Electronics: From Brain-Inspired Computing to Sensorimotor Nervetronics," *Accounts of Chemical Research*, vol. 52, no. 4, pp. 964–974, Apr. 2019.

[87] H. Seok, D. Lee, S. Son, H. Choi, G. Kim, and T. Kim, "Beyond von Neumann Architecture: Brain-Inspired Artificial Neuromorphic Devices and Integrated Computing," *Advanced Electronic Materials*, p. 2300839, Apr. 2024.

[88] L. Zhao, Z. Fan, S. Cheng, L. Hong, Y. Li, G. Tian, D. Chen, Z. Hou, M. Qin, M. Zeng, X. Lu, G. Zhou, X. Gao, and J.-M. Liu, "An Artificial Optoelectronic Synapse Based on a Photoelectric Memcapacitor," *Advanced Electronic Materials*, vol. 6, no. 2, p. 1900858, Feb. 2020.

[89] J. Zhu, T. Zhang, Y. Yang, and R. Huang, "A comprehensive review on emerging artificial neuromorphic devices," *Applied Physics Reviews*, vol. 7, no. 1, p. 011312, Mar. 2020.

[90] G. Zhou, Z. Wang, B. Sun, F. Zhou, L. Sun, H. Zhao, X. Hu, X. Peng, J. Yan, H. Wang, W. Wang, J. Li, B. Yan, D. Kuang, Y. Wang, L. Wang, and S. Duan, "Volatile and Nonvolatile Memristive Devices for Neuromorphic Computing," *Advanced Electronic Materials*, vol. 8, no. 7, p. 2101127, Jul. 2022.

[91] W. Xu, S.-Y. Min, H. Hwang, and T.-W. Lee, "Organic core-sheath nanowire artificial synapses with femtojoule energy consumption," *Science Advances*, vol. 2, no. 6, p. e1501326, Jun. 2016.

[92] A. E. Pereda, "Electrical synapses and their functional interactions with chemical synapses," *Nature Reviews Neuroscience*, vol. 15, no. 4, pp. 250–263, Apr. 2014.

[93] G. J. Tortora and B. Derrickson, *Introduction to the Human Body, the Essentials of Anatomy and Physiology*, 8th ed. John Wiley & Sons, 2012.

[94] S. Masoli and E. D'Angelo, "Synaptic Activation of a Detailed Purkinje Cell Model Predicts Voltage-Dependent Control of Burst-Pause Responses in Active Dendrites," *Frontiers in Cellular Neuroscience*, vol. 11, p. 278, Sep. 2017.

[95] Z. Wang, S. Joshi, S. E. Savel'ev, H. Jiang, R. Midya, P. Lin, M. Hu, N. Ge, J. P. Strachan, Z. Li, Q. Wu, M. Barnell, G.-L. Li, H. L. Xin, R. S. Williams, Q. Xia, and J. J. Yang, "Memristors with diffusive dynamics as synaptic emulators for neuromorphic computing," *Nature Materials*, vol. 16, no. 1, pp. 101–108, Jan. 2017.

[96] N. Cowan, "Chapter 20 What are the differences between long-term, short-term, and working memory?" in *Progress in Brain Research*. Elsevier, 2008, vol. 169, pp. 323–338.

[97] H.-L. Park, Y. Lee, N. Kim, D.-G. Seo, G.-T. Go, and T.-W. Lee, "Flexible Neuromorphic Electronics for Computing, Soft Robotics, and Neuroprosthetics," *Advanced Materials*, vol. 32, no. 15, p. 1903558, Apr. 2020.

[98] M. Häusser, "The Hodgkin-Huxley theory of the action potential," *Nature Neuroscience*, vol. 3, no. S11, pp. 1165–1165, Nov. 2000.

[99] A. L. Hodgkin and A. F. Huxley, "A quantitative description of membrane current and its application to conduction and excitation in nerve," *The Journal of Physiology*, vol. 117, no. 4, pp. 500–544, Aug. 1952.

[100] M. D. Pickett, G. Medeiros-Ribeiro, and R. S. Williams, "A scalable neuristor built with Mott memristors," *Nature Materials*, vol. 12, no. 2, pp. 114–117, Feb. 2013.

[101] K. Portner, M. Schmuck, P. Lehmann, C. Weilenmann, C. Haffner, P. Ma, J. Leuthold, M. Luisier, and A. Emboras, "Analog Nanoscale Electro-Optical Synapses for Neuromorphic Computing Applications," *ACS Nano*, vol. 15, no. 9, pp. 14 776–14 785, Sep. 2021.

[102] Y. van de Burgt, A. Melianas, S. T. Keene, G. Malliaras, and A. Salleo, "Organic electronics for neuromorphic computing," *Nature Electronics*, vol. 1, no. 7, pp. 386–397, Jul. 2018.

[103] X. Chen, J. Pan, J. Fu, X. Zhu, C. Zhang, L. Zhou, Y. Wang, Z. Lv, Y. Zhou, and S.-T. Han, "Polyoxometalates-Modulated Reduced Graphene Oxide Flash Memory with Ambipolar Trapping as Bidirectional Artificial Synapse," *Advanced Electronic Materials*, vol. 4, no. 12, p. 1800444, Dec. 2018.

[104] J. Sandkühler, "Models and Mechanisms of Hyperalgesia and Allodynia," *Physiological Reviews*, vol. 89, no. 2, pp. 707–758, Apr. 2009.

[105] R. A. John, N. Yantara, S. E. Ng, M. I. B. Patdillah, M. R. Kulkarni, N. F. Jamaludin, J. Basu, Ankit, S. G. Mhaisalkar, A. Basu, and N. Mathews, "Diffusive and Drift Halide Perovskite Memristive Barristors as Nociceptive and Synaptic Emulators for Neuromorphic Computing," *Advanced Materials*, vol. 33, no. 15, p. 2007851, Apr. 2021.

[106] J. H. Yoon, Z. Wang, K. M. Kim, H. Wu, V. Ravichandran, Q. Xia, C. S. Hwang, and J. J. Yang, "An artificial nociceptor based on a diffusive memristor," *Nature Communications*, vol. 9, no. 1, p. 417, Jan. 2018.

[107] S. Stathopoulos, L. Michalas, A. Khiat, A. Serb, and T. Prodromakis, "An Electrical Characterisation Methodology for Benchmarking Memristive Device Technologies," *Scientific Reports*, vol. 9, no. 1, p. 19412, Dec. 2019.

[108] L. Brackmann, A. Jafari, C. Bengel, M. Mayahinia, R. Waser, D. Wouters, S. Menzel, and M. Tahoori, "A failure analysis framework of ReRAM In-Memory Logic operations," in *2022 IEEE International Test Conference in Asia (ITC-Asia)*. Taipei, Taiwan: IEEE, Aug. 2022, pp. 67–72.

[109] U. Kortz, A. Müller, J. Van Slageren, J. Schnack, N. S. Dalal, and M. Dressel, "Polyoxometalates: Fascinating structures, unique magnetic properties," *Coordination Chemistry Reviews*, vol. 253, no. 19-20, pp. 2315–2327, Oct. 2009.

[110] M. T. Pope, *Introduction to Polyoxometalate Chemistry*. Dordrecht: Springer Netherlands, 2003, pp. 3–31.

[111] X. López, J. J. Carbó, C. Bo, and J. M. Poblet, "Structure, properties and reactivity of polyoxometalates: A theoretical perspective," *Chemical Society Reviews*, vol. 41, no. 22, p. 7537, 2012.

[112] L. Vilà-Nadal and L. Cronin, "Design and synthesis of polyoxometalate-framework materials from cluster precursors," *Nature Reviews Materials*, vol. 2, no. 10, p. 17054, Oct. 2017.

[113] D.-L. Long, E. Burkholder, and L. Cronin, "Polyoxometalate clusters, nanostructures and materials: From self assembly to designer materials and devices," *Chemical Society Reviews*, vol. 36, no. 1, pp. 105–121, Dec. 2006.

[114] Y. Nishimoto, D. Yokogawa, H. Yoshikawa, K. Awaga, and S. Irle, "Super-Reduced Polyoxometalates: Excellent Molecular Cluster Battery Components and Semipermeable Molecular Capacitors," *Journal of the American Chemical Society*, vol. 136, no. 25, pp. 9042–9052, Jun. 2014.

[115] J. B. Flanagan, S. Margel, A. J. Bard, and F. C. Anson, "Electron transfer to and from molecules containing multiple, noninteracting redox centers. Electrochemical oxidation of poly(vinylferrocene)," *Journal of the American Chemical Society*, vol. 100, no. 13, pp. 4248–4253, Jun. 1978.

[116] C. Rinfray, S. Renaudineau, G. Izzet, and A. Proust, "A covalent polyoxomolybdate-based hybrid with remarkable electron reservoir properties," *Chemical Communications*, vol. 50, no. 62, pp. 8575–8577, 2014.

[117] J. Liu, Z. Chen, S. Chen, B. Zhang, J. Wang, H. Wang, B. Tian, M. Chen, X. Fan, Y. Huang, T. C. Sum, J. Lin, and Z. X. Shen, ""Electron/Ion Sponge"-Like V-Based Polyoxometalate: Toward High-Performance Cathode for Rechargeable Sodium Ion Batteries," *ACS Nano*, vol. 11, no. 7, pp. 6911–6920, Jul. 2017.

[118] S.-S. Wang and G.-Y. Yang, "Recent Advances in Polyoxometalate-Catalyzed Reactions," *Chemical Reviews*, vol. 115, no. 11, pp. 4893–4962, Jun. 2015.

[119] S. Bhattacharya, W. W. Ayass, D. H. Taffa, T. Nisar, T. Balster, A. Hartwig, V. Wagner, M. Wark, and U. Kortz, "Polyoxopalladate-Loaded Metal–Organic Framework (POP@MOF): Synthesis and Heterogeneous Catalysis," *Inorganic Chemistry*, vol. 59, no. 15, pp. 10 512–10 521, Aug. 2020.

[120] C. Li, R. Cao, K. P. O'Halloran, H. Ma, and L. Wu, "Preparation, characterization and bifunctional electrocatalysis of an inorganic–organic complex with a vanadium-substituted polyoxometalate," *Electrochimica Acta*, vol. 54, no. 2, pp. 484–489, Dec. 2008.

[121] D. V. Jawale, F. Fossard, F. Miserque, V. Geertsen, A.-L. Teillout, P. de Oliveira, I. M. Mbomekallé, E. Gravel, and E. Doris, "Carbon nanotube-polyoxometalate nanohybrids as efficient electro-catalysts for the hydrogen evolution reaction," *Carbon*, vol. 188, pp. 523–532, Mar. 2022.

[122] D. Pan, J. Chen, W. Tao, L. Nie, and S. Yao, "Polyoxometalate-Modified Carbon Nanotubes: New Catalyst Support for Methanol Electro-oxidation," *Langmuir*, vol. 22, no. 13, pp. 5872–5876, Jun. 2006.

[123] G. Ji, Y. Wang, Q. Luo, K. Han, M. Xie, L. Zhang, N. Wu, J. Lin, S. Xiao, Y.-Q. Li, L.-Q. Luo, and C.-Q. Ma, "Fully Coated Semitransparent Organic Solar Cells with a Doctor-Blade-Coated Composite Anode Buffer Layer of Phosphomolybdic Acid and PEDOT:PSS and a Spray-Coated Silver Nanowire Top Electrode," *ACS Applied Materials & Interfaces*, vol. 10, no. 1, pp. 943–954, Jan. 2018.

[124] N. Aizawa, C. Fuentes-Hernandez, V. A. Kolesov, T. M. Khan, J. Kido, and B. Kippelen, "Simultaneous cross-linking and p-doping of a polymeric semiconductor film by immersion into a phosphomolybdic acid solution for use in organic solar cells," *Chemical Communications*, vol. 52, no. 19, pp. 3825–3827, 2016.

[125] Q. Zhu, B. Paci, A. Generosi, S. Renaudineau, P. Gouzerh, X. Liang, C. Mathieu, C. Rountree, G. Izzet, A. Proust, N. Barrett, and L. Tortech, "Conductivity via Thermally Induced Gap States in a Polyoxometalate Thin Layer," *The Journal of Physical Chemistry C*, vol. 123, no. 3, pp. 1922–1930, Jan. 2019.

[126] M. Vasilopoulou, E. Polydorou, A. M. Douvas, L. C. Palilis, S. Kennou, and P. Argitis, "Annealing-free highly crystalline solution-processed molecular metal oxides for efficient single-junction and tandem polymer solar cells," *Energy & Environmental Science*, vol. 8, no. 8, pp. 2448–2463, 2015.

[127] G. Dong, D. Xia, Y. Yang, L. Sheng, T. Ye, and R. Fan, "Keggin-Type $PMo_{11}V$ as a P-type Dopant for Enhancing the Efficiency and Reproducibility of Perovskite Solar Cells," *ACS Applied Materials & Interfaces*, vol. 9, no. 3, pp. 2378–2386, Jan. 2017.

[128] M. R. Horn, A. Singh, S. Alomari, S. Goberna-Ferrón, R. Benages-Vilau, N. Chodankar, N. Motta, K. K. Ostrikov, J. MacLeod, P. Sonar, P. Gomez-Romero, and D. Dubal, "Polyoxometalates (POMs): From electroactive clusters to energy materials," *Energy & Environmental Science*, vol. 14, no. 4, pp. 1652–1700, 2021.

[129] J. Friedl, M. V. Holland-Cunz, F. Cording, F. L. Pfanschilling, C. Wills, W. McFarlane, B. Schricker, R. Fleck, H. Wolfschmidt, and U. Stimming, "Asymmetric polyoxometalate electrolytes for advanced redox flow batteries," *Energy & Environmental Science*, vol. 11, no. 10, pp. 3010–3018, 2018.

[130] J.-J. Chen, L. Vilà-Nadal, A. Solé-Daura, G. Chisholm, T. Minato, C. Busche, T. Zhao, B. Kandasamy, A. Y. Ganin, R. M. Smith, I. Colliard, J. J. Carbó, J. M. Poblet, M. Nyman, and L. Cronin, "Effective Storage of Electrons in Water by the Formation of Highly Reduced Polyoxometalate Clusters," *Journal of the American Chemical Society*, vol. 144, no. 20, pp. 8951–8960, May 2022.

[131] J. C. Ye, J. J. Chen, R. M. Yuan, D. R. Deng, M. S. Zheng, L. Cronin, and Q. F. Dong, "Strategies to Explore and Develop Reversible Redox Reactions of Li–S in Electrode Architectures Using Silver-Polyoxometalate Clusters," *Journal of the American Chemical Society*, vol. 140, no. 8, pp. 3134–3138, Feb. 2018.

[132] S. Greiner, B. Schwarz, M. Ringenberg, M. Dürr, I. Ivanovic-Burmazovic, M. Fichtner, M. Anjass, and C. Streb, "Redox-inactive ions control the redox-activity of molecular vanadium oxides," *Chemical Science*, vol. 11, no. 17, pp. 4450–4455, 2020.

[133] D. P. Dubal, J. Suarez-Guevara, D. Tonti, E. Enciso, and P. Gomez-Romero, "A high voltage solid state symmetric supercapacitor based on graphene–polyoxometalate hybrid electrodes with a hydroquinone doped hybrid gel-electrolyte," *Journal of Materials Chemistry A*, vol. 3, no. 46, pp. 23 483–23 492, 2015.

[134] M. Palacios-Corella, K. Ghosh, E. Redondo, and M. Pumera, "Polyoxometalate-Enhanced 3D-Printed Supercapacitors," *ChemSusChem*, vol. 15, no. 23, p. e202201490, Dec. 2022.

[135] A. K. Cuentas-Gallegos, R. Martínez-Rosales, M. Baibarac, P. Gómez-Romero, and M. E. Rincón, "Electrochemical supercapacitors based on novel hybrid materials made of carbon nanotubes and polyoxometalates," *Electrochemistry Communications*, vol. 9, no. 8, pp. 2088–2092, Aug. 2007.

[136] X. Xu and S. Wei, "$(NH_4)_3PW_{12}O_{40}$-H_3PO_4 composites as efficient proton conductors at intermediate temperatures," *Journal of Materials Science & Technology*, vol. 37, pp. 128–134, Jan. 2020.

[137] O. Nakamura, T. Kodama, I. Ogino, and Y. Miyake, "High-Conductivity Solid Proton Conductors: Dodecamolybdophosphoric acid and Dodecatungstophosphoric acid crystals," *Chemistry Letters*, vol. 8, no. 1, pp. 17–18, Jan. 1979.

[138] A. Müller, E. Beckmann, H. Bögge, M. Schmidtmann, and A. Dress, "Inorganic Chemistry Goes Protein Size: A Mo_{368} Nano-Hedgehog Initiating Nanochemistry by Symmetry Breaking," *Angewandte Chemie International Edition*, vol. 41, no. 7, pp. 1162–1167, Apr. 2002.

[139] C. M. Granadeiro, D. Julião, S. O. Ribeiro, L. Cunha-Silva, and S. S. Balula, "Recent advances in lanthanide-coordinated polyoxometalates: From structural overview to functional materials," *Coordination Chemistry Reviews*, vol. 476, p. 214914, Feb. 2023.

[140] D. Yang, M. Babucci, W. H. Casey, and B. C. Gates, "The Surface Chemistry of Metal Oxide Clusters: From Metal–Organic Frameworks to Minerals," *ACS Central Science*, vol. 6, no. 9, pp. 1523–1533, Sep. 2020.

[141] B. Yu, X. Zhao, J. Ni, and F. Yang, "Multiscale assembly of polyoxometalates: From clusters to materials," *ChemPhysMater*, vol. 2, no. 1, pp. 20–29, Jan. 2023.

[142] A. Misra, K. Kozma, C. Streb, and M. Nyman, "Beyond Charge Balance: Counter-Cations in Polyoxometalate Chemistry," *Angewandte Chemie International Edition*, vol. 59, no. 2, pp. 596–612, Jan. 2020.

[143] T. Boyd, S. G. Mitchell, D. Gabb, D.-L. Long, Y.-F. Song, and L. Cronin, "POMzites: A Family of Zeolitic Polyoxometalate Frameworks from a Minimal Building Block Library," *Journal of the American Chemical Society*, vol. 139, no. 16, pp. 5930–5938, Apr. 2017.

[144] N. I. Gumerova and A. Rompel, "Polyoxometalates in solution: Speciation under spotlight," *Chemical Society Reviews*, vol. 49, no. 21, pp. 7568–7601, 2020.

[145] C. Kato, R. Machida, R. Maruyama, R. Tsunashima, X.-M. Ren, M. Kurmoo, K. Inoue, and S. Nishihara, "Giant Hysteretic Single-Molecule Electric Polarisation Switching above Room Temperature," *Angewandte Chemie*, vol. 130, no. 41, pp. 13 617–13 620, Oct. 2018.

[146] M. Guzel, Y. Torlak, H. Choi, and M. Ak, ""Perfect match" of the carbazole-based conducting polymer and polyoxometalate nanocomposite components for enhanced optical and electrical properties," *European Polymer Journal*, vol. 186, p. 111857, Mar. 2023.

[147] S. Mir, B. Yadollahi, and R. Omidyan, "Theoretical comparative survey on the structure and electronic properties of first row transition metal substituted Keggin type polyoxometalates," *Journal of Solid State Chemistry*, vol. 305, p. 122667, Jan. 2022.

[148] F. Steffler, G. F. De Lima, and H. A. Duarte, "The effect of the heteroatom (X=P, As, Si and Ge) on the geometrical and electronic properties of α-Keggin polyoxometalates (M=Mo, W and Nb) – A DFT investigation," *Journal of Molecular Structure*, vol. 1213, p. 128159, Aug. 2020.

[149] T. Minato, K. Suzuki, Y. Ohata, K. Yamaguchi, and N. Mizuno, "A modular synthesis approach to multinuclear heterometallic oxo clusters in polyoxometalates," *Chemical Communications*, vol. 53, no. 54, pp. 7533–7536, 2017.

[150] T. Minato, D. Salley, N. Mizuno, K. Yamaguchi, L. Cronin, and K. Suzuki, "Robotic Stepwise Synthesis of Hetero-Multinuclear Metal Oxo Clusters as Single-Molecule Magnets," *Journal of the American Chemical Society*, vol. 143, no. 32, pp. 12 809–12 816, Aug. 2021.

[151] V. Sasca, M. Stefanescu, and A. Popa, "Thermal behavior of the polyoxometalates derived from $H_3PMo_{12}O_{40}$ and $H_4PVMo_{11}O_{40}$," *Journal of Thermal Analysis and Calorimetry*, vol. 72, no. 1, pp. 311–322, 2003.

[152] Z.-Y. Yao, Z.-H. Li, X.-L. Xie, Y. Zou, and X.-M. Ren, "Reversible crystal-amorphous transformation assisted by loss and adsorption of coordination water molecules and ionic conduction in two isomorphous decavanadate-type polyoxometalates," *Journal of Solid State Chemistry*, vol. 314, p. 123309, Oct. 2022.

[153] M. Fujibayashi, Y. Watari, R. Tsunashima, S. Nishihara, S.-i. Noro, C.-G. Lin, Y.-F. Song, K. Takahashi, T. Nakamura, and T. Akutagawa, "Structural Phase Transitions of a Molecular Metal Oxide," *Angewandte Chemie International Edition*, vol. 59, no. 50, pp. 22 446–22 450, Dec. 2020.

[154] C. Zhan, J. M. Cameron, D. Gabb, T. Boyd, R. S. Winter, L. Vilà-Nadal, S. G. Mitchell, S. Glatzel, J. Breternitz, D. H. Gregory, D.-L. Long, A. Macdonell, and L. Cronin, "A metamorphic inorganic framework that can be switched between eight single-crystalline states," *Nature Communications*, vol. 8, no. 1, p. 14185, Apr. 2017.

[155] A. J. Kibler, V. S. Souza, J. A. Fernandes, W. Lewis, S. P. Argent, J. Dupont, and G. N. Newton, "A Cooperative Photoactive Class-I Hybrid Polyoxometalate With

Benzothiadiazole–Imidazolium Cations," *Frontiers in Chemistry*, vol. 8, p. 612535, Jan. 2021.

[156] A. Proust, B. Matt, R. Villanneau, G. Guillemot, P. Gouzerh, and G. Izzet, "Functionalization and post-functionalization: A step towards polyoxometalate-based materials," *Chemical Society Reviews*, vol. 41, no. 22, pp. 7605–7622, Oct. 2012.

[157] M. Stuckart and K. Y. Monakhov, "Polyoxometalates as components of supramolecular assemblies," *Chemical Science*, vol. 10, no. 16, pp. 4364–4376, 2019.

[158] Y. Zhang, R. Tao, X. Zhao, Z. Sun, Y. Wang, and L. Xu, "A highly photoconductive composite prepared by incorporating polyoxometalate into perovskite for photodetection application," *Chemical Communications*, vol. 52, no. 16, pp. 3304–3307, 2016.

[159] N. Sun, A. Wu, Y. Yu, X. Gao, and L. Zheng, "Polyoxometalate-Based Photochromic Supramolecular Hydrogels with Highly Ordered Spherical and Cylindrical Micellar Nanostructures," *Chemistry – A European Journal*, vol. 25, no. 24, pp. 6203–6211, Apr. 2019.

[160] Y. Wang, Z. Chen, N. Li, H. Zhang, and J. Wei, "Programmable photo-responsive self-healing hydrogels for optical information coding and encryption," *European Polymer Journal*, vol. 166, p. 111025, Mar. 2022.

[161] L. Jiang, J. Li, N. Peng, M. Gao, D.-Y. Fu, S. Zhao, and G. Li, "Reversible stimuli responsive lanthanide-polyoxometalate-based luminescent hydrogel with shape memory and self-healing properties for advanced information security storage," *Polymer*, vol. 263, p. 125509, Dec. 2022.

[162] X. Yi, N. V. Izarova, M. Stuckart, D. Guérin, L. Thomas, S. Lenfant, D. Vuillaume, J. van Leusen, T. Duchoň, S. Nemšák, S. D. M. Bourone, S. Schmitz, and P. Kögerler, "Probing Frontier Orbital Energies of $\{Co_9(P_2W_{15})_3\}$ Polyoxometalate Clusters at Molecule–Metal and Molecule–Water Interfaces," *Journal of the American Chemical Society*, vol. 139, no. 41, pp. 14 501–14 510, Oct. 2017.

[163] N. Li, S. Fang, Z. Sun, R. Liu, and L. Xu, "Investigation on the photoconductivity of polyoxometalates," *RSC Advances*, vol. 6, no. 85, pp. 81 466–81 470, 2016.

[164] J. Tian, B. Jiang, H. Shao, Y. Wang, T. Wang, F. Li, D. Li, Y. Yang, and X. Dong, "A new strategy to one-step construct polyoxometalate/semiconductor one-dimensional tandem heterojunctions toward optimized conductometric sensing performances of ethanol gas," *Sensors and Actuators B: Chemical*, vol. 374, p. 132797, Jan. 2023.

[165] M. T. Pope and A. Müller, "Polyoxometalate Chemistry: An Old Field with New Dimensions in Several Disciplines," *Angewandte Chemie International Edition in English*, vol. 30, no. 1, pp. 34–48, Jan. 1991.

[166] J. Viljas, "Molecular electronics, a brief introduction," Jan. 2011.

[167] A. Kahn, "Fermi level, work function and vacuum level," *Materials Horizons*, vol. 3, no. 1, pp. 7–10, 2016.

[168] K. Y. Monakhov, "Implication of counter-cations for polyoxometalate-based nano-electronics," *Comments on Inorganic Chemistry*, pp. 1–10, Dec. 2022.

[169] S. Paul, A. Kanwal, and M. Chhowalla, "Memory effect in thin films of insulating polymer and C_{60} nanocomposites," *Nanotechnology*, vol. 17, no. 1, pp. 145–151, Jan. 2006.

[170] F. Paul, K. Nama Manjunatha, and S. Paul, "Non-Zero and Open-Loop Current–Voltage Characteristics in Electronic Memory Devices," *Advanced Electronic Materials*, vol. 9, no. 10, p. 2300324, Oct. 2023.

[171] D. Ma, M. Aguiar, J. A. Freire, and I. A. Hümmelgen, "Organic Reversible Switching Devices for Memory Applications," *Advanced Materials*, vol. 12, no. 14, pp. 1063–1066, Jul. 2000.

[172] L. D. Bozano, B. W. Kean, V. R. Deline, J. R. Salem, and J. C. Scott, "Mechanism for bistability in organic memory elements," *Applied Physics Letters*, vol. 84, no. 4, pp. 607–609, Jan. 2004.

[173] G. Li, N. Govind, M. A. Ratner, C. J. Cramer, and L. Gagliardi, "Influence of Coherent Tunneling and Incoherent Hopping on the Charge Transfer Mechanism in Linear Donor–Bridge–Acceptor Systems," *The Journal of Physical Chemistry Letters*, vol. 6, no. 24, pp. 4889–4897, Dec. 2015.

[174] J. Ouyang, *Emerging Resistive Switching Memories*, ser. SpringerBriefs in Materials. Cham: Springer International Publishing, 2016.

[175] N. Glezos, A. M. Douvas, P. Argitis, F. Saurenbach, J. Chrost, and C. Livitsanos, "Electrical characterization of molecular monolayers containing tungsten polyoxometalates," *Microelectronic Engineering*, vol. 83, no. 4-9, pp. 1757–1760, Apr. 2006.

[176] S. K. Ghosh, V. K. Perla, K. Mallick, and T. Pal, "Ammonium phosphomolybdate: A material for dielectric crossover and resistive switching performance," *Nanoscale Advances*, vol. 2, no. 11, pp. 5343–5351, 2020.

[177] S. N. S., N. Basu, M. Cahay, S. M. N., S. S. Mal, and P. P. Das, "Redox-Active Vanadium-Based Polyoxometalate as an Active Element in Resistive Switching Based Nonvolatile Molecular Memory," *physica status solidi (a)*, vol. 217, no. 18, p. 2000306, Sep. 2020.

[178] Y.-R. Huang, X.-L. Lin, B. Chen, H.-D. Zheng, Z.-R. Chen, H.-H. Li, and S.-T. Zheng, "Thermal-Responsive Polyoxometalate–Metalloviologen Hybrid: Reversible Intermolecular Three-Component Reaction and Temperature-Regulated Resistive Switching Behaviors," *Angewandte Chemie International Edition*, vol. 60, no. 31, pp. 16 911–16 916, Jul. 2021.

[179] A. M. Douvas, E. Makarona, N. Glezos, P. Argitis, J. A. Mielczarski, and E. Mielczarski, "Polyoxometalate-Based Layered Structures for Charge Transport Control in Molecular Devices," *ACS Nano*, vol. 2, no. 4, pp. 733–742, Apr. 2008.

[180] D. Velessiotis, A. Douvas, S. Athanasiou, B. Nilsson, G. Petersson, U. Södervall, G. Alestig, P. Argitis, and N. Glezos, "Molecular junctions made of tungsten-polyoxometalate self-assembled monolayers: Towards polyoxometalate-based molecular electronics devices," *Microelectronic Engineering*, vol. 88, no. 8, pp. 2775–2777, Aug. 2011.

[181] E. Makarona, E. Kapetanakis, D. Velessiotis, A. Douvas, P. Argitis, P. Normand, T. Gotszalk, M. Woszczyna, and N. Glezos, "Vertical devices of self-assembled hybrid organic/inorganic monolayers based on tungsten polyoxometalates," *Microelectronic Engineering*, vol. 85, no. 5-6, pp. 1399–1402, May 2008.

[182] G. Chaidogiannos, "Tunneling and negative resistance effects for composite materials containing polyoxometalate molecules," *Microelectronic Engineering*, vol. 73–74, pp. 746–751, Jun. 2004.

[183] S. M. Amoroso, C. Monzio Compagnoni, A. Mauri, A. Maconi, A. S. Spinelli, and A. L. Lacaita, "Semi-Analytical Model for the Transient Operation of Gate-All-Around Charge-Trap Memories," *IEEE Transactions on Electron Devices*, vol. 58, no. 9, pp. 3116–3123, Sep. 2011.

[184] M. Moors, J. Warneke, X. López, C. de Graaf, B. Abel, and K. Y. Monakhov, "Insights from Adsorption and Electron Modification Studies of Polyoxometalates on Surfaces for Molecular Memory Applications," *Accounts of Chemical Research*, vol. 54, no. 17, pp. 3377–3389, Sep. 2021.

[185] M. Vasilopoulou, A. M. Douvas, L. C. Palilis, S. Kennou, and P. Argitis, "Old Metal Oxide Clusters in New Applications: Spontaneous Reduction of Keggin and Dawson Polyoxometalate Layers by a Metallic Electrode for Improving Efficiency in Organic Optoelectronics," *Journal of the American Chemical Society*, vol. 137, no. 21, pp. 6844–6856, Jun. 2015.

[186] B. E. Petel, W. W. Brennessel, and E. M. Matson, "Oxygen-Atom Vacancy Formation at Polyoxovanadate Clusters: Homogeneous Models for Reducible Metal Oxides," *Journal of the American Chemical Society*, vol. 140, no. 27, pp. 8424–8428, Jul. 2018.

[187] Y.-X. Zhou, Y. Li, Y.-T. Su, Z.-R. Wang, L.-Y. Shih, T.-C. Chang, K.-C. Chang, S.-B. Long, S. M. Sze, and X.-S. Miao, "Nonvolatile reconfigurable sequential logic in a HfO_2 resistive random access memory array," *Nanoscale*, vol. 9, no. 20, pp. 6649–6657, 2017.

[188] A. M. Douvas, D. Tsikritzis, C. Tselios, A. Haider, A. S. Mougharbel, U. Kortz, A. Hiskia, A. G. Coutsolelos, L. C. Palilis, M. Vasilopoulou, S. Kennou, and P. Argitis, "Multi-electron reduction of Wells–Dawson polyoxometalate films onto metallic, semiconducting and dielectric substrates," *Physical Chemistry Chemical Physics*, vol. 21, no. 1, pp. 427–437, 2019.

[189] V. P. Georgiev, S. M. Amoroso, T. M. Ali, L. Vila-Nadal, C. Busche, L. Cronin, and A. Asenov, "Comparison Between Bulk and FDSOI POM Flash Cell: A Multiscale Simulation Study," *IEEE Transactions on Electron Devices*, vol. 62, no. 2, pp. 680–684, Feb. 2015.

[190] O. Badami, T. Sadi, F. Adamu-Lema, P. Lapham, D. Mu, V. Georgiev, J. Ding, and A. Asenov, "A Kinetic Monte Carlo Study of Retention Time in a POM Molecule-Based Flash Memory," *IEEE Transactions on Nanotechnology*, vol. 19, pp. 704–710, 2020.

[191] L. Vilà-Nadal, S. G. Mitchell, S. Markov, C. Busche, V. Georgiev, A. Asenov, and L. Cronin, "Towards Polyoxometalate-Cluster-Based Nano-Electronics," *Chemistry – A European Journal*, vol. 19, no. 49, pp. 16 502–16 511, Dec. 2013.

[192] P. Lapham, O. Badami, C. Medina-Bailon, F. Adamu-Lema, T. Dutta, D. Nagy, V. Georgiev, and A. Asenov, "A Combined First Principles and Kinetic Monte Carlo study of Polyoxometalate based Molecular Memory Devices," in *2020 International Conference on Simulation of Semiconductor Processes and Devices (SISPAD)*. Kobe, Japan: IEEE, Sep. 2020, pp. 273–276.

[193] S. Kan, K. Nakajima, T. Asai, and M. Akai-Kasaya, "Physical Implementation of Reservoir Computing through Electrochemical Reaction," *Advanced Science*, vol. 9, no. 6, p. 8, Feb. 2022.

[194] H. Chen and J. Fraser Stoddart, "From molecular to supramolecular electronics," *Nature Reviews Materials*, vol. 6, no. 9, pp. 804–828, Sep. 2021.

[195] D. Velessiotis, A. Douvas, P. Dimitrakis, P. Argitis, and N. Glezos, "Conduction mechanisms in tungsten-polyoxometalate self-assembled molecular junctions," *Microelectronic Engineering*, vol. 97, pp. 150–153, Sep. 2012.

[196] A. Balliou, M. Bouroushian, A. M. Douvas, G. Skoulatakis, S. Kennou, and N. Glezos, "Size-dependent single electron transfer and semi-metal-to-insulator transitions in molecular metal oxide electronics," *Nanotechnology*, vol. 29, no. 27, p. 275204, Jul. 2018.

[197] C. Huez, D. Guérin, S. Lenfant, F. Volatron, M. L. Perrin, A. Proust, and D. Vuillaume, "Redox-controlled conductance of polyoxometalate molecular junctions." *ACS Nano*, p. 37, 2022.

[198] C. Huez, S. Renaudineau, F. Volatron, A. Proust, and D. Vuillaume, "Experimental observation of the role of countercations in modulating the electrical conductance of Preyssler-type polyoxometalate nanodevices," *Nanoscale*, vol. 15, no. 25, pp. 10 634–10 641, 2023.

[199] B. Hu, C. Wang, J. Wang, J. Gao, K. Wang, J. Wu, G. Zhang, W. Cheng, B. Venkateswarlu, M. Wang, P. S. Lee, and Q. Zhang, "Inorganic–organic hybrid polymer with multiple redox for high-density data storage," *Chemical Science*, vol. 5, no. 9, pp. 3404–3408, 2014.

[200] D. Velessiotis, N. Glezos, and V. Ioannou-Sougleridis, "Tungstate polyoxometalates as active components of molecular devices," *Journal of Applied Physics*, vol. 98, no. 8, p. 084503, Oct. 2005.

[201] P. Muthumari, S. Thangarasu, and S. A. Bahadur, "Preparation and characterization of proton conducting polymer blend electrolytes (PVC/PMMA/NH_4SCN)," *Journal of Polymer Research*, vol. 28, no. 9, p. 332, Sep. 2021.

[202] N. Glezos, D. Velessiotis, G. Chaidogiannos, P. Argitis, D. Tsamakis, and X. Zianni, "Transport properties of polyoxometalate containing polymeric materials," *Synthetic Metals*, vol. 138, no. 1-2, pp. 267–269, Jun. 2003.

[203] S. Azhari, D. Banerjee, T. Kotooka, Y. Usami, and H. Tanaka, "Influence of junction resistance on spatiotemporal dynamics and reservoir computing performance arising from an SWNT/POM 3D network formed *via* a scaffold template technique," *Nanoscale*, vol. 15, no. 18, pp. 8169–8180, 2023.

[204] M. Akai-Kasaya, Y. Takeshima, S. Kan, K. Nakajima, T. Oya, and T. Asai, "Performance of reservoir computing in a random network of single-walled carbon nanotubes complexed with polyoxometalate," *Neuromorphic Computing and Engineering*, vol. 2, no. 1, p. 014003, Mar. 2022.

[205] H. Tanaka, M. Akai-Kasaya, A. TermehYousefi, L. Hong, L. Fu, H. Tamukoh, D. Tanaka, T. Asai, and T. Ogawa, "A molecular neuromorphic network device consisting of single-walled carbon nanotubes complexed with polyoxometalate," *Nature Communications*, vol. 9, no. 1, p. 2693, Jul. 2018.

[206] S. Wu, W. Zhou, K. Wen, C. Li, and Q. Gong, "Improved Reservoir Computing by Carbon Nanotube Network with Polyoxometalate Decoration," in *2021 IEEE 16th International Conference on Nano/Micro Engineered and Molecular Systems (NEMS)*, Apr. 2021, pp. 994–997.

[207] G. Zhang, Z.-Y. Xiong, Y. Gong, Z. Zhu, Z. Lv, Y. Wang, J.-Q. Yang, X. Xing, Z.-P. Wang, J. Qin, Y. Zhou, and S.-T. Han, "Polyoxometalate Accelerated Cationic Migration for Reservoir Computing," *Advanced Functional Materials*, vol. 32, no. 45, p. 2204721, Nov. 2022.

[208] K. Y. Monakhov, M. Moors, E. Vogelsberg, J. Lorenz, J. Warneke, and F. Yang, "Solution-Processable Molecular Oxides for Integrated Memories," in *2023 IEEE International Interconnect Technology Conference (IITC) and IEEE Materials for Advanced Metallization Conference (MAM)(IITC/MAM)*. Dresden, Germany: IEEE, May 2023, pp. 1–3.

[209] S. K. Petrovskii, M. Moors, S. Schmitz, E. V. Grachova, and K. Y. Monakhov, "Increasing the redox switching capacity of Lindqvist-type hexavanadates by organogold post-functionalisation," *Chemical Communications*, vol. 59, no. 62, pp. 9517–9520, 2023.

[210] N. Joo, S. Renaudineau, G. Delapierre, G. Bidan, L.-M. Chamoreau, R. Thouvenot, P. Gouzerh, and A. Proust, "Organosilyl/-germyl Polyoxotungstate Hybrids for Covalent Grafting onto Silicon Surfaces: Towards Molecular Memories," *Chemistry - A European Journal*, vol. 16, no. 17, pp. 5043–5051, Mar. 2010.

[211] F. Yang, M. Moors, D. A. Hoang, S. Schmitz, M. Rohdenburg, H. Knorke, A. Charvat, X.-B. Wang, K. Y. Monakhov, and J. Warneke, "On-Surface Single-Molecule Identification of Mass-Selected Cyclodextrin-Supported Polyoxovanadates for Multistate Resistive-Switching Memory Applications," *ACS Applied Nano Materials*, vol. 5, no. 10, pp. 14 216–14 220, Oct. 2022.

[212] M. Laurans, K. Dalla Francesca, F. Volatron, G. Izzet, D. Guerin, D. Vuillaume, S. Lenfant, and A. Proust, "Molecular signature of polyoxometalates in electron transport of silicon-based molecular junctions," *Nanoscale*, vol. 10, no. 36, pp. 17 156–17 165, 2018.

[213] F. Volatron, J.-M. Noël, C. Rinfray, P. Decorse, C. Combellas, F. Kanoufi, and A. Proust, "Electron transfer properties of a monolayer of hybrid polyoxometalates on silicon," *Journal of Materials Chemistry C*, vol. 3, no. 24, pp. 6266–6275, 2015.

[214] A. Gillet, S. Cher, M. Tassé, T. Blon, S. Alves, G. Izzet, B. Chaudret, A. Proust, P. Demont, F. Volatron, and S. Tricard, "Polarizability is a key parameter for molecular electronics," *Nanoscale Horizons*, vol. 6, no. 3, pp. 271–276, 2021.

[215] E. Vogelsberg, M. Moors, A. S. Sorokina, D. A. Ryndyk, S. Schmitz, J. S. Freitag, A. V. Subbotina, T. Heine, B. Abel, and K. Y. Monakhov, "Solution-Processed Formation of DNA-Origami-Supported Polyoxometalate Multi-Level Switches with Countercation-Controlled Conductance Tunability," *Chemistry of Materials*, vol. 35, no. 14, pp. 5447–5457, Jul. 2023.

[216] S. G. Mitchell, T. Boyd, H. N. Miras, D.-L. Long, and L. Cronin, "Extended Polyoxometalate Framework Solids: Two Mn(II)-Linked $\{P_8W_{48}\}$ Network Arrays," *Inorganic Chemistry*, vol. 50, no. 1, pp. 136–143, Jan. 2011.

[217] B. Chen, Y.-R. Huang, K.-Y. Song, X.-L. Lin, H.-H. Li, and Z.-R. Chen, "Molecular Nonvolatile Memory Based on $[\alpha\text{-}GeW_{12}O_{40}]^{4-}$/Metalloviologen Hybrids Can Work at High Temperature Monitored by Chromism," *Chemistry of Materials*, vol. 33, no. 6, pp. 2178–2186, Mar. 2021.

[218] T. Yamase, "Photo- and Electrochromism of Polyoxometalates and Related Materials," *Chemical Reviews*, vol. 98, no. 1, pp. 307–326, Feb. 1998.

[219] S. Yu, A. Tian, Q. Lu, X. Xu, S. Ma, X. Wang, and Z. Wang, "Polyoxometalate–Viologen Thermochromic Hybrids for Organic Amine Detectors and Memristors with Temperature-Regulating Resistance Switching Characteristics," *Inorganic Chemistry*, vol. 62, no. 4, pp. 1549–1560, Jan. 2023.

[220] A. Balliou, A. M. Douvas, P. Normand, D. Tsikritzis, S. Kennou, P. Argitis, and N. Glezos, "Tungsten polyoxometalate molecules as active nodes for dynamic carrier exchange in hybrid molecular/semiconductor capacitors," *Journal of Applied Physics*, vol. 116, no. 14, p. 143703, Oct. 2014.

[221] A. Balliou, G. Papadimitropoulos, G. Skoulatakis, S. Kennou, D. Davazoglou, S. Gardelis, and N. Glezos, "Low-Dimensional Polyoxometalate Molecules/Tantalum Oxide Hybrids for Non-Volatile Capacitive Memories," *ACS Applied Materials & Interfaces*, vol. 8, no. 11, pp. 7212–7220, Mar. 2016.

[222] A. Hiskia, A. Mylonas, and E. Papaconstantinou, "Comparison of the photoredox properties of polyoxometallates and semiconducting particles," *Chemical Society Reviews*, vol. 30, no. 1, pp. 62–69, 2001.

[223] J.-Y. Liu, X.-H. Zhang, H. Fang, S.-Q. Zhang, Y. Chen, Q. Liao, H.-M. Chen, H.-P. Chen, and M.-J. Lin, "Novel Semiconductive Ternary Hybrid Heterostructures for Artificial Optoelectronic Synapses," *Small*, p. 2302197, Jul. 2023.

[224] D. G. Georgiadou, Y.-H. Lin, J. Lim, S. Ratnasingham, M. A. McLachlan, H. J. Snaith, and T. D. Anthopoulos, "High Responsivity and Response Speed Single-Layer Mixed-Cation Lead Mixed-Halide Perovskite Photodetectors Based on Nanogap Electrodes Manufactured on Large-Area Rigid and Flexible Substrates," *Advanced Functional Materials*, vol. 29, no. 28, p. 1901371, Jul. 2019.

[225] J. Semple, G. Wyatt-Moon, D. G. Georgiadou, M. A. McLachlan, and T. D. Anthopoulos, "Semiconductor-Free Nonvolatile Resistive Switching Memory Devices Based on Metal Nanogaps Fabricated on Flexible Substrates via Adhesion Lithography," *IEEE Transactions on Electron Devices*, vol. 64, no. 5, pp. 1973–1980, May 2017.

[226] A. Kuhn and D. Martel, "Localized Electrodeposition by Patterned Redox-active Monolayers," *ChemPhysChem*, vol. 2, no. 11, pp. 688–691, Nov. 2001.

[227] S. Fletcher, C. Halliday, D. Gates, M. Westcott, T. Lwin, and G. Nelson, "The response of some nucleation/growth processes to triangular scans of potential," *Journal of Electroanalytical Chemistry and Interfacial Electrochemistry*, vol. 159, no. 2, pp. 267–285, Dec. 1983.

[228] T. K. Gupta, *Handbook of Thick- and Thin-Film Hybrid Microelectronics*, 1st ed. Wiley, Apr. 2003.

[229] D. Grosso, C. Boissière, and M. Faustini, "Thin Film Deposition Techniques," in *The Sol-Gel Handbook*, 1st ed., D. Levy and M. Zayat, Eds. Wiley, Sep. 2015, pp. 277–316.

[230] D. G. Georgiadou, J. Semple, A. A. Sagade, H. Forstén, P. Rantakari, Y.-H. Lin, F. Alkhalil, A. Seitkhan, K. Loganathan, H. Faber, and T. D. Anthopoulos, "100 GHz zinc oxide Schottky diodes processed from solution on a wafer scale," *Nature Electronics*, vol. 3, no. 11, pp. 718–725, Nov. 2020.

[231] S. Himeno and M. Takamoto, "Difference in voltammetric properties between the Keggin-type $[XW_{12}O_{40}]^{n-}$ and $[XMo_{12}O_{40}]^{n-}$ complexes," *Journal of Electroanalytical Chemistry*, vol. 528, no. 1-2, pp. 170–174, Jun. 2002.

[232] T. Rui Zhang, W. Feng, R. Lu, C. Yan Bao, X. Tong Zhang, T. Jin Li, Y. Ying Zhao, and J. Nian Yao, "Self assembly PMO_{12}^{3-}/$DODA^{+}$ composite superlattice thin films with photochromic properties," *Journal of Materials Science: Materials in Electronics*, vol. 13, no. 6, pp. 331–334, 2002.

[233] N. Elgrishi, K. J. Rountree, B. D. McCarthy, E. S. Rountree, T. T. Eisenhart, and J. L. Dempsey, "A Practical Beginner's Guide to Cyclic Voltammetry," *Journal of Chemical Education*, vol. 95, no. 2, pp. 197–206, Feb. 2018.

[234] T. Schoetz, L. Gordon, S. Ivanov, A. Bund, D. Mandler, and R. Messinger, "Disentangling faradaic, pseudocapacitive, and capacitive charge storage: A tutorial for the characterization of batteries, supercapacitors, and hybrid systems," *Electrochimica Acta*, vol. 412, p. 140072, Apr. 2022.

[235] I. Valov, E. Linn, S. Tappertzhofen, S. Schmelzer, J. Van Den Hurk, F. Lentz, and R. Waser, "Nanobatteries in redox-based resistive switches require extension of memristor theory," *Nature Communications*, vol. 4, no. 1, p. 1771, Apr. 2013.

[236] J.-J. J. Chen and M. A. Barteau, "Electrochemical Properties of Keggin-Structure Polyoxometalates in Acetonitrile: Effects of Countercation, Heteroatom, and Framework Metal Exchange," *Industrial & Engineering Chemistry Research*, vol. 55, no. 37, pp. 9857–9864, Sep. 2016.

[237] M. T. Pope and G. M. Varga, "Heteropoly Blues. I. Reduction Stoichiometries and Reduction Potentials of Some 12-Tungstates," *Inorganic Chemistry*, vol. 5, no. 7, pp. 1249–1254, Jul. 1966.

[238] S. Himeno, M. Takamoto, T. Ueda, R. Santo, and A. Ichimura, "Solvation effect of Li^+ on the voltammetric properties of $[PMo_{12}O_{40}]^{3-}$. part 2: Comparative studies on the preferential solvation in acetonitrile+s and acetone+s mixtures," *Electroanalysis*, vol. 16, no. 8, pp. 656–660, 2004.

[239] J. J. Altenau, M. T. Pope, R. A. Prados, and Hyunsoo. So, "Models for heteropoly blues. Degrees of valence trapping in vanadium(IV)- and molybdenum(V)-substituted Keggin anions," *Inorganic Chemistry*, vol. 14, no. 2, pp. 417–421, Feb. 1975.

[240] K. Maeda, S. Himeno, T. Osakai, A. Saito, and T. Hori, "A voltammetric study of Keggin-type heteropolymolybdate anions," *Journal of Electroanalytical Chemistry*, vol. 364, no. 1-2, pp. 149–154, Jan. 1994.

[241] K. Maeda, H. Katano, T. Osakai, S. Himeno, and A. Saito, "Charge dependence of one-electron redox potentials of Keggin-type heteropolyoxometalate anions," *Journal of Electroanalytical Chemistry*, vol. 389, no. 1-2, pp. 167–173, Jun. 1995.

[242] B. Keita and L. Nadjo, "New aspects of the electrochemistry of heteropolyacids," *Journal of Electroanalytical Chemistry and Interfacial Electrochemistry*, vol. 227, no. 1-2, pp. 77–98, Jul. 1987.

[243] H. Taketa, S. Katsuki, K. Eguchi, T. Seiyama, and N. Yamazoe, "Electronic structure and redox mechanism of dodecamolybdophosphate," *The Journal of Physical Chemistry*, vol. 90, no. 13, pp. 2959–2962, Jun. 1986.

[244] M. Sadakane and E. Steckhan, "Electrochemical Properties of Polyoxometalates as Electrocatalysts," *Chemical Reviews*, vol. 98, no. 1, pp. 219–238, Feb. 1998.

[245] K. Unoura, A. Iwashita, E. Itabashi, and N. Tanaka, "Catalytic Effects of Chlorate Ions on the Electrode Reaction Processes of 12-Molybdophosphate and 12-Molybdosilicate," *Bulletin of the Chemical Society of Japan*, vol. 57, no. 2, pp. 597–598, Feb. 1984.

[246] S. Karthäuser, B. Lüssem, M. Weides, M. Alba, A. Besmehn, R. Oligschlaeger, and R. Waser, "Resistive switching of rose bengal devices: A molecular effect?" *Journal of Applied Physics*, vol. 100, no. 9, p. 094504, Nov. 2006.

[247] A. Martin, B. Chang, J. Cutinho, L. Shen, T. Ward, E. W. Cochran, and M. M. Thuo, "Passivation-driven speciation, dealloying and purification," *Materials Horizons*, vol. 8, no. 3, pp. 925–931, 2021.

[248] J. F. Moulder, W. F. Stickle, P. E. Sobol, and K. D. Bomben, *Handbook of X-ray Photoelectron Spectroscopy: A Reference Book of Standard Spectra for Identification and Interpretation of XPS Data*, update ed., J. Chastain, Ed. Eden Prairie, Minn: Perkin-Elmer Corporation, 1992.

[249] M. Genovese, Y. W. Foong, and K. Lian, "The unique properties of aqueous polyoxometalate (POM) mixtures and their role in the design of molecular coatings for electrochemical energy storage," *Electrochimica Acta*, vol. 199, pp. 261–269, May 2016.

[250] B. Kruizinga, P. Wouters, and E. Steennis, "Accelerated aluminum corrosion upon water ingress in damaged low voltage underground power cables," in *9th International Conference on Insulated Power Cables (Jicable'15) 21-25 Juni 2015, Versailles, Paris, France*. s.n., 2015, pp. 1–5.

[251] Y. Wang, S. R. Narayanan, and W. Wu, "Field-Assisted Splitting of Pure Water Based on Deep-Sub-Debye-Length Nanogap Electrochemical Cells," *ACS Nano*, vol. 11, no. 8, pp. 8421–8428, Aug. 2017.

[252] S. Herculano-Houzel, "The human brain in numbers: A linearly scaled-up primate brain," *Frontiers in Human Neuroscience*, vol. 3, 2009.

[253] "Intel Builds World's Largest Neuromorphic System to Enable More Sustainable AI," https://www.intc.com/news-events/press-releases/detail/1691/intel-builds-worlds-largest-neuromorphic-system-to, Apr. 2024.

[254] Y. Noguchi, Y. Tanaka, Y. Miyazaki, N. Sato, Y. Nakayama, and H. Ishii, "Displacement Current Measurement for Exploring Charge Carrier Dynamics in Organic Semiconductor Devices," in *Physics of Organic Semiconductors*, 1st ed., W. Brütting and C. Adachi, Eds. Wiley, Nov. 2012, pp. 119–154.

[255] T. Yamada, Y. Noguchi, Y. Ouchi, and H. Ishii, "Displacement Current Measurement of MIS Devices with Ionic Liquids to Explore Carrier Behaviors in Model Interfaces of Organic Devices," *MRS Proceedings*, vol. 1286, pp. mrsf10–1286–e03–39, 2011.

[256] L. Wen and C. K. Ong, "Study of Short-Term and Long-Term Memories by Hodgkin–Huxley Memristor," *International Journal of Bifurcation and Chaos*, vol. 34, no. 02, p. 2450040, Feb. 2024.

[257] T. Ohno, T. Hasegawa, T. Tsuruoka, K. Terabe, J. K. Gimzewski, and M. Aono, "Short-term plasticity and long-term potentiation mimicked in single inorganic synapses," *Nature Materials*, vol. 10, no. 8, pp. 591–595, Aug. 2011.

[258] M. Yang, X. Zhao, Q. Tang, N. Cui, Z. Wang, Y. Tong, and Y. Liu, "Stretchable and conformable synapse memristors for wearable and implantable electronics," *Nanoscale*, vol. 10, no. 38, pp. 18 135–18 144, 2018.

[259] Y. Park and J.-S. Lee, "Artificial Synapses with Short- and Long-Term Memory for Spiking Neural Networks Based on Renewable Materials," *ACS Nano*, vol. 11, no. 9, pp. 8962–8969, Sep. 2017.

[260] P. Mateos-Aparicio and A. Rodríguez-Moreno, "The Impact of Studying Brain Plasticity," *Frontiers in Cellular Neuroscience*, vol. 13, p. 66, Feb. 2019.

[261] B. Rapp and R. W. Wiley, "Re-learning and remembering in the lesioned brain," *Neuropsychologia*, vol. 132, p. 107126, Sep. 2019.

[262] J. Simpson and W. Fitch, "Sensation," in *Applied Neurophysiology*. Elsevier, 1988, pp. 55–62.

[263] E. T. Walters, R. J. Crook, G. G. Neely, T. J. Price, and E. S. J. Smith, "Persistent nociceptor hyperactivity as a painful evolutionary adaptation," *Trends in Neurosciences*, vol. 46, no. 3, pp. 211–227, Mar. 2023.

[264] W. Lu and C. M. Lieber, "Nanoelectronics from the bottom up," *Nature Materials*, vol. 6, no. 11, pp. 841–850, Nov. 2007.

[265] C. D. Schuman, T. E. Potok, R. M. Patton, J. D. Birdwell, M. E. Dean, G. S. Rose, and J. S. Plank, "A Survey of Neuromorphic Computing and Neural Networks in Hardware," 2017.